

**AN ACOUSTIC METHOD FOR REAL TIME AIR BUBBLE DETECTION  
IN SIMULATED BLOOD VESSELS**

by

FRANCISCO IVAN VALENTIN RODRIGUEZ

A thesis submitted in partial fulfillment of the requirements for the degree of

MASTER OF SCIENCE

in

MECHANICAL ENGINEERING

UNIVERSITY OF PUERTO RICO  
MAYAGÜEZ CAMPUS

2012

Approved by:

---

Stefano Leonardi, PhD  
Member, Graduate Committee

---

Date

---

Gustavo Gutiérrez, PhD  
Member, Graduate Committee

---

Date

---

Silvina Cancelos, PhD  
President, Graduate Committee

---

Date

---

Barbara Calcagno, PhD  
Member, Graduate Committee  
Representative of Graduate Studies

---

Date

---

Gustavo Gutiérrez, PhD  
Chairperson of the Department

---

Date

Abstract of Dissertation Presented to the Graduate School  
Of the University of Puerto Rico in Partial Fulfillment of the  
Requirements for the Degree of Master of Science

**AN ACOUSTIC METHOD FOR REAL TIME AIR BUBBLE DETECTION  
IN SIMULATED BLOOD VESSELS**

by

FRANCISCO IVAN VALENTIN RODRIGUEZ

Chair: SILVINA CANCELOS

Major Department: MECHANICAL ENGINEERING

**ABSTRACT**

Exposure to significant changes in ambient pressure commonly occurs in divers during surfacing. These changes induce the formation of nitrogen bubbles in tissues and the presence of these bubbles can cause symptoms of decompression sickness (DCS) to appear. Existing methods to minimize the formation of bubbles include denitrogenation strategies and the use of decompression tables. Although these tables are calculated using large safety margins, they are not guaranteed and the occurrence of DCS has been reported even in those who followed suggested protocols. Therefore, the development of a system capable of monitoring bubble presence, number and size, in real time, would be a reliable method for DCS prevention.

In this work, we demonstrate a novel technique for bubble detection using a piezoelectric ring (PZT) placed around the human upper thigh and set to resonate at a specific frequency. Our approach uses microphones to monitor distortions in the resonant condition that were induced by the presence of bubbles.

A prototype of a simplified human upper thigh was built and bubbles of controlled size were injected into the artificial blood vessel. Using a digitalized data acquisition system, electrical signals on the PZT and microphone were acquired. The results suggested that the presence of a single bubble within the chamber disrupted the signal, displaying a peak in current and phase angles as the bubble crossed the actuation area of the PZT ring. For stationary bubbles, electrical admittance (measured as a function of frequency) demonstrated a higher Pearson correlation coefficient as the bubble was insonated near its resonance frequency than in the absence of bubbles. A summation of Fourier coefficients of voltage signals captured from the pill microphones in the presence of bubbles demonstrated a 94% accuracy in detecting single bubbles, when compared to signals taken in the absence of bubbles. It was concluded that the proposed system produced a measurable response to the presence of large bubbles.

Resumen de Disertación Presentado a Escuela Graduada  
De la Universidad de Puerto Rico como requisito parcial de los  
Requerimientos para el grado de Maestría en Ciencias

## **METODO ACUSTICO PARA LA DETECCION DE BURBUJAS DE SANGRE EN VASOS SANGUINEOS SIMULADOS EN TIEMPO REAL**

Por

FRANCISCO IVAN VALENTIN RODRIGUEZ

2012

Consejera: SILVINA CANCELOS

Departamento: INGENIERIA MECANICA

### **RESUMEN**

La exposición a cambios significativos en la presión ambiental es común en los buceadores al regresar a la superficie. Estos cambios inducen la formación de burbujas de nitrógeno en los tejidos y la presencia de estas burbujas provoca síntomas del Síndrome de Descompresión (DCS por sus siglas en inglés). Los métodos existentes para reducir la formación de burbujas incluyen estrategias como desnitrogenación y el uso de tablas de descompresión. A pesar de que éstas ofrecen valores que incluyen márgenes amplios de seguridad, la aparición de DCS se ha informado, incluso, en individuos que siguieron los protocolos sugeridos por las tablas. Por lo tanto, el desarrollo de un sistema capaz de dar seguimiento, en tiempo real, a la presencia, número y tamaño de burbujas sería un método confiable para la prevención de DCS.

En este trabajo, se presenta una técnica nueva para la detección de burbujas utilizando un anillo piezoeléctrico (PZT) colocado alrededor de la parte superior del muslo humano y que está fijado para resonar a una frecuencia específica. Nuestro método utiliza micrófonos para

monitorear las distorsiones en la condición de resonancia que fueron inducidas por la presencia de burbujas.

Se construyó un prototipo simplificado de la parte superior del muslo humano y se inyectaron burbujas de un tamaño controlado en el vaso sanguíneo artificial. Se utilizó un sistema digitalizado de adquisición de datos para obtener las señales eléctricas del PZT y del micrófono. Los resultados mostraron que la presencia de una sola burbuja dentro de la cámara distorsiona la señal, formando un pico en la corriente y en el ángulo de fase a medida que la burbuja cruza el área de actuación del anillo PZT. Para burbujas estacionarias, la admitancia eléctrica (medida como una función de la frecuencia) demostró un coeficiente de correlación de Pearson mayor para burbujas cerca de su frecuencia de resonancia que en la ausencia de ellas. La suma de coeficientes de Fourier de las señales de voltaje capturadas de los micrófonos en la presencia de burbujas, demostró una precisión de 94% en la detección de burbujas individuales, cuando se compara con las señales tomadas en la ausencia de burbujas. Se concluyó que el sistema propuesto produce una respuesta medible en la presencia de burbujas grandes.

Copyright © 2012

By

FRANCISCO IVAN VALENTIN RODRIGUEZ

To my family...

To my father, for teaching me two important lessons: to show passion for what I love and the true significance of sacrifice. To my mother, because she believed in me like no one else and she taught me to acknowledge my potential. To my uncle: for showing me the many ways to define “genius”. To my big sister: for showing me that there are many paths to achieve true genius. To my little sister: for showing me that there is beauty in the simplicity of life.

To my advisor, Silvina Cancelos, for I recognize in her great excellence and dedication and I have been taught to applaud this.

## **Acknowledgements**

I take this opportunity to thank all of those who were with me along this long journey. First, I mention those who made this work possible from the very beginning: Miguel Riccetti and Dr. Stefano Leonardi. I would like to express great gratitude to my fellow graduate companions and lab partners, especially Juan Carlos, for all the help I received from him with the experimental part of this work and Ronald Cruz, for his mayor contributions concerning the analytical solutions to my experimental problems. In addition, I would like to thank another group of friends who have become a big part of my life: Freddy, Luis Alexis and Carlos and other graduate students who have always been there to contribute ideas and offer support.

I sincerely appreciate the financial aid that I received from the following organizations and/or agencies, without which this research could not have been completed: the Deans' Office of Engineering, PR Space Grant Consortium, the Mechanical Engineering Department, the Rise 2 Best Program, NASA Ideas, the Department of Defense (DoD), the National Science Foundation (NSF), the Nuclear Regulatory Commission (NRC) and the National Institute of Health (NIH).

## Table of Contents

1	INTRODUCTION .....	1
1.1	Decompression Sickness.....	2
1.1.1	DCS Classification and Manifestation.....	3
1.2	DCS History.....	5
1.3	DCS in Puerto Rico.....	8
1.4	Problem Statement.....	9
1.5	Research Strategy and objectives.....	9
2	THEORETICAL BACKGROUND.....	12
2.1	Acoustic Waves .....	12
2.1.1	Propagation of sound in fluids .....	13
2.1.2	Propagation of sound in solids.....	15
2.1.2.1	Piezoelectricity .....	17
2.2	Bubble Dynamics.....	20
2.2.1.1	Acoustic Cavitation .....	22
2.2.1.2	Acoustic Streaming.....	24
2.2.1.3	Bjerknes Force.....	25
2.2.1.3.1	Bjerknes Force for a linear bubble response .....	27
2.2.1.4	Bubble extinction cross-section.....	28
2.3	Bubble Detection Methods .....	31
2.3.1	Current Bubble Detection Techniques.....	35
2.3.1.1	Ultrasound Imaging .....	35
2.3.1.2	Doppler Ultrasound .....	36
2.3.1.3	Second Harmonic Emissions.....	39
2.3.2	Bubble Formation in DCS .....	40
2.3.2.1	Nitrogen exchange under well-stirred tissue assumption .....	40
2.4	Theory and work related to Acoustic Chambers.....	44
2.4.1	Acoustic Chambers and Resonance Conditions .....	45
2.4.2	Bulk modulus difference in a bubbly liquid .....	47
2.4.3	Balance of forces on the bubble inside the acoustic chamber .....	51
3	EXPERIMENTAL DESIGN AND METHODOLOGY .....	54

3.1	Simplified Artificial Thigh Design .....	54
3.2	Bubble Generation System .....	61
3.3	Degassing Protocol .....	66
3.4	Expected artificial thigh response to bubbles leading to experimental protocols.....	69
3.5	Data Acquisition system .....	74
3.5.1	Resonance Frequency Identification.....	76
3.5.2	DSO3000 Oscilloscope interface: “Fixed sample size” transient experiments .....	78
3.5.3	LabVIEW code: “variable sample size” time analysis .....	79
3.6	Overview of Experiments Conducted.....	80
3.6.1	Pill Microphone Response to Bubble Presence at the resonance frequency of the artificial thigh.....	82
3.6.2	Piezoelectric Ring Response to Bubble Presence at the resonance frequency of the artificial thigh: “Fixed sample size” time analysis .....	83
3.6.2.1	Bubble breakage .....	84
3.6.3	Piezoelectric Ring Response to Bubble Presence at the resonance frequency of the artificial thigh: “Variable sample size” time analysis on the inner tubes .....	85
3.6.4	Piezoelectric Ring Response to Bubble Presence at the resonance frequency of the artificial thigh: “Variable sample size” time analysis on the outside of the inner tubes .....	86
3.6.5	Pill microphone and Piezoelectric ring response to excitation frequency in the vicinity of the bubble resonance frequency .....	87
4	NUMERICAL MODEL.....	88
4.1	Model Geometry and Boundary Conditions .....	88
4.2	Force on an oscillating bubble subjected to a stationary acoustic field.....	92
4.3	Analytical solution of the Wave equation.....	92
4.4	Numerical Bjerknes Force Distribution for the analytically solved geometry .....	93
4.5	Simulations Description.....	95
4.5.1	Coordinate Systems .....	96
4.5.2	Mesh Description .....	97
4.6	Numerical Results.....	101
4.6.1	Numerical Results: Harmonic Analysis.....	102
4.6.1.1	Electrical Measurements.....	116
4.6.1.2	Detailed Simulation Study inside the Vein and Artery .....	118
4.6.2	Numerical Results: System Response to Slug Flow .....	127
5	EXPERIMENTAL RESULTS AND ANALYSIS .....	137
5.1	Artificial Thigh Characterization.....	137
5.1.1	Determination of the Resonance Frequency .....	137

5.1.2	Comparison of Numerical and Experimental Results.....	142
5.1.3	Pill Microphone Characterization.....	145
5.2	Bubble Entrapment.....	147
5.3	Pill Microphone Response to Presence of Bubbles.....	153
5.3.1	Effect of multiple bubbles within the vein and artery on the pill microphone signal .....	153
5.3.2	Effect of a Single Bubble on the pill microphone voltage.....	155
5.3.2.1	Analyzing differences in pill microphone voltage signal induced by bubble presence.....	156
5.3.2.1.1	Signals Displaying lower signal difference amplitude.....	158
5.3.2.1.2	Signals Displaying higher signal difference amplitude.....	161
5.3.2.2	Analyzing voltage signal ratios.....	164
5.3.2.3	Fast Fourier Detection Analysis.....	169
5.3.2.3.1	Preliminary Results.....	171
5.3.2.3.2	Harmonic analysis through the use of Fast Fourier Transforms.....	173
5.3.2.3.2.1	Analyzing Fourier Component summations.....	178
5.3.2.3.2.2	Analyzing the Ratio of the Fourier Component of the Fundamental Frequency.....	181
5.3.2.3.2.3	Analyzing the Ratio of higher order harmonics.....	182
5.4	Piezoelectric Ring Response to Bubble Presence.....	183
5.4.1	Transient Effect of Large bubbles: Slug flow.....	184
5.4.2	Continuous bubble injection outside tubes.....	191
5.4.3	Current Analysis.....	195
5.5	System response around bubble resonant frequency.....	199
5.5.1	Piezoelectric Ring Response.....	200
5.6	Closing Remarks.....	206
6	CONCLUSIONS AND FUTURE WORK.....	208
6.1	Conclusions.....	208
6.2	Future Work.....	210
7	REFERENCES.....	212
	Appendix A.....	218
A.1	Linearized Wave Equation Derivation.....	218
A.2	Wave Equation generalization for any material described by a bulk modulus.....	220
A.3	Bjerknes Force Derivation.....	222
A.4	Piezoelectric Material Supplementary Information.....	223

A.5	Understanding the forced lightly damped oscillator through an electrical circuit comparison .....	229
A.6	Analytical solution for the wave equation in a hollow water cylinder surrounded by air .....	231
Appendix B	.....	253
B.1	Changes induced by the addition of acrylic flanges .....	253
B.2	Different material properties at outer cylinder.....	254
B.3	Simulations performed with two piezoelectric rings .....	257
B.4	Acoustic impedance boundary condition justification.....	258
B.5	Inner tube displacement .....	261
B.6	Mesh Refinement Analysis .....	264
B.7	Three dimensional analysis justification.....	268

## List of Tables

Table 3-1 Acoustic chamber specifications .....	60
Table 3-2 Specifications of the Bubble Generation System construction .....	62
Table 3-3 Average bubble sizes produces by different needles.....	64
Table 4-1 Frequencies obtained analytically for the first 4 resonance modes in Hz. ....	239
Table 4-2 Numerical resonance modes for the analytically solved problem.....	241
Table 4-3 Domain properties of the model. ....	96
Table 4-4 Vein and artery meshing parameters .....	98
Table 4-5 Meshing parameters under a “fine” meshing setting.....	99
Table 4-6 Meshing parameters under a “finer” meshing setting .....	99
Table 8-1 Frequencies obtained analytically for the first 4 resonance modes in Hz. ....	250
Table 9-1 Transmission and reflection coefficients between outer cylinder and flanges for different outer cylinder materials.....	256
Table 9-2 Transmission and reflection coefficients between the fluid and flanges for different flange materials.....	257
Table 9-3 "Coarser" mesh parameters as defined by COMSOL Multiphysics .....	264
Table 9-4 Estimated Resonance Frequency Percentage Difference per Refinement .....	265

## List of Figures

Figure 1-1 (a) and (b) depict MRIs of a cervical spine trailing decompression effects : a) 3 days after injury b)10 weeks after injury (Jallul et al., 2006); c) Bone x-ray that shows the effects of rapid decompression on the body (Shaikh & Ummunisa, 2009).....	3
Figure 1-2 Image: Diving tables including diving depth and time; closely watch diving instructions/assumption in the remember section [Joiner, 2009].....	6
Figure 1-3 (b) Image of the proposed model, including microphone and piezoelectric ring, and general positional schematic (a) [National Institute of Technology and Evaluation, Osaka] .....	11
Figure 2-1 Propagation of an acoustic perturbation (Nave, 2010).....	13
Figure 2-2 Acoustic Propagation in solids.....	16
Figure 2-3 Point source piezoelectric transducer and selected wave pressure profiles presenting the near and the far field area (Larson, 2001).....	18
Figure 2-4 Scattering cross-section of a bubble, where damping is assumed to be constant with frequency. Linear harmonic pulsations assumed (Leighton, 1994). .....	29
Figure 2-5 Change in bubble scattering and absorption cross sections across the bubble resonance threshold.....	29
Figure 2-6 Consecutive wave fronts emitted by moving source at an interval $\Delta t = T$ .....	37
Figure 2-7 Well-stirred or perfusion-limited model for nitrogen absorption in tissue .....	42
Figure 2-8 Blood-tissue nitrogen exchange .....	43
Figure 2-9 Top Image (A and B): Microphone signal with bubbles (B) and without bubbles (A), Bottom image(C and D) Fourier transforms of signals on Top image (Cancelos et al., 2010) ....	45
Figure 2-10 Forces acting on the bubble once inside the acoustic chamber.....	51
Figure 3-1 Cross Section of Human Thigh.....	55
Figure 3-2 Sketch of the acoustic chamber (Artificial Thigh) and bubble generation device interconnected.....	58
Figure 3-3 Numerical simulation of artificial thigh, rotated 2D axisymmetric model displaying wall deformation only. ....	59
Figure 3-4 Line graph displaying wall displacement at the system resonance frequency obtained from a 2-D axisymmetric simulation. The axial position displaying maximum deformation is shown by the arrow. B) The pill microphone was glued at this location, indicated by the arrow in (A). .....	59
Figure 3-5 Bubble Generation System.....	63
Figure 3-6 (A) Continuous bubble injection within the “bubble fitting”, estimated bubbles ranging from 70 to 250 $\mu\text{m}$ in diameter. (B) Histogram of Bubbles produced within the bubble fitting.....	65
Figure 3-7 Experimental setup including: acoustic chamber, bubble generation system, electrical components, bubble sizing equipment, fluid circulation diagram and degassing equipment.....	68
Figure 3-8 Bubble oscillating at higher modes, displaying an elevated deformation at the bubble’s wall.....	71
Figure 3-9 Bubble oscillations driven by a plan acoustic wave emitting acoustic emissions to be captured by pill microphone .....	72
Figure 3-10 Simplified equivalent R-L-C circuit describing motional impedance .....	73
Figure 3-11 Two typical conductance curves showing differences in resonance conditions due to changes in material properties .....	74

Figure 3-12 (A) Electrical configuration for pill microphone voltage readings. (B) Electrical configuration for admittance measurements. ....	75
Figure 3-13 Voltage Divider (A) Manufactured Voltage Divider (B) Circuit Diagram.....	75
Figure 3-14 Graphic Code Interface. LabVIEW code for resonance frequency identification and frequency response experiments .....	78
Figure 3-15 DS0 3000 Agilent oscilloscope interface showing signals captures in the oscilloscope on channels 1 and 2. “fixed sample size” time analysis readings were captured through this interface. ....	79
Figure 3-16 Lab View code to measure voltage, current and phase angle in the PZT ring used during “variable sample size” .....	80
Figure 3-17 Simplified artificial thigh test section mimicking actual thigh mechanical properties .....	81
Figure 4-1 Acoustic Chamber Simulated Model .....	89
Figure 4-2 Geometry of the problem .....	231
Figure 4-3 Analytical acoustic pressure field for $m=1, n=1, c=1490.56\text{m/s}$ and $f=16481.80\text{ Hz}$ .....	239
Figure 4-4 Analytical acoustic pressure field for $m=2, n=1, c=1490.56\text{ m/s}$ and $f=17034.22\text{ Hz}$ .....	240
Figure 4-5 Analytical acoustic pressure field for $m=1, n=2, c=1490.56\text{ m/s}$ and $f=33064.63\text{ Hz}$ .....	240
Figure 4-6 Analytical acoustic pressure field for $m=2, n=2, c=1490.56\text{ m/s}$ and $f=33343.43\text{ Hz}$ .....	241
Figure 4-7 Force in z-direction on a 1 mm in diameter bubble $F_z(r,z)$ for first resonance mode where: $m=1, n=1, c=1490.56\text{m/s}, f=16481.8\text{Hz}$ .....	94
Figure 4-8 Radial force on a oscillating 1mm in diameter bubble $F_r(r,z)$ for first resonance mode where: $m=1, n=1, c=1490.56\text{m/s}$ . Frequency: 16,381 Hz.....	94
Figure 4-9 A) PZT ring coordinate system B) Pill microphone coordinate system .....	97
Figure 4-10 Mesh Quality Plots for Numerical Model Mesh consisting of 1,185,922 elements A) Isometric and B) Top view .....	101
Figure 4-11 Pressure Amplitude graphs of two defined points inside the artificial thigh .....	103
Figure 4-12 Resonance Frequency of the structure corresponding to fundamental mode of the fluid: A) Top View, B) Isometric view frequency: 12,760 Hz. ....	106
Figure 4-13 Resonance Frequency of the structure corresponding to fundamental mode of the fluid: A) Top View, B) Isometric view, frequency: 13,010 Hz. ....	107
Figure 4-14 Resonance Frequency of the structure corresponding to fundamental mode of the fluid: A) Top View, B) Isometric view, frequency: 14,070 Hz. ....	108
Figure 4-15 Longitudinal (A) and Radial (B) Pressure Profiles at 12, 760 Hz. at vertical and horizontal lines on the outside of the inner tubes .....	109
Figure 4-16 Longitudinal (A) and Radial (B) Pressure Profiles at 13, 010 Hz. at vertical and horizontal lines on the outside of the inner tubes .....	110
Figure 4-17 Longitudinal (A) and Radial (B) Pressure Profiles at 14, 070 Hz., at vertical and horizontal lines on the outside of the inner tubes .....	111
Figure 4-18 Total surface displacement and Wall deformation at a frequency of 13,030 Hz. Isometric (A) and Top views (B). ....	113

Figure 4-19 Resonance Frequency of the structure displaying the acoustic pressure field corresponding to second longitudinal mode $m=2$ , $n=1$ and $f=15570$ Hz. Obtained through Eigen frequency analysis.....	114
Figure 4-20 Resonance Frequency of the structure displaying the acoustic pressure field corresponding to third fluid mode $m=1$ , $n=2$ and $f=26,977$ Hz. A) Top View B) Radial Distribution. Obtained through Eigen frequency analysis.....	114
Figure 4-21 Resonance Frequency of the structure displaying the acoustic pressure field corresponding to fourth fluid mode $m=2$ , $n=2$ and $f=30,455$ Hz. A) Isometric view B) Top view. Obtained through Eigen frequency analysis.....	115
Figure 4-22 Pressure Profile of third longitudinal mode (16.23 kHz); displaying 2 pressure nodes and 3 pressure antinodes. B) Bjerknes Force longitudinal distribution highlighting 2 bubble entrapment possibilities for bubbles with $r \geq 0.5$ mm. Simulations are a result of a harmonic analysis.....	115
Figure 4-23 Admittance of the PZT ring as a function of frequency.....	117
Figure 4-24 Gain as a function of frequency.....	117
Figure 4-25 Correspondence between fluid pressure and pill microphone voltage.....	118
Figure 4-26 Longitudinal pressure profiles taken inside and outside the artery at 13,010 Hz. ..	120
Figure 4-27 Acoustic Pressure Field inside the artery at 13.01 kHz, A) Front view, B) Top View.....	120
Figure 4-28 Longitudinal pressure profiles taken inside and outside the artery at 14,070 Hz. ..	121
Figure 4-29 A) Artery surface total displacement and volumetric deformation at 13.01kHz. ...	121
Figure 4-30 Frequency spectrum obtained from a FFT analysis of pressure profiles for a simpler geometry, displaying additional Fourier components affecting the pressure distribution inside the artery attributed to structural deformation.....	122
Figure 4-31 A) Pressure distribution outside the small tubes (Frequency 13.01 kHz) B) Bjerknes force distribution at the same location as the pressure distribution shown in A) displaying Bjerknes force nodes which correspond to bubble entrapment locations for a 0.5 mm radius bubble.....	124
Figure 4-32 A) Pressure distribution inside artery showing particular pressure nodes of these frequencies B) Bjerknes force distribution at the same location as the pressure distribution shown in A) displaying Bjerknes force nodes which correspond to bubble entrapment locations. At a frequency of 13,010 Hz.....	125
Figure 4-33 Bjerknes Radial Force at 13.01 kHz (N) Distribution at Hz. Inside the artery tube for a 1 mm equilibrium diameter bubble $\omega_0=6.4$ kHz.....	126
Figure 4-34 A) Pressure distribution adjacent to the small tube showing particular pressure nodes of these frequencies corresponding to experimentally observed nodes. B) Bjerknes force distribution at the same location as the pressure distribution shown in A) displaying Bjerknes force nodes corresponding to bubble entrapment locations.....	127
Figure 4-35 Tubes containing the air pocket simulating slug flow conditions. A) No air B) 1 mm air pocket C) 5 mm air pocket D) 10 mm air pocket E) 15 mm air pocket F) 25.07 mm air pocket G) 50 mm air pocket.....	129
Figure 4-36 Simulated geometry containing a 10 mm. air pocket.....	129
Figure 4-37 Longitudinal pressure profile inside the vein (half arterial change shown, due to symmetry) for different slug flow conditions at 13.01 kHz.....	131

Figure 4-38 Impedance Frequency Sweeps for different slug flows, highlighting the 14 to 14.5 kHz range, where the greatest difference can be observed, corresponding to an eigenfrequency of the PZT ring structure .....	131
Figure 4-39 Surface total displacement at 14.193 kHz obtained from an eigenfrequency analysis .....	132
Figure 4-40 A) PZT Ring impedance as a function of slug flow volume B) Selected air pocket volume range corresponding to 0.5 to 25.07 column heights. A power correlation between these two variables is presented. ....	133
Figure 4-41 Pill microphone voltage frequency Sweeps for different slug flows .....	135
Figure 4-42 Pill microphone voltage as a function of the air pocket volume at 12.78 kHz displaying a general decreasing trend .....	135
Figure 5-1 Electrical admittance as a function of frequency measured in the PZT Ring; showing average values for eight trials .....	138
Figure 5-2 Conductance as a function of frequency measured in the PZT Ring; showing average values for eight trials.....	138
Figure 5-3 Frequency response measured with the microphone pill .....	140
Figure 5-4 Correspondence of frequencies displaying maximum conductance (measured in the piezoelectric ring) and gain (measured in the pill microphone). ....	141
Figure 5-5 Admittance measured in the PZT Ring presenting admittance values higher than average values (each represent an average from three conducted trials).....	142
Figure 5-6 Comparisons of numerical and experimental admittance plots .....	144
Figure 5-7 Comparisons of numerical and experimental gain plots .....	145
Figure 5-8 Pill microphone RMS voltage as a function of time .....	146
Figure 5-9 Two images of a bubble entrapment due to the generated Bjerknes force within the artery like tubes, giving the opportunity to carry out measurements.....	148
Figure 5-10 A) Pressure distribution adjacent to the small tube showing particular pressure nodes of these frequencies corresponding to experimentally observed nodes. B) Bjerknes force distribution at the same location as the pressure distribution shown in A) displaying Bjerknes force nodes which correspond to bubble entrapment locations ( $R_0=0.5$ mm).....	149
Figure 5-11 Pressure inside acoustic chamber displaying similar fluid behavior on the outside and inside of the small tubes. A) At 8.09 kHz and B) at 9.24 kHz.....	150
Figure 5-12 Experimental Bubble displacement. Images captured with a resolution of 1200 x 300 pixels and at 600 fps .....	152
Figure 5-13 Representative image of the amount of bubbles present along the inner tubes during these readings.....	153
Figure 5-14 Upper: Clean signal driving the PZT. Lower: Perturbed signal due to the presence of multiple bubbles.....	154
Figure 5-15 Histogram of bubble sizes for single bubble experiments measuring the effect of single bubbles inside the vein and artery like tubes on the pill microphone voltage for a total of 250 experiments conducted.....	156
Figure 5-16 Pill microphone voltage signals taken in the absence of bubbles displaying a signal difference amplitude of 0.01 V. Time interval: 45 minutes.....	157
Figure 5-17 Bubble with a 0.66 mm radius within the “artery like” tubes. B) Bubble with a 454 $\mu$ m diameter. C) Signal Prior and Following Bubble injection from Bubble presented in (A). D) Signal Prior and Following Bubble injection from Bubble presented in (B). ....	159

Figure 5-18 A) Bubble with a 150 $\mu\text{m}$ radius within the “artery like” tubes. B) Bubble with a 558 $\mu\text{m}$ radius with resonant frequencies: 21,292 Hz and 5,740 Hz respectively. C) Signal Prior and Following Bubble injection from Bubble presented in (A). D) Signal Prior and following bubble injection presented in (B).....	162
Figure 5-19 Successive images of a violent oscillating bubble. Average radius: 264 $\mu\text{m}$ , $\omega_0 \approx 12.2$ kHz.....	163
Figure 5-20 Three trials presenting the normalized voltage as a function of bubble radius. Patterns where observed which could lead to bubble size to voltage signal correlation. ....	167
Figure 5-21 Readings obtained from wave generator at 5 V, 10 kHz (left) Fast Fourier Transform (Right).....	169
Figure 5-22 A) 3.2 mm diameter bubble near PZT ring B) Measured signal prior and after bubble presence C) Fast Fourier Transform of signals presented in (B) D) Difference between signals in (C) corresponding additional frequency components.....	172
Figure 5-23 Data for the (i) waveform and (ii) the corresponding spectra recorded at 1.0m from an ultrasound transducer faceplate operating in water at 1 MHz with a hydrophone (Leighton, 1994).....	173
Figure 5-24 A) Bubble radius: 0.890 mm B) FFT of the signal before and after injection of bubble in (A) C) Bubble radius: 0.630 mm D) FFT of the signal before and after injection of bubble in (C). Fourier components experiencing decreased amplitude in relation to the signal obtained before bubble injection.....	175
Figure 5-25 A) Bubble of 1.16 mm radius B) FFT Transforms of signal before and after injecting bubble in (A). C) Bubble radius: 0.431 mm D) FFT Transform of signal before and after injecting bubble in (C). Fourier components exhibit increased amplitude in relation to signals before bubble injection.....	176
Figure 5-26 A) Bubble radius: 0.303 mm B) FFT of the signal corresponding to bubble in (A).....	177
Figure 5-27 Sum of FFT Differences against bubble radius at transducer 1 located closest to the injected bubble.....	179
Figure 5-28 Sum of FFT Differences against bubble radius at transducer 2 located farther away from the injected bubble.....	179
Figure 5-29 Normalized sum of FFT (Eq. (5.8)) components as a function of bubble radius for three different trials totaling 93 measured bubbles.....	180
Figure 5-30 Slug Flow present within the artery-like tube (A), vein-like tube (B).....	186
Figure 5-31 Electric measurements on the PZT. Column of air injected in the “vein”. (A) Corresponds to current and (B) to the phase angle between the current and voltage in the PZT. ....	187
Figure 5-32 Two typical phase angle curves showing differences in resonance conditions due to changes in material properties.....	188
Figure 5-33 Three injected bubbles moving through the artery-like tubes.....	189
Figure 5-34 Current (A) and Phase angle (B) and Voltage (C) in the PZT ring as three bubbles move through the artery.....	190
Figure 5-35 Bubble injected outside the inner tubes forced towards the middle of the chamber ( $R_0 = 418$ $\mu\text{m}$ ).....	191
Figure 5-36 (A)Current and (B) Phase Readings, describing the continuous injection of bubbles into the artificial thigh. Seventeen bubbles were injected one at a time. A peak correspondence is highlighted.....	193

Figure 5-37 A) Bubble radius: 0.8855 mm for which current measurements were taken. B) Measurements comparing current values before and after bubble injection taken in the PZT ring highlighting high frequency components.....	196
Figure 5-38 Fast Fourier Transform of signals in Figure 0 37 displaying differences in Fourier components .....	197
Figure 5-39 Normalized current trend, including the analysis of 61 bubbles.....	199
Figure 5-40 Bubble around which frequency response analysis was carried out.....	201
Figure 5-41 Admittance in the PZT decreases upon sensing a bubble due to signal attenuation which intensifies damping. A higher correlation coefficient is also measured. ( $r_{\text{bubble}} > r_{\text{No}}$ ) ...	202
Figure 5-42 Phase angle variations due to changes in electrical inductance in the properties of the media due to the presence of a bubble. Higher correlation coefficient is calculated without bubbles. ( $r_{\text{No}} > r_{\text{bubble}}$ ) .....	202
Figure 5-43 A) Bubble object of analysis, radius: 0.6 mm Gain (B) and phase angle (C) in the pill microphone displaying similar correlation coefficients to the PZT ring analysis .....	204
Figure 5-44 A) Bubble object of analysis, radius: 0.6 mm Gain (B) and phase angle (C) in the pill microphone displaying adverse trend in correlation coefficients in comparison to the PZT ring analysis.....	205
Figure 8-1 Flow of water through nozzle; fluid velocity varies with location and with time. ...	218
Figure 8-2 Bulk Material .....	220
Figure 8-3 stationary volume element in the fluid.....	222
Figure 8-4 A) Simplified equivalent R-L-C circuit describing motional impedance B) Form of equivalent circuit separating elements with real and imaginary components.....	223
Figure 8-5 Piezoelectric material conductance .....	225
Figure 8-6 Piezoelectric material susceptance .....	225
Figure 8-7 Piezoelectric material admittance .....	226
Figure 8-8 Piezoelectric material phase angle .....	226
Figure 8-9 Piezoelectric material susceptance, $R_M=0$ .....	227
Figure 8-10 Piezoelectric material admittance, $R_M=0$ .....	227
Figure 8-11 Piezoelectric material phase angle, $R_M=0$ .....	228
Figure 8-12 Electrical circuit containing a resistor, a capacitor and an inductor in parallel; resembling a lightly damped oscillator system. ....	229
Figure 8-13 Geometry of the problem .....	242
Figure 8-14 Zeros of $f(x)$ , where $x = \sqrt{\alpha_n}$ .....	247
Figure 8-15 Analytical acoustic pressure field for $m=1, n=1, c=1490.56\text{m/s}$ and $f=10542.53\text{ Hz}$ .....	250
Figure 8-16 Analytical acoustic pressure field for $m=2, n=1, c=1490.56\text{m/s}$ and $f=11386.82\text{ Hz}$ .....	251
Figure 8-17 Analytical acoustic pressure field for $m=1, n=2, c=1490.56\text{m/s}$ and $f=25896.3\text{ Hz}$ .....	251
Figure 8-18 Analytical acoustic pressure field for $m=2, n=2, c=1490.56\text{m/s}$ and $f=26251.34\text{ Hz}$ .....	252
Figure 9-1 A) Structure with flanges, resonance frequency: 15,302 Hz B) No flanges, resonance frequency: 15, 452 Hz. Simulations product of 2D axisymmetric eigenfrequency analysis. ....	253
Figure 9-2 A) Glass outer cylinder, Frequency: 15,302 Hz B) Steel outer cylinder, Frequency: 15,318 Hz C) Acrylic outer cylinder, Frequency: 13, 145 Hz D) Acrylic outer cylinder, Frequency: 13, 518 Hz.....	255

Figure 9-3 Acoustic chamber with two piezoelectric rings. A) Frequency: 15, 850 Hz. B) Frequency: 14,260 Hz. C) Frequency: 29,310 Hz. D) Frequency: 30,610 Hz. ....	258
Figure 9-4 A) Geometry with the addition of the outer tubes B) Geometry whose outer boundary was defined by boundary conditions defined in (i) water acoustic impedance and (ii) $P=0$ . ....	259
Figure 9-5 Pressure Profile inside the inner tubes; A) Addition of outer tubes (geometry shown in .....	260
Figure 9-6 Inner tube deformation inside the artificial thigh at 14.07 kHz .....	261
Figure 9-7 Total artery displacement at 14.07 kHz .....	262
Figure 9-8 Fourier components of total displacement signal.....	262
Figure 9-9 Artery deformation shown as surface displacement (mm), Eigen frequency: 14.29 kHz.....	263
Figure 9-10 A) Tube total displacement and B) Fourier Transform of signal shown in (A).....	263
Figure 9-11 “Coarser” mesh. Starting mesh of mesh refinement analysis A) Isometric view B) Top view .....	266
Figure 9-12 Mesh after 3 mesh refinements. Number of elements: 1,214,717 .....	266
Figure 9-13 Zoom in of inner tubes area in the automatic refined mesh.....	267
Figure 9-14 User defined mesh consisting of three different meshing parameters throughout the structure. Total number of elements: 1,185,922 .....	267
Figure 9-15 Zoom in of inner tubes in the user defined mesh.....	268
Figure 9-16 Pill microphone structure and mesh.....	269
Figure 9-17 Inner tubes structure and mesh.....	269
Figure 9-18 Pressure profiles comparing symmetric (A) and non-symmetric (B) structures. Frequencies: 12,708 Hz and 12,694 Hz respectively.....	270

# 1 INTRODUCTION

As the human imagination challenges geographical and technological limitations, we become more eager to discover new horizons that are deeper into space. Each new voyage presents new challenges for human explorers; challenges that do not exclude technological and physiological limitations. The brave explorers who reach into space are exposed to great risk, including dangerous levels of radiation and changes in gravitational conditions. These risks can induce low muscular loading and decompression sickness, among others illnesses. These medical challenges must be dealt with if we are to be more successful at our endeavors to study space. Of the above mentioned illnesses, the focus of this research will be decompression sickness (DCS).

When the body is subjected to a sudden reduction of surrounding pressure, decompression sickness (DSC) may occur (Mathieu, 2006). This sickness occurs more frequently during deep sea diving or when flying in a non-pressurized aircraft, causing the formation of gas bubbles in blood and tissues. These gas bubbles can block or interfere with the blood flow and can be fatal if not treated quickly (Badash, 2008). Bubble size alone, is not indicative of the threat imposed; the location of the bubbles can mean the difference between a warning and a serious threat.

Monitoring the formation of bubbles that accumulate in the blood stream could contribute to providing a safer environment for explorers. In order to investigate decompression sickness, an environment that possesses conditions similar to those that lead to DCS in the human body must be recreated. In order to identify said conditions, we must understand the nature of this sickness.

## 1.1 Decompression Sickness

DCS is a condition caused when inert gases (mainly nitrogen) which are normally dissolved in the blood, rapidly leave their solution state due to a sudden drop in barometric pressure, causing the formation of bubbles (Brown and Antuñano, 2010). Pressure gradients affect only compressible substances. The human body is primarily made of water, which can be considered to be non-compressible. However, the gases in hollow spaces, such as bowels, as well as those dissolved in the blood are at the mercy of pressure changes such as those experimented during extra vehicular activities (EVA) or sub-aquatic activities. It is during these ventures that humans are subjected to risks, including exposure to atmospheric pressure, at fractions of normal conditions or well above them, when under sea level.

Figure 1-1(a) and Figure 1-1(b) depict examples of tissues damaged as a consequence of decompression sickness in two distinct locations within the body of a diver. Figure 1-1(a) illustrates an MRI of the cervical spine taken 3 days post injury. Figure 1-1(b) presents an axial view of the same region, 10 weeks after the accident. The arrows are used to illustrate the site where DCS caused disk herniation. Figure 1-1(c) depicts possible sites of vascular air embolisms possibly leading to DCS symptoms. The symptoms and the severity of the illness depend on the location of the air bubble.

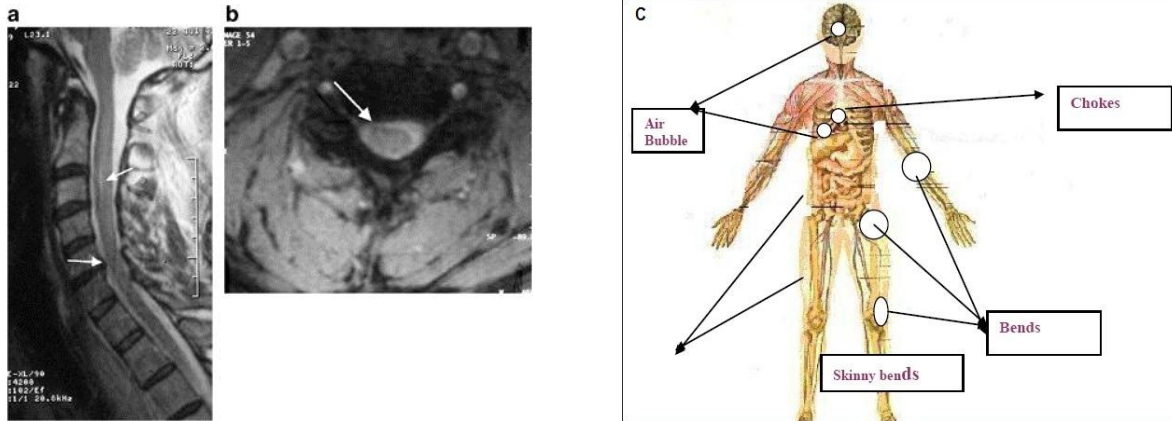


Figure 1-1 (a) and (b) depict MRIs of a cervical spine trailing decompression effects : a) 3 days after injury b) 10 weeks after injury (Jallul et al., 2006); c) Bone x-ray that shows the effects of rapid decompression on the body (Shaikh & Ummunisa, 2009).

### 1.1.1 DCS Classification and Manifestation

In general, DCS can be characterized into two types; each type can be identified due to their respective symptoms, the organ systems affected and their severity.

Type I includes cases with musculoskeletal manifestations (pain), cutaneous or lymphatic involvement and more diffuse symptoms such as malaise, anorexia and fatigue (Chapel, 2006). DCS presents itself in its initial state and it is not associated to any particular body region (mostly tissue and skeletal joints). Cutaneous and musculoskeletal manifestations of DCS are most commonly characterized by tissue swelling and limb pain (usually in or in close proximity to synovial joints) respectively. Most pathophysiology hypotheses propose that musculoskeletal and cutaneous DCS arise as a result of autochthonous bubble formation. The exact location of these bubbles and the mechanisms causing pain remain debated (Francis & Mitchell, 2003).

Type II is a progressive state generally associated with symptoms presented in the central nervous system and or cardiorespiratory system (“chokes”). Cardiopulmonary DCS though rare, represents one of the potentially lethal forms of DCS. “Chokes” are believed to be caused by severe accumulation of gas bubbles in the pulmonary capillaries (Balladin et al., 2002) and are

mostly generated after very aggressive exposures. The first symptoms usually occur shortly after decompression. If left untreated, the condition might progressively lead to reduced cardiac output, cardiac arrest and death (Francis & Mitchell, 2003).

Concerning neurologic DCS referring to a direct effect upon the nervous central system, the most common symptoms include sensorial disturbances like paresthesias and numbness (Dick & Massey, 1985). The primary targets of decompression induced injury in the nervous system involve the spinal cord (Francis et al., 1988) and the brain. Animal studies performed by Francis et al. (1990), presented that 77% of the cases of the central nervous decompression sickness corresponded to bubble formation in the white matter of the spinal cord of these animals. Possible mechanisms leading to spinal cord injuries include mechanical damage caused by the bubble on the nerve cell axons and inflammatory responses induced by the bubble surface; (Francis et al., 1990; Broome et al., 1994) while cerebrum and cerebellum damage has been mainly attributed to arterial gas emboli (Reuter et al., 1997; Warren et al., 1988).

Furthermore, inflammatory responses to gas bubbles might manifest themselves in symptoms like: headache, fatigue, flu-like symptoms and diffuse muscular Pain. Additional Type II DCS appearances display: vertigo, nausea, vomiting, tinnitus, nystagmus and impaired hearing (Francis & Mitchell, 2003). Pure oxygen mask treatment might be enough to alleviate Type I DCS however, a hyperbaric chamber is needed for the more severe Type II. Cavitation of such nitrogen nucleated bubbles will also result in bone and joint deterioration (Mathieu, 2006). This classification is a useful clinical setting for treatment.

## 1.2 DCS History

The existence of decompression sickness, its causes and its symptoms have been known for centuries. Earliest work observing the formation of bubbles under decompression can be attributed to Boyle in the late 1600's. The first actual DCS cases (Caisson Disease) were reported in 1841, where it was observed in coal miners exposed to air-pressurized mine shafts (Brown & Antuñano, 2010). Still this phenomenon remained undescribed until 1878 when Paul Bert, a French physiologist known as the "Father of Aviation Medicine", recognized the role of bubble formation in DCS and provided the initial scientific understanding of the phenomenon (Bove, 1997). His work laid the foundation to further DCS pathophysiology study in the late 1900's. Bert's hypothesis relating bubbles presence as a necessary factor in DCS was central in Haldane's theory who provided a most extensive description of the dynamics of the dissolved gases (Boycott et al., 1908).

J. S. Haldane (1908) proposed scheme argued that a bubble-free environment would exist as long as the super-saturation ratio did not exceed some critical value; where super-saturation was defined as the ratio of tissue nitrogen tension to absolute pressure. Haldane presented a model consisting of 5 tissues each with their respective perfusion rates. The nitrogen diffusion model, refers to what is nowadays described as: well-stirred or perfusion-limited compartments; with effectively instantaneous diffusion of nitrogen between blood and tissue (additional information concerning Nitrogen Exchange in Perfusion-Limited Tissue will be provided in Chapter 2). Through these models, Haldane concluded that slow linear ascending methods, accepted at the time, were both unsafe and unnecessarily long. He then suggested an alternative method, which he called stage decompression. The stages were chosen so that a 2:1 pressure ratio was never exceeded in any tissue (Admiralty Report: Deep Water Diving, 1907).



attainable for rate of gas transfer out of the body. Most of the computer algorithms used to develop these tables, subdivide the body into a series of compartments into which the flow and absorption of nitrogen is modeled (Francis & Gorman, 1993).

Researchers continued associating bubbles formed under decompression to DCS symptoms; thus encouraging the development of ultrasonic techniques to observe bubbles in stationary tissue and vasculature as well as bubbles moving within the blood flow (Ribosow & Mackay, 1971; Daniels et al., 1980; Daniels, 1984). Moving bubbles are commonly observed through the use of Doppler ultrasound devices (Nishi et al., 2003). Despite several limitations, which will be addressed later in this chapter, Doppler continues being the most practical method to use for bubble detection on a large scale (Chapel, 2006). In the next chapter literature in relation to bubble detection through the use of acoustic techniques is presented and discussed.

Up to date, the only satisfactory treatment for DCS is recompression therapy. Once the diagnosis is made, the patient should be transported as quickly as possible to a recompression chamber where appropriate therapy can be administered according to current protocols. This involves putting the victim back under pressure to reduce the size of the bubbles which should cause them to dissolve. Additionally, oxygen can be administered directly to hypoxic tissues. This type of treatment is performed in a recompression chamber, but can sometimes be accomplished in the water if a chamber cannot be reached in a reasonable period of time. The more recently developed oxygen treatment tables pressurize the patient with air, but oxygen is available for breathing by mask. The increased oxygen partial pressure provides life-sustaining oxygen to tissues compromised by bubbles.

Current research demonstrates DCS symptoms depend upon the bubbles ultimate location and not their origin. Bubbles arising from diverse body organs exhibit the exact same effects

since they are eventually led to the arterial circulation system. These findings have proven to be advantageous; concluding that the treatment method of bubble related diseases is predominantly related to the symptoms and their severity, rather than the source of the bubbles. In the long run, new treatment protocols have concurred on the same initial treatments: recompression to 60 FSW or the designated pressure under 60 feet of salt water (guide).

Currently, Doppler and other ultrasound methods continue being examined and considered as potential techniques to effectively diagnose decompression in humans. Each of them exhibits similar approaches by initially considering peak bubble grades (based on bubble quantity and amplitude of signals based on a pre-established datum) and then differentiating between different profiles. However, no simple evidence suggests correlations between bubble grade and DCS symptoms have been suggested (Nishi, 1993).

### **1.3 DCS in Puerto Rico**

For a local deep sea diver, Ahmed Pérez, the occurrence of DCS is common place. Even though he is a commercial diver, statistics show a growing trend in the frequency of DCS symptoms in both commercial and recreational diving (Pollock et al., 2003). Local divers complain of experiencing headaches, articular pain and facial discomfort. These symptoms are a precondition to DCS and are treated with home remedies such as the use of oxygen masks and a doses of aspirin. If the condition worsens, it requires scarce and expensive medical treatment with a decompression chamber. At the moment, Puerto Rico and surrounding islands have only four (4) operating decompression chambers.

## **1.4 Problem Statement**

All studied methods, currently possess an applicability limitation; none of them have been designed as a portable instrument capable of providing real time measurements, without interfering with operational procedures. In general, the equipment is large and very costly, thus restricting it to laboratory use.

Existing technologies are unable to monitor real time bubble nucleation associated with this disease. In addition, existing treatment methods are not capable of detecting bubble presence without bubble motion, or are only capable of detecting them after such bubbles have reached a determined size where DCS symptoms might have already occurred (Nishi, 1993). Early detection of bubble nucleation is beneficial and necessary since small bubbles subjected to growth are a potential cause of DCS. The development of improved and individualized diagnostic strategies for DCS, aside from existing methods would be highly advantageous. A need for the creation of a system and instrumentation which is able to detect both size and bubble number would lower risks and thus improve working conditions far beyond actual existing bubble detection technologies.

## **1.5 Research Strategy and objectives**

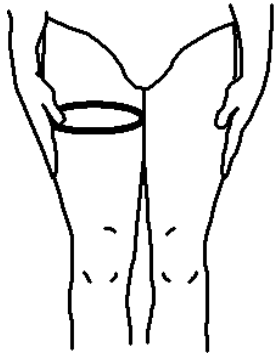
An alternate, non-invasive air bubble detection system is presented here. The discussed method explores differences in the fluid media bulk acoustic properties induced by the presence of bubbles within a complicated geometrical system. A simulated experimental set-up that mimics in a very simplified manner the passage of bubbles within the arteries or veins of a human thigh was built. The environment was developed based on research in acoustic chamber designs (Cancelos et al., 2005). The device to be worn by the explorer, will offer a real time

description of the bubble population and bubble passage determined in a respective study area, which will depend on the device actuation range. Information regarding this specific area could then be extended to provide estimations on global bubble sizes and number in the body of the subject. This will create a detection system that takes into account the fact that susceptibility to DCS varies greatly among subjects. The proposed detection system, as can be observed in Figure 1-3, would be considered a breakthrough over existing procedures since it would allow for individualized attention and offer a prevention method tailored to the subjects working limits.

It is the purpose of this work to test the viability of the proposed method as a technically feasible device to detect bubble presence and characterize a bubble population in human extremities on a range of bubbles sizes including the sub-millimeter scale. Several bubble detection schemes will be designed and implemented through the use of the same experimental setup. Each technique will be evaluated based on their bubble sensing capabilities within our artificial thigh. A correlation between bubble presence and/or size to electrical signal will be attempted. The type of correlation attempted depends on the bubble detection method to be utilized. The analysis might take into consideration patterns obtained in the frequency spectrum of bubbles resonating at their specific resonant frequency and deviations from standard resonant conditions inside a simplified artificial thigh based on electrical measurements. The presented work aims to determine which bubble detection scheme is the most appropriate to be used in conjunction to our innovative bubble detection device. If a successful method is attained it would be possible to design and develop a bubble detection and sizing instrument that could be implemented to monitor in real time the presence, size and amount of nitrogen bubbles in the bloodstream and tissue. This device could be worn by astronauts during EVA or by divers during subaquatic activities. Such a device is intended to be worn without interrupting working

conditions in an attempt to secure or increase the safety of the subject, thus preventing the dangers of Decompression Sickness. Such a device would beneficially impact space agencies and it can also be implemented in subaquatic activities.

a)



b)



Figure 1-3 (a) Image of the proposed model, including microphone and piezoelectric ring, and general positional schematic (b) [National Institute of Technology and Evaluation, Osaka]

## 2 THEORETICAL BACKGROUND

### 2.1 Acoustic Waves

Sound refers to mechanical waves propagating in a medium. This term, which goes as far back as 550 B.C., was originally considered the sensation of “sound” due to mechanical activation of the ear drum. Later on, these concepts pertaining to the study of sound, its generation, transmission, and the reception of energy as vibrational waves in matter became known as acoustics. Since then, the acoustic phenomenon has been observed in numerous situations including: musical instruments, vibrating strings and water waves (Enflo & Hedberg, 2004). Through these real-life models, evidence was collected that sustains the view of sound as a wave traveling in a medium; its propagation limited exclusively to the presence of a medium.

Acoustic waves, like all waves, describe the propagation of some kind of disturbance with a velocity characteristic of the medium. This disturbance might be observed in the form of height variations (in the case of a water waves) or pressure fluctuations (in the case of sound). When particles in a medium are displaced from their equilibrium position, internal restoration forces arise. The combination of these internal forces with the inertial tendencies of the particles, sum up to obtain an oscillatory motion (Auld, 1990). A mathematical description of the physics of acoustics evolved around the wave equation which was named after D’Alembert who derived its one-dimensional form for the string motion. Linear acoustics, modeled by D’Alembert’s equation, have had an eminent success in describing most acoustic phenomena. The one-dimensional wave equation description of the behavior of sinusoidal waves holds as long as the amplitude of the wave is quite small in comparison to the wavelength. Thus the requirement:  $\partial y/\partial x \ll 1$  where  $\partial x/\partial y$  itself must be a sinusoidal function (Towne, 1967) where

$y$  is the amplitude of the wave (whether it be: displacement, pressure, etc.) as it propagates through a distance  $x$ . This restriction is known as: The small slopes approximation.

### 2.1.1 Propagation of sound in fluids

Two fundamental elements ensure acoustic transmission: a source (emitter) and a propagation medium. Waves can either be transverse or longitudinal. Transverse waves define a particle displacement perpendicular to the direction of propagation while, for longitudinal waves, particle displacement occurs in the direction of propagation. In liquids, the two types of waves always coexist, even though the longitudinal vibrations are dominant (Bruneasu, 2006).

Acoustic waves propagate by means of adiabatic compression and decompression of particles as can be observed in Figure 2-1. In order for a wave to travel, individual elements in the fluid move back and forth in the direction of the restoring forces produced as the fluid is compressed or expanded due to pressure changes. This movement can be considered as changes in density of the continuum medium, which exhibit patterns of adjacent regions of compression and rarefaction (see Figure 2-1).

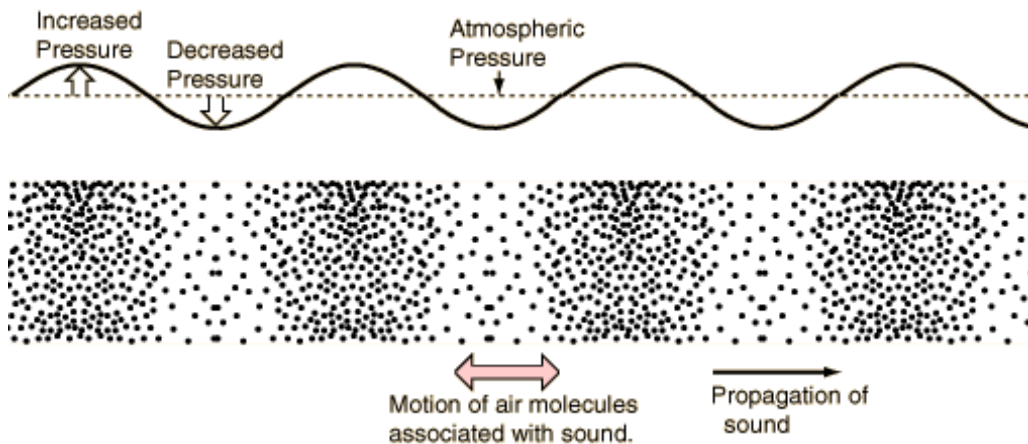


Figure 2-1 Propagation of an acoustic perturbation (Nave, 2010)

A certain compressibility of the fluid is necessary in order for the propagation of an acoustic perturbation to occur. Changes in density however, are small compared to the equilibrium value. This implies that density is a function of location and time. Consequently, it depends on spatial variations of the velocity field, and on the velocity of the volume element (Bruneau, 2006).

A one dimensional model of wave propagation relating time, space and pressure variables is given by Eq. (2.1).

$$\frac{\partial^2 p}{\partial x^2} - \frac{1}{c^2} \frac{\partial^2 p}{\partial t^2} = 0 \quad (2.1)$$

where  $p$  is sound pressure in Pa,  $x$  is particle position in m,  $c$  is speed of sound in m/s and  $t$  is time in s.

This well-known acoustic wave equation is obtained by combining the mass and momentum conservation equations. One of many possible derivations is provided in Appendix A.1. D'Alembert gave the general solution for the wave equation. With a dimensionalized sound pressure with  $p' = p/p_0$ , a solution would take the form:  $p = R_1 \cos(\omega t - kx) + R_2 - R_3 \cos(\omega t + kx)$  where  $\omega$  is angular frequency in rad/s,  $t$  is time in s,  $k$  is the wave number in  $\text{rad}\cdot\text{m}^{-1}$ , and  $R_i$  is a non-dimensional coefficient.

Equation (2.1), can be extended into a three dimensional environment. Pressure in a fluid domain will then be described by the wave equation according to:

$$\frac{1}{\rho_0 c^2} \frac{\partial^2 p}{\partial t^2} + \nabla \cdot \left( -\frac{1}{\rho_0} \nabla p \right) = 0 \quad (2.2)$$

Here  $\rho_0$ ,  $c$ , and  $p$  denote fluid density, speed of sound in the fluid, and the acoustic pressure respectively. The wave equation (Eq.(2.2)) is obtained by combining the mass and momentum conservation equations under the assumptions of small perturbations, irrotational flow, lossless fluid and isentropic equations of state. A detailed derivation of the linearized wave equation for any material characterized by a bulk modulus is also provided in Appendix A.2.

By assuming that Eq.(2.2) is separable in both time and space, for which it is necessary that the initial boundary conditions are separate as well, a solution can be represented using complex variables, as:  $p = p(x)e^{j\omega t}$  with  $\omega = 2\pi f$  (rad/s) being the angular frequency, where  $f$  (Hz) denotes frequency; thus arriving at the well-known homogeneous Helmholtz equation:

$$\nabla \cdot \left( -\frac{1}{\rho_0} \nabla p \right) - \frac{\omega^2 p}{\rho_0 c^2} = 0. \quad (2.3)$$

In addition to Eq. (2.3), a lossy media description can be obtained through the addition of a first order time derivative, where the coefficient  $d_a$  depends on the fluid viscosity, introduced in order to model attenuation of sound waves (Cancelos et al., 2005):

$$\frac{1}{\rho_0 c^2} \frac{\partial^2 p}{\partial t^2} - d_a \frac{\partial p}{\partial t} + \nabla \cdot \left( -\frac{1}{\rho_0} \nabla p \right) = 0. \quad (2.4)$$

### 2.1.2 Propagation of sound in solids

Unlike in fluids, in solids, any given excitation will result in an acoustic wave composed of a longitudinal and a transverse component. In solids, a number of different types of sound waves are possible since molecular vibration is supported in multiple directions. Bruneau (2006) describes the types of vibrations observed in solids in very simple terms. Figure 2-2 shows that if particle A (the arrows denote particle displacement) is set in a time-dependent motion, adjacent particle B will be excited via bonding forces with a little delay. In this case, particle A

will be the driving source for particle B, particle B being the source for particle C and so on. This type of pattern will be reproduced by the adjacent particles (Bruneau, 2006).

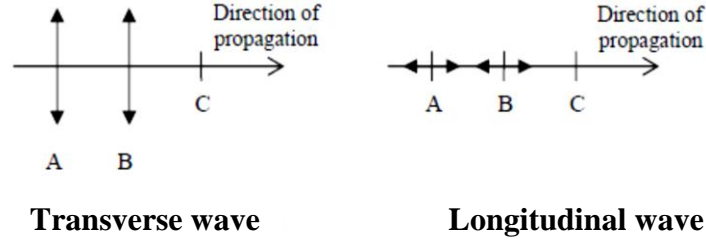


Figure 2-2 Acoustic Propagation in solids

The description of particle motion in a solid in the absence of external forces is obtained by applying conservation of momentum to an elastic solid. By doing this the equation known as the elastic wave equation is derived:

$$\rho \frac{\partial^2 u}{\partial t^2} - \nabla(\underline{T}) = 0 \quad (2.5)$$

where  $\rho$  is the mass density of the material,  $\underline{T}$  represents Cauchy's stress tensor and  $u$  denotes particle displacement.

As it was assumed for the liquid medium, a similar complex time-harmonic solution,  $u(x, y, z, t) = u(x, y, z)e^{j\omega t}$  with  $\omega = 2\pi f$  being the angular frequency is proposed, which leads to the homogeneous Helmholtz equation:

$$-\rho\omega^2 u - \nabla \cdot (\underline{T}) = 0 \quad (2.6)$$

Considering all solid domains as elastic solids; Hooke's law can be applied. Neglecting temperature variations the most general linear relation between stress and strain tensors expressed as a constitutive equation can be written as:

$$\underline{T} = \underline{c} : \underline{S}, \quad (2.7)$$

where  $\underline{T}$  has already been defined,  $\underline{c}$  is a fourth-order elasticity tensor and  $\underline{S}$  is the strain tensor,

which for small deformations can be defined as

$$\underline{S} = \frac{1}{2}(\nabla u + \nabla u^T) \quad (2.8)$$

By replacing Eq. (2.8) and Eq. (2.7) in Eq. (2.6) the wave equation for the displacement in a solid is obtained.

$$\rho \omega^2 u - \nabla \cdot \left( \underline{c} : \frac{1}{2}(\nabla u + \nabla u^T) \right) = 0 \quad (2.9)$$

The homogeneous Helmholtz equation Eq. (2.6) is, thus, solved in all elastic solid domains.

Equations (2.3) and (2.9) describe the propagation of an acoustic wave through their respective mediums. These equations alone define the behavior within the fluid and the structural domains respectively. In the case of fluid/structure interaction, a coupling between these regions must be defined in order to correctly describe and compute the continuation of the acoustic wave throughout the entire region of interest. This coupling is achieved through the accurate selection of boundary conditions; thus introducing a physical connection between both domains. A full description of this boundary condition will be presented in Chapter 4.

### ***2.1.2.1 Piezoelectricity***

Sound waves propagate differently in a particular kind of solid known as piezoelectric material. Piezoelectric materials mainly consist of Lead-Zirconate-Titanate (PZT) and are capable of becoming generating an electric current when they are strained. This effect is known as the direct piezoelectric effect. External stresses to the crystalline structure of the material alter the symmetry of the crystal thus creating ionic charges responsible for generating an electric field (Jordan & Ounaies, 2001).

Conversely, when an electric field is applied to piezoelectric material, polarized molecules inside the material align themselves with the electric field, resulting in induced dipoles within the molecular structure of the material. This alignment of molecules will cause the material to change dimensions.

Piezoelectricity is found in applications such as the production and detection of sound, generation of high voltages, electronic frequency generation, microbalances, and ultrafine focusing of optical assemblies. Piezoelectric devices fit into four general categories, depending on the type of physical effect used: generators, sensors, actuators, and transducers.

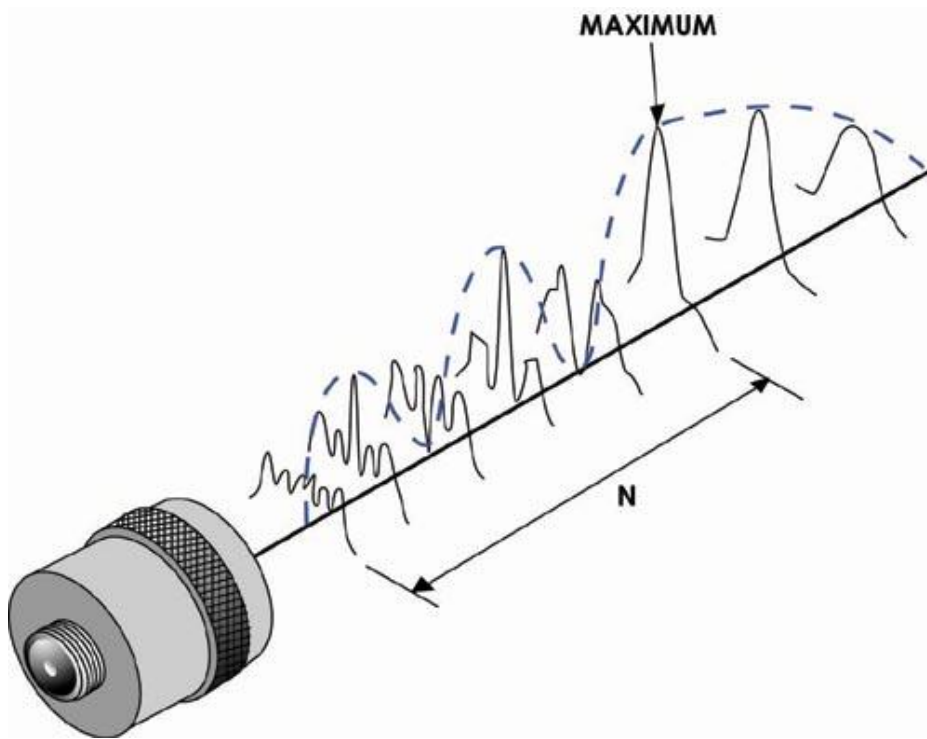


**Figure 2-3 Point source piezoelectric transducer and selected wave pressure profiles presenting the near and the far field area (Larson, 2001)**

Figure 2-3 presents pressure waves and selected pressure profiles distributed along the actuation area of a piezoelectric transducer. The sound that emanates from a piezoelectric transducer does not originate from a point, but instead originates from most of the surface of the

piezoelectric element. Since the sound originates from a number of points along the transducer face, wave interference leads to extensive fluctuations in the sound intensity near the source. This area, known as the near field, is one of high acoustic variations making it extremely difficult to accurately evaluate flaws in materials positioned within this area.

At the end of the near field, however, the pressure waves combine to form a relatively uniform front. This uniform area is known as the far field. In the far field, the beam spreads out in a pattern originating from the center of the transducer. The area just beyond the near field is where the sound wave is well behaved and it has its maximum strength. Therefore, optimal detection results will be obtained when flaws occur in this area (Larson, 2001).

Piezoelectricity assumes linear coupling between the strain and the electric field and this is taken into account through the constitutive equations, which can be expressed in stress-charge form as:

$$\underline{\underline{T}} = \underline{\underline{c}}_E \underline{\underline{S}} - \underline{\underline{e}}_T \underline{\underline{E}} \quad (2.10)$$

$$\underline{\underline{D}} = \underline{\underline{e}} \underline{\underline{S}} + \underline{\underline{\epsilon}}_S \underline{\underline{E}}, \quad (2.11)$$

where  $\underline{\underline{T}}$  is the stress tensor,  $\underline{\underline{\epsilon}}$  is the strain tensor,  $\underline{\underline{E}}$  is the electric field,  $\underline{\underline{D}}$  is the electrical displacement field,  $\underline{\underline{c}}_E$  is the elasticity matrix (four order stiffness tensor),  $\underline{\underline{e}}$  is the third order piezoelectric stress tensor,  $\underline{\underline{\epsilon}}_S$  is the second order permittivity tensor of the material, and subscripts  $S$ ,  $T$ , and  $E$  denote properties measured at constant strain, stress and electric field respectively. Supplementary information concerning piezoelectric material description is provided in Appendix A.3.

## 2.2 Bubble Dynamics

### 2.2.1 Bubbles in Equilibrium Conditions

In this section we briefly introduce and discuss topics involved in the generation and maintenance of a bubble under equilibrium conditions in a fluid. Bubbles grow from the gas held in solutions through gas exchange processes. In order for bubble formation to take place a continuous equilibrium must exist between gas content in the atmosphere and the nucleation sites. The kinetics of this gas exchange process determines how quickly the gas concentration within a possible nucleation site responds to perturbations to this equilibrium, for example, an atmospheric pressure change.

The kinetics of bubble stabilization can be described through the Laplace equation. This equation describes the balance of normal stresses across the bubble interphase.

$$\sum_1^N p_i = p_{amb} + \frac{2\sigma}{R_0}. \quad (2.12)$$

The terms on the left-hand side act to cause the bubble to expand and those on the right-hand side act to collapse the bubble. In this expression  $p_i$  is the partial pressure of the gases inside the bubble  $p_{amb}$  is the ambient pressure acting on the bubble through the liquid,  $\sigma$  is the surface tension and  $R$  is the radius of curvature of the gas-liquid interface. In the case of a reduction in ambient pressure, and of bubbles formed in aqueous media,  $p_v$  would be included in the left hand summation; where  $p_v$  is the partial vapor pressure of the liquid in which the bubble is suspended and would be taken as the vapor saturation pressure at  $T_\infty$  ( $T_\infty$  is the temperature far from the bubble.) (Chapel, 2006).

When a spherical bubble is stable, the left and right hand side of Eq. (2.12) will be equal. However, in most situations, there is a transfer of gas between the bubble and the surrounding fluid. The direction of this transfer is controlled by the respective gas concentrations across the bubble interfaces and can be studied through Fick's law. In the case of DCS, for example, a reduction in pressure causes the total pressure of gases and vapor inside the bubble to be greater than the ambient pressure. These conditions could be used to describe the fluid as super-saturated fluid, thus inducing conditions leading to bubble growth. Under decompression, the kinetics will thus determine the degree and duration of the super-saturation of air found in the tissues and blood (Chapel, 2006).

## 2.2.2 Bubble subjected to an acoustic pressure field

### 2.2.2.1 Rayleigh-Plesset Equation

Considering a spherical bubble in a liquid medium in absence of thermal effects, the Rayleigh-Plesset equation can be used to determine radial fluctuations of gas and vapor filled bubbles when they are subject to pressure fluctuations (Brennen, 1995),

$$\frac{p_v - P(t)}{\rho_0} + \frac{p_{G_0}}{\rho_0} \left( \frac{R_0}{R} \right)^{3k} = R \frac{d^2 R}{dt^2} + \frac{3}{2} \left( \frac{dR}{dt} \right)^2 + \frac{4\nu_0}{R} \frac{dR}{dt} + \frac{2\sigma}{\rho_0 R} \quad (2.13)$$

where  $P(t)$  is the total pressure outside the bubble (neglecting gravity effects),  $p_{G_0}$  and  $R_0$  are the partial pressure of gas inside the bubble and the bubble radius at the initial time  $t=0$ ;  $\rho_0$ ,  $\nu_0$ ,  $\sigma$ , and  $k$  are the fluid density, kinematic viscosity, surface tension of the liquid and polytropic gas constant;  $R$  is the instantaneous radius of the bubble.

If the initial radius is the equilibrium radius ( $R_E$ ), hence  $p_{G_0} = p_{G_E}$  and the equilibrium condition at interface gives:

$$P_v - P(t) + p_{G_E} - \frac{2\sigma}{R_E} = 0 \quad (2.14)$$

Replacing Eq. (2.13) in Eq. (2.12) we obtain:

$$\frac{p_v - P(t)}{\rho_0} + \frac{p_{G_E}}{\rho_0} \left( \frac{R_E}{R} \right)^{3k} = R \frac{d^2 R}{dt^2} + \frac{3}{2} \left( \frac{dR}{dt} \right)^2 + \frac{4v_0}{R} \frac{dR}{dt} + \frac{2\sigma}{\rho_0 R} \quad (2.15)$$

Using a first order Taylor series approximation to linearize Eq. (2.15), neglecting second order terms, and simplifying; we obtain:

$$\frac{d^2 \tilde{R}}{dt^2} + \frac{4v_0}{R_E^2} \frac{d\tilde{R}}{dt} + \frac{1}{\rho_0 R_E^2} \left( 3kp_{G_E} - \frac{2\sigma}{R_E} \right) \tilde{R} + \frac{p}{\rho_0 R_E} = 0 \quad (2.16)$$

Where  $R(t) = R_0 + R_\varepsilon$  and  $P(t) = p_0 + p(t)$ , being  $p_0$  the pressure in the fluid in the absence of a sound field. Eq. (2.16) will provide a solution for the instantaneous bubble radius, based on the instantaneous acoustic pressure. Eq. (2.16) can then be used to calculate the magnitude of forces experienced by a bubble affected by an acoustic pressure field.

A variety of phenomena are observed when a bubble is subjected to an acoustic pressure field, including: radiation force interaction, rectified diffusion, surface wave activity, microstreaming, subharmonic emissions and chaotic oscillations. These are directly linked to forces experienced by the bubble due to volume oscillations.

### **2.2.1.1 Acoustic Cavitation**

Cavitation was first broadly defined as the formation of a vapor cavity, created from the expansion of existing surfaces (Apfel, 1984). This definition was extended to include any observable activity involving a bubble that is stimulated into motion by an acoustic field. Examples of cavitation were observed both in passive cavitation and gas body activation. Passive cavitation included situations in which the bubble oscillation itself excited the sound

wave instead of the usual opposite phenomenon. Gas body activation included gas cavities which were often not spherical and that oscillated in response to an acoustic field (Miller, 1984).

Specifically, acoustic cavitation can be described as the creation of new surfaces obtained from pre-existing gas nuclei or as the shape modification (including expansion, contraction and distortion) of cavities found within the body of a liquid. These shape oscillations occur during a process known to be coupled to acoustic energy (Leighton, 1994). The acoustic energy creates acoustic fields which take their form as acoustic waves that reflect themselves in strong pressure fluctuations evoking dramatic bubble reactions, such as changes in shape, acoustic emission and sonoluminescence among others.

The action of initiating acoustic cavitation in a homogeneous liquid can be seen as the action of tearing the liquid apart. The newly formed cavity is then filled with a liquid vapor or any gas dissolved in the liquid. However, this can only be achieved if the generated tension within the liquid is equal or greater than the tensile strength of the liquid. Generally, two wide debatable divisions exist for acoustic cavitation: stable or non-inertial cavitation and transient or inertial cavitation.

Stable cavitation is characterized by the repetitive nature of low energy oscillations. In this passive type of acoustic cavitation, bubbles can be expected to generate sound through linear free oscillations and affect the propagation of sound through the medium. On the other hand, transient or inertial cavitation is characterized by conditions where bubble collapse phenomena are controlled by inertial forces generated by the spherical compression of the liquid. In this type of cavitation, bubble growth to many times their initial size is observed, followed by violent collapses to a minimum size. Definitions exist offering ratios of the work done on the bubble

over dissipative losses; as well as a ratio between the maximum expansion radius and the equilibrium radius exceeding a value of 2 (Leighton, 1994).

Other models have been formulated, including the one by Leeman and Vaughan (Vaughan and Leeman, 1989), in which they suggested subdividing acoustic cavitation into 3 classes: subsonic, gas phase and liquid phase cavitation. These divisions were based on the velocity of the wall of the bubble in relation to the speed of sound. However, the conventional classification discussed previously still stands.

In the interest of bubble detection in humans, a low-amplitude sound field should be generated, thus bubbles will pulsate at low amplitudes and the process can be considered stable cavitation. Many of the phenomena observed under stable cavitation do involve nonlinearities; however a linearization of the analysis is often necessary due to increased complexity. All bubble oscillations are non-linear, only due to the amplitude of this oscillation can they be considered to be linear (Leighton, 1994).

### ***2.2.1.2 Acoustic Streaming***

Under cavitation the events known as: streaming and microstreaming also manifest themselves. As the wave travels through a medium, and encounters an obstacle (such as a bubble), the wave will experience a loss in momentum absorbed by the bubble. A force will be generated in the direction of the sound field, due to this momentum gradient. This force will cause flow acceleration in the direction of wave propagation. The flow generated from any acoustically oscillating object present within an aqueous media (Leighton, 1994) is known as acoustic streaming.

The characteristic behavior of acoustically oscillating objects has been employed as a mixing enhancer for specific fluid mixing applications where the acoustically oscillating object

agitates the surrounding fluid (Liu et al., 2002). In particular, when small scale bubbles in a liquid are subject to acoustic oscillation, Reynolds stresses are induced on the surface of the bubble, thus producing an oscillatory boundary layer around the bubble surface (Lee et al., 2011). This type of time dependent circulation is only observed in this layer. The case of small scale bubbles, the acoustic oscillation is known as cavitation microstreaming; a term suggesting the small size of the acting boundary layer and not necessarily micron scale bubbles. The microstreaming boundary layer is defined as:

$$L_{ms} = \sqrt{2\eta/\rho_0\omega} \quad (2.17)$$

where  $\eta$  is the fluid shear viscosity.

Bubble oscillations manipulated by acoustic fields present three distinct oscillations modes. They can either be: translational in nature, reflect as volumetric oscillations or display the occurrence of surface waves. Each of these modes exhibits its own, distinct, flow pattern.

Microstreaming has exhibited potential as an efficient propulsion mechanism. Rotors have been empowered by bubble microstreaming and power generation has been observed at the femtowatt level (Kao et al, 2007). Microstreaming has also been studied in microfluidic applications. It was observed to have a defined effect on rectified diffusion. Rectified diffusion describes the process by which a bubble subjected to a sound field experiences a net inflow of gas across the bubble-fluid interphase. It has also been used as a bubble dissolution tool since rectified diffusion causes bubble growth which can later lead to the collapse of the bubble (Leighton, 1994).

### **2.2.1.3 Bjerknes Force**

Microbubble manipulation using ultrasonic waves has also found its way into the promising fields of medicine and biotechnology. Bubble entrapment knowledge obtained

through the use of standing acoustic pressure waves has demonstrated encouraging results in the entrapment of drugs or genes as delivery systems to be dispersed near diseased tissue (Yamakoshi & Koganezawa, 2005).

Acoustic chambers generate a non-zero acoustic pressure gradient, which produces a translational force on the bubble, known as the primary Bjerknes force. The net radiation force acting on a spherical bubble in a standing-wave sound field is termed the primary Bjerknes force (Akhatov et al., 1997; Holzfuss et al., 1998).

The primary Bjerknes force was first ascertained by Bjerknes in 1909, while Blake, in 1949, gave the first satisfactory account of its effect (Brennen, 1995). Essentially, a bubble of volume  $\Omega$  in a pressure gradient  $\nabla p$  experiences a force  $-\Omega \nabla p$ . If  $\Omega$  and  $\nabla p$  vary in time, then the net force on the bubble is the time average

$$\underline{F} = \langle -\Omega(x_1, x_2, x_3, t) \nabla p(x_1, x_2, x_3, t) \rangle, \quad (2.18)$$

where  $x_i$  is the spatial coordinate and  $t$  is the time coordinate. The designated pressure gradient appears when a part of the incident acoustic wave is scattered by the bubble.

The Bjerknes force alone predicts and explains bubble migration towards pressure nodes or antinodes of an acoustic standing wave. The equilibrium position depends on the bubble radius and the excitation frequency. Manipulation of the Bjerknes force allows the use of an acoustic standing wave to trap bubbles at particular locations despite the influence of buoyancy and even during flow.

The Bjerknes force is clearly not the only force experienced by the bubble when it is subjected to an acoustic field. Among others, the buoyancy and drag forces (to a greater or lesser extent) are always present. Other forces appear under special conditions, for example, the added mass as well as the history force, take effect when the bubble is accelerated; the bubble-wall

interaction force and the lift force are experienced near walls. However, it has been demonstrated that excluding buoyancy, the Bjerknes forces are the most potent driving forces for bubble translations in a non-flowing liquid (Leighton, 1994; Leighton et al., 1990).

### 2.2.1.3.1 Bjerknes Force for a linear bubble response

The Bjerknes force for an instantaneous pressure field and volume was defined in Eq. (2.18). As seen, pressure gradients and volume are needed to compute its value. Considering a spherical bubble, Eq. (2.18) yields:

$$\underline{F} = \left\langle -\frac{4}{3} \pi R^3 \nabla P(x, y, z, t) \right\rangle \quad (2.19)$$

where  $R$  arises as a solution to the Raleigh-Plesset equation discussed in section 2.2.2.1. For a linear response of a bubble, Eq. (2.22) can be approximated as (Brennen, 1995):

$$\underline{F} = -2\pi R_0^3 \operatorname{Re}\{\varphi\} \nabla \tilde{p}(x, y, z) \quad (2.20)$$

where,

$$\operatorname{Re}\{\varphi\} = \frac{\tilde{p}(x, y, z)(\omega^2 - \omega_0^2)}{\rho_L R_0^2 \left( (\omega^2 - \omega_0^2)^2 + \left( \frac{4V_L}{R_0^2} \omega \right)^2 \right)} \quad (2.21)$$

$$\text{and } p(x, y, z, t) = \operatorname{Re} \left\{ \tilde{p} e^{j\omega t} \right\} \quad (2.22)$$

$\omega_0$  is the bubble natural frequency as a function of equilibrium radius and is given by:

$$\omega_0 = \frac{1}{R_0} \left( \left( \frac{3\gamma P_0}{\rho_0} \right) \left( 1 + \frac{2\sigma}{P_0 R_0} \right) - \frac{2\sigma}{P_0 R_0} \right)^{1/2} \quad (2.23)$$

In Eq. (2.23),  $\omega_0$  is the resonant frequency,  $\gamma$  is the polytropic gas phase constant,  $R_0$  is the equilibrium radius,  $P_0$  is the ambient liquid pressure (Pa),  $\sigma$  is the surface tension and  $\rho_0$  is the fluid density.

Observing Eq. (2.20) and Eq. (2.21) it can be concluded that a bubble subjected to Bjerknes forces is translated toward the nodes when  $\omega_0 < \omega$  or to the pressure antinodes when  $\omega_0 > \omega$ . Knowledge of Bjerknes force distribution would aid in the prediction of bubble migration patterns in our experimental system. More details on the derivation of the Bjerknes force is provided in Appendix. A.3.

### 2.2.1.4 Bubble extinction cross-section

A bubble driven by an acoustic pressure field with amplitude  $P_A$  and frequency  $\omega$  will experience volumetric fluctuations and oscillate in phase with the excitatory frequency. An oscillating bubble is a source of sound on its own. Therefore, the sound field emanated by the oscillating bubble will partially scatter some energy from the incident pressure wave. The amount of scattered energy can be quantified according to the scattering cross section of the bubble. The scattering cross section is defined as (Leighton T. , 1994):

$$\Omega_b^{scat} = \frac{\omega^2 R_{so}^2 b_{RF}^{rad} \rho c}{P_A^2} = \frac{4\pi R_0^2}{\left(\left(\frac{\omega_0}{\omega}\right)^2 - 1\right)^2 + \left(2\beta_{tot}/\omega\right)^2} \quad (2.24)$$

where  $A$  represents the amplitude of radial fluctuations,  $b_{RF}^{rad}$  is the dissipative constant for energy loss through radiation mechanisms, and  $\beta_{tot}$ , incorporates all dissipative processes that occur. Scattering will convert energy from a coherent to an incoherent wave field (Leighton, 1994).

Bubble scattering cross sections, are known to increase one to two orders of magnitude at resonance. This occurs because at resonance, bubble surface oscillations are more coupled to the incident pressure field; rendering bubble scattering cross section measurements useful in identifying bubble populations. The only problem with using bubble scattering qualities as size

identifiers, is that even though scattering cross-sections peak at bubble resonance ( $\omega = \omega_0$ ), this peak is a local maximum. Thus the scattering cross section of bubbles will continue to increase with increasing size and the scattering cross section of bigger bubbles might eventually become higher than resonant bubbles. This is illustrated in Figure 2-4.

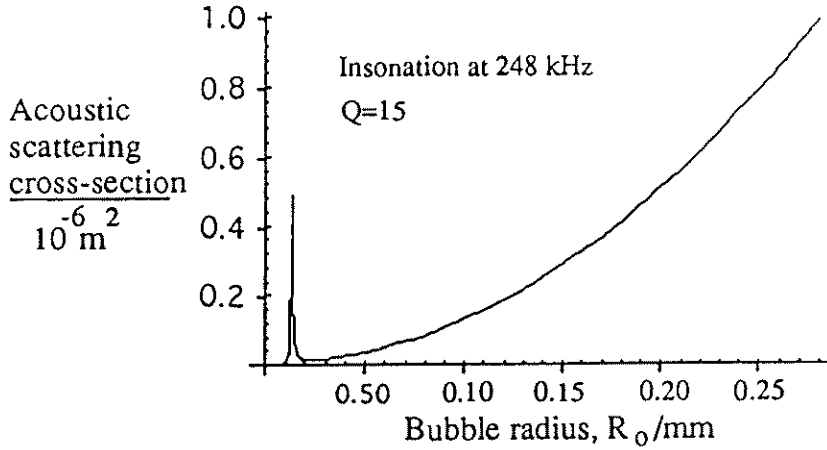


Figure 2-4 Scattering cross-section of a bubble, where damping is assumed to be constant with frequency. Linear harmonic pulsations assumed (Leighton, 1994).

In addition to the scattering of energy by a bubble (known as radiation losses), a bubble will also absorb energy; which in part will be used to fuel its volumetric expansions and contractions (additional energy is converted into heat). These are known as the bubble thermal losses and are a combination of thermal and viscous dissipation. They are evaluated based on the bubble absorption coefficient ( $\Omega_b^{abs}$ ):

$$\Omega_b^{abs} = \Omega_b^{th} + \Omega_b^{vis} = \frac{d_{th} + d_{vis}}{d_{rad}} \Omega_b^{scat} \quad (2.25)$$

defined in terms of thermal ( $d_{th}$ ), viscous ( $d_{vis}$ ) and radiation ( $d_{rad}$ ) dimensionless damping coefficients. The thermal, viscous and radiation coefficients are fractions of a total damping constant,  $d_{tot}$ , and each one is defined based on their respective mechanisms of energy loss.

Together these two contributions are described by a single bubble cross section known as the bubble extinction coefficient. By definition it is the ratio of time average power loss per bubble ( $\langle \dot{W} \rangle$ ) to the intensity of the incident acoustic beam ( $I$ ):

$$\Omega_b^{ext} = \frac{\langle \dot{W} \rangle}{I} = \Omega_b^{scat} + \Omega_b^{abs} \quad (2.26)$$

where  $I$  is the acoustic intensity for a plane wave and can be expressed as:

$$I = \frac{P_A^2}{2Z} \quad (2.27)$$

where  $Z$  is the specific acoustic impedance.

These scattering cross sections are maximal when the excitatory frequency  $\omega$  equals the bubble resonance frequency  $\omega_0$ . The extinction coefficient is known to have measurable effects in order to identify the presence of a bubble.

In addition absorption and scattering cross sections differ for frequencies higher and lower than bubble resonance. A summary of the results obtained by Eller (1970), while studying bubble damping constants during insonation is presented in Figure 2-5.

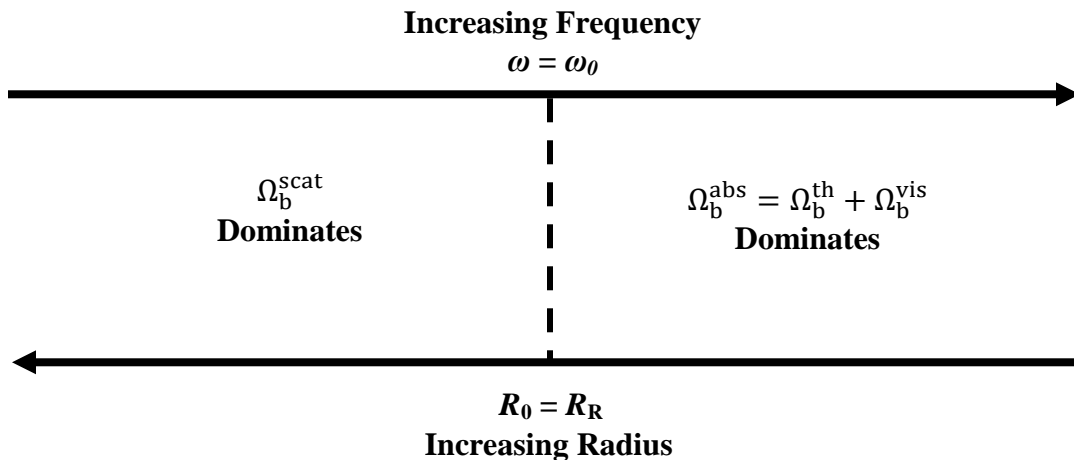


Figure 2-5 Change in bubble scattering and absorption cross sections across the bubble resonance threshold; where  $R_R$  denotes the radius of a bubble whose resonant frequency matches the excitation frequency

## 2.3 Bubble Detection Methods

Following, a brief discussion of a series of terms which characterize bubble behavior is presented. These bubble properties will allow the reader to understand why acoustic techniques are encouraged in the detection and sizing of bubbles.

When bubble oscillations are mechanically induced by an acoustic signal, they generate what has been described by Leighton as an acoustic “signature”, which is an exponentially decaying sinusoid; resembling a slightly damped oscillator (Leighton et al., 1995). Surface waves observed at the surface of an oscillating bubble, are strongest at a specific frequency known as the bubbles resonant frequency. This specific frequency defined by Eq. (2.23) is known as the Minnaert equation (Minnaert, 1933). It describes the bubbles resonant frequency as being a direct function of the bubbles equilibrium radius.

Acoustic techniques based on bubble resonance properties exploit this acoustic resonance. When an ultrasonic wave propagating in a liquid encounters a gas bubble, it will cause forced vibrations of the air within the bubble. These periodic pressure fluctuations will lead to scattering and absorption of the incident wave. It is precisely during resonance that bubble scattering and absorption are also maximal. These properties make bubbles excellent ultrasound reflectors, since they provide an acoustic impedance mismatch between gas and liquid phases (Nishi, 1993). For a gas bubble larger than the resonant size, the amplitude of the ultrasound echo is proportional to its radius, which should permit bubble size to be determined. However, in practice variable attenuation of the ultrasound signal throughout the sample volume makes accurate estimation of bubble size difficult (Nishi et al., 2003).

When bubble oscillations are being driven by a sinusoidal ultrasonic wave, it will oscillate at a fundamental frequency. If the driving frequency is set to match the resonant

frequency of the bubble, signal interaction with the interface of the bubble will generate harmonics. Harmonics can be measured as nonlinearities:  $2\omega_0$ ,  $3\omega_0$  ( $\omega_0$  being the resonant frequency of the bubble) which cause a distortion on the fundamental oscillation waveform of the bubble (Leighton, *The Acoustic Bubble*, 1994). Measuring these nonlinearities can lead to an accurate detection of the specific bubble size.

However, in order for such systems to be used as perfect bubble detectors,  $\omega_0$  must appear only for resonant bubbles. In the techniques that exploit bubble resonance as a bubble size indicator, “false triggering” can occur in which sources other than the bubbles can generate frequencies or signals similar to those generated by a resonant bubble. Similarly, the geometric non-resonant scattering method relies on the acoustic impedance mismatch between the inhomogeneity and the surrounding liquid. However, in practice, one might not be able to distinguish between bubbles or solid bodies of similar size (Leighton et al., 1995).

In the last two decades research on bubble dynamics has intensified due to its application in the biomedical field. Methods for an accurate characterization of a gas bubble population contained within a fluid media have been one of the topics of such investigations (Leighton et al., 1995). Difficulties that arise with the use of bubble detection strategies based on acoustic techniques, have been observed. It has been shown that the highly non-linear behavior of bubbles causes inconsistency in the signal obtained from the bubble populated media. This inconsistency leads to an incorrect and imprecise description of the bubble population. These difficulties appear to have momentarily halted the development of a portable device capable of providing accurate, real time information about bubble nucleation in a human body.

In relation to our research, few selective methods have been used to detect and measure naturally occurring bubbles in tubes or blood vessels such as those produced as a result of

decompression. These findings have recently produced interest in biomedical fields including drug delivery systems and decompression sickness, among others. Primarily optical, acoustic and equivalent bulk properties methods have been used; each exploiting unique characteristics of bubbles (Leighton et al., 1995). Among these, Doppler techniques are the most widely used in relation to DCS bubble monitoring and detection.

Among the pioneers in the bubble detection field were Spencer and Johanson (1974), who created a rather qualitative method to analyze a Doppler monitored signal in the precordial area and classified it in a 0-4 scale relating the signal to bubble population (bubble grade). This became known as the Spencer Method for classifying bubbles. Issues arose concerning Doppler methods due to the fundamental assumptions these classification methods were based on. Doppler ultrasound techniques assumed that signal changes interpreted as bubbles were actually caused by bubbles. There were also doubts on bubble count and to what extent was this “bubble grade” a correct indicator of the total number of bubbles present in the blood stream (Nishi, 1993).

Later on, research was also conducted applying optical-acoustic techniques which exploit bubble strong scattering properties. Mackay and Rubbisson (1978), and Haar and Daniels (1981) attempted to correlate an echo’s high frequency (7.5-8 MHz) return signal to bubble size, in bubbles resulting from decompression. These experiments were done *in vivo* on humans, fish and guinea pigs. Ultrasonic bubble detection was also conducted on guinea pigs hind legs using continuous wave cycles (Haar & Daniels, 1981). Accurate bubble size could not be extracted from the magnitude of the bubble reflection. A semi-quantitative analysis of their results grouped the specific bubble population into three ranges: <100  $\mu\text{m}$ , 100-500  $\mu\text{m}$ , >500  $\mu\text{m}$ .

(Daniels *et al.*, 1980). These methods presented ambivalent results between bubble size and quantity; as later on confirmed by Leighton in similar experiments (Leighton, 1994).

Leighton *et al.*, (1995) studied multiple techniques for characterizing bubble populations within liquids. He concluded that all known methods had their limitations and to appropriately describe a particular population, a combination of methods should be used. Leighton summarizes that a possible perfect bubble characterization method might proceed accordingly: 1) detecting liquid inhomogeneities 2) distinguishing gas bubbles from solids 3) measuring the radii of the bubbles present and, finally, 4) measuring the number of bubbles in each radius class.

Currently, Doppler ultrasound and second harmonic emissions (Lam *et al.*, 1999) have been techniques used to detect and measure bubbles within fluid media. One disadvantage of the Doppler method is that bubbles must be in motion (generally monitored in the venous system) and this is not generally the case for bubbles nucleated in the tissue or stationed near a joint. Bubbles must also be larger than 80  $\mu\text{m}$  in diameter in order to be detected or a minimum number of bubbles must be present. Differentiating between bubble generated sounds and background sounds due to blood cell movement can also prove to be difficult (Nishi *et al.*, 2003).

Several attempts have been made to develop automatic bubble counting systems based on Doppler ultrasound. These systems either focus on interpreting the background signal in time; where the reflected energy must exceed some predetermined threshold, or, obtain information on the bubble population by comparing the energy spectra of signals with and without bubbles. This method has been successful in transducers implanted around the blood vessel in animal studies; yet this method has performed poorly in humans (Nishi *et al.*, 2003).

Doppler ultrasonography has been also effective in detecting gaseous and solid emboli introduced into the circulation during some operative procedures (Gibby, 1993). Since then, a

number of different commercial systems have been developed capable of detecting emboli in the peripheral blood vessels. These systems, however, collect samples at the base of the skull. Few studies addressing the precordial site have also been performed. The difficulty to produce encouraging results arises from the necessity of excluding all false positives which is complicated as reflections inside the human body can be captured from numerous moving structures. Nevertheless, considering the most recent advances in signal processing technology and the high computer power available; the development of low cost fully automatic bubble detection systems has become more practical.

### **2.3.1 Current Bubble Detection Techniques**

In this section specific information is presented regarding the main ultrasonic techniques which can be used to detect bubbles in the body. This review will concentrate on the technologies which have a more proven track record for their use in bubble detection: Doppler ultrasonography and ultrasonic imaging (Ozeri et al., 2006; Jenderka et al., 2002). Ultrasound works by transmitting sound waves into the body. The desired information is obtained by interpreting the returning echoes. The waves are generated by transducers, mostly in the form of piezoelectric crystals. This type of smart material is used to produce an ultrasound pulse in response to an electrical driving signal. Details on piezoelectricity were discussed on section 2.1.2.1.

#### ***2.3.1.1 Ultrasound Imaging***

Ultrasonic echoes occur at interfaces between media with different acoustic properties. For a plane wave, incident at right angles to a plane interface, the ratio between the reflected ( $E_r$ ) and incident ( $E_i$ ) energy is given by:

$$R = \frac{E_r}{E_i} = \left( \frac{Z_2 - Z_1}{Z_2 + Z_1} \right)^2 \quad (2.28)$$

where  $Z_1$  and  $Z_2$  are the acoustic impedances of the two media. Extending this analysis for medical purposes, impedance would take into account the relation between density and speed of sound in the tissues. Large differences in acoustic impedance yield high-energy echoes: since the acoustic impedance of tissues and blood is typically 3000 - 4000 times higher than that of air, Nishi (1975), a tissue-air will reflect almost all of an incident ultrasound wave, i.e.  $R \approx 1$ .

Ultrasound frequencies used for the detection of decompression-induced bubbles typically lie on the 1-10 MHz range. The choice of frequency depends on the desired penetration depth for the study and the selected body structure; taking into consideration that higher frequencies will attenuate faster within the body but would also produce a greater spatial resolution.

### ***2.3.1.2 Doppler Ultrasound***

Two types of ultrasound techniques for ultrasound imaging have been developed, some which have already been commercially exploited for specific applications: continuous wave (CW) and pulsed wave (PW). Continuous wave systems contain two transducers; one produces the pulse and a second one convert echoes from the body into electrical signals, which must then be correlated in order to study the desired phenomenon. PW systems utilize only one transducer. The same transducer receives the transmitted pulse after a delay. PW systems, also known as Pulse-Echo, are mostly used in the DCS field, since additional depth information can be obtained from the echo returning time.

Both, CW and PW can be used for Doppler monitoring of intra-vascular bubbles. One advantage of PW systems is that since they offer depth information, the system could target specific depths thus discarding non-interest areas. However, these types of systems would possess the need to be adjusted for each individual. In practice, PW systems are also more electronically complex than CW systems (Nishi et al., 2003).

Doppler ultrasound systems are the most common method for decompression monitoring, because the instrumentation is cheap, compact and simple to operate. Doppler ultrasound systems exploit the Doppler Effect, which describes a change in the waves frequency in relation to an observer moving relative to the source of sound.

For instance, consider Figure 2-6. A moving sound source is located at point S and moves with velocity  $v_s$ . This source emits a wave front every  $t = T$ , where  $t$  is time and  $T$  is one wave period.

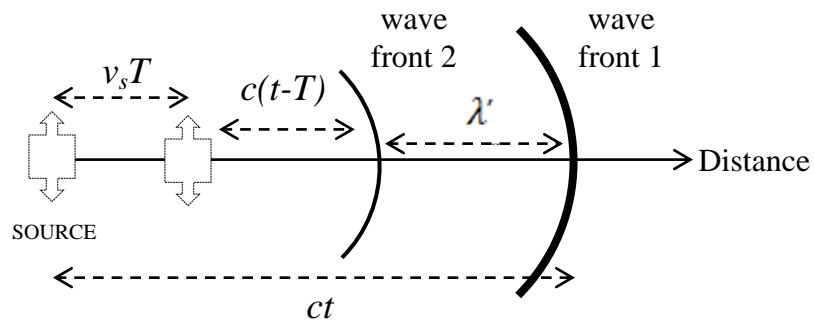


Figure 2-6 Consecutive wave fronts emitted by moving source at an interval  $\Delta t = T$

In this scenario it can be shown that the distance between consecutive wave fronts will change by a value equal to  $\lambda'$ ; this is known to occur because of the Doppler shift. Observe Figure 2-6, the distance traveled by wave 1 after time equal to  $t$  would be:

$$ct = v_s T + c(t-T) + \lambda' \quad (2.29)$$

where  $c(t-T)$  is the distance traveled by a wave front released following wave 1. It follows that:

$$\lambda' = (c - v_s)T \quad (2.30)$$

Taking into account that  $T = 1/f_s$ , and that, for any longitudinal wave,  $\lambda = c/f$  an expression for the wavelength measured by someone at rest in the medium is obtained:

$$f' = f_0 \left( \frac{c}{c - v_s} \right) \quad (2.31)$$

Pertaining to ultrasound being used as a bubble detection tool,  $f_s$  would be the frequency of the ultrasound probe,  $c$  is the speed of sound in the medium and  $v_s$  is the velocity of the source and  $f'$  is the frequency measured by an observer (the bubble) in the medium. If the counterpart case is considered (in which the source is stationary but the detector or observer is the one moving), Eq. (2.31) still applies, only in this case there would be a role exchange between the detector and the source thus obtaining:

$$f_D = f_0 \left( \frac{c \pm v_s}{c} \right) \quad (2.32)$$

Eq. (2.30) is an expression describing the change in frequency experienced by the stationary source as the detector moves toward the source (+) or away (-).

When used as ultrasonic diagnostic tools, the reflections are generated from acoustic interfaces in the body; the equation for a moving reflector is required. This expression is obtained through the combination of Eq. (2.31) and Eq.(2.32). In a physical sense, in the first case, the change in frequency was due to a moving source as seen by a stationary observer. Merging this analysis, it is now supposed that this wave front came from a stationary source and now it is the detector which is moving. Therefore, the solution found in Eq. (2.31), now becomes the source in Eq.(2.32), thus achieving the expression known to describe the frequency change when both the source and detector are moving toward each other:

$$f = f_0 \left( \frac{c+v}{c-v} \right) \quad (2.33)$$

In general this analysis could be further extended to include cases on which the medium is moving as well.

In a Doppler ultrasound system the electronic signal generated by the echoes can be filtered to obtain information regarding the Doppler shifted frequency only. This frequency (assuming that  $v$  is much smaller than  $c$ ) is approximately  $2vf_0/c$  and is typically an audio signal since it lies within the audio range.

### ***2.3.1.3 Second Harmonic Emissions***

Finally, the dual-frequency ultrasound is a method which emits waves at two different frequencies. The first signal, known as the pump, induces bubbles of a determined radius to resonate. Bubble sizing is determined through the second signal, known as the image. Several investigators have suggested that using harmonics as bubble size indicator was limited to the use of small bubbles ( $<10\mu\text{m}$ ) and of selected sizes of resonance or half resonance size (Eatock, Nishi, & Johnston, 1985).

Similar methods using the second harmonics were attempted *in vitro* by Miller et al., (1984), using second harmonic emissions of resonant bubbles to measure the number of bubbles created. Buckey et al., (2005) worked on a system which uses the dual-frequency ultrasound method to detect and size bubbles *in vivo*. Agitated saline was injected and bubbles were created through decompression. A response to transducers located transthoracically in the right atrium was obtained sizing bubbles from  $55 \mu\text{m}$  to  $200 \mu\text{m}$  in diameter. The possibility for bubble nucleation exists also in the tissue. Bubbles generated in soft tissue would be smaller in size (2-3

µm mean diameter). The applicability of this method is being tested here as well (Bollinger, et al., 2009). However, it is unclear to what extent these methods, developed so far primarily *in vitro* or in animal models, transfer to the *in vivo* detection of decompression bubbles, especially with the need for monitoring in the pre-cordial area.

### **2.3.2 Bubble Formation in DCS**

Bubble formation, regarding decompression, is a global phenomenon and its mechanisms are still not completely understood. Experimental evidence (Vann et al., 1980) substantiates theories of ever present populations of gas nuclei in the body. Experimentation supporting this theory was performed by exposing animal subjects to moderate compression-decompression profiles. Such procedures destroyed some of the pre-existing gas nuclei causing a reduction in DCS occurrence. This suggests that bubbles growing under decompression either must be formed spontaneously under decompression or have already been present in the liquid, but achieved surface tension stability by some mechanism which prevented their collapse. In general, decompression bubbles occur through heterogeneous nucleation mechanisms known as “nucleation events”; where the formation of a bubble arises due to pre-existing stable gas pockets or nuclei (Chapel, 2006).

#### ***2.3.2.1 Nitrogen exchange under well-stirred tissue assumption***

In Chapter 1, it was discussed that DCS occurs after nitrogen bubbles form in the bloodstream and tissue as a result of decompression. Atmospheric air is approximately 78% nitrogen. Nitrogen is predominantly found in its natural diatomic state. It has been discussed that DCS is caused by the appearance of nitrogen bubbles and strong precautions must be taken in order to prevent the occurrence of these venomous bubbles. Nevertheless, it must be clarified

that nitrogen is present in all living organisms, in proteins, nucleic acids, and other molecules. Molecular nitrogen ( $N_2$ ) is a fundamental building block of amino and nucleic acids; all in all essential to life on Earth (Gray, 2009). This might justify nitrogen dissolution into the bloodstream and body fats. However when inhaled at high partial pressures (which occurs during scuba diving below 30 m) nitrogen begins to act as an anesthetic agent; causing nitrogen narcosis, defined as a temporary semi-anesthetized state of mental impairment (Fowler et al., 1985). The effects are similar to those caused by alcohol or to those experienced by exposure to nitrous oxide. In reality, this is the only reason why nitrogen bubbles specifically, could be considered additionally harmful after their formation in the bloodstream, nerves, joints, and other vital areas as a result of rapid decompression. Bubbles formed from other "inert" gases (those gases other than carbon dioxide and oxygen) cause the same effects as nitrogen bubbles, so replacement of nitrogen in breathing gases may prevent nitrogen narcosis, but does not prevent decompression sickness (Navy 2006).

Following, a mathematical model is presented which describes the nitrogen exchange between blood and tissue based on a well-stirred tissue. This model resembles those used by Haldane (Boycott, et al., 1908) in an attempt to justify his theories relating the presence of nitrogen bubbles to DCS in which he defined the permissible decompression pressure ratios based on nitrogen body absorption. This model suggests that a diver would absorb nitrogen progressively as dissolved nitrogen is carried through the blood stream from the lungs to the tissue. As implied by the solution of the mathematical model, nitrogen absorption would continue until the partial pressure of nitrogen in the tissue ( $P_tN_2$ ) approached the alveolar nitrogen partial pressure ( $P_A N_2$ ). Once this point of equity between both partial pressures was reached the diver would be nitrogen saturated (Bove, 1997).

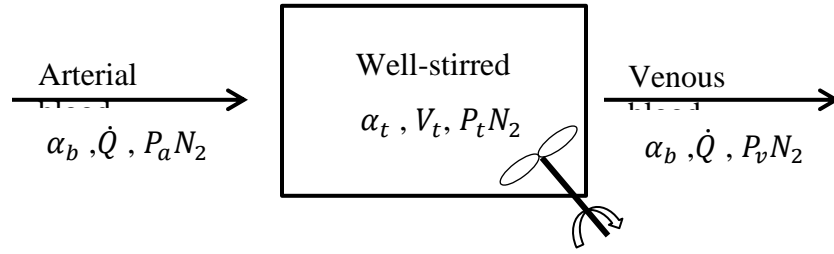


Figure 2-7 Well-stirred or perfusion-limited model for nitrogen absorption in tissue

Figure 2-7 displays the well-stirred model proposed. This model assumes that due to the small distance between tissue capillaries, an effective and instantaneous diffusion of nitrogen occurs between the venous blood and tissue. Consequently, the partial pressure of nitrogen in venous blood and tissues is assumed equal. Also, the alveolar and arterial partial pressures of nitrogen are assumed to be equal. Performing a nitrogen mass balance in a capillary gives:

$$(N_2)_{stored} = (N_2)_{in} - (N_2)_{out} \quad (2.34)$$

Using the parameters displayed in Figure 2-7, where  $\alpha$  denotes nitrogen solubility, the subscripts  $t, b, a$  denote tissue, blood, and arterial properties, respectively,  $V$  represents volume, and  $\dot{Q}$ , represents blood flow, Eq. (2.34) extends to:

$$\alpha_t V_t \frac{dP_t N_2}{dt} = \alpha_b \dot{Q} (P_a N_2 - P_v N_2) \quad (2.35)$$

In Eq. (2.35) the left hand differential represents an expression defining the rate at which nitrogen is stored in tissue. The right side describes the difference between the incoming nitrogen dissolved in blood (carried by the arteries) and the dissolved nitrogen in the outgoing venous blood as a result of the nitrogen absorbed by the tissue. Under the assumptions of the well stirred model presented, Eq. (2.17) becomes:

$$\frac{dP_t N_2}{dt} = \frac{\alpha_b \dot{Q}}{\alpha_t V_t} (P_a N_2 - P_t N_2) \quad (2.36)$$

With solution:

$$P_t(t) = P_a [1 - e^{-kt}] + P_0 e^{-kt} \quad (2.37)$$

Where  $P_0$  is the initial partial pressure of nitrogen ( $N_2$ ) and  $k = \frac{\alpha_b \dot{Q}}{\alpha_t V_t}$ .

Figure 2-8 shows a plot of Eq. (2.37). It presents the increase of the nitrogen partial pressure in the tissue as nitrogen is stored in the tissue. As can be observed in the figure,  $P(t)$  is represented by the sum of initial nitrogen partial pressure ( $P_0$ ), and the response to a step change in alveolar nitrogen partial pressure due to the increased overall pressure; as could occur as a diver descends. The initial arterial partial nitrogen pressure is assumed to change instantaneously to a constant value at time  $t = 0$ . Presented values were obtained assuming a unit tissue volume, nitrogen solubility 5 times in tissue than in blood and an arterial partial pressure and initial nitrogen partial pressures of 1 atm and 0.4 atm respectively (Bove, 1997).

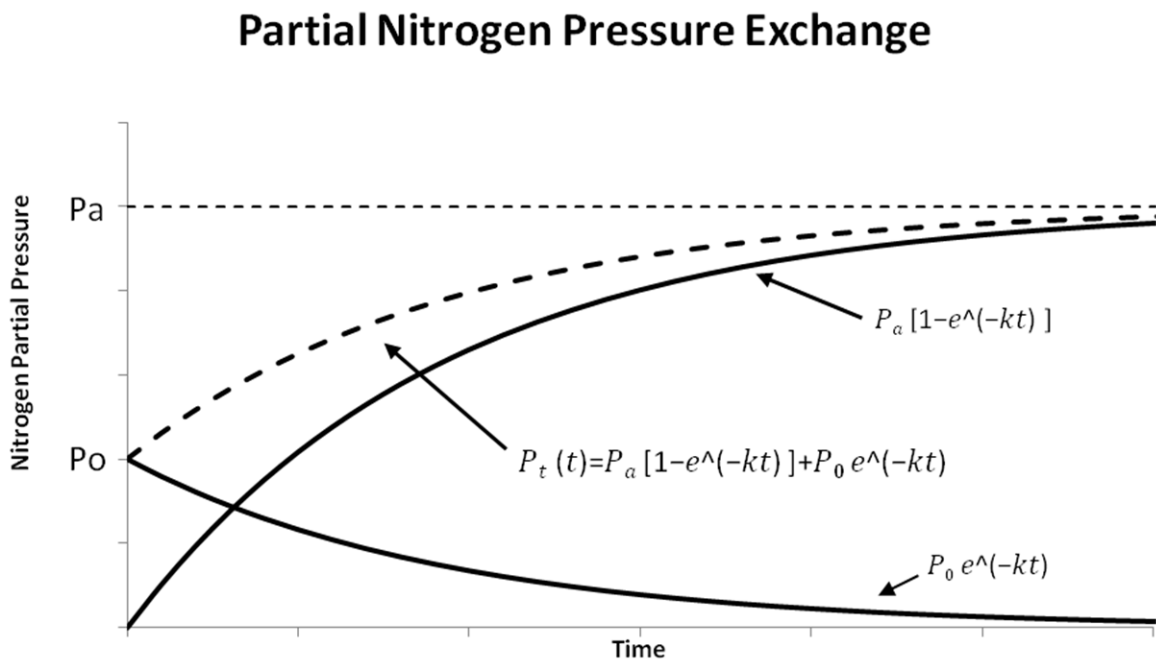


Figure 2-8 Blood-tissue nitrogen exchange

## **2.4 Theory and work related to Acoustic Chambers**

The proposed bubble detection method derives from research in the design of acoustic chambers. Acoustic chambers are rather simple structures, made to generate large and controlled pressure oscillations. They consist of a cylinder which is belted by a glued piezoelectric device (Cancelos et al., 2005). The PZT ceramic provides the driving force of the acoustic chamber. In fact, acoustic chambers have also been used in other areas of experimentation including sonoluminescence (Gaitan et al., 1992) and ultrasound induced drug delivery (Cancelos et al., 2010).

Avoiding bubble presence and nucleation in these areas was also a mayor challenge for researchers. Signal deviations and fluctuations could be observed upon the presence of bubbles. In such experiments, the presence of bubbles was detectable and observable, then similarly we expected the presence of bubbles to be measurable as well. This was one of the fundamental ideas leading to our proposed methodology (see Figure 2-9).

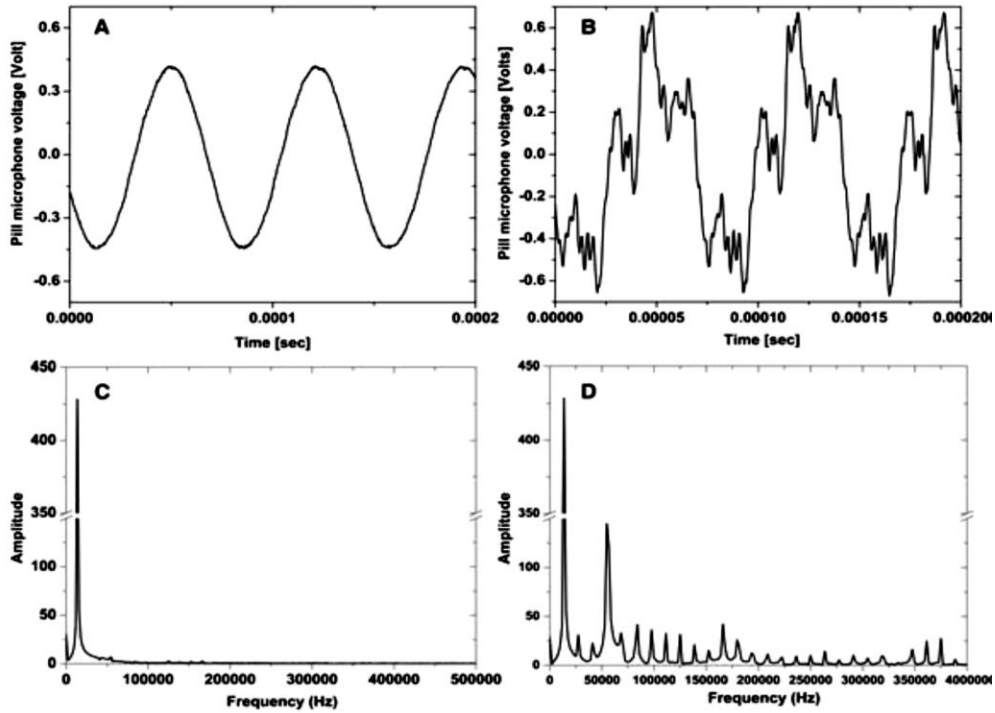


Figure 2-9 Top Image (A and B): Microphone signal with bubbles (B) and without bubbles (A), Bottom image(C and D) Fourier transforms of signals on Top image (Cancelos et al., 2010)

## 2.4.1 Acoustic Chambers and Resonance Conditions

Within the acoustic chamber, a standing acoustic wave is produced by the piezoelectric transducer. When correctly built, large pressure and controlled oscillations are generated, with little pressure fluctuations at the walls (thus small losses depending on the Q factor of the chamber). The piezoelectric ring deforms when subjected to time varying voltage oscillations. The motion of the piezoelectric ring is elastically transferred to the walls of the cylinder thus expanding and compressing the radius of the structure. It is the motion of the wall that produces and maintains the standing acoustic wave in the liquid.

A standing wave is a special kind of wave that can occur in a resonator if superposition of incident and reflected waves occurs. Under this conditions, pressure and particle displacement are 90 degrees out of phase in a standing wave. A hypothetical can be considered as a tube with two closed ends acting as a resonator. At the ends particle velocity becomes zero since there can be no particle displacement. Pressure however doubles at the ends because of interference of the incident wave with the reflective wave. As pressure is maximum at the ends while velocity is zero, there is a 90 degrees phase difference between them.

Generally, the applied voltages at the PZT of an acoustic chamber will be such, that frequency oscillations match its normal resonance modes. A structure contains infinite natural vibration modes. However the greatest acoustic pressure obtained in the fluid occurs when an oscillating voltage with a frequency that matches the first resonance mode is applied. Thus, a resonance condition will be achieved as the natural modes of vibration are stimulated (Cancelos et al., 2005).

All systems have natural modes of oscillation. This value is characteristic of the system and, is a function of many mechanical properties including: density, young modulus and geometry among others. At these frequencies it is the tendency of the system to absorb more energy. It will easily vibrate at those frequencies, and vibrate less strongly at others; thus filtering out all frequencies other than its resonance. The mechanical system will then begin to oscillate in sympathy with the external source. The resonance behavior is manifested in two different ways. The amplitude at the resonance is maximum, and the phase of resonance, (which is the angular shift between the external driver and the oscillating object), will become a driving source supplying maximum power to the oscillator. The lowest natural frequency of a vibrating

system is termed the fundamental mode; higher natural frequencies are termed overtones. Overtones are harmonics only if the boundary conditions are perfectly rigid.

Resonance conditions are extremely sensitive to minor changes in the elastic properties of the medium. If changes in the fluid within the acoustic chamber were to occur which alter the properties of the fluid, this changes will reflect themselves as changes in the electrical properties of the PZT. These changes in elastic properties could be induced by introduction of bubbles within the system, altering the normal resonance conditions. Bubbles can be expected to affect the elastic properties of the medium since they are compressible and greatly affected by frequency fluctuations and acoustic fields due to pressure oscillations. It is believed that signal fluctuations obtained from the normal resonance conditions can be correlated to those induced by the presence of bubbles. Signal fluctuation will give us information on bubble size and bubble number.

#### **2.4.2 Bulk modulus difference in a bubbly liquid**

It has been discussed that one of the characteristics of the presented method for bubble detection, arises from the ability of the system to respond to changes in the bulk properties of the media. Speed of sound is one of the characteristic properties of a compressible fluid. The speed of sound in terms of bulk modulus ( $B$ ) is defined as:

$$c = \sqrt{B/\rho_0} \quad (2.38)$$

where the bulk modulus is defined as:

$$B = -V \frac{dp}{dV} \quad (2.39)$$

The relation between bulk modulus and the propagation of a wave in a fluid is elaborated in Appendix A.2. Based on Eq. (2.38) and the definition of bulk modulus Eq. (2.39), the speed of

sound in a liquid containing gas bubbles is expected to decrease. The volume change experienced by a bubble due to a change in pressure is greater than the one experience by the surrounding liquid. As a result the overall bulk modulus of a bubbly liquid, if treated as a continuum, is expected to decrease as will the speed of sound for this particular fluid.

Accordingly the bulk modulus of a bubbly media will be compared to the free bubble bulk modulus. The bulk modulus of a bubbly liquid  $B_l$  can be expressed as the sum of the bulk modulus of the liquid  $B_0$  in the absence of bubbles plus a term  $B_b$  which can be attributed to volume changes due to the response of the bubble population to pressure changes. In order to calculate its value for a total number of  $n_B$  bubbles, supposing each of them experiences a change in volume  $\Delta V_B$  and applying the same definition of bulk modulus the resulting property value would be equal to:

$$B_b = -\frac{\Delta p}{n_B \Delta V_B} \quad (2.40).$$

Remembering that the presented analysis is being derived considering small oscillation amplitudes and recalling  $R(t) = R_0 + R_\varepsilon$  and the bubble volume was defined as  $V_B = 4\pi R_0^3 (1 + R_\varepsilon/R_0)^3 / 3$ , where  $R_\varepsilon$  denotes the change in bubble radius from the equilibrium radius, expanding the bubble volume expression and considering only linear terms,  $\Delta V_B$  can be obtained, equal to:

$$\Delta V_B \approx \frac{3V_0 R_\varepsilon}{R_0} \quad (2.41).$$

Substituting this back into equation (2.34) this equation becomes:

$$B_b = -\frac{R_0 \Delta p}{3n_B V_0 R_\varepsilon}; \quad (2.42)$$

an expression which relates the bulk modulus of a bubbly continuum (Eq. (2.42)) as a function of  $\Delta p$  and  $R\varepsilon$ , which will be discussed accordingly.

$R_\varepsilon$  Derivation:

The equation of motion for a spring-bob system where damping is included is:

$$m\ddot{\varepsilon} + b\dot{\varepsilon} + k\varepsilon = F_0 e^{j\omega t} \quad (2.43)$$

Oscillatory solutions of Eq. (2.43) assuming lightly damped conditions are found by substituting

particular solution:  $R_\varepsilon(t) = Ae^{j\omega t}$ . After dividing by  $m$  and introducing:  $\omega_0 = \sqrt{k/m}$  and

$\beta = b/2m$  Eq. (2.37) becomes:

$$((\omega_0^2 - \omega^2) + i2\beta\omega)\varepsilon = \frac{F_0}{m} e^{i\omega t} \quad (2.44).$$

In the particular case being presented  $\varepsilon$  resembles radius displacement  $R_\varepsilon$  and  $F_0$  can be defined as  $-P4\pi R_0^2$  since the acoustic pressure at equilibrium can be defined as the ratio of acoustic force to the bubble surface area. Pulsating bubbles possess a characteristic mass, termed “radiation mass” which is an additional mass associated with the inertia of the oscillating fluid caused by an oscillator; in this case the bubble emitting acoustic pressure waves into the surrounding fluid. The maximum radiation mass occurs at the equilibrium radius of the bubble and is defined as:

$$m^{rad} = 4\pi\rho_0 R_0^3 m^{rad} = 4\pi R_0^3 \quad (2.45)$$

This is also known as the virtual mass of the bubble.

This is found by solving for the kinetic energy of the liquid found around an oscillating bubble:

$$\phi_K = \int_R^\infty (4\pi r^2 \rho dr) \dot{r}^2 \quad \phi_K = \dot{r}^2 \int_R^\infty (4\pi r^2 \rho dr) \quad (2.46)$$

From the solution of Eq.(2.46), the maximum radiation mass Eq. (2.45) follows by defining an expression for virtual mass corresponding to the maximum kinetic energy which occurs at  $R=R_0$ . The discussed terms are substituted into Eq. (2.44). Solving for  $R_\varepsilon$ , and replacing this expression back into Eq. (2.42) which was the intended goal of the analysis, an expression for the bulk modulus of the bubbly liquid is obtained:

$$B_B \approx \frac{R_0^2 \rho_w ((\omega_0^2 - \omega^2) + i2\beta\omega)}{3n_b} \quad (2.47)$$

For a detailed derivation of Eq.(2.47) refer to Leighton, 1994. As deduced from Eq. (2.47) the bulk modulus in a bubbly liquid when treated as a continuum is a complex property. From this analysis it follows that the wave number of the medium and the speed of sound are complex entities; where the real part corresponds to effective propagation of the wave and the imaginary part describes wave attenuation in the media as a result of viscous, thermal and radiation losses. The first two would subtract energy from the wave while radiation losses do not necessarily decrease wave energy but are due to the scattering properties of the bubble.

### 2.4.3 Balance of forces on the bubble inside the acoustic chamber

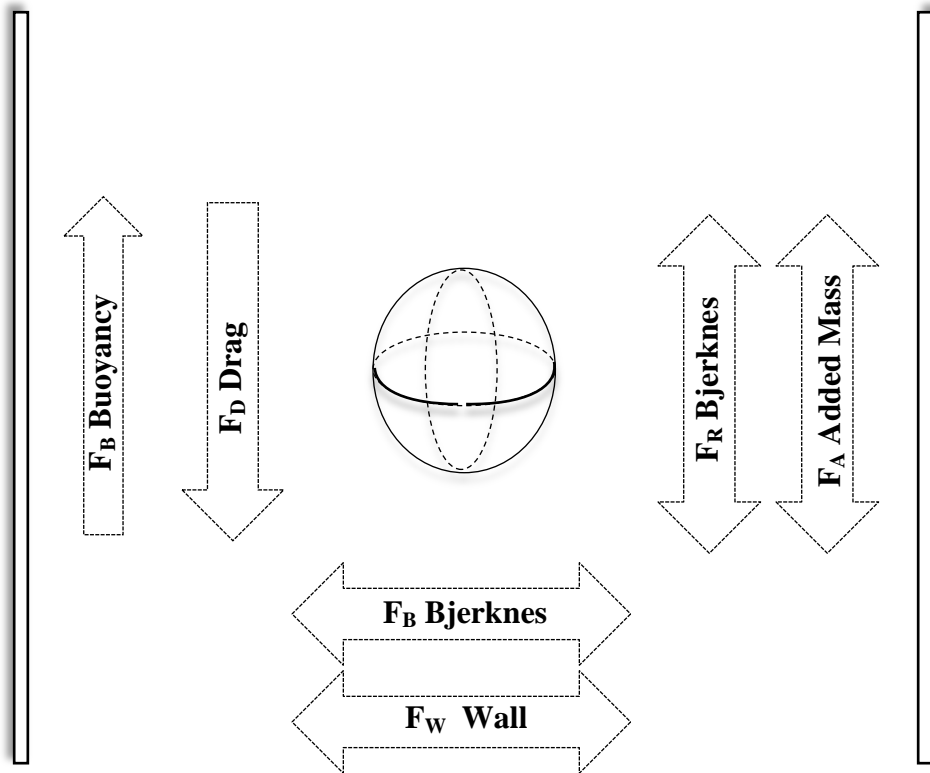


Figure 2-10 Forces acting on the bubble once inside the acoustic chamber

Finally, a discussion of the forces which control the motion of bubbles inside the chamber is presented. The dynamic behavior of a bubble inside the acoustic chamber will be described by a combination of a body force, a hydrodynamic force, an acoustic-radiation force and a wall force. All of these applied at the center of gravity of the bubble.

Body forces are characterized by the unique action of gravity, expressed as the buoyancy force. The hydrodynamic forces are a result of the presence of the fluid around the bubble and can be divided into a drag force and an added mass force as a result of bubble acceleration. The acoustic force is dictated by the primary Bjerknes force supposing the presence of only one

bubble inside the chamber. Using these forces in addition to a wall force, product of a bubble-wall interaction, the bubble equation of motion in an inertial reference frame can be written as follows:

$$m_b \frac{d\vec{V}}{dt} = \vec{F}_b + \vec{F}_D + \vec{F}_A + \vec{F}_R + \vec{F}_W, \quad (2.48)$$

where  $m_b$  and  $\vec{V}$  represent the mass and centroid velocity of the bubble. The forces acting on the bubble are denoted by  $\vec{F}$  in which the subscripts  $B$ ,  $D$ ,  $A$ ,  $R$  and  $W$  indicate the buoyancy, drag, added mass, Bjerknes force and the bubble-wall interaction forces.

In terms of an equivalent radius and constant bubble density, bubble mass can be expressed as:

$$m_b = \frac{4}{3}\pi R^3 \rho_b \quad (2.49)$$

The buoyancy force could be calculated as:

$$\vec{F}_B = \frac{4}{3}\pi R^3 (\rho_0 - \rho_b) \vec{g} \quad (2.50)$$

The drag and added mass terms depend on the instantaneous Reynolds number defined as:

$$R_e = \frac{\rho_l 2R |\vec{V}|}{\mu_l}. \quad \text{This drag force is determined by integrating the normal (pressure) and tangential (shear) forces which are produced by the normal and shear stress at the bubble surface.}$$

Calculations of such values arise from the use of empirical correlations. De la Cruz and Cancelos (2011) for example, performed a numerical study of the motion of an ascending bubble colliding with a horizontal wall. The equations for added mass and drag forces used were:

$$\vec{F}_A = -C_A \rho_l \frac{4}{3}\pi R^3 \frac{d\vec{V}}{dt} \quad (2.51)$$

and

$$\vec{F}_D = -C_D R_s \frac{\pi}{4} \mu_l R \vec{V} \quad (2.52)$$

The primary Bjerknes force was discussed in section 2.2.2.3 and is defined by Eq. (2.23).

This work does not present analytical nor numerical solutions of this equation nor of the bubble interactions produced as a result of these forces. This work anticipates behavior within the acoustic chamber taken into consideration that the Bjerknes force is the dominant force due to the set up pressure gradients in the by the acoustic field.

Recalling, a balance of forces will imply bubble entrapment within the artificial thigh. Efficient bubble entrapment will enable the capture of signals in the presence of bubbles. These signals will later be compared to signals obtained from a bubble free environment.

## 3 EXPERIMENTAL DESIGN AND METHODOLOGY

### 3.1 Simplified Artificial Thigh Design

The acoustic chamber concept described in section 2.4 was adapted to a device that could be worn in the human thigh. The femoral bone found in the thigh is the longest bone in the human body and presents the largest nominal radius. Therefore, standing acoustic waves formed in this region of the human body will exhibit the highest wavelengths and the lowest frequencies, with a consequent simpler and lower cost of electronic components for producing the acoustic field. Figure 3-1 presents a cross-section of the human thigh, illustrating its anatomical components.

The simplified artificial thigh (i.e. acoustic chamber) design was based on the average dimensions of the human thigh, femur, veins and arteries. The constructed artificial thigh mimics 5 main structures contained in a human thigh: the cutaneous and subcutaneous layer (skin), the soft tissue (containing muscles and fatty tissue), the femoral artery, the femoral vein, and the femur; all of these are shown in the thigh cross-section (see Figure 3-1). The scaling of the model presented a 3 to 2 scale factor. This factor was found by dividing an average thigh circumference by the inner diameter of the available PZT ring. An average human femur is 465 mm in length and 27 mm in radius (Steele & Bramblett, 1988). This length takes into consideration the epiphysis (femur head) and the diaphysis (bone shaft). For scaling purposes only, the diaphysis length was taken into consideration. Due to the availability of inner tubes and fittings, the inner tubes were not scaled. Any future artificial thigh construction should take this scaling factor into account for all structures. Following the dimensions of the simplified artificial thigh are presented.

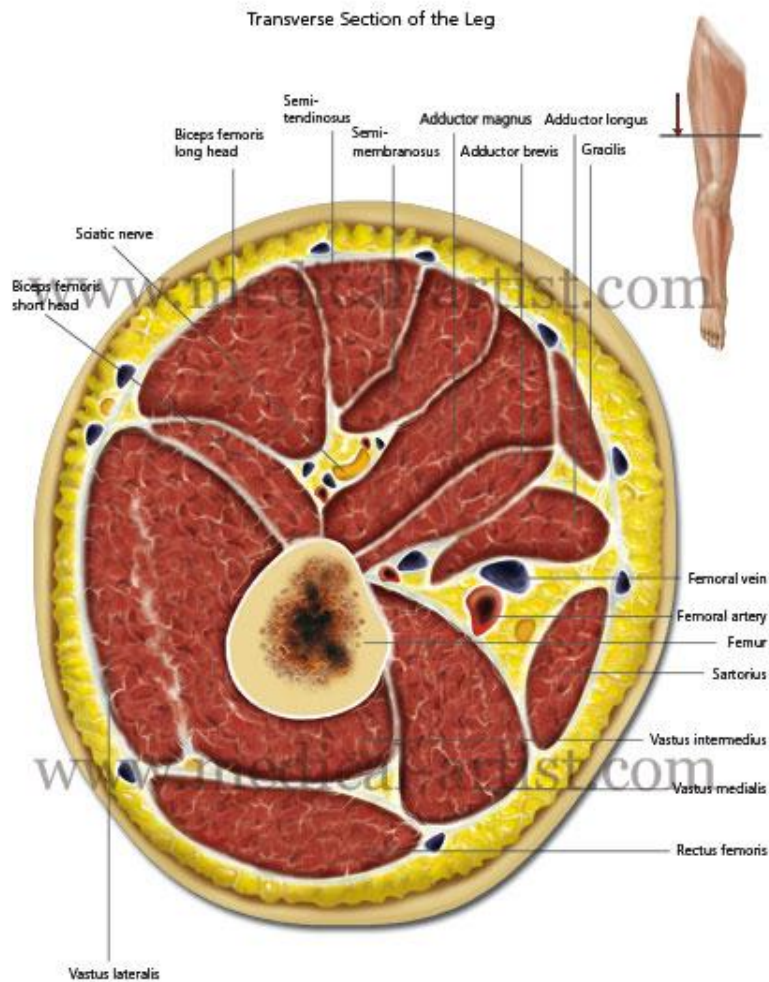


**Figure 3-1 Cross Section of Human Thigh**

The artificial thigh consisted of an inner cylinder with 20 mm in outside diameter (OD) and 300 mm in length, an outer cylinder of pyrex glass with fire treated ends with  $95 \pm 0.4$  mm OD and  $300 \pm 5$  mm length (pyrex 7740, Ace Glass, Vineland, NJ) and a bottom and top flanges (see Figure 3-2). The inner cylinder consisted of short-fiber-filled epoxy which simulated human bone properties. This material is primarily used as an alternative testing medium to human cortical bone (3403-09, Sawbones, Vashon, WA), and can be acquired in the form of a cylinder with properties similar to those of cortical bone and filled with polyurethane foam to mimic

cancellous material. Numerical modeling was used to describe the pressure distribution inside a water cylinder surrounded by a thin wall. The wall properties were changed to match glass, acrylic and steel aluminum properties. Both, glass and acrylic materials result in pressure profiles within the liquid resembling a soft wall boundary condition ( $p=0$ ) at the wall. If a different material with much higher density or young modulus is used, the pressure profile would much closer resemble a hard wall boundary condition ( $\nabla p = 0$ ). For more information concerning these results, refer to Appendix C. Since glass was used in the outer cylinder and for displaying similar acoustic properties to this material, acrylic was chosen for the top and bottom flanges. In addition, acrylic also provided easiness when working with this material in a manufacturing ambient. The flanges were sealed together with the glass with the use of a silicone gasket maker RTV. The addition of the flanges is not far gone, when taking into consideration that in real life, the thigh would extend until encountering bone like boundaries such as the ones found in the hip bone and knee.

The presence of acrylic in the top and lower boundaries illustrated in Figure 3-2 will have minor effects on the development of the standing wave within the fluid. In numerical simulations performed with the acrylic flanges, the fluid behavior displayed (observed in the pressure profiles) was similar to the behavior displayed by simulations in which the acrylic structure was replaced with a soft wall boundary condition (pressure = 0). Changes in resonance frequency present a 0.1 % difference, thus confirming that the addition of the acrylic flanges can be considered trivial. The pressure profile similarity can be seen in Appendix C.

Average vein and artery radii are 9 mm and 6 mm respectively (Sharifian & Gharekhanloo, (2003); Treiber et al., (1997)). Two vinyl tubes inside the artificial thigh mimicked the femoral artery (small tube) and vein (big tube) ( $6.35 \pm 0.1$  mm and  $7.94 \pm 0.16$

mm OD respectively). Since approximately 65% of soft tissue composition is water (Ellis, 2000), degassed water took the place of soft body tissue within the artificial thigh. It provided a media for the propagation of the acoustic signal as well as the stationary wave formation. Water supplied the means for bubble nucleation and transport into our test section.

The additional components that made up the artificial thigh (shown in Figure 3-2), fall under the smart material category. A piezoelectric (PZT) ring (BM400, Sensor Technology Ltd., Canada) radially polarized  $110 \pm 0.1$ mm OD, 98 mm ID, and  $25.07 \pm 0.8$  mm height. The BM400 material is equivalent to Navy PZT Type IV materials (Sensor Technology, Collingwood, ON, Canada). The PZT belts the glass cylinder and was glued with a Stycast 1264 (Emerson & Cumming, Billerica, MA) epoxy, cured at room temperature. Multiple piezoelectric discs (C-5400, Santa Barbara, CA), hereafter called pill microphones, were placed on the structure in pre-defined locations of maximum wall displacement which were determined numerically (see Figure 3-3 and Figure 3-4). Pill microphones are transducers, which constantly monitor pressure fluctuations within the liquid. Pill microphones ( $6.35 \pm 0.1$  mm OD,  $2 \pm 0.07$  mm thickness) have proven to be extremely sensitive to cavitation activity within acoustic chambers (Cancelos et al., 2010), therefore we expected them to assist in the measurements of sound waves produced as an effect of bubble pulsations within the artificial thigh.

In order to resemble blood flow through the veins and arteries, water was also flowing through the experimental setup. The force pumping the fluid was provided by a peristaltic pump (323U/D, Watson-Marlow, Wilmington, WA). The flow rate of the peristaltic pump was regulated so that it would facilitate bubble detachment from the needle and transport along with the fluid. The regulated flow rate used ( $\approx 110$  ml/min) was also an acceptable value compared to typical arterial blood rate. Femoral arterial and vein blood flow rates are known to have

extensive ranges of acceptable values (Flam et al., 1996; Fromy et al., 1997). Blood velocity values are known to vary from 5.3 to 39.5 cm/s and 0.08 to 0.36 cm/s in the vein and artery respectively corresponding to 56 to 422 ml/min and 38 to 171 ml/min in the vein and artery respectively.

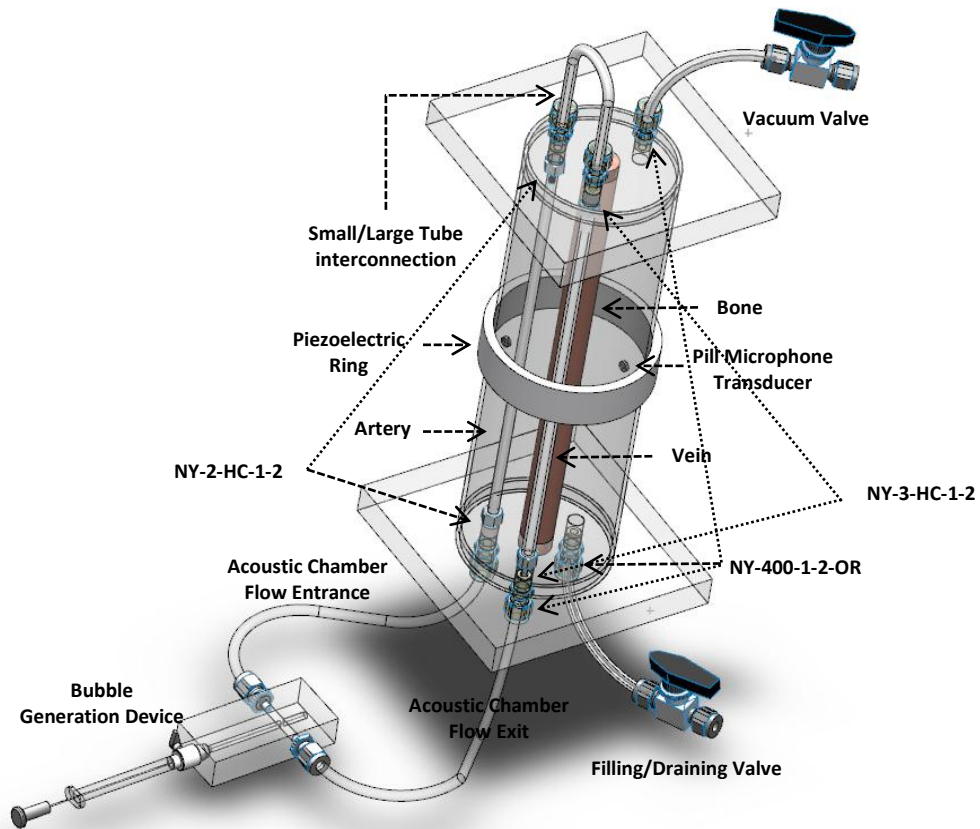


Figure 3-2 Sketch of the acoustic chamber (Artificial Thigh) and bubble generation device interconnected

### Frequency: 14.07 kHz Surface Total Displacement Plot

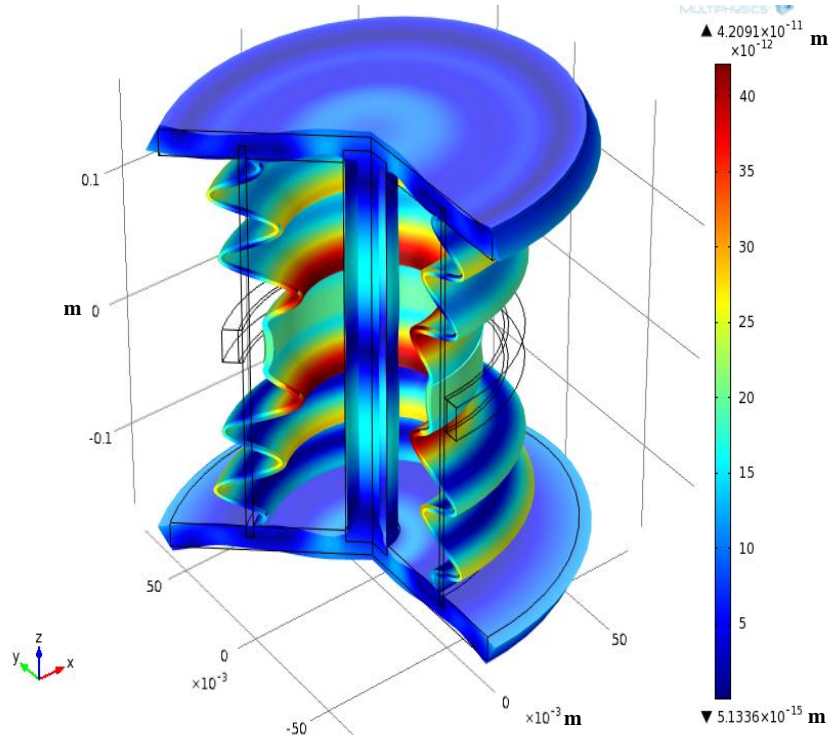


Figure 3-3 Numerical simulation of artificial thigh, rotated 2D axisymmetric model displaying wall deformation only.

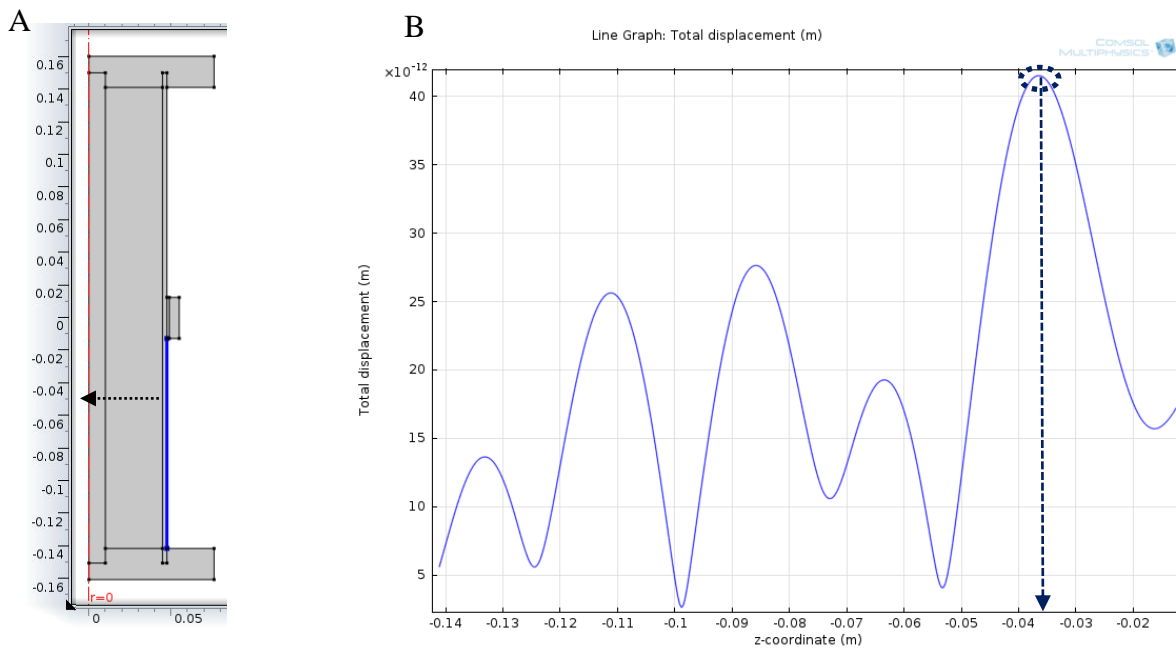


Figure 3-4 Line graph displaying wall displacement at the system resonance frequency obtained from a 2-D axisymmetric simulation. The axial position displaying maximum deformation is shown by the arrow. B) The pill microphone was glued at this location, indicated by the arrow in (A).

All fittings used for the construction of the artificial thigh were Swagelok vacuum rated (Swagelok, Schenectady, NY). The NY-400-1-2-OR fittings can be observed in Figure 3-2 on the outer part of the top and bottom flanges. NY-2-HC-1-2 and NY-3-HC-1-2 fitting (2 of each) connect the small and the big inner vinyl tubes to the acrylic flange respectively. Table 3-1 lists all the dimensions of all the artificial thigh components.

**Table 3-1 Acoustic chamber specifications**

<b>Model Specification</b>	
<b>Model Part</b>	<b>Description</b>
Pyrex Glass cylinder	95 OD X 2.4 Wall thk X 300 length (mm)
Acrylic Flange	152 x 152 x 19 (mm)
PZT BM400	110 OD x 98 ID x 25 height mm
Disks C-5400	6.35 mm OD x 2.03 thk (mm)
Vinyl tubes	8 x 4.8 x 282 and 6.35 x 3.175 x 282 (mm)
NY-400-1-2-OR	Nylon 1/4 in. Tube OD x 1/8 in. Male NPT
NY-2-HC-1-2	Nylon 1/8 in. Male NPT, 1/8 in. Hose ID
NY-3-HC-1-2	Nylon 1/8 in. Male NPT, 3/16 in. Hose ID
SS-42GS4	Stainless Steel Series Ball Valve, 0.6 Cv, 1/4 in.

## 3.2 Bubble Generation System

Bubble injection was the chosen method for the recreation of DCS conditions. It involved injecting small amounts of air into a water environment. Micro-bubbles were released inside a specifically designed compartment, bridging the bubble generation system to the tubes leading to the artificial thigh. Acrylic was chosen as the material for this compartment, since its translucent qualities allowed for the visualization and sizing of the generated bubbles prior to entering the test section. The bubble-generation system presented in Figure 3-5 consisted of a 33 gauge needle with a point style number 3 (91033, Hamilton Company, Reno, NV) connected to an inert gas Sampling Valve (86580, Hamilton Company, Reno, NV). This was attached to a 0.5 ml plunger type syringe (81242, Hamilton Company, Reno, NV). The acrylic body was 88 mm in length, 40 mm wide and 19 mm thick. The hole for the 10-32 fittings was located at 63 mm from the top of the acrylic. This hole agreed with the end of the needle located inside where the air bubbles were to be injected. The outside of the acrylic was covered with a clear nail polish. While manufacturing the acrylic body of the generation device, drilling through the acrylic left thread marks. These marks were coated with a clear molding resin, specifically designed for applications requiring absolute clarity (Crystal Clear 200, Smooth-on, Easton, PA) in order to correct surface defects. Unfortunately, during this procedure, air bubbles were trapped within this coating. These are the material imperfections being referred to in Figure 3-6 (A). Nevertheless, this coating was necessary in order to observe bubbles. A summary of the fitting components is presented in Table 3-2. The needle system was characterized, thus determining the average bubble size generated from particular needles was determined as was presented in Table 3-3. A bubble diameter histogram of the bubbles produced within the fitting is presented in Figure 3-6 (B). The bubble histogram presents two main bubble groups. The first group

represents the bubble size of bubbles leaving the needle tip. The stable diameter observed in the bubbles presented in Figure 3-6 (A) is described by the second diameter group shown in Figure 3-6 (B).

**Table 3-2 Specifications of the Bubble Generation System construction**

<b>Parts</b>	<b>Specifications</b>
Male Adapters	Male Connector, ¼ in Tube OD x #10-32 Male Thread
Metal Hub (nickel plated brass) needles model: 91033	33 gauge, 2 inch (51mm), point style 3
Small hub removable needle, model: 207434	34 gauge, (51mm),point style 3
Kel-F hub needles, model: 7750-22	31 gauge, (51mm),point style 3
Kel-F hub needles, model: 90533	31 gauge, (51mm),point style 3
Micro-liter syringe, model:7636-01	25 µL syringe, removable needles
Threaded Plunger Syringe, model:81242	500 µL, Luer tip (LT) syringe termination. Dispensing capability: from 0.33 to 37.79 µL per plunger revolution
Inert Gas Sampling SYR Valve, model: 86580	lever-actuated on/off valve. Valves are pressure tested to 100 psig and are autoclavable. The bore I.D. is .039".
WP	Width of Acrylic Plate equal to 40 mm
LP	Length of Acrylic Plate equal to 90 mm
HP	Height of Acrylic Plate equal to 0.75 in.
Vinyl tubes Model: LT-2-4	7.94 (OD) x 4.76 (ID), 6.35(OD) x 3.175 (ID) (mm).

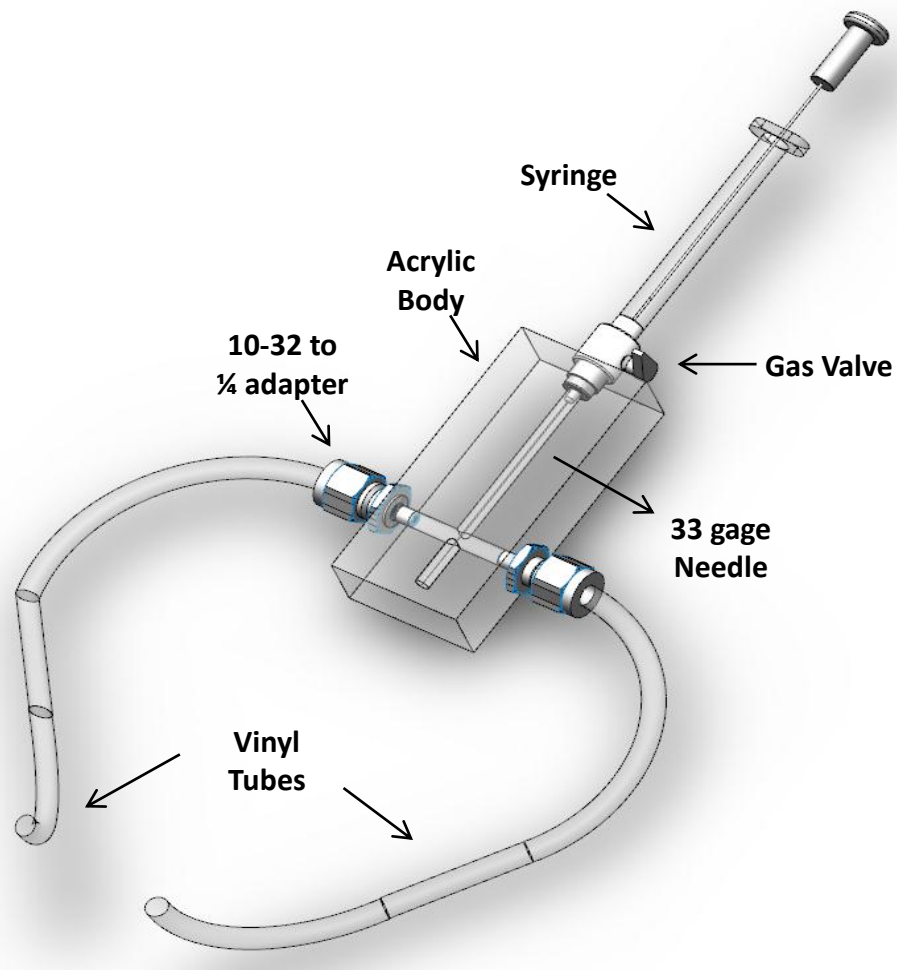


Figure 3-5 Bubble Generation System

The bubble generation system was designed so that different needles and syringes could be connected to the gas valve. The obtained bubble size was basically controlled by the size of the needle utilized. Three different needles were used. The needles were Gage: 34, 33, 31 and 26.

The maximum average diameter size of bubbles obtained through the use of these needles is shown below:

**Table 3-3 Average bubble sizes produces by different needles**

<b>Needle Gauge Size</b>	<b>Average Bubble Diameter (mm)</b>
33	$0.882408 \pm 0.215$
31	$0.966 \pm 0.217$
26	$1.39 \pm 0.436$

This was described as the maximum average diameter since air was injected through the needle till the bubble grew to its maximum size and left the needle tip due to buoyancy. In these tests there was a continuous amount of air supplied as bubbles left the needle tip and where sized. It is believed that by administering controlled air quantities, smaller individual bubbles could be obtained.

While bubble size was related to the needle used inside the bubble generation system, the amount of bubbles that could be obtained depended on the air flow rate administered to the system through the use of different syringes having different volume capacities. Two different syringes were used in trials, before integrating the bubble generation system with the rest of the experimental setup leading to the artificial thigh.

Figure 3-5 illustrates the bubble generation system with the 25  $\mu\text{L}$  syringe (7636-01, Hamilton Company, Reno, NV). The use of this syringe allowed for the injection from one to two bubbles, at most. On the other hand by using the threaded plunger syringe, which held up to 500 micro liters, it was possible to obtain a continuous bubble generation rate. Gage 33 needles came with an 80  $\mu\text{m}$  OD metal cleaning wire. It was found that by injecting bubbles with the cleaning wire within the needle even smaller bubbles could be obtained as a result of a smaller orifice at the needle tip. Using this technique steady bubble flow rates were achieved for bubbles as small as 70-80  $\mu\text{m}$  in diameter. These bubbles were sized inside the bubble generation device (presented in Figure 3-2), and once again inside the artificial thigh, through the use of a high

speed camera with 1,000 frames/s at standard resolution of 2MPx (Phantom v9.1, Vision Research, NJ) synchronized with a particle characterization algorithm through a shadow sizing technique (Dantec Dynamics, Skovlunde, Denmark). Figure 3-6 (A) shows an image of a bubble column with bubbles of 175  $\mu\text{m}$  in diameter produced inside the bubble generation device. The bubble flow rate was obtained using the 33 gauge needle and the threaded plunger syringe. Injected air bubbles are marked with an arrow while the additional bubbles observed are the result of coating imperfections within the acrylic.

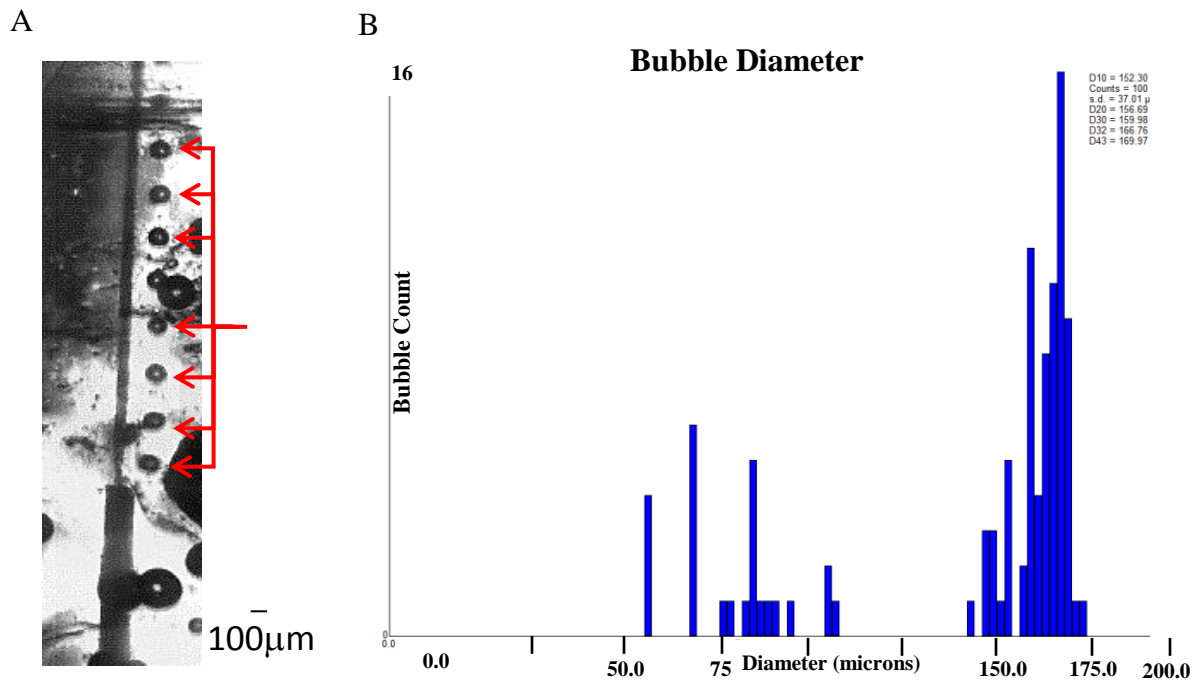


Figure 3-6 (A) Continuous bubble injection within the “bubble fitting”, estimated bubbles ranging from 70 to 250  $\mu\text{m}$  in diameter. (B) Histogram of Bubbles produced within the bubble fitting.

### 3.3 Degassing Protocol

The use of normal tap water and even filtered water can have a great impact on the acoustic signal captured by a pill microphone in an acoustic chamber (Cancelos et al., 2010). This is due to the presence of air and particles in water that cause a change in the speed of sound in the fluid, introducing dissipation and, thus increasing the attenuation of the acoustic signal (Leighton T. , *The Acoustic Bubble*, 1994). For these reasons, the artificial thigh was degassed prior to conducting experiments in order to eliminate possible bubble nucleation sites which could lead to the formation of random bubbles that might interfere with the characterization of the system. Under these ideal conditions, pill microphone and PZT electric measurements have minimum noise influence. In experiments conducted by Cancelos et al. (2010), it was shown that a clean sinusoidal signal was obtained in the pill microphones when using degassed water, while an unclear signal was captured while performing measurements in a liquid with controlled bubble formation as a result of cavitation. Recall that the principal objective of this research is to detect the presence of a bubble within the artificial thigh structure; this was done by identifying specific characteristics in the electrical measurements which responded to the presence of bubbles. Once this general pattern attributed to bubble presence was identified it will be possible to identify these trends in more complicated models, closer to real life scenarios.

The working fluid was degassed in a four liter filtering flask connected in a closed loop with the artificial thigh and bubble generation system (see Figure 3-7). The liquid in the filtering flask was magnetically stirred (11-100-100S Isotemp, Fisher Scientific, Waltham, MA) to promote off-gassing while a continuous vacuum was applied by a vacuum pump (8890A, Welch, Niles, IL). Vacuum was pulled from the artificial thigh prior to filling in order to avoid heterogeneous bubble nucleation due to the presence of pre-existing bubbles on the crevices of

the acoustic chamber down to  $1.5 \pm 0.5$  torr. Vacuum was measured with a digital vacuum gauge (1520, Welch, Monroe, LA). Air leaks in the were quantified as 0.12 Torr/min and did not interfere with a successful filling of the artificial thigh since vacuum was continuously pulled from the artificial thigh until water had completely filled the cylinder and all tubing.

The protocol used in the experiments conducted by Cancelos et al. (2010), consisted of degassing 2 liters of water for 30 minutes, lowering air concentration in water from 26 mg/l to 0.014 mg/l. Following this idea, approximately 2.5 liters of water were degassed for 75 minutes. Additional degassing time was needed which took into consideration air minor air leaks which occurred at a fitting located on the outside of the Erlenmeyer flask through which degassed water was fed to the experimental setup. By this time no more bubbles were observed on this fitting area. After this time, oxygen concentration percentage levels in the water were measured in  $4.1 \pm 1.2$  % of saturation. Oxygen concentration levels were measured using a hand-held dissolved oxygen meter (DO 6, Oakton, Vernon Hills, IL). Later, the liquid, assisted by gravity, was allowed to fill the experimental setup including the artificial thigh and bubble generation system. The vacuum pressure measured inside the filtering flask after filling the acoustic chamber was  $14 \pm 2$  Torr.

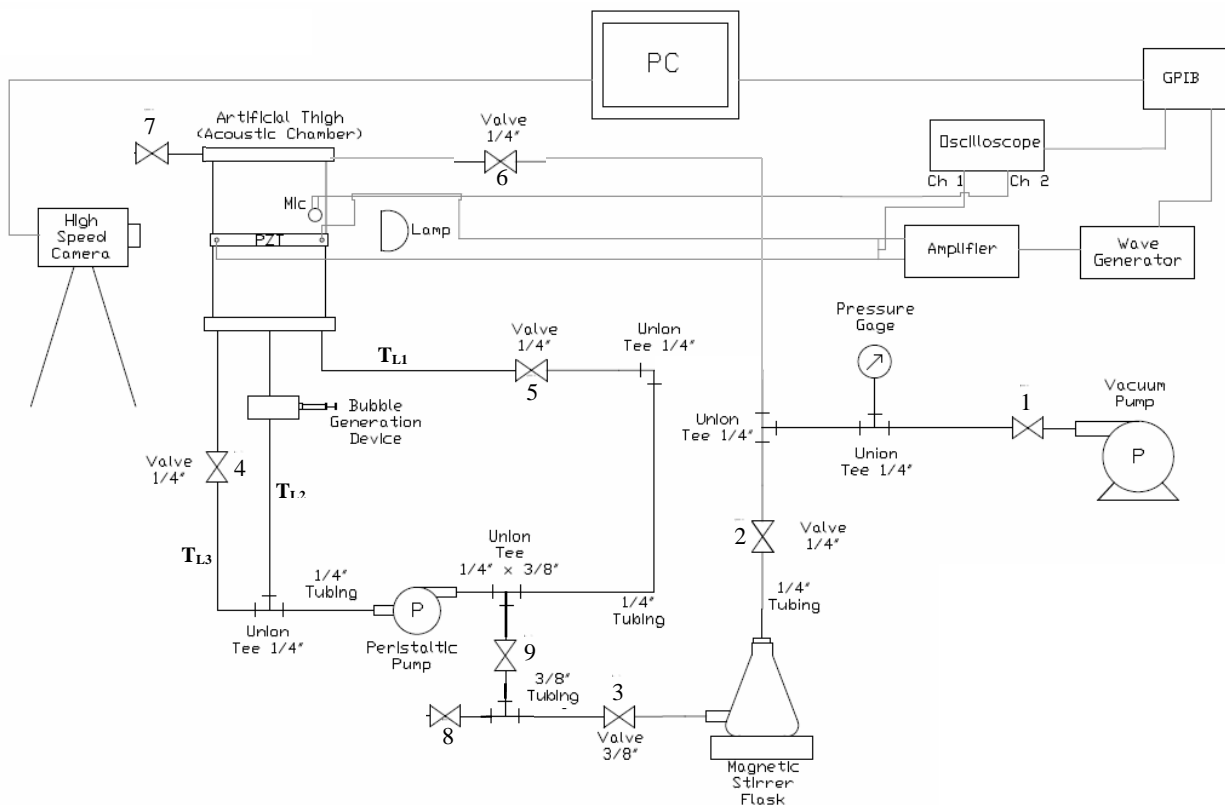


**Figure 3-7 Experimental setup including: acoustic chamber, bubble generation system, electrical components, bubble sizing equipment, fluid circulation diagram and degassing equipment.**

**The protocol used for degassing and filling is detailed below (refer to Figure 3-7):**

1. With all valves closed turn on vacuum pump. Open valves 1, 6, 5, 4, and 9. This procedure removes air from the artificial thigh and tubing.
2. Close valve 6. Open valve 2 and turn on magnetic stirrer. This procedure degasses the water in the Erlenmeyer flask.
3. Turn off magnetic stirrer. Close valve 2. Open valve 6.
4. Open valve 3 to proceed to filling up the artificial thigh with the degassed water. As the water reaches the top of the artificial thigh, close valve 6. Close valve 1 and turn off the vacuum pump.

5. Open valve 8 in order to break the vacuum and equalize ambient and artificial thigh pressures.
6. Close valve 8 and 9.

The setup in Figure 3-7 illustrates the case in which bubbles were injected into the artery like tube. The bubble would leave the bubble generation system through the line labeled “T<sub>L2</sub>”. The majority of experiments followed this setup. The experiments described in section 3.5.2 and 3.5.4 specifically describe experiments in which bubbles were injected outside of the inner tubes into the artificial thigh, resembling the nucleation of bubbles in soft tissue. These experiments were performed by exchanging the tubes labeled “T<sub>L2</sub>” and “T<sub>L1</sub>”. Degassing and filling protocols continued as explained in this section with the only difference that injected air bubbles would now follow directly to the fluid outside the inner tubes.

### **3.4 Expected artificial thigh response to bubbles leading to experimental protocols**

This section is dedicated to discuss the expected bubble behavior inside the artificial thigh in accordance to the bubble dynamics models discussed in chapter 2 (theoretical background). Understanding of this was essential in designing effective bubble detection protocols.

A bubble whose motion is dominated by an acoustic standing pressure wave has a characteristic behavior. Presented in Appendix A.5, the motion of a bubble can be described by a damped oscillator. A bubble will oscillate in phase with the excitation frequency if its resonance frequency is below the driving frequency (as will occur for large bubbles). Additionally, the bubble will oscillate  $\pi$  out of phase if its resonance frequency is above this value. When the resonance frequency of the bubble matches the excitation frequency in the

medium, a greater bubble oscillation is expected. This specific resonance frequency can be related to bubble radius using the Miinaert equation (Eq. (2.23)).

The kinetic energy driving these steady bubble oscillations at a frequency equal to the excitation frequency is provided by the standing wave. As the pressure waves travel through the medium, part of the energy will be absorbed by the bubble and changed to kinetic energy. Another part will be dissipated in the form of heat and other viscous effects. Consequently, it is expected to observe a decrease in the amplitude of the pill microphone signal captured in the presence of bubbles within the system when compared to the signal measured in the absence of bubbles. Furthermore, another part of the incident wave might be further scattered due to bubble scattering properties. Bubbles scattering cross sections are maximal near resonance (Leighton T. , 1994). Therefore the difference in the electric measurements collected from the PZT ring and pill microphones, in the presence of a bubble is expected to increase for a resonant bubble (bubble whose resonant frequency  $\omega_0$  matches or is close to the excitation frequency  $\omega$ ).

Figure 3-8 presents examples of the non-linear oscillations of a bubble captured within the inner tubes of the acoustic chamber. These non-linear oscillations were obtained by setting the voltage in the PZT to 400V peak to peak. Therefore, in order for our numerical model (discussed in Chapter 3) to accurately predict bubble migration patterns (small linear oscillation assumption) the applied voltage must be lower than 400V. For this reason the majority of experiments were conducted at 200 Volts. At this voltage rapid oscillations and translations were still observed for small bubbles ( $R_0 \approx \leq 0.24$  mm); radius where the working frequency matches the bubble resonating frequency.

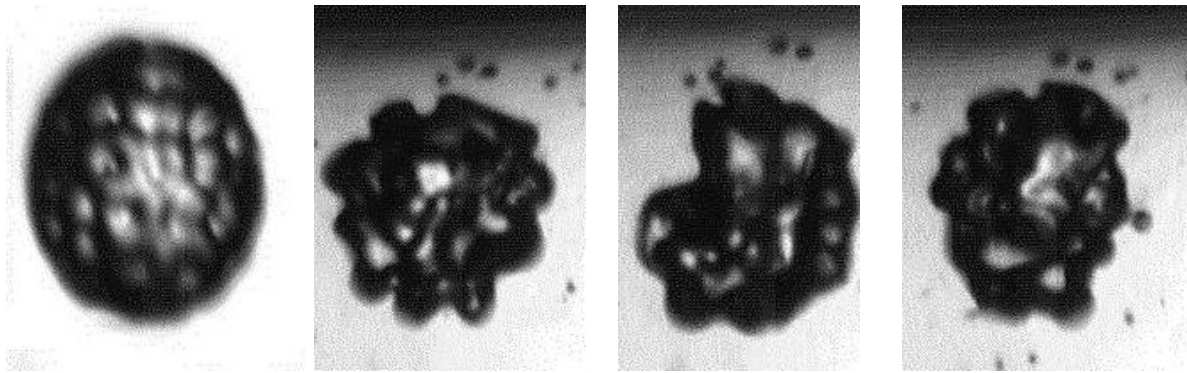


**Figure 3-8 Bubble oscillating at higher modes, displaying an elevated deformation at the bubble's wall.**

When bubbles are subjected to this type of multimode excitation, harmonics are produced. Harmonics can be attributed to surface waves produce and to rapid volumetric changes. They occur as the bubble undergoes nonlinear oscillations, though there are ranges when these oscillations can still be considered stable cavitation. If measured directly in the fluid, this type of dynamic behavior could be highlighted in a Fourier frequency spectrum as the appearance of frequencies, multiples of the bubble resonant frequency; attributed to the acoustic emission of bubbles. However in the case at hand, fluid pressure could not be monitored directly, as it could not happen in any real case where intravenous bubble detection is the main goal. Because of this, alternative methods to evaluate bubble harmonics as a results of bubble oscillation had to be assessed. The following is discussed based on the model illustrated in Figure 3-9.

In Figure 3-9 waves generated by the oscillating bubble will travel across the fluid. Part of these bubbles would dissipate due to fluid viscosity. Some of them will eventually reach and impact the glass cylinder walls of the artificial thigh and interfere with its normal vibration conditions. As presented in Appendix B, the glass cylinder is characterized by many structural resonance modes. At the moment these bubble sonic waves travel through the fluid, and reach the walls, the pressure wave will generate a force. This force will initiate particle acceleration

within the glass structure. The glass cylinder, which was normally oscillating at the excitation frequency, could now be incited to oscillate with additional frequency components corresponding to higher resonating frequencies. These frequencies would be captured by the pill microphones and could be observed in a Fourier frequency spectrum.

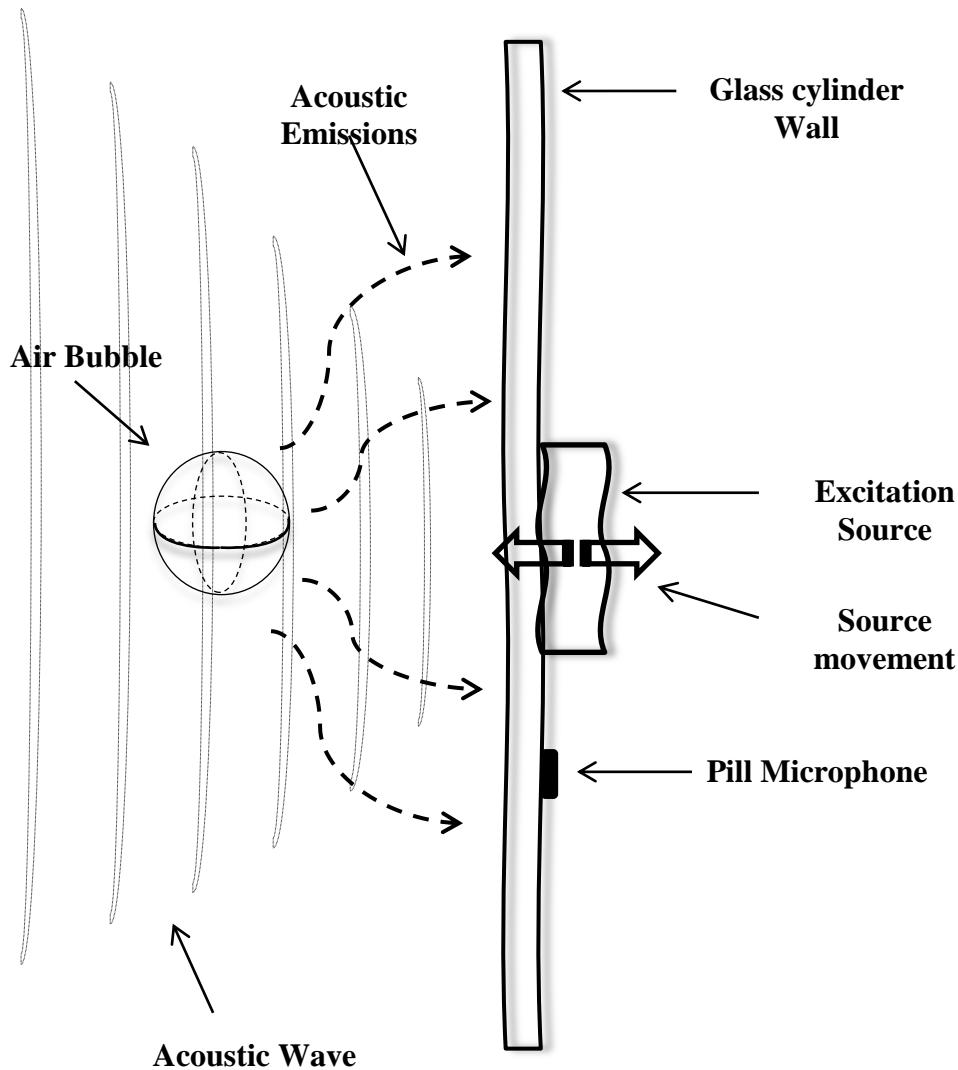


**Figure 3-9** Bubble oscillations driven by a plan acoustic wave emitting acoustic emissions to be captured by pill microphone

In addition to the effect of individual bubbles, bubbles are expected to change the overall bulk properties of the medium, as discussed in chapter 2. Therefore the presence of bubbles will induce observable changes in an admittance frequency response. Figure 3-11 presents a typical

resonance curve for a piezoelectric device. However, as previously discussed the presence of bubbles within the media will produce overall changes in the elastic properties of the system which will cause changes in the motion induced on the PZT ring. Additional details on equivalent circuits for a piezoelectric material can be found on Appendix A.4.

A typical piezoelectric material can be modeled as: a capacitor, an inductor and a resistor in parallel with another capacitor (see Figure 3-10). The two curves presented in Figure 3-11 show similar behaviors. They display a different value for maximum conductance and at a different frequency. The difference in these curves lies in dissimilarities in the resistance and the capacitor values in their respective equivalent circuits. Similarly the presence of bubbles within the system will add losses to the system by increasing dissipation (larger resistance) and providing a change in elastic properties to the system (change in capacitance). This new system, with new properties, is expected to have a similar behavior to the initial one, though with different resonance amplitude and frequency. Thus, if the working frequency is kept constant, deviations in the captured electric signals from those captured under normal resonant conditions could be attributed precisely to the presence of bubbles within the system.

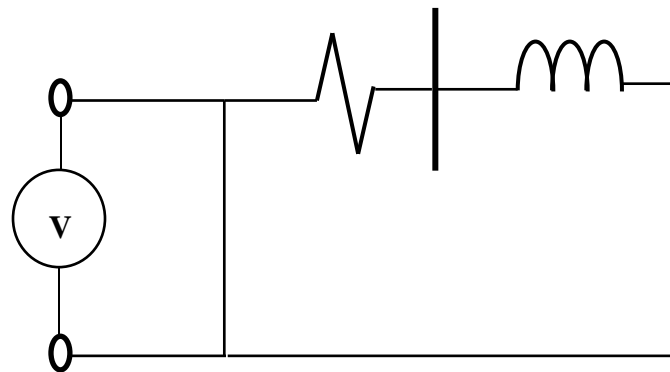


**Figure 3-10 Simplified equivalent R-L-C circuit describing motional impedance**

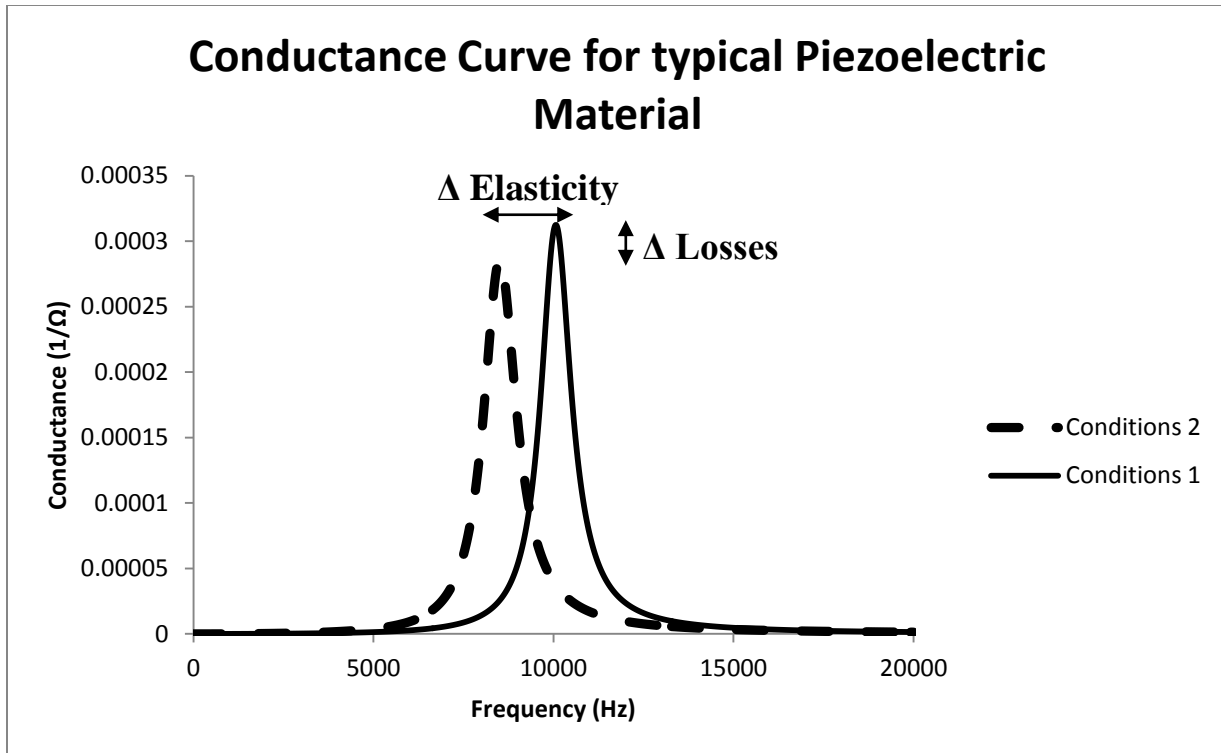


Figure 3-11 Two typical conductance curves showing differences in resonance conditions due to changes in material properties

Based on the ideology discussed in this section, experimental protocols were designed in order to effectively investigate the artificial thigh response to the presence of bubbles. Voltage signals will be obtained from the pill microphone through which harmonics components can be investigated. In addition voltage, current and phase angles will be obtained from the PZT ring component. This device is expected to respond to changes in the bulk properties of the system as was discussed.

### 3.5 Data Acquisition system

A schematic of the electrical components that constitute the data acquisition part of the experimental set-up is shown in Figure 3-12. The PZT transducer was driven by a wave generator (33220A, Agilent Technologies, Santa Clara, CA), connected to a PZT amplifier (EPA 102, Piezo Systems Inc., Cambridge, MA). Voltage in the pill microphones, and current in the

piezoelectric ring were monitored using an oscilloscope (DSO 3202A, Agilent Technologies, Santa Clara, CA;). All instruments were interconnected and controlled via a GPIB-USB-HS (488.1, Austin, TX) interface connected to a personal computer (see Figure 3-7).

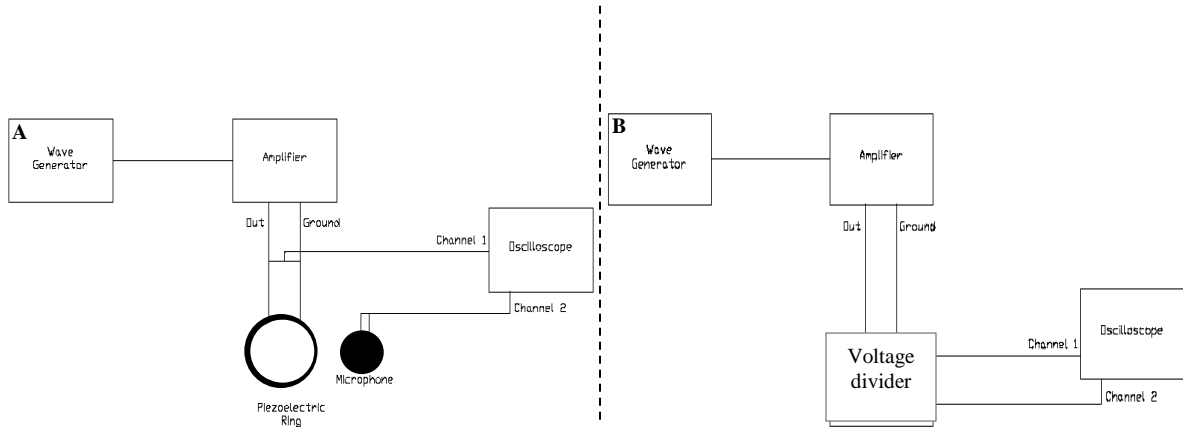


**Figure 3-12 (A) Electrical configuration for pill microphone voltage readings. (B) Electrical configuration for admittance measurements.**

Two different configurations were used and they are presented in Figure 3-12. Electrical configuration (A) was used for experiments measuring voltage in the pill microphones whereas voltage and current in the PZT ring were measured using configuration (B). These measurements were made through the circuit shown in Figure 3-13 which consisted of a current divider (see Figure 3-13). Voltage and current were read in channels one and two of the oscilloscope, respectively. Additionally, information regarding the phase angle (angle between voltage and current) could be determined.

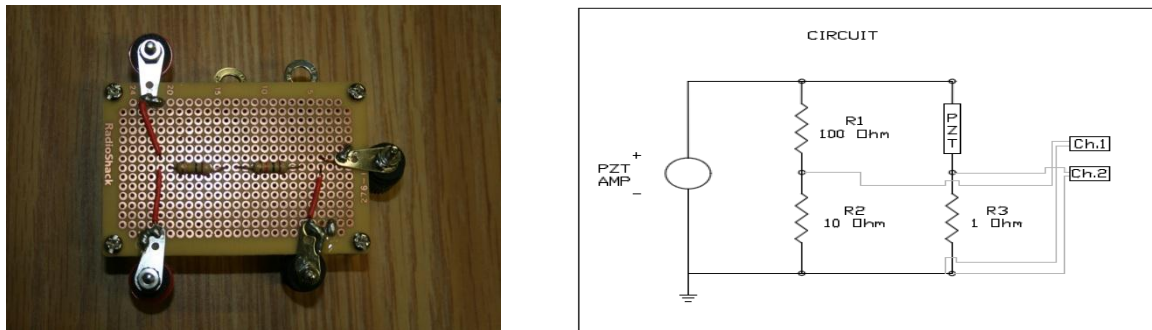


**Figure 3-13 Voltage Divider (A) Manufactured Voltage Divider (B) Circuit Diagram**

### 3.5.1 Resonance Frequency Identification

Figure 3-14 shows a screen shot of the LabVIEW code interphase used to control the oscilloscope and the wave generator through a GPIB interphase. Through this code, the output parameters of the wave generators were controlled: the amplitude of the sinusoidal voltage wave, the frequency range and the frequency step size. After regulating these wave generators output parameters: gain ( $V_{out}/V_{in}$ ) and phase angle were obtained as a function of the input frequency in the artificial thigh. When using configuration (A) in Figure 3-12 the data acquired from the code was used to identify the frequencies of maximum pressure amplitude within the artificial thigh. When the analysis was performed using configuration (B), the acquired data corresponded to the electrical admittance on the PZT ring as a function of frequency.

Electrical admittance is a complex quantity; it is a measure of the material resistance to the flow of a current. The real part of the electrical admittance corresponds to the conductance on the PZT ring, and the maximum of conductance matches the mechanical resonance of the system (Cancelos et al., 2005). A clarification concerning the correspondence of these maximum admittance and conductance values to electrical and mechanical resonance is provided in Appendix A.4 (Cancelos et al., 2005).

#### **Resonance Frequency identification protocol by measuring electrical signals in the PZT ring and in the pill microphone:**

1. Once the filling procedure was accomplished, the PZT and the pill microphones were connected as shown in Figure 3-12 (A). Channel 1 in the oscilloscope records the voltage on the PZT ring, while channel 2 measures the voltage on the pill microphone.

2. The LabVIEW program shown in Figure 3-14 was started.
3. GPIB addresses were set. The output voltage in the wave generator was set to 2 Volts. The range of frequencies was set (12,000 to 15,000 Hz for example). The number of points was usually defined in order to produce a frequency step-size of 5 Hz.
4. The program was set to run and return the Gain (Channel 2/Channel 1), and phase angles (between Channel 1 and Channel 2 in radians) as a function of frequency. These data was then recorded.
5. The procedure was the same for measurements in the PZT ring, except that the connection of electrical instruments corresponds to those presented in Figure 3-12 (B); thus the pill microphone unused. Channel 1 measures voltage in the PZT ring while channel 2 measures the current passing through it. The LabVIEW code returns admittance and phase angles as a function of frequency.
6. With the data acquired the resonance frequency was determined as the value giving maximum conductance or maximum voltage in the pill microphone.

This LabVIEW code was provided by project PI and advisor Dr. Silvina Cancelos, and was later modified by former graduate student and co-worker Juan Fernandez.

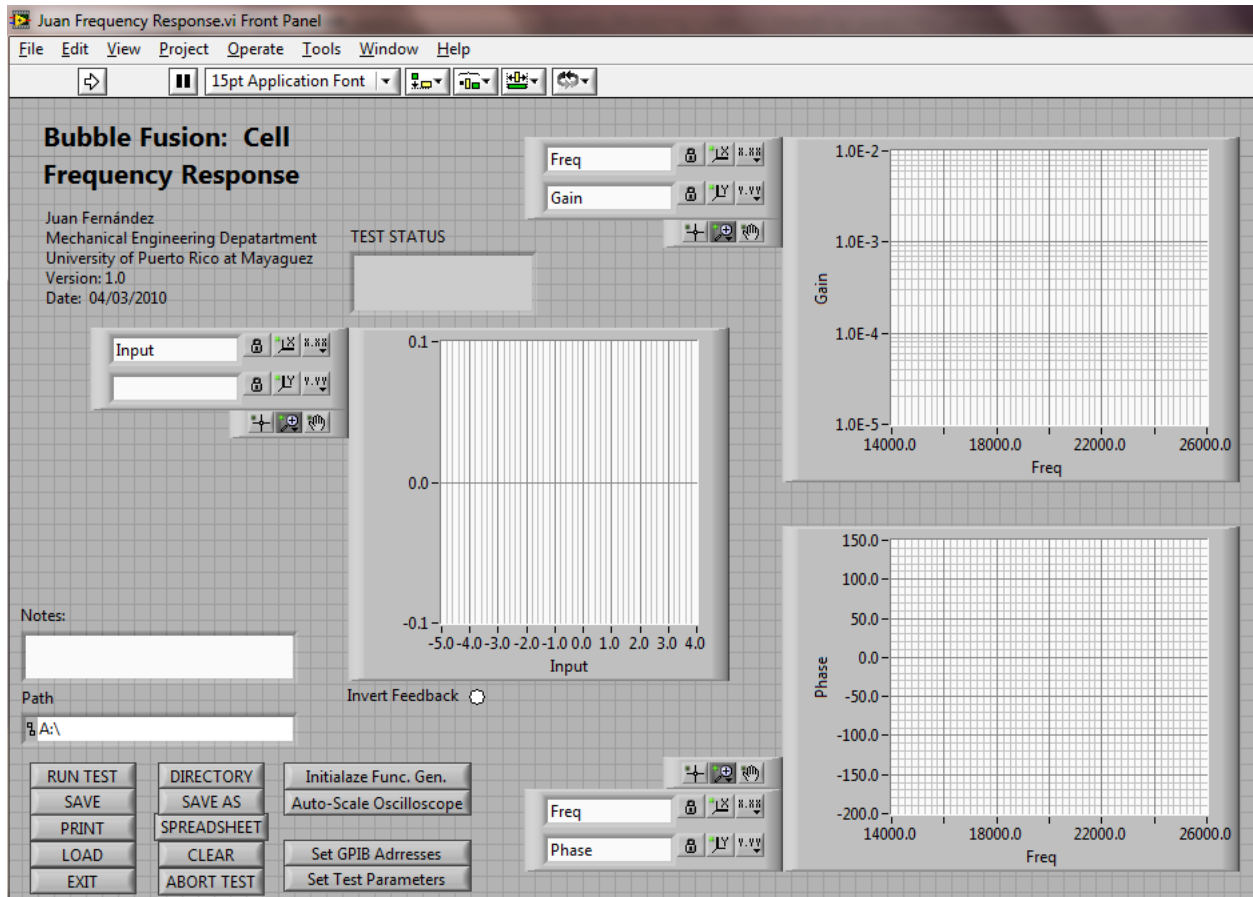


Figure 3-14 Graphic Code Interface. LabVIEW code for resonance frequency identification and frequency response experiments

### 3.5.2 DS03000 Oscilloscope interface: “Fixed sample size” transient experiments

Agilent Technologies, offers a default program that comes with the Agilent Technologies oscilloscope. The DSO 3000 program creates a virtual panel with the ability to control all oscilloscope functions from the computer screen. This interface is presented in Figure 3-15. This program allowed for a maximum capture of 4,000 data points. The sample interval was set to 20  $\mu$ s per sample. This type of analysis, consisting of readings captured from the oscilloscope, will be referred to as a “Fixed sample size” time analysis, simply because the number of data points was automatically determined. All fixed sample size time readings were captured using

this program. This type of analysis was carried out on both the pill microphone and the PZT ring. When used in the pill microphones, voltage was acquired as a function of time. While carrying out readings in the PZT ring through the voltage divider circuit, both: current and voltage data was acquired as a function of time for the time range specified by the sample interval set in the oscilloscope. Experiments conducted with the DSO3000 interface will be described in Section 3.6.1 and Section 3.6.2.

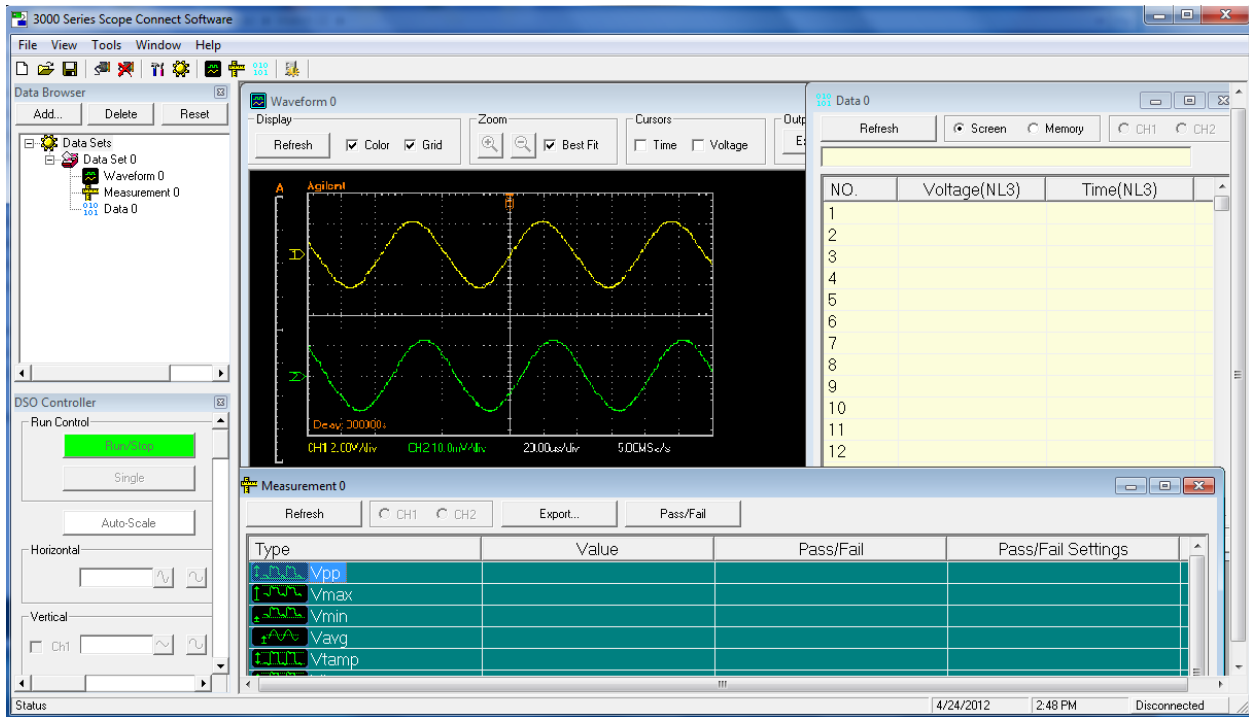


Figure 3-15 DSO 3000 Agilent oscilloscope interface showing signals captures in the oscilloscope on channels 1 and 2. “fixed sample size” time analysis readings were captured through this interface.

### 3.5.3 LabVIEW code: “variable sample size” time analysis

Data acquisition for transient experiments in which voltage and current were measured as functions of time, was also performed with another LabVIEW code. This code, collected rms voltage, rms current and the phase angle in the PZT Ring. Data points were collected at 0.1 sec intervals. Measurements were constantly recorded at this sampling interval, from the moment the program was started, until it was set to stop. This time interval corresponded to a time just

before the bubble entered the chamber, to the moment it exited the inner tube. This type of experiment in which the range of time and the amount of captured data points was defined by the user will be referred to as “variable sample size” time analysis; as opposed to the 4,000 data points determined by the oscilloscope program. A screenshot of this LabVIEW interphase is shown in Figure 3-16.

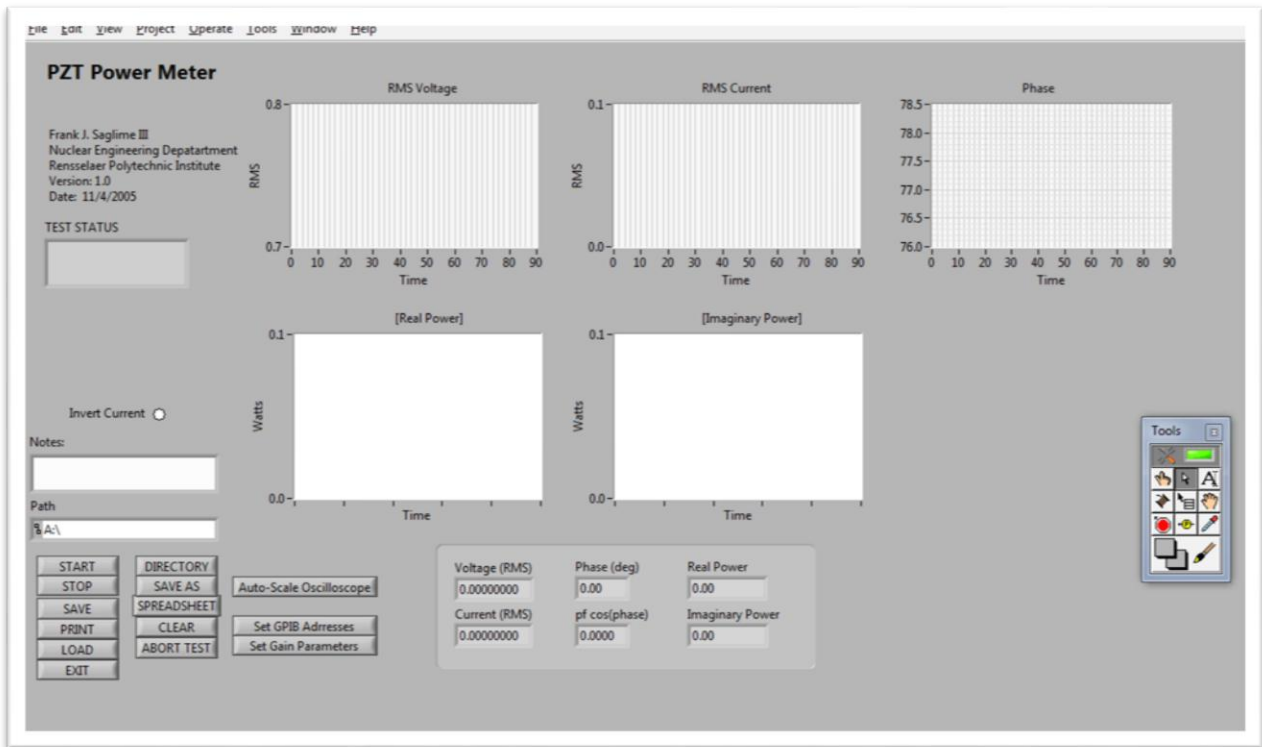
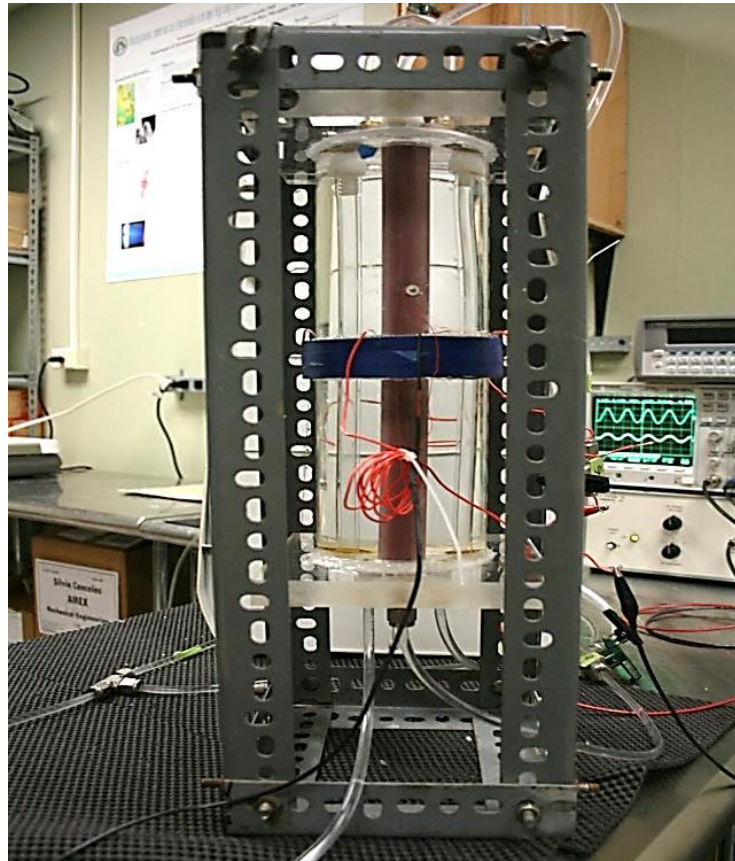


Figure 3-16 Lab View code to measure voltage, current and phase angle in the PZT ring used during “variable sample size”

### 3.6 Overview of Experiments Conducted

As a sinusoidal voltage wave is fed to the PZT ring, time harmonic oscillations are induced in this material through the reverse piezoelectric effect. The PZT ring simultaneously causes harmonic radial deformations on the wall of the artificial thigh, which induces the formation of a pressure wave within the fluid. Within the acoustic chamber, a standing wave is created by the generated acoustic-pressure wave. Pill microphone transducers located around the

structure; monitor the fluid pressure within the structure as a function of wall oscillation. The bubble generation device is then activated to create a determined number of bubbles and channel them into the artificial thigh, thus recreating decompression sickness conditions within the artificial thigh. The manufactured artificial thigh following the design presented in Figure 3-2 is presented in Figure 3-17.



**Figure 3-17 Simplified artificial thigh test section mimicking actual thigh mechanical properties**

Injected bubbles were “trapped” inside the artificial thigh. This entrapment was caused by the balance of forces experienced by the micro-bubble including: drag force, gravity, buoyancy force and the Bjerknes force (Metin et al., 1997). Pulsating bubbles are also attracted to rigid boundaries (Leighton T. , 1994). Therefore, once trapped, either by the acoustic field in the fluid media or by adhesive forces to the wall, the signal reading process was carried out.

Experiments were conducted at different voltage regimes: 100 V, 200 V and 400 V, beginning with 100 Volts. At a steady frequency and voltage, time dependent readings were taken at the pill microphones and at the PZT ring, prior and after bubble injection.

Preliminary results obtained from numerical simulations indicated that frequency ranges for the standing waves within the artificial thigh are less than 100 kHz (see Figure 3-3 for an example). In order to comply with the proposed goal of this research, low powers should be sufficient to detect micro-scale bubbles. If this was not the case the acoustically induced pressure might rise above the threshold for transient cavitation, the acoustic field would then induce the formation of bubbles, which was an undesired effect in this case (Brennen, 1995).

### **3.6.1 Pill Microphone Response to Bubble Presence at the resonance frequency of the artificial thigh**

Initially, a frequency response analysis was carried out in order to determine the resonance frequency of the system. Bubbles were set to enter the artificial thigh through the artery-like tubes resembling the travel of bubbles in the blood through the body. Bubbles could be forced to enter through the artery or the vein depending on the direction of the force provided by the peristaltic pump. Bubbles of varying sizes were injected one at a time. Once inside the artificial thigh, the sizing was carried out through the use of a CMOS high speed camera. Voltage measurement readings were carried out using the DSO 3000 program, while the bubble was present within the artificial thigh. These readings were compared to those readings taken prior to bubble injection. Bubble sizing was performed through the analysis of captured images of the bubble within the inner tubes. Relating bubble presence and size to the captured electrical signal, was attempted.

**Pill microphone testing protocol:**

1. Resonance frequency for the particular trial was determined during the first five minutes after filling the artificial thigh with the working fluid. The wave generator was set at this frequency.
2. DSO 3000 readings were taken prior to bubble injection. This occurred at 100, 200, and 400 Volts defined at the wave generator.
3. Bubble was generated in the bubble system and carried by the flow induced by the peristaltic pump.
4. With the bubble inside the inner tubes, DSO 3000 readings were taken once again.
5. Bubbles dissolution occurred as a result of rectified diffusion causing a reduction in bubble size. Readings were, eventually, repeated using the same bubble, with a smaller diameter.

**3.6.2 Piezoelectric Ring Response to Bubble Presence at the resonance frequency of the artificial thigh: “Fixed sample size” time analysis**

Like for the pill microphone, DSO 3000 program was used to record voltage and current values in the PZT as a function of time, with bubbles being injected inside and outside the “vein” and “artery” like tubes. The electrical configuration for these readings follows configuration (B) in Figure 3-12. These type of experiments, followed a similar procedure to the one described in the previous section. The difference lies in that electrical measurements were performed on the PZT ring.

### ***3.6.2.1 Bubble breakage***

For experiments described in sections 3.6.1 and 3.6.2 bubbles entered the system through the interconnections described in section 3.2. Bubbles produced by the generation system were described in section 3.2 as having average diameters in less than 200  $\mu\text{m}$ . However it was observed that as these bubbles left the needle of the bubble generation system bubble, accumulation would occur in the fittings leading to the artificial thigh. As a result bubbles entering through the artery like tubes could have grown to as much as 1.6 mm in radius. Because of bubble entrapment and growth occurring near corners and borders initially it was difficult to carry out readings for bubble sizes less than 1mm in radius.

During these initial trials it was observed that there were certain frequencies to which bubbles would respond with major surface oscillations. These frequencies were below the fundamental frequency of the artificial thigh. As a result, it was observed that frequencies  $\leq 10$  kHz could be used as a catalyst tool to stimulate, force and speed up the bubble breakage process. With a final intent to study the response of the artificial thigh as the bubble decreased in size in order to investigate overall effects of the bubble size on the electric signals.

This process could be described as follows: a large bubble was initially trapped inside the tubes (radius ranging from 1 to 1.6 mm). Electrical readings (either pill microphone readings or PZT readings) were collected. The frequency was lowered to a frequency to which a greater bubble oscillation was observed. The voltage at the PZT was increased to values ranging from 200 and 400 volts. The selected voltage was enough to observe a greater bubble oscillation while maintaining a control over the location of the bubble. Due to a low concentration of air in the water, and as a result of additional oscillation at the surface of the bubble wall (an increase in

the air diffusion rate), the bubble would start dissolving, thus its size decreasing. The voltage was then returned to the value used for the respective experiment, and the frequency returned to the fundamental frequency of the artificial thigh. Once again, measurements were performed and the process repeated once again to obtain a smaller bubble radius. Depending on the initial size of the bubble, this procedure could take up to 45 minutes until the bubble completely dissolved. As the bubble size approached 480  $\mu\text{m}$ , drastic bubble oscillation occurred at low voltages and bubble life was only a few minutes therefore for these small sizes the described bubble breakage procedure was unnecessary since the bubble would quickly dissolve naturally.

The experimental procedures described in section 3.6.1 and 3.6.2 used the method described in this section to further study the effect of bubble size on the electrical signal pertaining to each method.

### **3.6.3 Piezoelectric Ring Response to Bubble Presence at the resonance frequency of the artificial thigh: “Variable sample size” time analysis on the inner tubes**

Initially in these tests, the entrance of an air pocket was allowed into the vein-like tubes in order to observe the exaggerated effect of air moving within the system. This type of flow is also known as slug flow. In order to produce the air pockets, no needle was utilized in the bubble generation system. Therefore the large air bubbles arose from direct injection from the syringe through the valve illustrated in Figure 3-5. Tests continued with smaller bubbles as well.

Data acquisition for these transient experiments was performed with the LabVIEW code discussed in section 3.5.3. Measurements started being recorded before the bubble entered the inner tubes, until the moment it left the tubes, due to fluid flow. A higher flow rate was used for large air pockets corresponding to 160 ml/min.

### **3.6.4 Piezoelectric Ring Response to Bubble Presence at the resonance frequency of the artificial thigh: “Variable sample size” time analysis on the outside of the inner tubes**

A ‘Variable sample size’ time analysis was also performed on bubbles being fed to the artificial thigh in the confined area outside the inner tubes. These bubbles were, ultimately, introduced in a continuous manner in order to resemble bubbles nucleated and accumulated within the soft tissue. In order to inject bubbles outside, the tubes connecting the bubble generation system were exchanged with the tubes which were previously used to fill the artificial thigh (“T<sub>L1</sub>” for “T<sub>L2</sub>” in Figure 3-7) as was described in Section 3.3. The threaded plunger syringe was used in the bubble generation system. This would allow for air bubbles to be continuously generated. These were forced into the artificial thigh by action of the peristaltic pump. Capturing the entrance and passage of bubbles was difficult due to the bone, and the inner tubes located in the field of view. Bubble with average radius of 1 mm would enter the artificial thigh.

Once again: voltage, current and phase angle readings were performed on the PZT ring (see electrical configuration Figure 3-12(B)) while air bubbles moved through the chamber. The effect of the passing of a bubble near the PZT ring was observed. Deviations from signals recorded in the absence of bubbles were examined.

### 3.6.5 Pill microphone and Piezoelectric ring response to excitation frequency in the vicinity of the bubble resonance frequency

A frequency response analysis (resembling the one discussed in section 3.4.1) was carried out with bubbles injected within the ‘‘artery’’ like tubes. In this case, the size of the bubble was determined immediately upon bubble entrapment within the inner tubes. Longitudinal and radial radius measurements were performed. Based on these immediate measurements, the bubbles resonance frequency was determined following Eq. 2.23. Subsequently a frequency response analysis was performed around the determined resonance frequency. The analysis was compared to frequency responses prior to bubble injection. This analysis was performed using both electrical configurations presented in Figure 3-12.

#### **Bubble resonance frequency response protocol:**

1. Artificial thigh chamber was filled with degassed water.
2. Frequency response analysis (following the procedure discussed in section 3.4.1) was carried out from (500 to 15,000 Hz).
3. Bubble was injected into the inner tubes. Image was captured. From the image bubble, size was immediately determined, followed by the determination of an approximate bubble resonance frequency using  $f_0 = \frac{3.2}{R_0}$ .
4. Frequency response analysis was carried out at a frequency range of ( $f_0-500$  Hz.  $f_0+500$  Hz) using 10 Hz intervals.
5. Frequency responses prior to and during bubble presence were compared.

## 4 NUMERICAL MODEL

COMSOL Multiphysics v4.2a, a numerical Finite Element Method (FEM) software, was chosen to analyze the dynamic behavior of the experimental system built for the study of decompression sickness. This software can specifically aid in the analysis of acoustic chambers through the use of the Acoustic-Piezoelectric interaction module (Comsol, 2011). When solving problems in a frequency domain interface and eigenfrequency domains, combinations of pressure-acoustics and piezoelectric effects exist with predefined couplings at the boundary between the acoustic domain and the piezoelectric (PZT) device (Comsol, 2011). The Acoustic-Piezoelectric interaction module uses a linear formulation, valid only for the case of small excitations. The solution includes the displacement of the elastic structure, the induced acoustic pressure field in the fluid and the electric field in the PZT. The Bjerknes force field within the whole assembly can then be numerically computed after solving for the pressure gradient. A forced computational harmonic analysis was carried out; solving for the variables:  $p$ ,  $\underline{u}$ , and  $V$  at a selection of system driving frequencies ranging from 12.5 kHz to 14.5 kHz in 10 Hz intervals. This was done to predict the experimental behavior of the system and the bubbles.

### 4.1 Model Geometry and Boundary Conditions

A schematic of the system to be analyzed is shown in Figure 4-1. Figure 4-1 can be subdivided into three computational domains: (i) the fluid, (ii) the solid elastic structures, and (iii) the piezoelectric ceramics. The piezoelectric material was driven by a harmonic electric voltage with angular frequency  $\omega$ . A pill microphone was located in the outer cylinder.

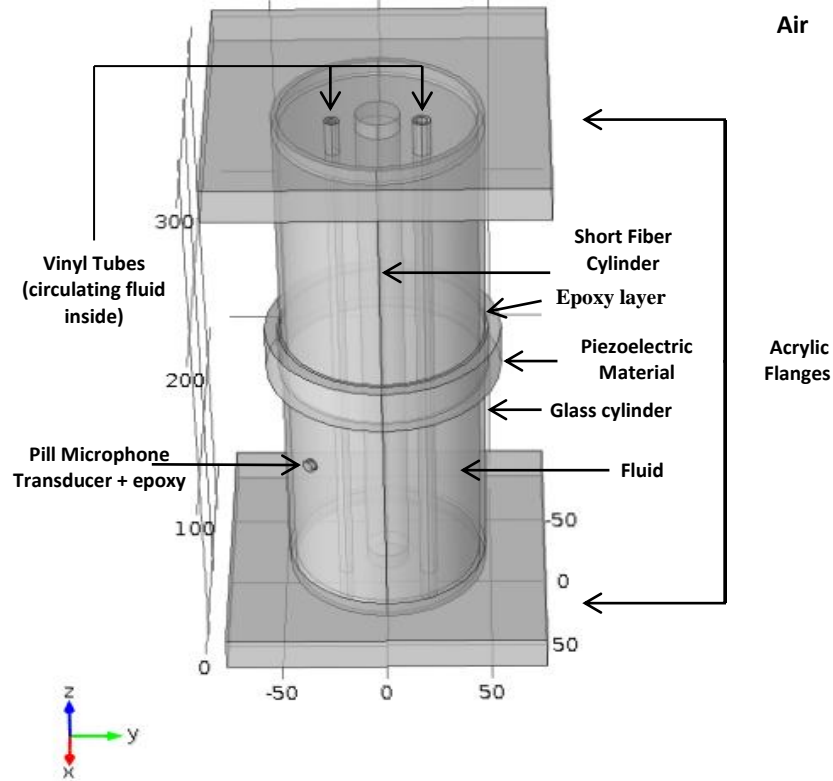


Figure 4-1 Acoustic Chamber Simulated Model

A detailed analysis of the acoustic chamber was performed to predict the system experimental response. The conservation equations were solved in all domains including all walls restraining the fluid, epoxy materials, and piezoelectric ceramics. In the fluid domain, the well-known Helmholtz equation (Eq. (2.3)) was solved. Additionally, neglecting temperature variations, Eq. (2.7) was solved in all elastic solid domains including the piezoelectric materials. The difference between the elastic solids and the piezoelectric material lies in the constitutive equations used in which piezoelectric materials assume a linear coupling between the acoustic field equations and Maxwell's electromagnetic equations (details provided in Appendix A.4).

In order to solve the system of equations in the three domains, it is necessary to apply boundary conditions. Continuity conditions dictate that fluid velocity must match structural velocity at the fluid-structure interface. Therefore  $\underline{v} = i\omega \underline{u}_{solid}$  where  $\underline{u}_{solid}$  is the deformation field and  $\underline{v}$  is the fluid velocity, where the multiplication by  $i\omega$  corresponds to a time derivative in the solid domain. Additionally, a dynamic boundary condition needs to be specified. This condition is specified in the fluid domain through the use of an inward normal acceleration ( $a_n$ ). Fluid acceleration is defined in terms of pressure in the fluid domain in the next equation.

$$\underline{a}_n = -\underline{n} \cdot \left( -\frac{1}{\rho_0} \nabla p \right) \quad (4.1)$$

In the structural domain, the normal acceleration is equal to the second derivative of the structural displacements  $\underline{u}$  with time.

$$\underline{a}_n = \underline{n} \cdot \underline{u}_{tt} \quad (4.2)$$

$$\text{therefore, } -\underline{n} \cdot \left( -\frac{1}{\rho_0} \nabla p \right) = \underline{n} \cdot \underline{u}_{tt}.$$

While the fluid receives an inward acceleration due to the acceleration of the structure, the fluid interacts with the wall with a reactive force due to pressure fluctuations in the fluid in the normal direction. This interaction is defined as

$$\overline{F}_n = -\overline{pn} \quad (4.3)$$

where  $n$  is the outward-pointing unit normal vector seen from inside the solid domain. In the structural domain, a free boundary constraint is applied at all the boundaries with the surroundings, implying that the structure can deform freely.

Similarly, kinematic and dynamic boundary conditions hold for the interface between the PZT and the epoxy, as well as the interface between the epoxy and the cylindrical glass domain where displacements and traction forces must be continuous along the interface,

$$\begin{aligned}\underline{u}_1 \cdot \underline{n} &= \underline{u}_2 \cdot \underline{n} \\ \underline{T}_1 \cdot \underline{n} &= \underline{T}_2 \cdot \underline{n}\end{aligned}\tag{4.4}$$

where  $u_k$  is the displacement vector of the material,  $\underline{T}_k$  is the stress tensor in the material  $-k$ , and  $\underline{n}$  is the vector normal to the interface.

The electrical boundary conditions in the PZT correspond to an applied electric voltage at the inner radius and a ground condition at the other outside electrode.

The top flange observed in Figure 3.3, displays the connection between the two small inner tubes. As can be observed in Figure 4-1, this outside tube was excluded from the numerical model. This outside tube was replaced by a specific acoustic impedance boundary condition to coincide with the experimental model. The acoustic impedance is the ratio between pressure and normal particle velocity and implies the continuation of the liquid media. The specific acoustic impedance is defined as,

$$Z_0 = \rho_0 \cdot c\tag{4.5}$$

where  $Z_0$  is the acoustic impedance of the fluid domain and  $c$  is the speed of sound in the fluid.

Simulations were carried out to verify that the usage of this boundary condition is appropriate. The results are shown in Appendix B.

## **4.2 Force on an oscillating bubble subjected to a stationary acoustic field**

Numerical simulations were used to predict the Bjerknes force effect on bubble migration and accumulation in the simulated environment. A numerical solution of the acoustic pressure field was obtained for this geometry, valid in the range of small pressure oscillations. The derivation of the linearized form of the Rayleigh-Plesset equation was presented in chapter 2. This equation gives the volumetric oscillations of a bubble subjected to an acoustic field. From this solution, the Bjerknes force was numerically computed. By obtaining the Bjerknes force, bubble entrapment through the use of acoustic waves was studied. Bubble entrapment will assist in the measurement readings, which will then be correlated to bubble presence within the chamber.

Knowledge of Bjerknes force distribution will also aid in predicting a bubble migration pattern upon entering the system. As demonstrated by Bjerknes, bubbles subjected to an acoustic field are expected to travel either up or down the pressure gradients towards the nodes or antinodes of pressure depending on their radius and the frequency at which the system is being driven. Therefore, knowing the pressure profile at specific frequencies makes it possible to identify locations at which the bubble would most likely translate to. Equations (2.20), Eq. (2.21), and Eq. (2.23) were the equations defined in the software to numerically analyze the Bjerknes force distribution inside the chamber.

## **4.3 Analytical solution of the Wave equation**

An analytical solution was computed and compared to numerical results using COMSOL to obtain an initial guess on the behavior of our system and for bench mark purposes. Neglecting

the effect of losses, the wave equation (Eq. (2.1)) is solved on a hollow water cylinder. An analytical expression for the resonance modes of the tube can be found by solving this equation. These results, including the solved geometry and numerical and experimental comparisons are presented in Appendix A.6.

#### **4.4 Numerical Bjerknes Force Distribution for the analytically solved geometry**

The geometry shown in Figure A-13 was also numerically solved in a 3D environment. Equations (2.22), Eq. (2.23) and Eq (2.25) were defined into the COMSOL software; thus obtaining the Bjerknes force distribution for this simplified geometry. Figure 4-2 and Figure 4-3 present the Bjerknes force distribution at the fundamental mode of the liquid for an oscillating bubble of 1 mm in diameter. This simulated fluid domain, resembles the fluid domain inside the acoustic chamber. Relevant information obtained from this analysis includes a prediction of the translation of the bubble once inside the acoustic chamber. This analysis assumes only the effects of the Bjerknes force. All other forces are overlooked.

As concluded from Bjerknes force theory, bubbles of a resonant size larger than the resonant radius of a bubble at the excitation frequency of the media (Eq. (2.25)) will be translated toward the pressure nodes. Figure 4-2 displays Bjerknes force distribution in the longitudinal direction and Figure 4-3 displays a radial force distribution. From this analysis and using a fundamental mode of the fluid of 16,381 Hz, bubbles smaller than 0.2 mm radius will be forced into the middle of the chamber ( $z = 0.15$  m and  $r = 0.0425$  m); while, larger bubbles will either move to the top or the bottom of the chamber and will be pushed toward the inner or outer walls.

**Bjerknes Force Longitudinal Distribution (N)**  
**Eigenfrequency = 16,381 Hz**

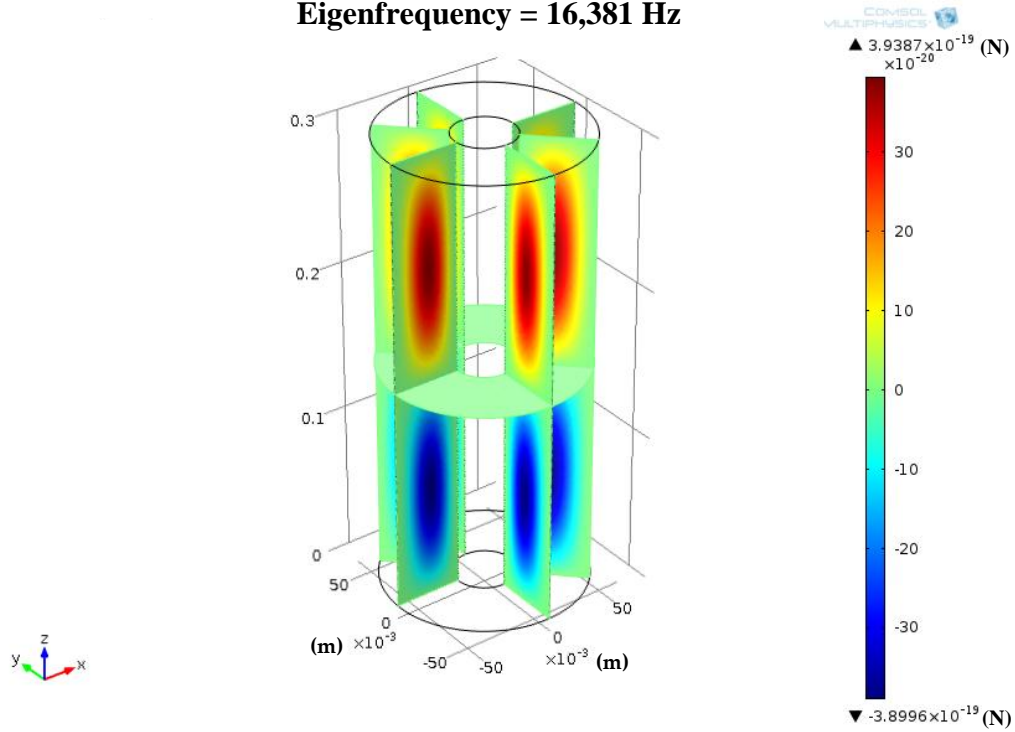


**Figure 4-2** Force in z-direction on a 1 mm in diameter bubble  $F_z(r,z)$  for first resonance mode where:  $m=1$ ,  $n=1$ ,  $c=1490.56\text{m/s}$ ,  $f=16481.8\text{Hz}$

**Bjerknes Force Radial Distribution (N)**

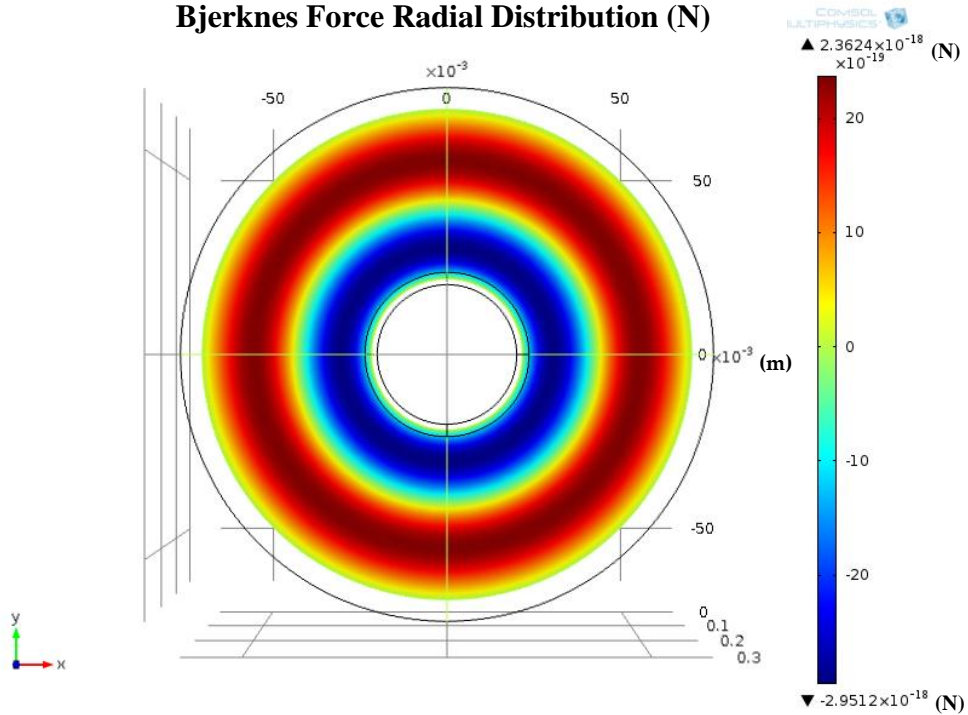


**Figure 4-3** Radial force on a oscillating 1mm in diameter bubble  $F_r(r,z)$  for first resonance mode where:  $m=1$ ,  $n=1$ ,  $c=1490.56\text{m/s}$ . Frequency: 16,381 Hz

## 4.5 Simulations Description

Numerical modeling was used as a tool to determine the fundamental mode of the confined liquid. This was achieved by performing a type of harmonic analysis known as a frequency response in which pressure, displacement, and electrical impedance are calculated as a function of the frequency. Maximum absolute values of these variables denote the existence of a resonance frequency. These frequencies must agree with Eigen frequencies obtained through an Eigen value analysis.

Pressure profiles were studied at these frequencies identified as possible resonance frequency candidates. Pressure profiles provide information about the magnitude and direction of radiation forces generated by the standing wave that was created within the liquid. Radiation forces, specifically Bjerknes forces, will define bubble movement and behavior within the structure. Special attention was given to the bubble entrapment possibilities predicted from numerical results.

In addition, electrical impedance readings calculated at the PZT device were studied in order to numerically substantiate the capabilities of the system to respond to a change in flow conditions within its inner tubes through the addition of an air column. This new fluid domain provides a method to observe the effects of bubble flow within our structure through the introduction of this additional fluid interphase.

Table 4-1 presents a summary of the domain properties of the numerical model.

Table 4-1 Domain properties of the model.

<b>Fluid Domain</b>	<b>Structural Domain</b>	<b>PZT Domain</b>
<p><b>Water</b>  <math>\rho_0</math>: 1000 kg/m<sup>3</sup>  <math>c</math>: 1489.966 m/s                      Acoustic Impedance: 1.489 x 10<sup>6</sup> Pa.s/m</p> <p><b>Air</b>  <math>\rho</math>: 1.204 kg/m<sup>3</sup>  <math>c</math>: 343 m/s                      Acoustic Impedance: 413 Pa.s/m</p>	<p><b>Acrylic Flanges</b>                      Density: 1170 kg/m<sup>3</sup>                      Young's Modulus: 3.2x10<sup>9</sup> Pa <math>\nu</math>=0.41</p> <p><b>Vinyl Tubes</b>                      Density: 1263 kg/m<sup>3</sup>                      Young's Modulus: 2.15x10<sup>9</sup> Pa <math>\nu</math>=0.4</p> <p><b>Glass Cylinder</b>                      Density: 2540 kg/m<sup>3</sup>                      Young's Modulus: 0.73x10<sup>11</sup> Pa <math>\nu</math>=0.22                      Isotropic structural loss factor: 0.02</p> <p><b>Bone-like Cylinder</b>                      Density: 1.64 g/m<sup>3</sup>                      Young's Modulus: 16x10<sup>9</sup> Pa <math>\nu</math>=0.31</p> <p><b>Epoxy Layer</b>                      Density: 1190 kg/m<sup>3</sup>                      Young's Modulus: 5.86x10<sup>9</sup> Pa <math>\nu</math>=0.3</p>	<p><b>PZT-4</b>  <math>\rho</math>: 7500 kg/m<sup>3</sup>                      Structural loss Factor: 0.002                      Dielectric loss Factor: 0.02                      Coupling loss Factor: 0</p>

### 4.5.1 Coordinate Systems

Numerical simulations included three general coordinate systems for the problem solution. Two of these coordinate systems were applied to the piezoelectric materials, while a common XYZ system was used on the rest of the simulation. Therefore it is necessary to define local coordinate systems for the piezoelectric materials. The piezoelectric ring was radially polarized; consequently the coordinate system for the PZT ring was defined as follows:

$$\begin{array}{cccc}
 & x & y & z \\
 x_1 & -\sin(\tan^{-1}(y/x)) & \cos(\tan^{-1}(y/x)) & 0 \\
 x_2 & 0 & 0 & 1 \\
 x_3 & \cos(\tan^{-1}(y/x)) & \sin(\tan^{-1}(y/x)) & 0
 \end{array}$$

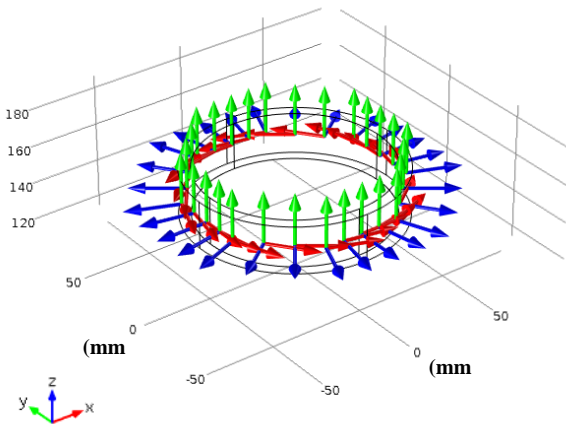
The pill microphone is polarized in the longitudinal axis; consequently, the coordinate system matrix was defined as follows.

$$\begin{array}{cccc}
 & x & y & z \\
 x_1 & 0 & 0 & 1 \\
 x_2 & -\cos(\pi/4) & -\cos(\pi/4) & 0 \\
 x_3 & -\cos(\pi/4) & -\cos(\pi/4) & 0
 \end{array}$$

Images of the respective coordinate system of each material are shown in Figure 4-4. This clearly illustrates the radial polarization of the PZT ring and the axial polarization in the pill microphone.

A)

**Coordinate system for the PZT Ring**



B)

**Coordinate system for the pill microphone**

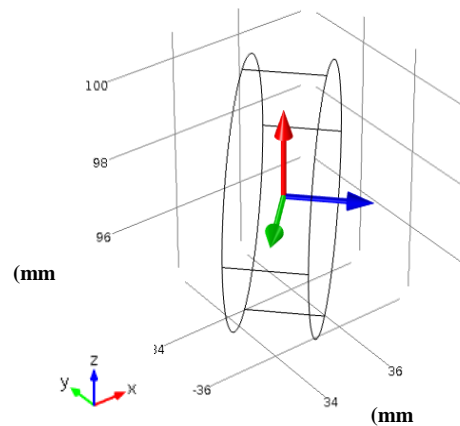


**Figure 4-4 A) PZT ring coordinate system B) Pill microphone coordinate system**

## 4.5.2 Mesh Description

A schematic representation of the non-structural mesh can be observed in Figure 4-5. In solutions to acoustic problems the direction of propagation is generally not known beforehand. Therefore non-structured meshes allow for a constructed mesh which is independent of direction.

Acoustic problems are characterized by a wavelength ( $\lambda$ ) in space whose value depends on the frequency ( $f$ ) and the speed of sound in the medium ( $c$ ). This relationship is described by

$$\lambda = c/f \quad (4.6)$$

Acoustic problems involving wave like solutions achieve numeric convergence and reliable solutions when using ten to twelve degrees of freedom per wavelength (Comsol, 2011).

The solved model consisted of 1,185,922 tetrahedral and triangular elements. The computational domain was divided into three meshing subdomains:

- (i) Included the vein and the artery-like tubes and the liquid inside them. This mesh consisted of a total of 694,903 elements. The sub-domain was meshed at an “extra-fine” mesh setting with the following properties:

**Table 4-2 Vein and artery meshing parameters**

Maximum element size	11.2 mm
Minimum element size	0.48 mm
Maximum element growth rate	1.35
Resolution of curvature	0.3
Resolution of narrow regions	0.85

- (ii) Included the liquid inside the cylinder, the bone, the epoxy layer, and the pill microphones. Mesh consisted on a total of 413,907 elements. The sub-domain was meshed at an “finer” mesh setting with the following properties:

**Table 4-3 Meshing parameters under a “fine” meshing setting**

Maximum element size	17.6 mm
Minimum element size	1.28 mm
Maximum element growth rate	1.4
Resolution of curvature	0.4
Resolution of narrow regions	0.7

- (iii) Included the glass cylinder, the PZT ring, and the top and bottom flanges. Mesh consisted on a total of 77,112 elements. The sub-domain was meshed at an “finer” mesh setting with the following properties:

**Table 4-4 Meshing parameters under a “finer” meshing setting**

Maximum element size	25.6 mm
Minimum element size	3.2 mm
Maximum element growth rate	1.45
Resolution of curvature	0.5
Resolution of narrow regions	0.6

The meaning of maximum and minimum element size is evident. Correctly defining the minimum element size is essential, especially in preventing the generation of many elements in narrow regions. The maximum element growth rate defines the maximum factor by which an element size increases from regions of smaller element sizes to larger ones. The resolution of

curvature describes the relationship between the size of the boundary elements and the curvature of the geometric boundary. The relationship is defined as:

*Maximum allowed element size along boundary = Radius of curvature  $\times$  resolution of curvature.*

The resolution of narrow regions parameter allows the user to control the approximate number of layers that are created in narrow regions; when this number is less than one the mesh generator will create elements that are anisotropic in size in narrow regions.

According to Eq. (4.6) the wavelength of sound waves in water around an excitation frequency of 14 kHz is approximately 100 mm. Therefore, through the described mesh more than 10 degrees of freedom per wavelength could be obtained. Thus, the solved meshed for the acoustic problem is substantiated.

Additional results leading to this final mesh are presented in Appendix B. The problem presented 3.46 million degrees of freedom, which was solved through a PARDISO algorithm solver, provided by COMSOL Multiphysics. Isometric and top views of the mesh are illustrated in Figure 4-5.

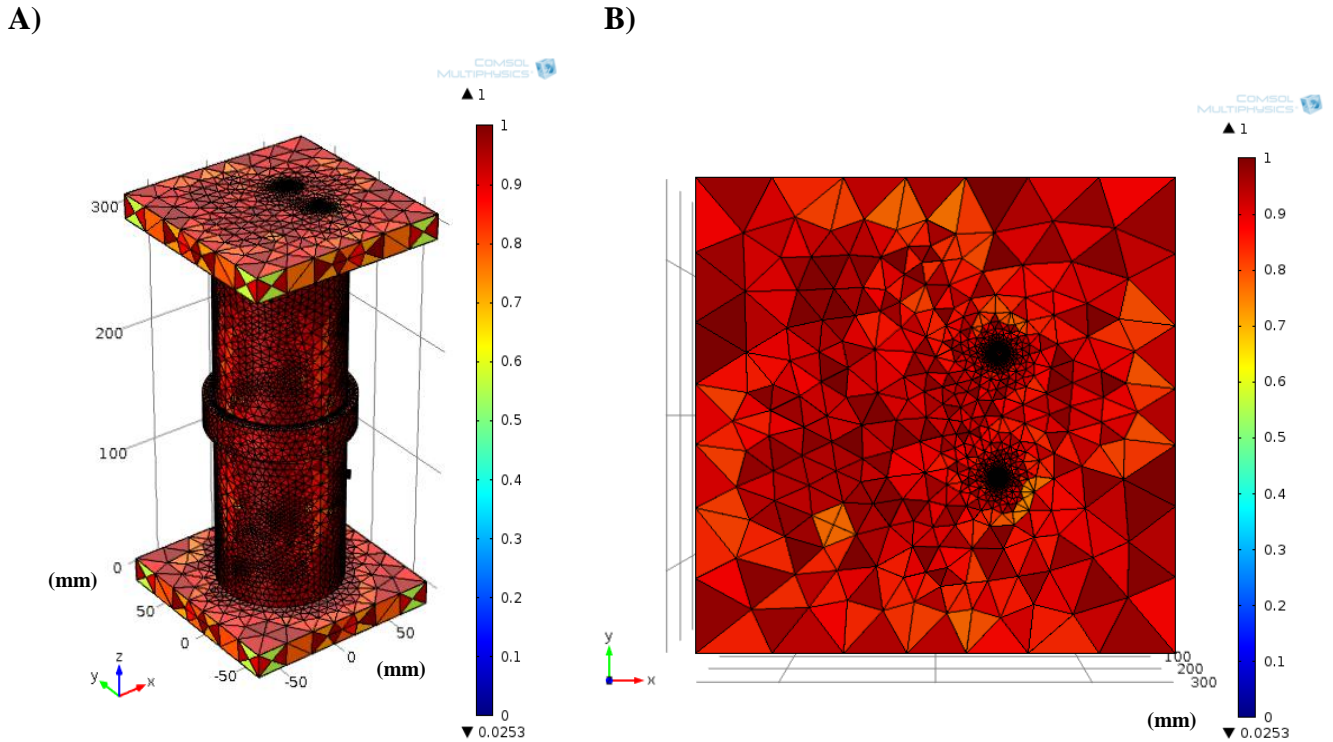


Figure 4-5 Mesh Quality Plots for Numerical Model Mesh consisting of 1,185,922 elements A) Isometric and B) Top view

## 4.6 Numerical Results

A time harmonic analysis, also called a frequency response analysis was conducted using the mesh presented in Figure 4-5. This type of analysis performs a frequency parametric sweep, calculating independent variables values, as a function of frequency. In order to calculate the resonance modes of the confined liquid pressure was observed as a function of frequency. The frequency parametric sweep was performed in a 10 Hz step size. Several parameters are used to investigate the vibrational response of the system and to locate its mechanical resonance frequencies. Among these parameters, pressure, pill microphone gain, electrical impedance on the PZT ring, and wall displacement were studied and will be discussed. Pill microphone gain is the ratio of output voltage on the inner surface of the pill microphone to the applied voltage on the inner surface of the PZT Ring. Voltage in the pill microphone is a function of wall

displacement which triggers the direct piezoelectric effect. Wall displacement (deformation) will take these effects into account. Finally, electrical impedance will be calculated as the ratio of the voltage in the PZT to the current passing through the PZT.

#### **4.6.1 Numerical Results: Harmonic Analysis**

Figure 4-6 presents the pressure amplitude graph at two defined points located inside the artificial thigh. The shown amplitude pressure curves correspond to absolute pressure at two points, one located inside the inner tubes and one located outside of the tubes, at an equal height. Overall, pressure peaks should agree everywhere unless pressure is measured at a pressure node. The pressure induced in a point inside the tube (continuous line) will be more influenced by structural vibrations than the dotted line. For instance, the peak around 14 kHz presents the same pressure amplitude in both cases. This could suggest that this pertains to a fluid resonance frequency; whereas, the 12 and 13 kHz peaks display amplitude changes. Damping is known to increase with frequency values; thus, this change in pressure amplitude peaks observed in the 12 and 13 kHz frequencies might suggest that at these frequencies are results of a fluid-structure interaction. These peaks can be observed in Figure 4-6 and represent resonance frequencies of the artificial thigh.

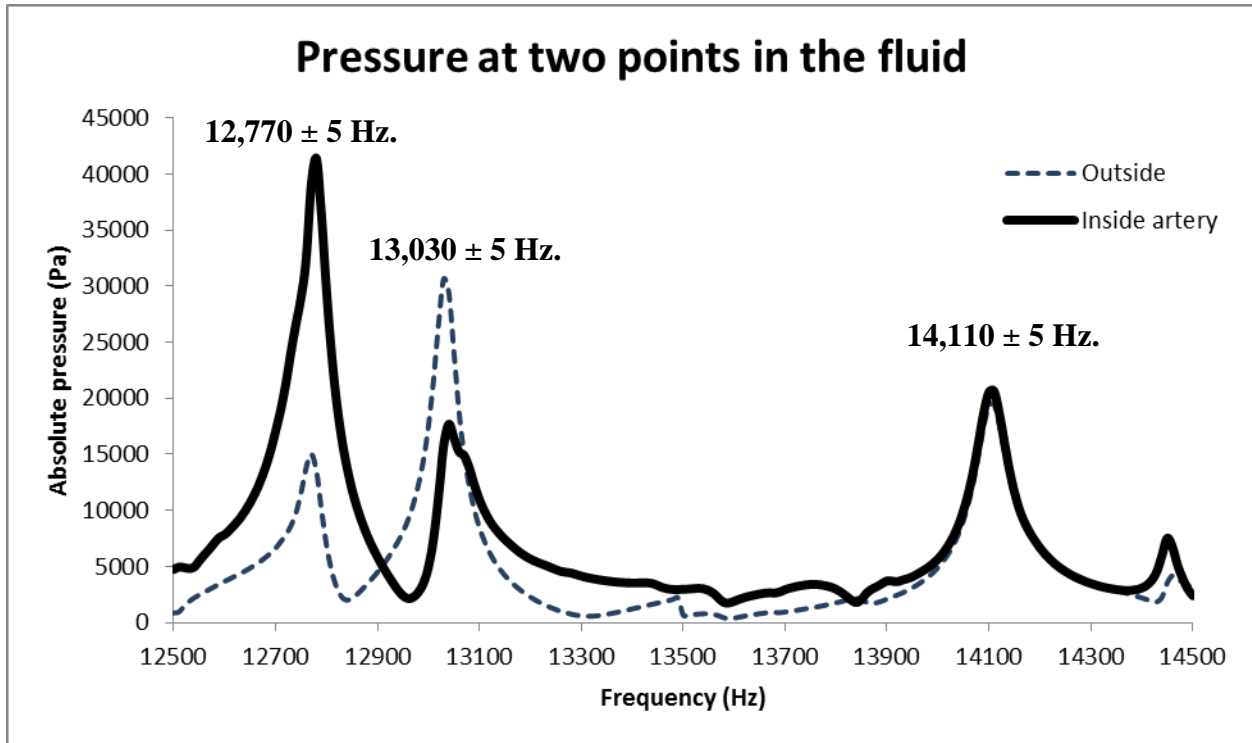


Figure 4-6 Pressure Amplitude graphs of two defined points inside the artificial thigh

The artificial thigh presents several resonance frequencies in the 10-20 kHz range. In this range, the system displays the first and the second resonance longitudinal modes ( $\omega_{1,1}, \omega_{1,2}$ ) that present a pressure distribution similar to the one obtained when only the fluid is considered (see Figure 4-7 through Figure 4-9 and Figure 4-14). Figure 4-7 through Figure 4-9 display selected pressure profiles denoting selected resonant modes of the structure. At the fundamental mode of the liquid (Figure 4-7), a pressure antinode develops at the surface of the bone. Figure 4-10 through Figure 4-12 show the corresponding pressure distribution, in the longitudinal and radial directions at the respective frequencies. The system presents, second radial modes akin to  $\omega_{1,2}$  and  $\omega_{2,2}$  close to 30 kHz (see Figure 4-15 and Figure 4-16). In order to confirm the validity of the indicated resonance frequencies an Eigen Frequency analysis was performed. The resonance

frequencies obtained from Figure 4-6 agree with Eigen frequencies obtained through this Eigen Frequency Analysis.

A complicated geometry, such as the one presented in Figure 4-1, contains infinite normal modes of resonance. The liquid domain, the structural domain, and the PZT domain are all characterized by independent resonance frequencies. Therefore, calculated Eigen frequencies contain a combination of the independent fluid and structural domains, as well as new additional resonance frequencies obtained as a result of the domain coupling (Axisa & Antunes, 2007). In general, acoustic chambers work by exciting resonant modes of the fluid domain. As can be observed in Figure 4-6, there are multiple peaks (points presenting maximum pressure). These peaks might denote a characteristic natural mode of vibration of the fluid, structure or the coupling of both.

The simulated geometry is a simplified version of what would ultimate be a complicated human thigh. If this many pressure peaks are observed in this geometry, many more peaks can be expected to be found in a more complex and physiological-like system. Although the manifestation of multiple resonance frequencies might make the analysis more difficult, we believe this to be a positive characteristic since it opens the possibilities to be able to excite the system in many frequencies. Each of them could potentially contribute to the ultimate bubble detection goal.

Initial simulations, performed without damping, displayed additional pressure amplitude peaks (figures obtained in simulations without damping are not presented in this work) than those observed in Figure 4-6. However the analysis presented in this figure was done by adding damping on the structural parameters; thus, lowering the value of less relevant frequencies. Structural damping parameters are shown in Table 4-1. From this analysis three interesting

study frequencies arise. Each frequency must be analyzed in detail to describe the dynamic behavior of the artificial thigh under the conditions imposed by each characteristic frequency.

As previously discussed in this chapter, very small bubbles (natural frequencies higher than the excitation frequency) will migrate toward the antinodes, while big bubbles (natural frequencies lower than the excitation frequency) will migrate towards the nodes. This bubble behavior is caused by the Bjerknes force, which is a non-linear effect resulting from the finite wavelength of the sound waves in the liquid. The natural frequency of a bubble with a diameter of 100  $\mu\text{m}$  is approximately 60 kHz. Consequently, if the frequency used in the artificial thigh is less than 60 kHz, a micron-sized bubble will be trapped at the antinodes. This type of analysis was taken into consideration when selecting the system excitation frequency to be studied experimentally. Investigating the possibility of working additional frequencies should be considered in further investigations taking into consideration these bubble manipulation possibilities.

From Figure 4-7 it can be observed that pressure waves display an asymmetrical pattern due to the existence of the inner tubes; justifying the importance of the three dimensional analysis. Also, a change in resonance frequency is observed in simulations performed with the inner tubes (refer to Appendix B).

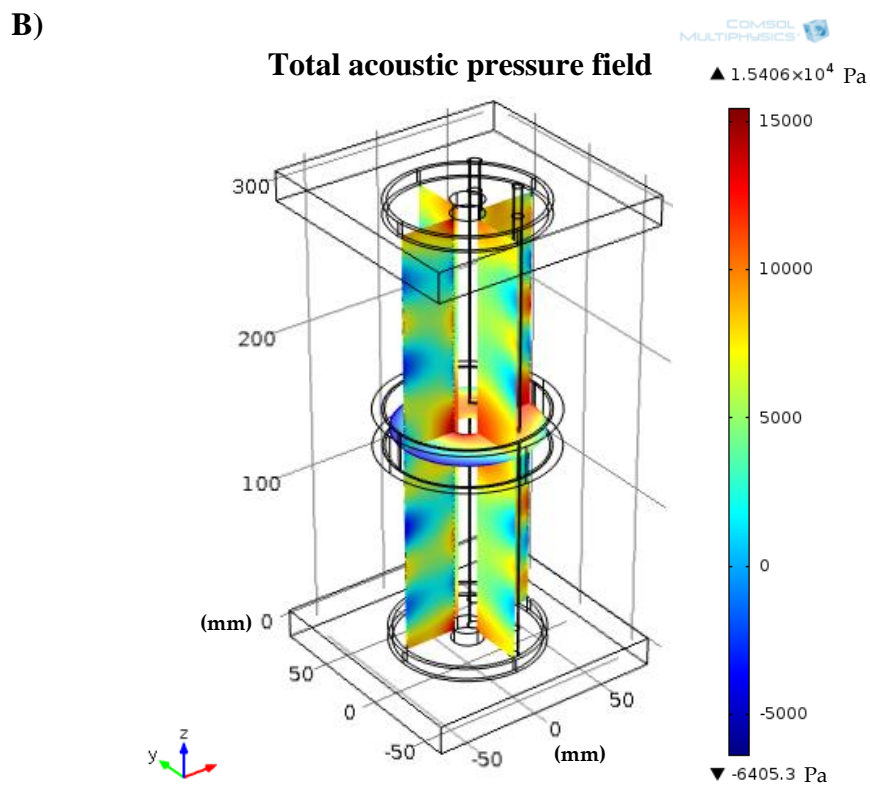
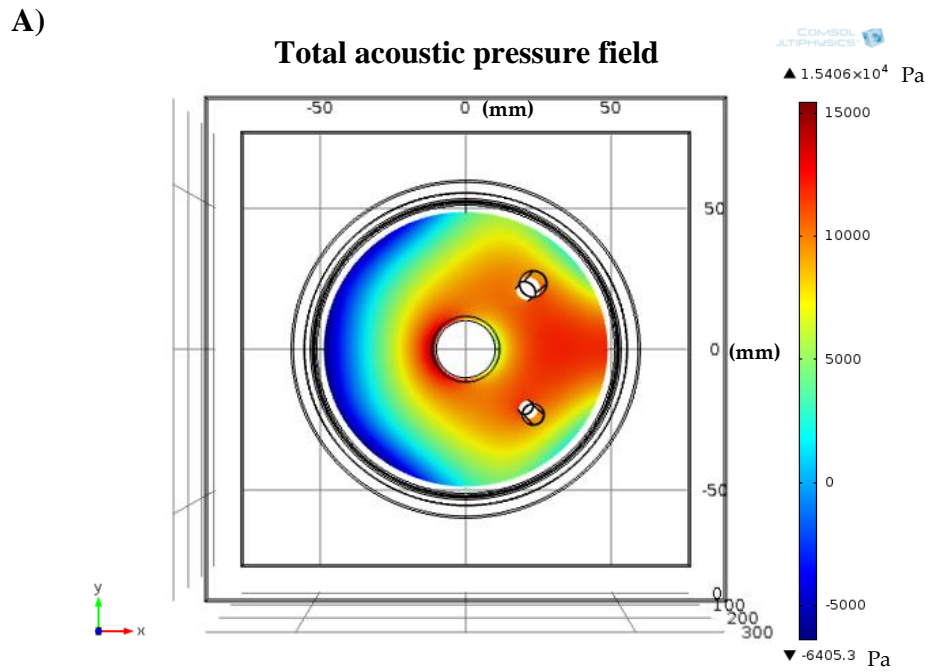
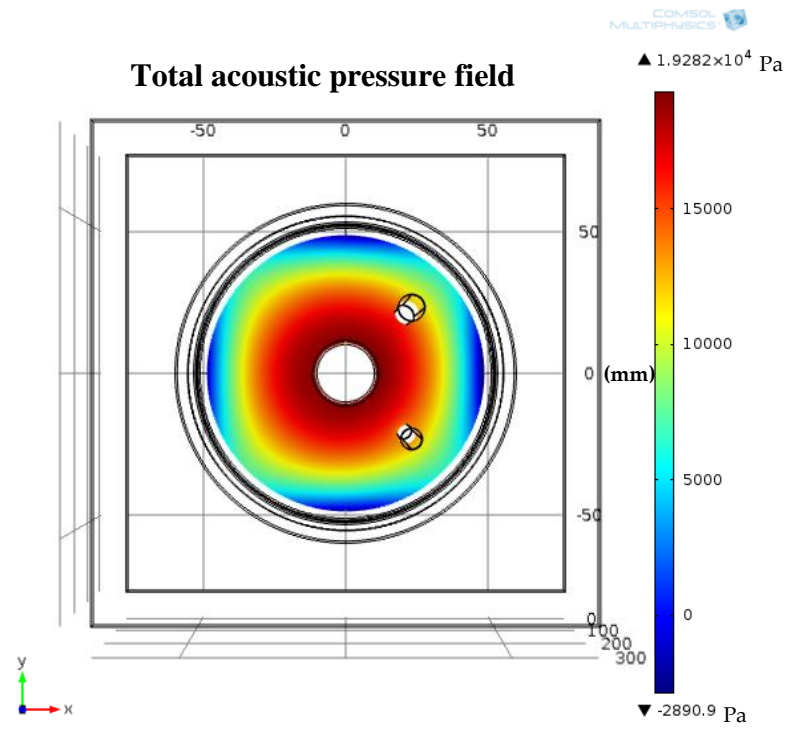


Figure 4-7 Resonance Frequency of the structure corresponding to fundamental mode of the fluid: A) Top View, B) Isometric view frequency: 12,760 Hz.

A)



B)

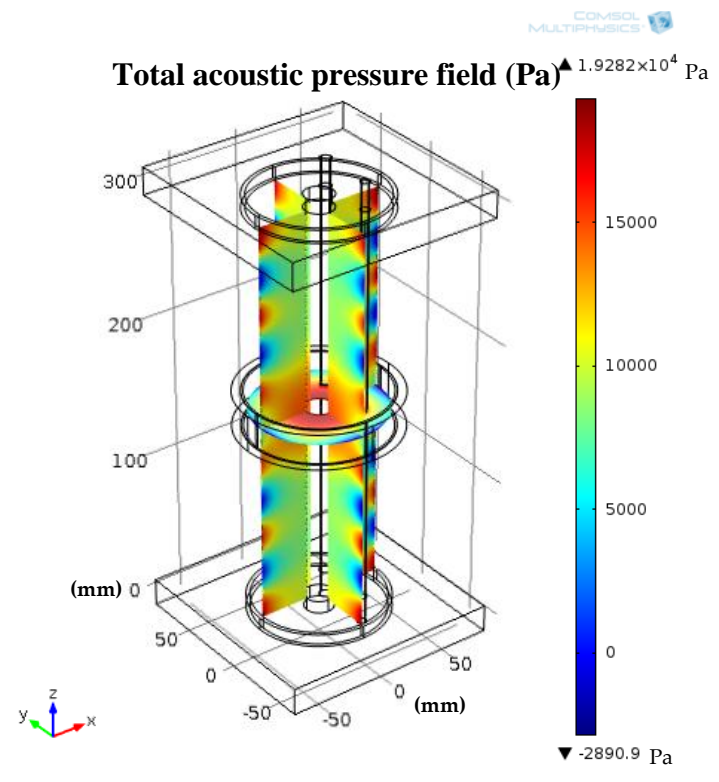
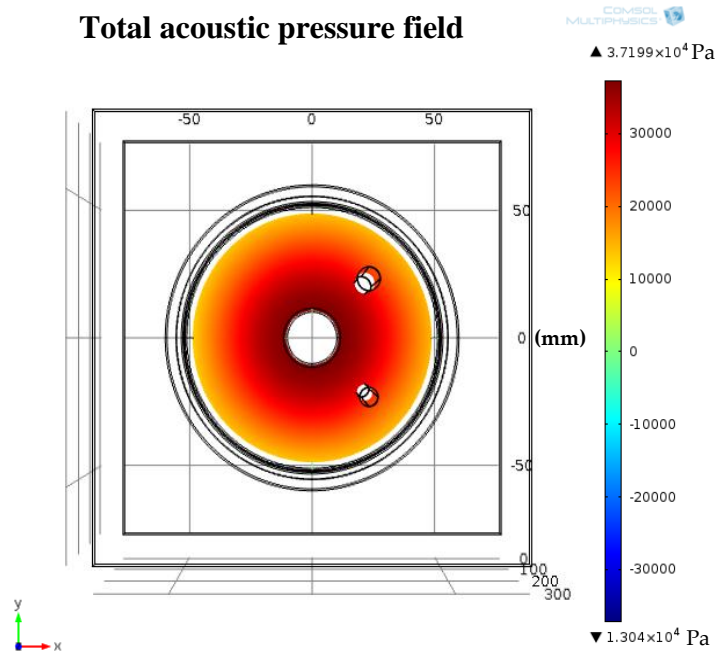


Figure 4-8 Resonance Frequency of the structure corresponding to fundamental mode of the fluid: A) Top View, B) Isometric view, frequency: 13,010 Hz.

A)

### Total acoustic pressure field



B)

### Total acoustic pressure field

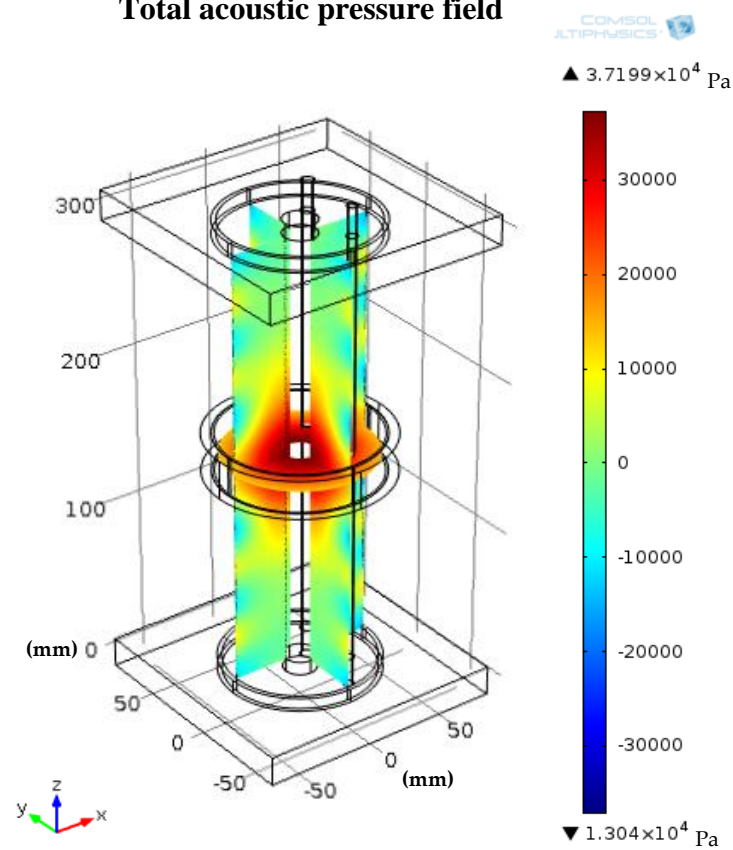
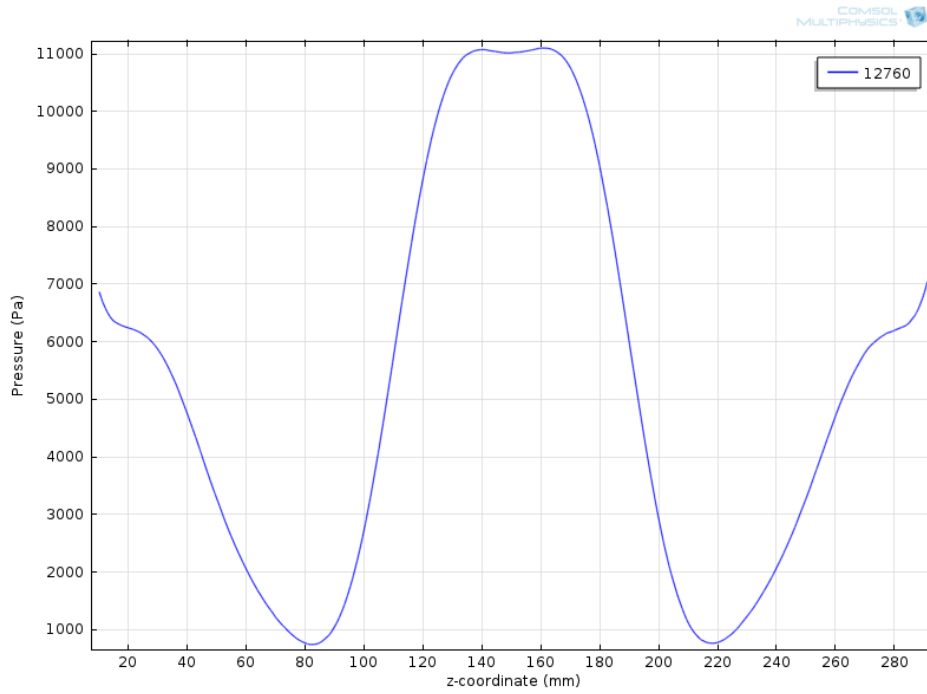
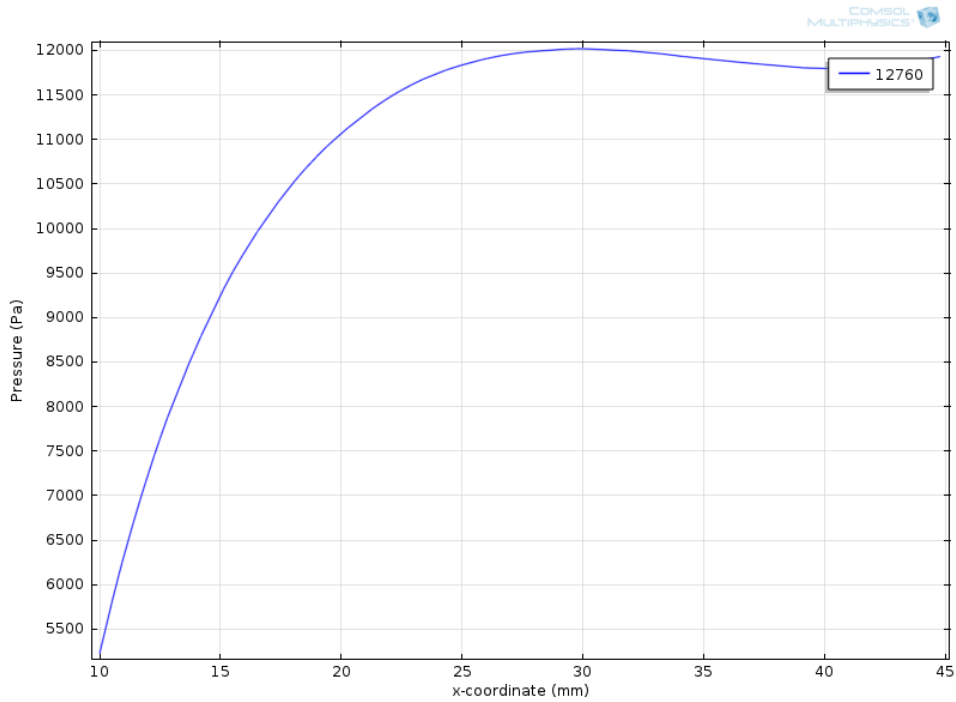


Figure 4-9 Resonance Frequency of the structure corresponding to fundamental mode of the fluid: A) Top View, B) Isometric view, frequency: 14,070 Hz.

**A)**

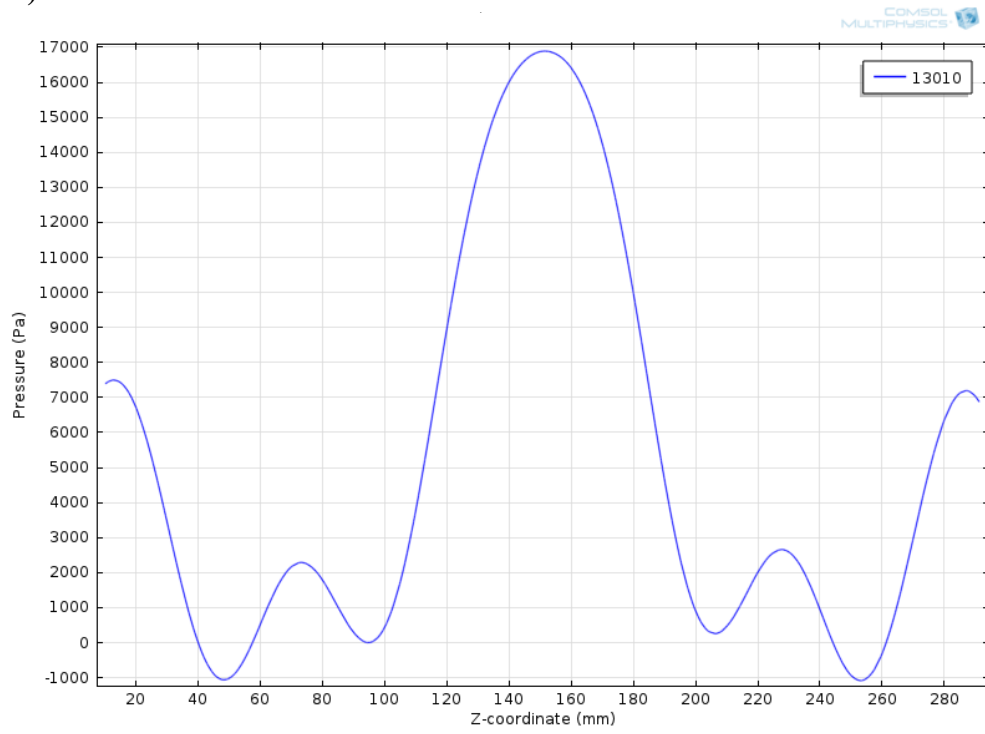


**B)**



**Figure 4-10 Longitudinal (A) and Radial (B) Pressure Profiles at 12, 760 Hz. at vertical and horizontal lines on the outside of the inner tubes**

**A)**



**B)**

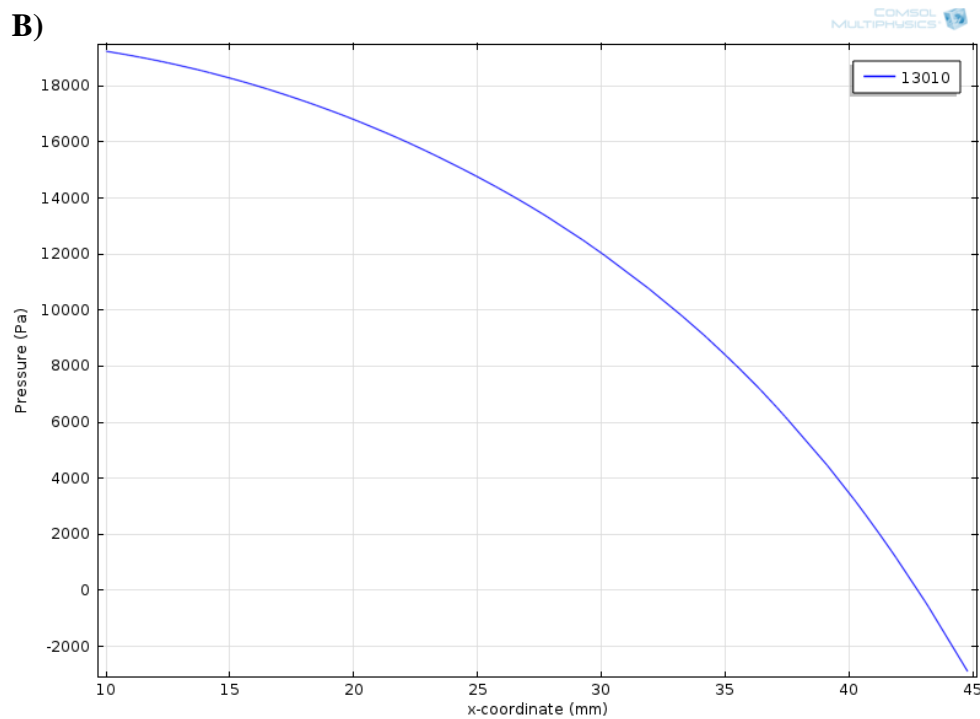
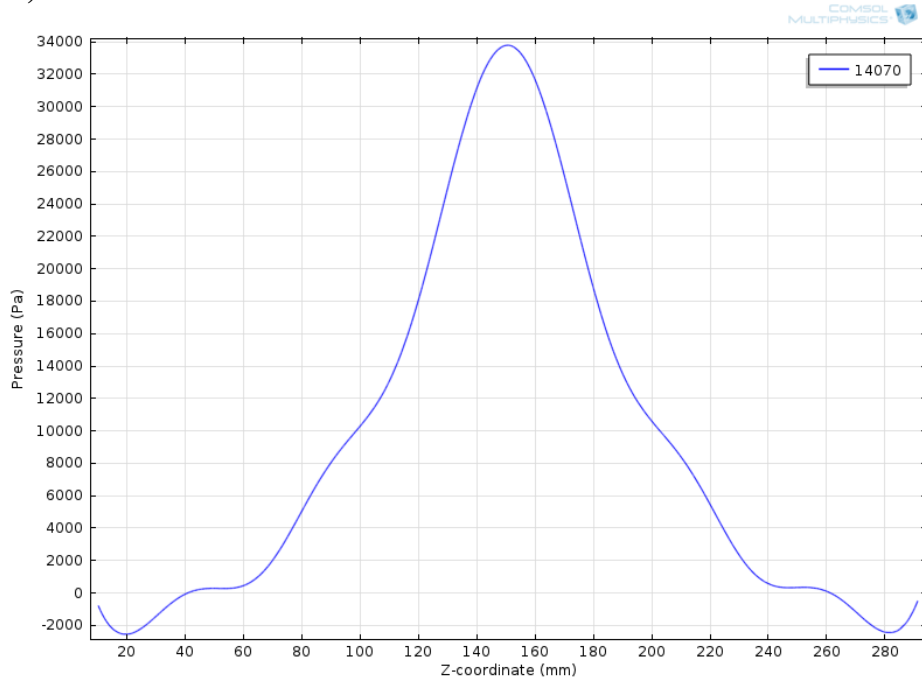


**Figure 4-11 Longitudinal (A) and Radial (B) Pressure Profiles at 13, 010 Hz. at vertical and horizontal lines on the outside of the inner tubes**

A)



B)

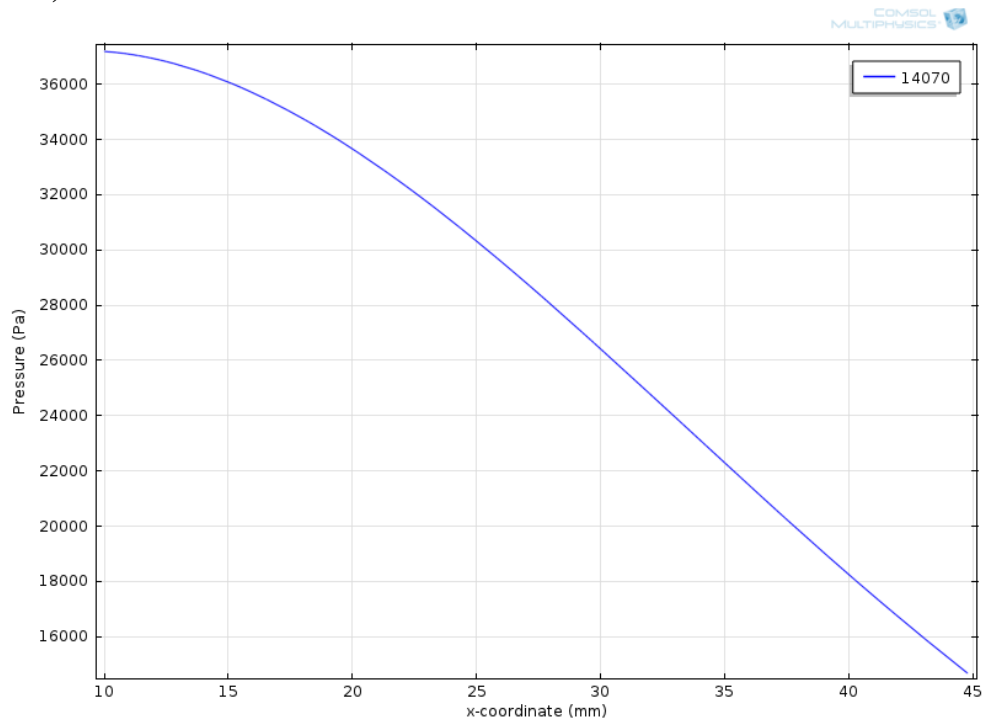


Figure 4-12 Longitudinal (A) and Radial (B) Pressure Profiles at 14,070 Hz., at vertical and horizontal lines on the outside of the inner tubes

As previously discussed, the PZT ring, polarized in the radial direction, will undergo harmonic oscillations, thus deforming the cylinder wall. These wall deformations will affect the fluid, creating a standing wave, thus achieving the pressure distribution profile provided in Figure 4-7. The wall deformation shown in

Figure 4-13 at an excitation frequency of 13,010 kHz illustrates the deformations driving the voltage given off by the pill microphone. The pill microphone is a key component, necessary to monitor the fluid pressure and identify the resonance modes of the system.

Due to the Bjerknes forces, bubbles migrate towards the pressure antinodes or nodes. The number of bubble entrapment locations varies with  $2n+1$  where  $n$  is the number of pressure antinodes in the pressure profile.  $n$  entrapment locations correspond to entrapment sites for small bubbles (smaller than resonance), and  $n+1$  would correspond to entrapment sites for large bubbles (larger than resonance). Note that with the PZT located at the center of the structure, the easiest mode to excite is the first resonant mode. This occurs because the area experiencing the greatest excitation coincides with the points of maximum pressure. To excite higher resonance modes (such as those presented in Figure 4-14 through Figure 4-17) would imply having the PZT positioned at different axial locations or the necessary addition of a second piezoelectric ring. Simulations performed with two piezoelectric rings are depicted in Appendix B.

Second longitudinal modes display a pressure node at the center of the structure. Since the center of the structure is where the PZT is located, obtaining a pressure node in this region is unlikely, since this is the exact place of wall excitation. Figure 4-14 through Figure 4-16 were obtained through an Eigen frequency analysis. These frequencies describe possible behaviors on the system based on Eigen values of the system. However, as expected these pressure profiles were not obtained in a time harmonic analysis for the above explained reasons.

If bubble entrapment of any size is the desired objective, it might be more beneficial to excite higher order resonant modes. For instance, exciting a third longitudinal mode would generate a Bjerknes force profile which would provide four locations where bubbles larger than resonance would be captured, two which are of interest since they would be inside the artificial thigh system, and three locations towards where bubbles smaller than resonance would most likely be translated to. The discussed pressure profile, containing three pressure antinodes is illustrated in Figure 4-17.

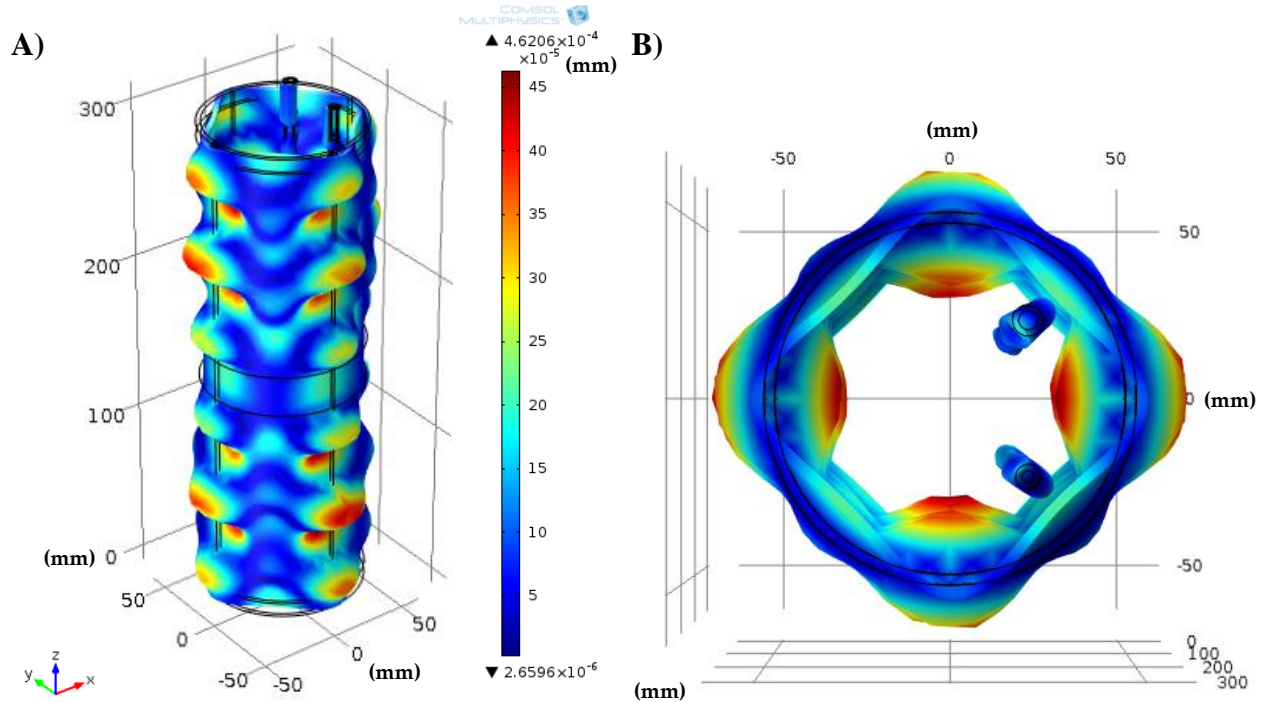


Figure 4-13 Total surface displacement and Wall deformation at a frequency of 13,030 Hz. Isometric (A) and Top views (B).

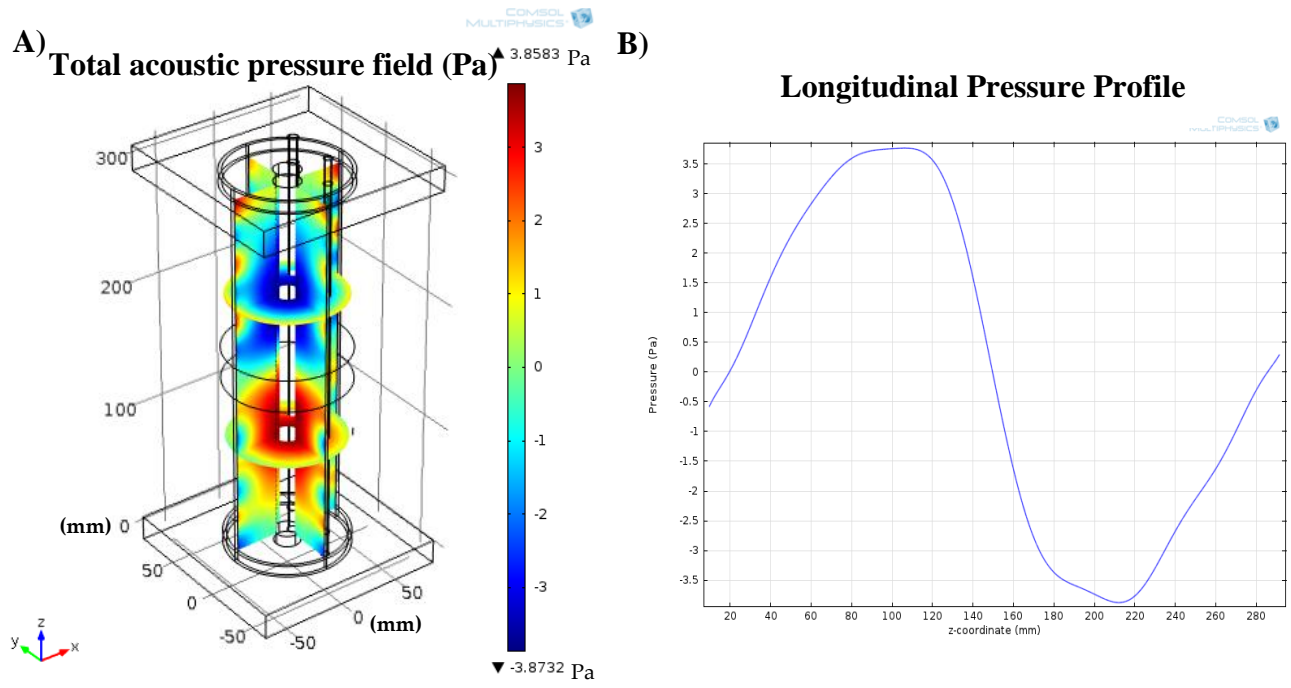


Figure 4-14 Resonance Frequency of the structure displaying the acoustic pressure field corresponding to second longitudinal mode  $m=2$ ,  $n=1$  and  $f=15570$  Hz. Obtained through Eigen frequency analysis.

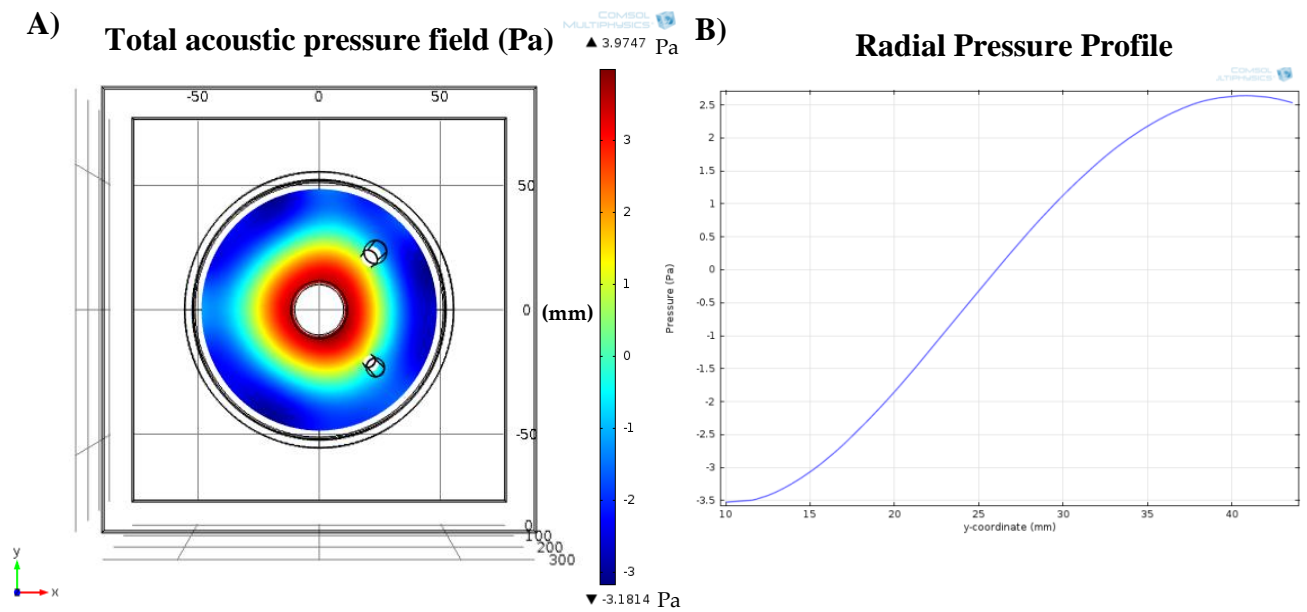


Figure 4-15 Resonance Frequency of the structure displaying the acoustic pressure field corresponding to third fluid mode  $m=1$ ,  $n=2$  and  $f=26,977$  Hz. A) Top View B) Radial Distribution. Obtained through Eigen frequency analysis.

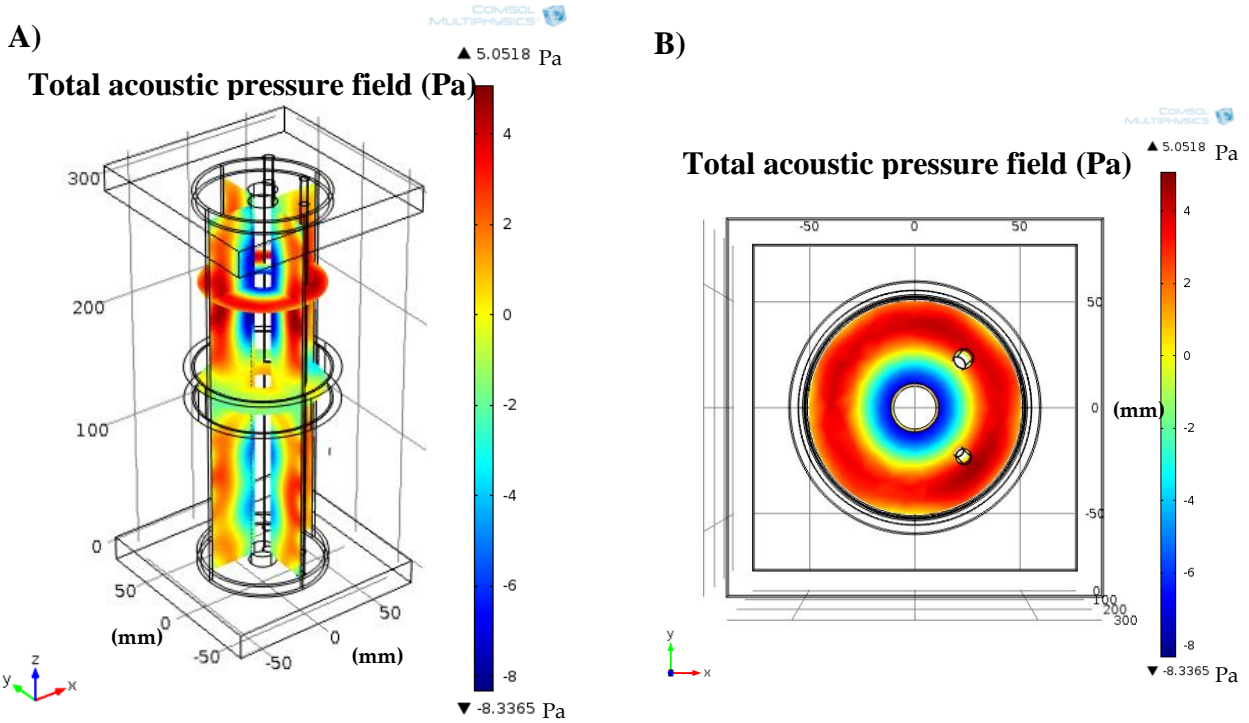


Figure 4-16 Resonance Frequency of the structure displaying the acoustic pressure field corresponding to fourth fluid mode  $m=2, n=2$  and  $f=30,455$  Hz. A) Isometric view B) Top view. Obtained through Eigen frequency analysis.

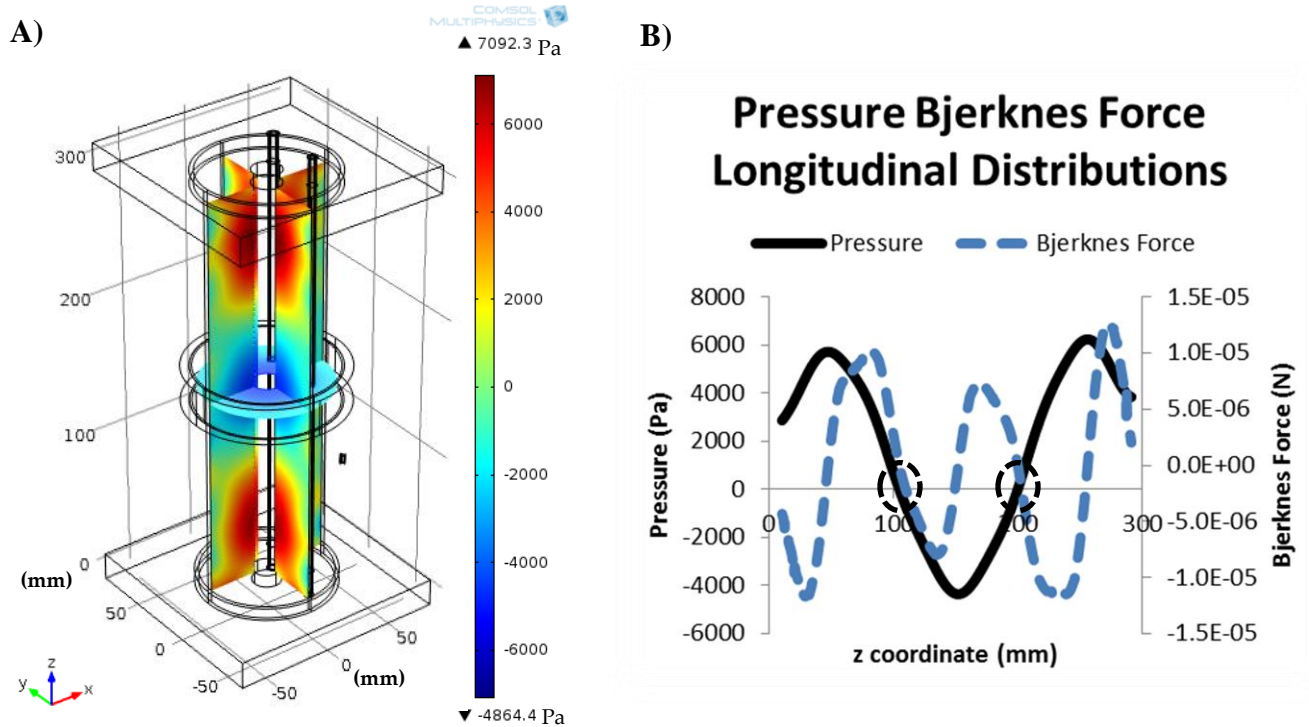


Figure 4-17 Pressure Profile of third longitudinal mode (16.23 kHz); displaying 2 pressure nodes and 3 pressure antinodes. B) Bjerknnes Force longitudinal distribution highlighting 2 bubble entrapment possibilities for bubbles with  $r \geq 0.5$  mm. Simulations are a result of a harmonic analysis.

#### 4.6.1.1 *Electrical Measurements*

The same electrical readings which were to be carried out experimentally were extracted from numerical simulations to anticipate the response of the simplified artificial thigh. Figure 4-18 shows the admittance response graph obtained by integrating the normal current density ( $J$ ) over the inner surface of the PZT Ring and dividing it by the voltage on the PZT ring ( $V_{PZT}$ ).

$$Y = \oint_{H_1}^{H_2} \frac{J}{V_{PZT}} dzd\theta \quad (4.7)$$

Where  $H_2-H_1$  defines the height of the PZT ring and  $\theta$  varies from 0 to  $2\pi$ .

Additionally, by dividing the voltage on the pill microphone by the voltage at a point in the surface of the PZT ring, a ratio defined as pill microphone Gain is obtained. Figure 4-19 displays the value of this ratio as a function of frequency. Furthermore, Figure 4-20 shows the correspondence of peaks between fluid pressure and pill microphone voltage. These results validate the utilization of pill microphones as fluid pressure monitors in the experimental part of this work. Figure 4-20 shows the correspondence of 3 out of 4 peaks in the frequency sweep. This additional peak could be the result of an additional wall or pill microphone resonance mode or an interaction between these and should be objects of further study. Take into consideration that the pill microphone responds to the cylinder wall excitation. In this range of frequencies the pill microphone response could also indicate the response of the glass cylinder, exhibiting amplified vibrations at a structural resonance frequency.

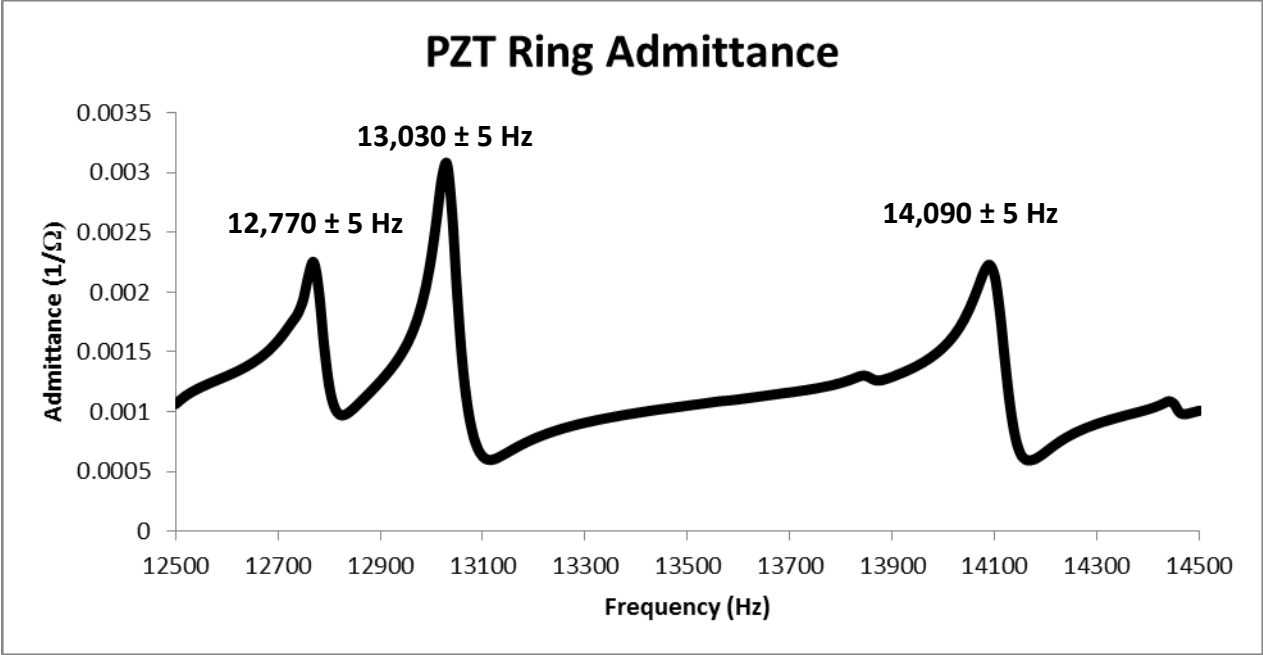


Figure 4-18 Admittance of the PZT ring as a function of frequency

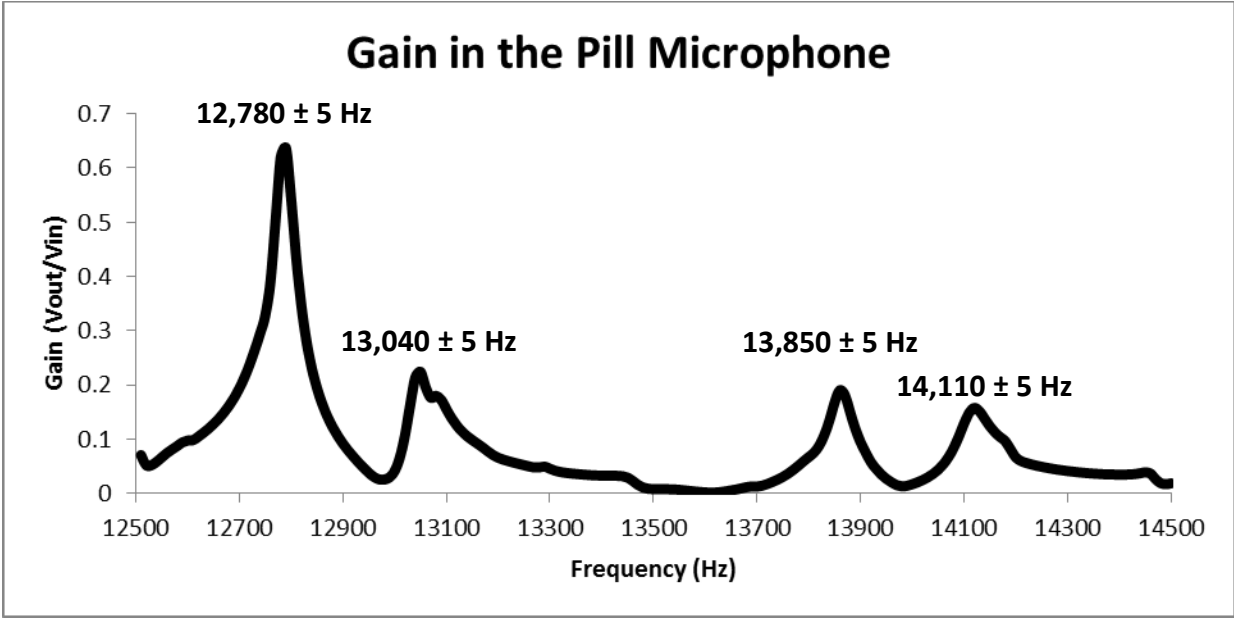


Figure 4-19 Gain as a function of frequency

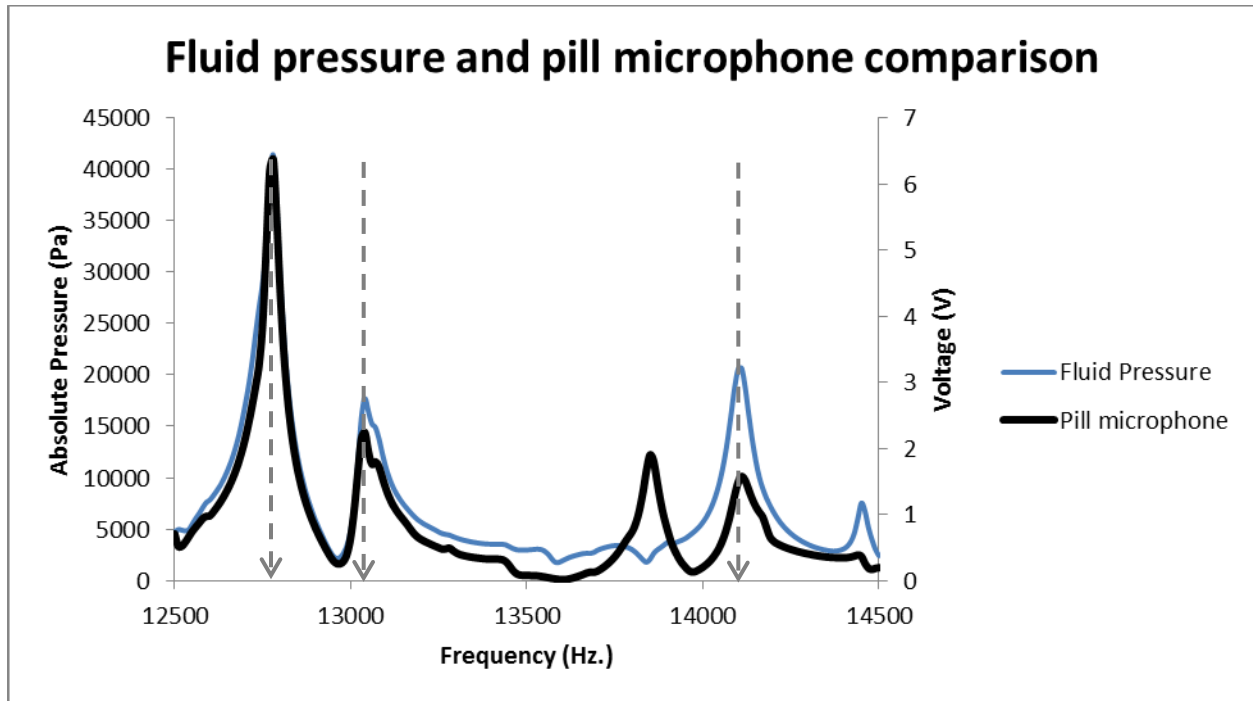


Figure 4-20 Correspondence between fluid pressure and pill microphone voltage

This chapter, so far, has presented results concerning the overall dynamic behavior of artificial thigh structure. From the results obtained bubble migration patterns could be predicted as explained by Bjerknes force theory. However, for a greater part of the experimental analysis, bubbles will be traveling through the artificial vein and artery structures. Therefore, the next section will focus on details regarding these subdomains.

#### ***4.6.1.2 Detailed Simulation Study inside the Vein and Artery***

Bubble detection within blood vessels has proven to be an easier task than in soft tissue (Buckey et al., 2005; Jenderka, et al., 2002). Therefore, initial experimental trials targeted bubble detection within the inner tubes instead of on the outside. Thus, in this section, the fluid and structure behavior of the inner tubes as a result of the induced acoustic pressure gradients is numerically studied. Results confirming the capabilities of the system to produce accurate bubble entrapment through the use of the acoustic force and correct manipulation of the Bjerknes force are also discussed in this section.

Figure 4-21 illustrates two pressure profiles. The continuous line previously shown in Figure 4-11, presented the pressure profile of the fluid, measured outside of the inner tubes. Figure 4-21 complements this analysis by showing a vertical pressure profile at a defined line inside the artery at a frequency identified as a possible fundamental mode of the fluid. These pressure distributions display significant differences as can also be illustrated in the pressure distribution observed in Figure 4-22. Figure 4-22 illustrates the pressure distribution inside the artery; a similar one is obtained inside the vein. The same marked differences are explained in other frequencies as illustrated in Figure 4-23. Figure 4-24 displays the deformation of the artery tube at a frequency of 13,010 Hz. The pressure within the tubes is affected by this deformation. Therefore, the pressure obtained within the tubes is due to a fluid-structure interaction. This pressure profile is a combination of the fluid resonance mode and the structural vibration mode of the tube at this frequency.

A Fourier transform analysis was performed on the curves describing the longitudinal pressure profiles taken on the outside and the inside of the tubes presented in Figure 4-23. Figure 4-25 illustrates the wave number spectrum obtained through this Fourier analysis. The pressure inside the tubes is mostly dominated by the pressure experienced in the overall fluid domain, as can be observed by sharing the same wave numbers. Figure 4-25 clearly illustrates additional Fourier components, in the wave number spectrum of the pressure profile obtained inside the artery. These additional components can be directly attributed to the structural interaction with the pressure wave. The structure deforms and as a result influences fluid pressure as well. The magnitude of structural influence on total pressure was less drastic at lower frequencies. Additional details of this analysis are presented in Appendix B.

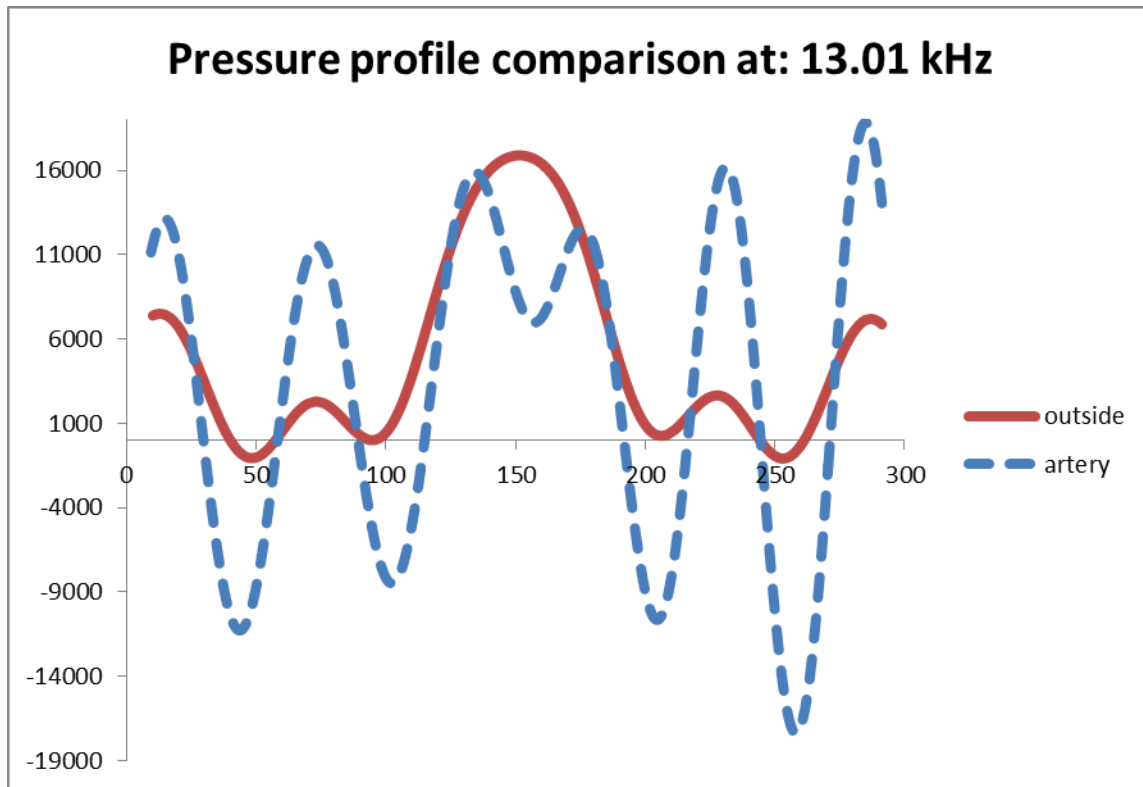


Figure 4-21 Longitudinal pressure profiles taken inside and outside the artery at 13,010 Hz.

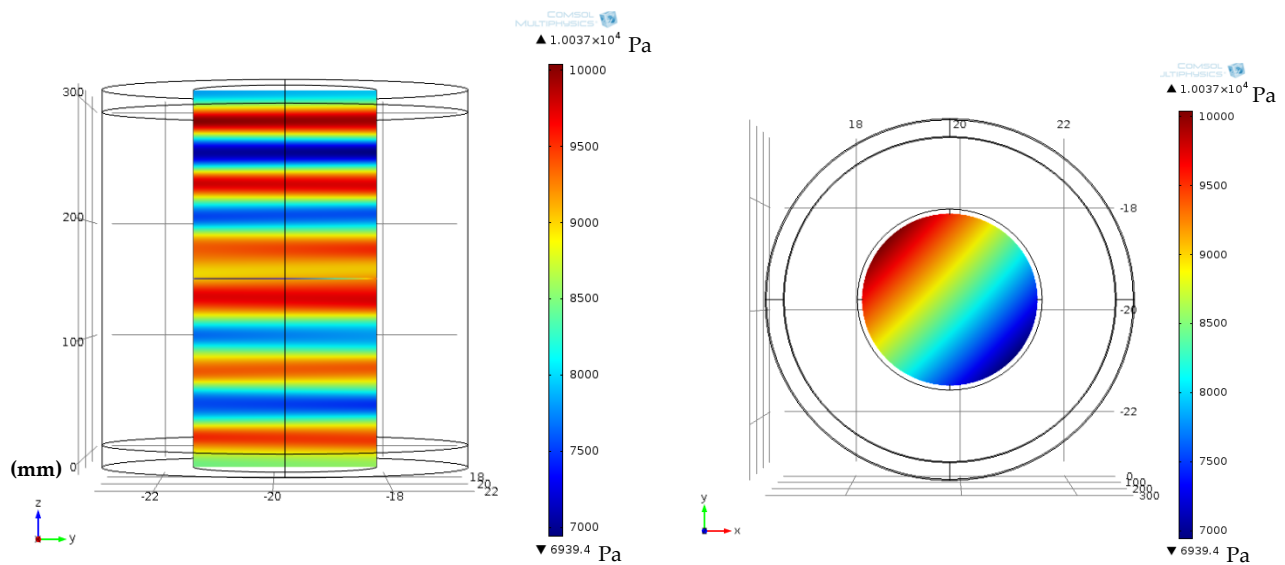


Figure 4-22 Acoustic Pressure Field inside the artery at 13.01 kHz, A) Front view, B) Top View

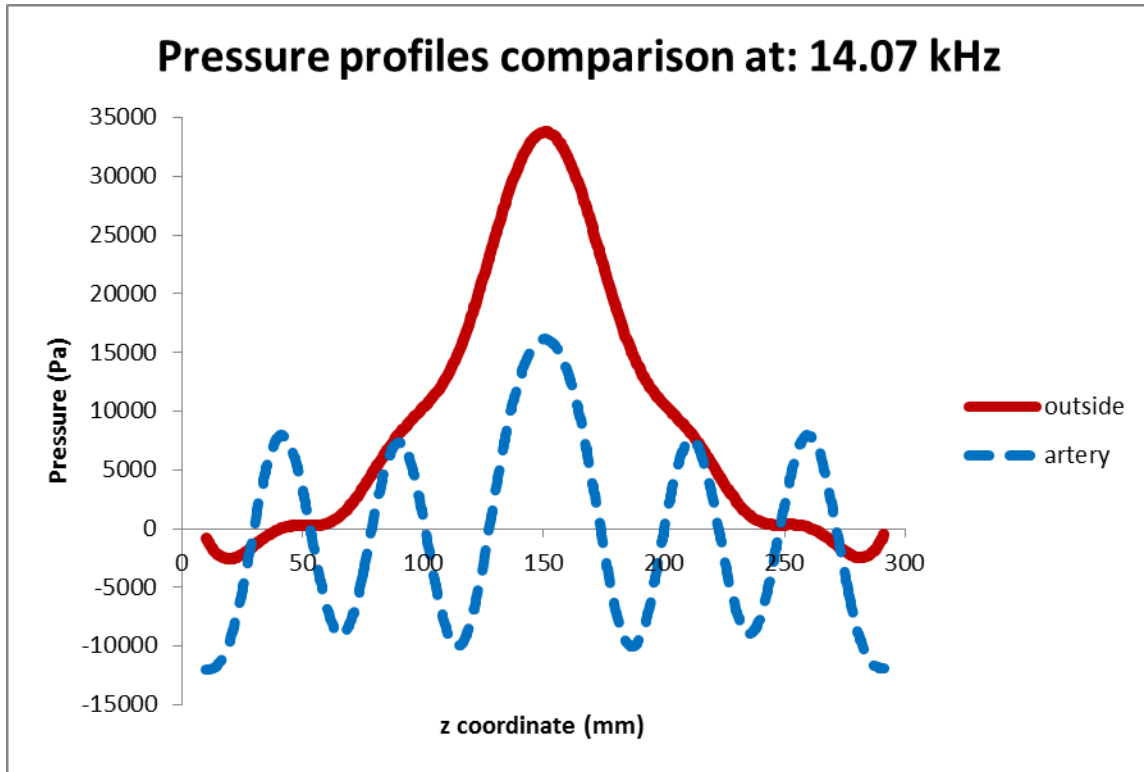


Figure 4-23 Longitudinal pressure profiles taken inside and outside the artery at 14,070 Hz.

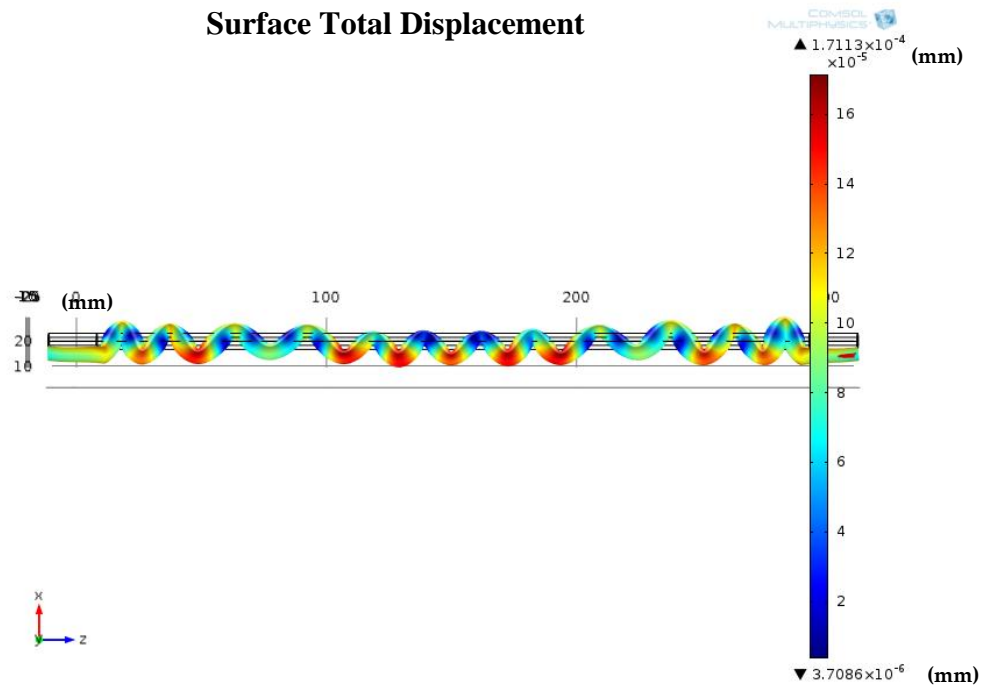


Figure 4-24 A) Artery surface total displacement and volumetric deformation at 13.01kHz.

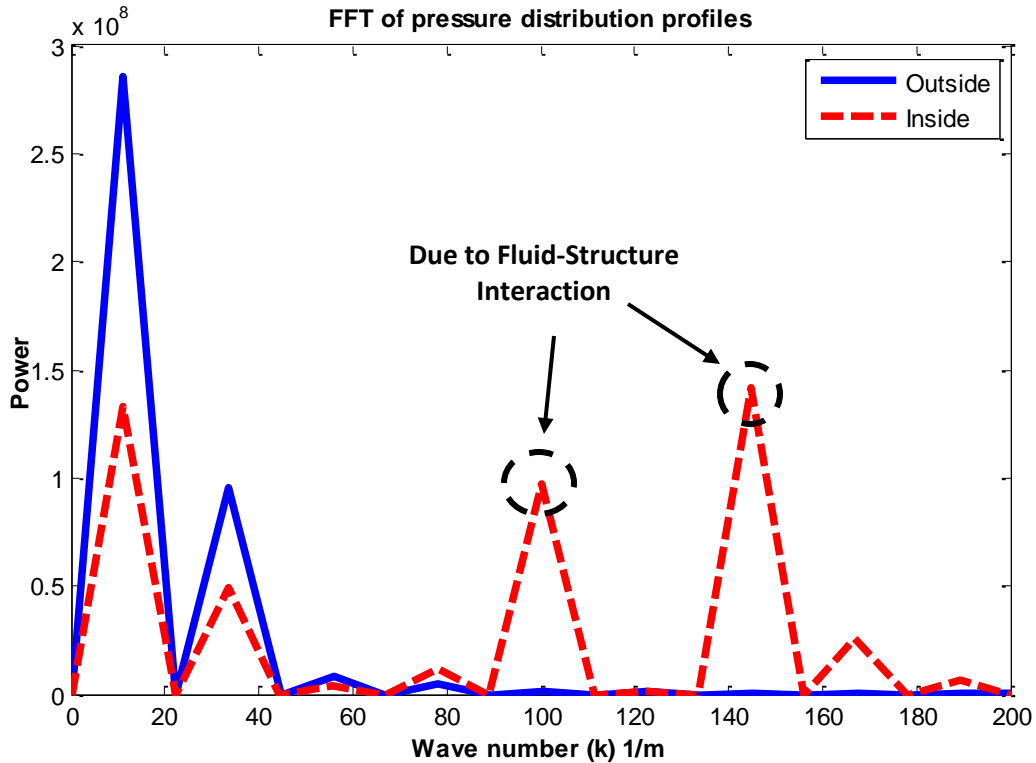
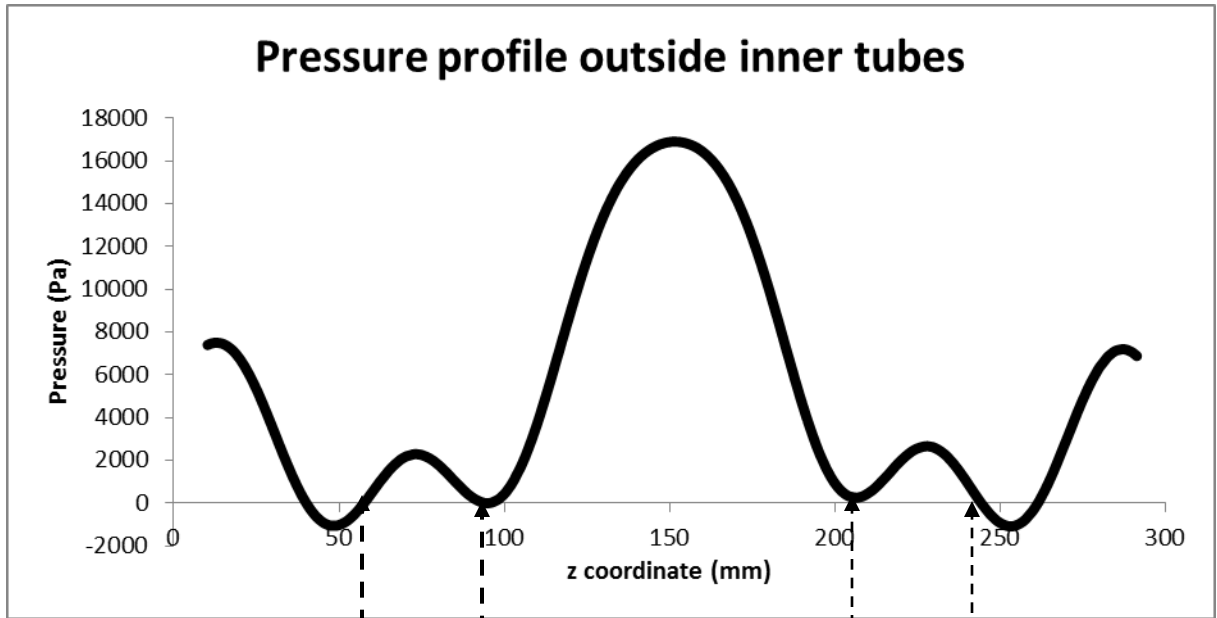


Figure 4-25 Frequency spectrum obtained from a FFT analysis of pressure profiles for a simpler geometry, displaying additional Fourier components affecting the pressure distribution inside the artery attributed to structural deformation

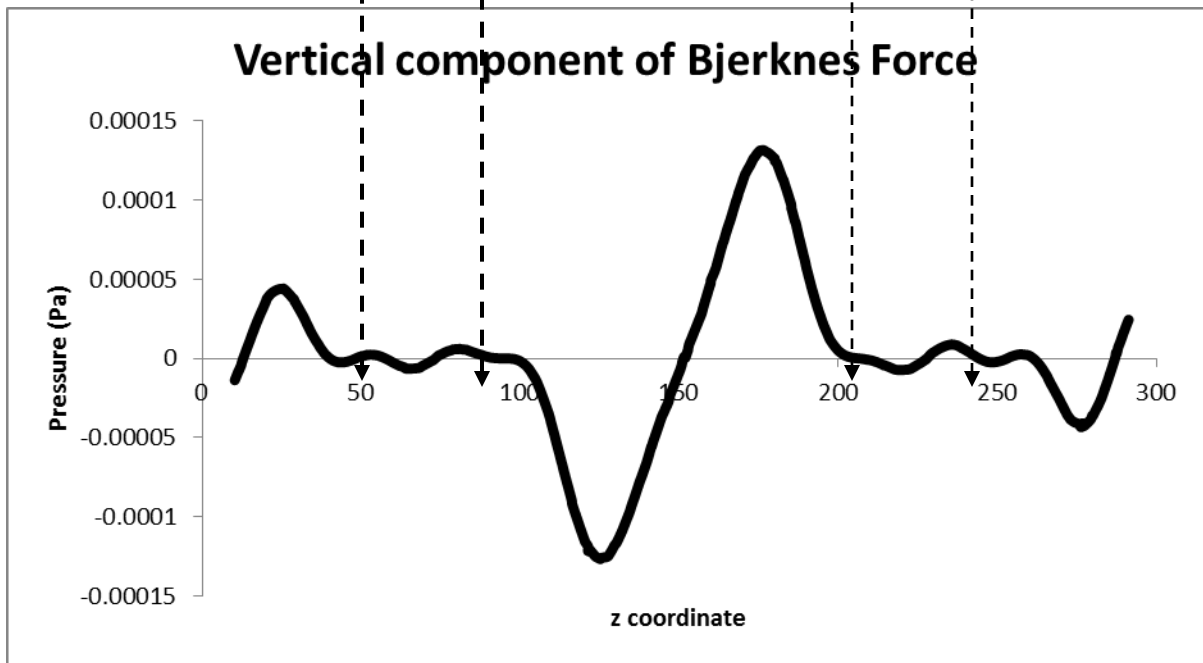
Once the pressure and the pressure gradient information inside the tubes were obtained, by implementing Eq. (2.22) and Eq. (2.23), it was possible to determine the magnitude of the Bjerknes forces induced by the pressure gradients. Vertical and radial component of the Bjerknes force distributions are illustrated in Figure 4-26 through Figure 4-28. Figure 4-26 displays the vertical component of Bjerknes forces from a longitudinal pressure distribution obtained outside the tubes, while Figure 4-27 shows the Bjerknes force distribution for a pressure profile obtained inside the artery, both at 13.01 kHz. These forces were calculated for a 1 mm diameter bubble. The resonance frequency of a 1 mm diameter bubble is approximately 6.4 kHz. Since the excitation frequencies lie above this value, a bubble of this size will be translated toward the pressure nodes. Considering the frequencies being studied, only bubbles smaller than 0.5 mm in diameter will be forced toward the pressure antinodes.

Figure 4-26 displays multiple bubble allocation possibilities (pressure nodes) for a 0.5 mm radius bubble. At these pressure nodes, the bubble will be in a stable equilibrium. From Figure 4-26(B) it can be observed that this particular position agrees with a Bjerknes force node. Therefore, once the bubble is translated near this location by the primary Bjerknes force, the bubble will be trapped because of a balance of forces in this particular position. Bubbles smaller than 500  $\mu\text{m}$ , will experience forces with opposite signs as those displayed in Figure 4-26 (B). Consequently they will be forced toward the middle of the chamber. Otherwise, bubbles with a radius  $\geq 500 \mu\text{m}$ , will be forced into the artificial thigh into positions between 40 and 100 mm, or 200 and 250 mm if they move past the PZT ring. However, inside the tubes, due to a pressure profile containing many more pressure nodes due to the effect of structural displacement, bubble entrapment can occur in many more locations as shown in Figure 4-27.

A)



B)



**Figure 4-26 A) Pressure distribution outside the small tubes (Frequency 13.01 kHz) B) Bjerknes force distribution at the same location as the pressure distribution shown in A) displaying Bjerknes force nodes which correspond to bubble entrapment locations for a 0.5 mm radius bubble.**

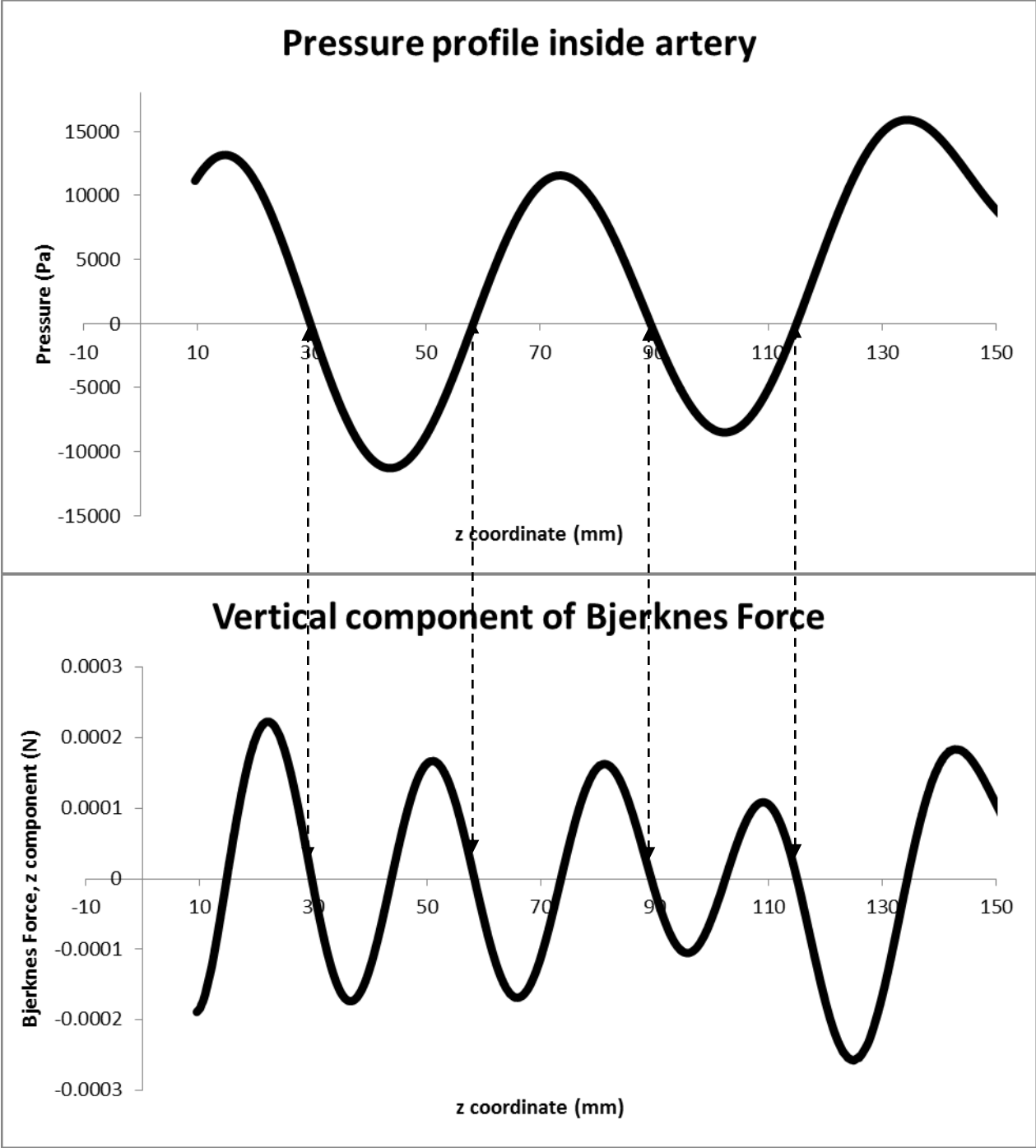


Figure 4-27 A) Pressure distribution inside artery showing particular pressure nodes of these frequencies B) Bjerknes force distribution at the same location as the pressure distribution shown in A) displaying Bjerknes force nodes which correspond to bubble entrainment locations. At a frequency of 13,010 Hz

Figure 4-28 presents an x-y slice cut of the overall distribution of the Bjerknes force in the radial direction at a frequency of 13.01 kHz. The figure displays highest Bjerknes force values in opposing ends of the small tubes inner diameter, highlighted in the figure. Therefore, a bubble in free flow will be forced towards the walls of the tube. This behavior was continuously observed experimentally as bubbles entering the chamber were eventually driven into the tube walls (observe for example Figure 5.10) and is a behavior observed by several investigators (Leighton,1994).

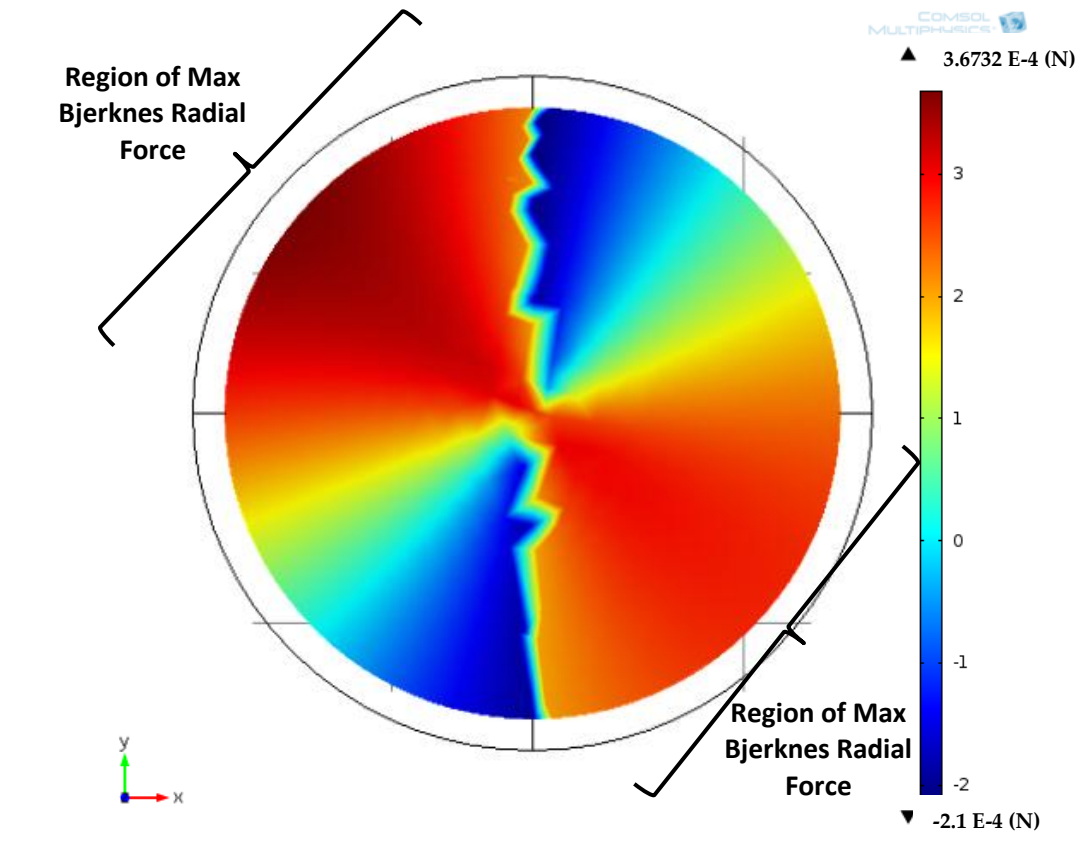


Figure 4-28 Bjerknes Radial Force at 13.01 kHz (N) Distribution at Hz. Inside the artery tube for a 1 mm equilibrium diameter bubble  $\omega_0 \approx 1.02$  kHz

Obtaining this pressure distribution was of utmost importance due to the inability to obtain pressure readings from the experimental model. Experiments were conducted for lower

frequency values. The pressure distribution at these selected frequencies and their respective vertical components of Bjerknes force distribution are illustrated in Figure 4-29. For these frequency range and selected frequencies analyzed a pressure node was located at 83 mm.

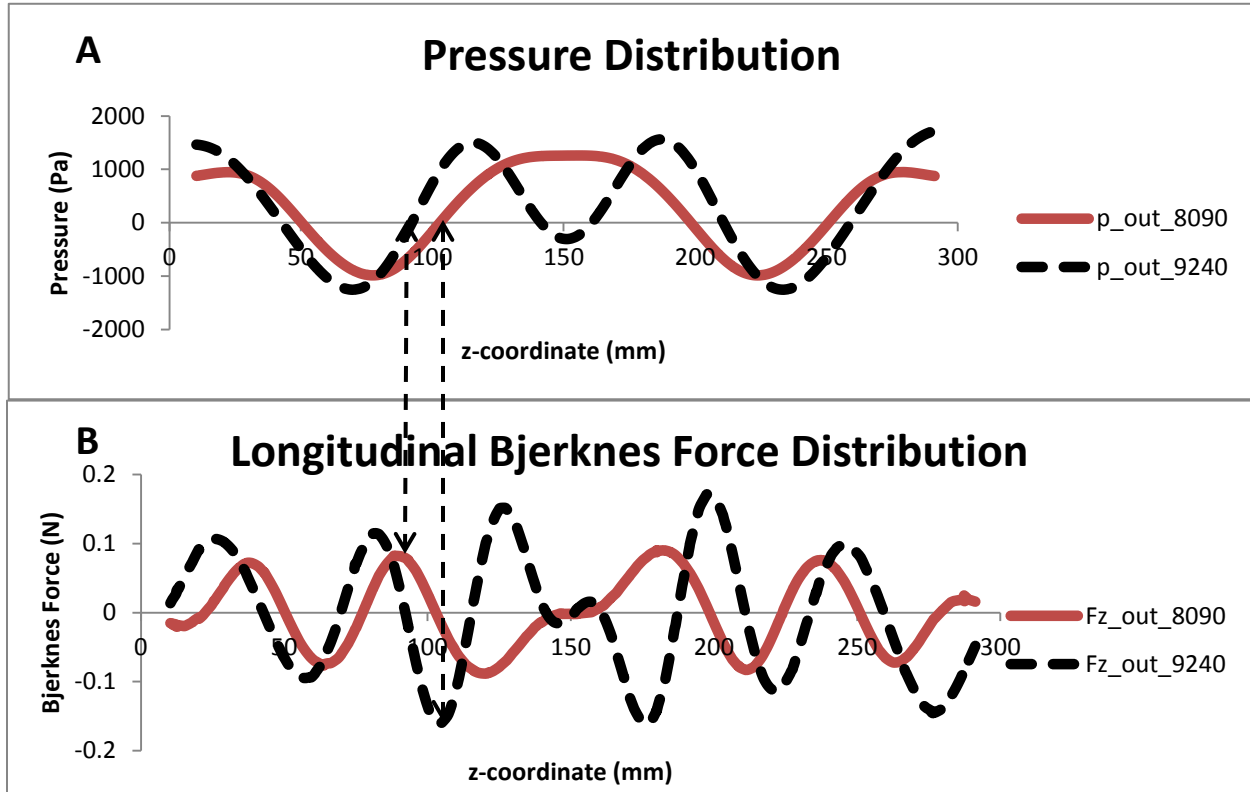


Figure 4-29 A) Pressure distribution adjacent to the small tube showing particular pressure nodes of these frequencies corresponding to experimentally observed nodes. B) Bjerknes force distribution at the same location as the pressure distribution shown in A) displaying Bjerknes force nodes corresponding to bubble entrapment locations.

#### 4.6.2 Numerical Results: System Response to Slug Flow

After characterizing the system with numerical simulations, the capabilities of the system to produce bubble entrapment were studied. This analysis was based on electrical readings and on a comparison of the effects of different pressure profiles; contrasting instants with and without bubbles. This was accomplished for a special kind of bubbly flow known as slug flow. Slug flow, refers to a special type of two-phase flow characterized by the presence of large air bubbles generally produced as a result of small bubble accumulation and coalescence. It is generally observed in pipe flows. The artificial thigh geometry was solved with the addition of a cylindrical gas pocket placed

in the arterial tube, right at the center of the structure. This was done in an attempt to explore the PZT and the pill microphone response to changes in the media. Electric impedance on the PZT ring was calculated as a function of frequency and compared to numerical results obtained in the absence of the air pocket. In order to numerically calculate the response of the system to a single bubble, the equations describing the dynamic behavior of bubbles would have to be defined into COMSOL Multiphysics. Although this is possible it is beyond the scope of this work.

Resonance conditions are extremely sensitive to minor changes in the elastic properties of the system; therefore the addition of an air pocket to the system, introduces a new domain, with different acoustical impedances. Hence, overall elastic properties are expected to change, inducing a change in the resonance frequencies. Ultimately, substantial impedance difference was expected.

The cylindrical air pockets were 2.38 mm in radius. Numerical simulations were carried out a variety of column heights: 0.5, 1, 3, 5, 7.5, 8.75, 10, 11.25, 12.5, 15, 25.07 and 50 mm in height in order to correlate the air pockets volume to the changes in electrical impedance (see Figure 4-30). Figure 4-31 displays the simulated geometry with the addition of the air pocket. An air pocket introduces a new subdomain with new density properties and speed of sound. These changes cause an overall change of the bulk properties of the media. Figure 4-32 illustrates the different longitudinal pressure profiles obtained inside the vein for the different air pockets. The presented profiles were taken at a frequency equal to 13.01 kHz, which is one of the frequencies being studied throughout this chapter. The pressure profile is symmetric. Because of this only a half section of the tubes is presented in.

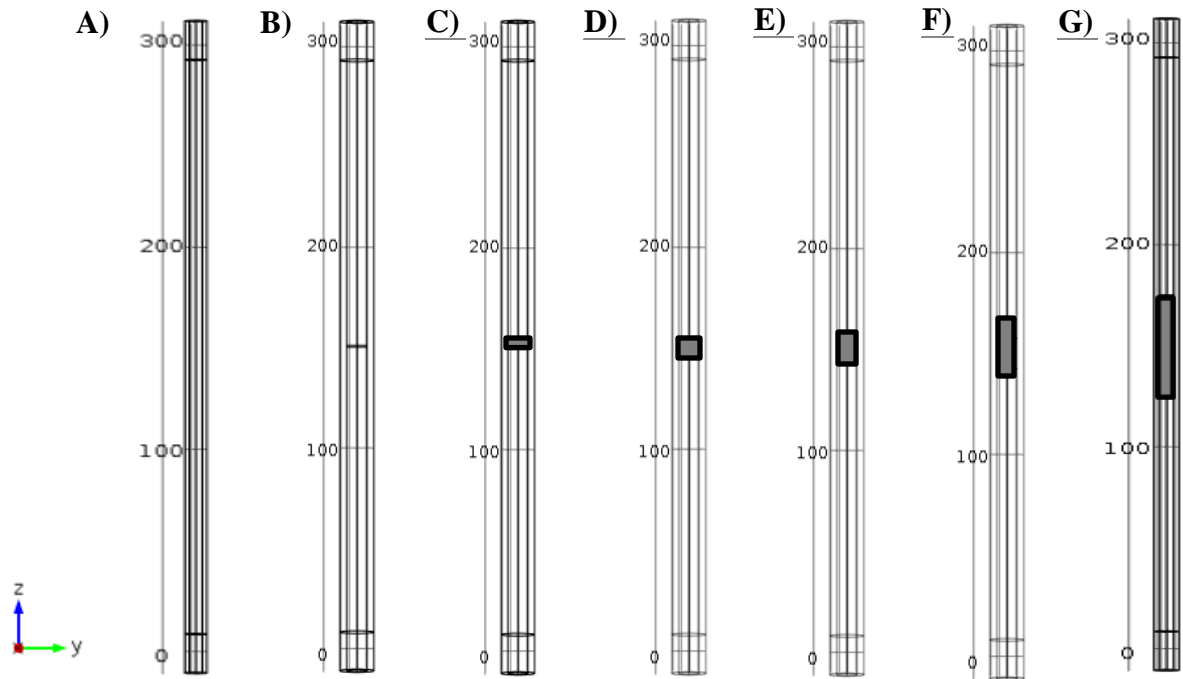


Figure 4-30 Tubes containing the air pocket simulating slug flow conditions. A) No air B) 1 mm air pocket C) 5 mm air pocket D) 10 mm air pocket E) 15 mm air pocket F) 25.07 mm air pocket G) 50 mm air pocket

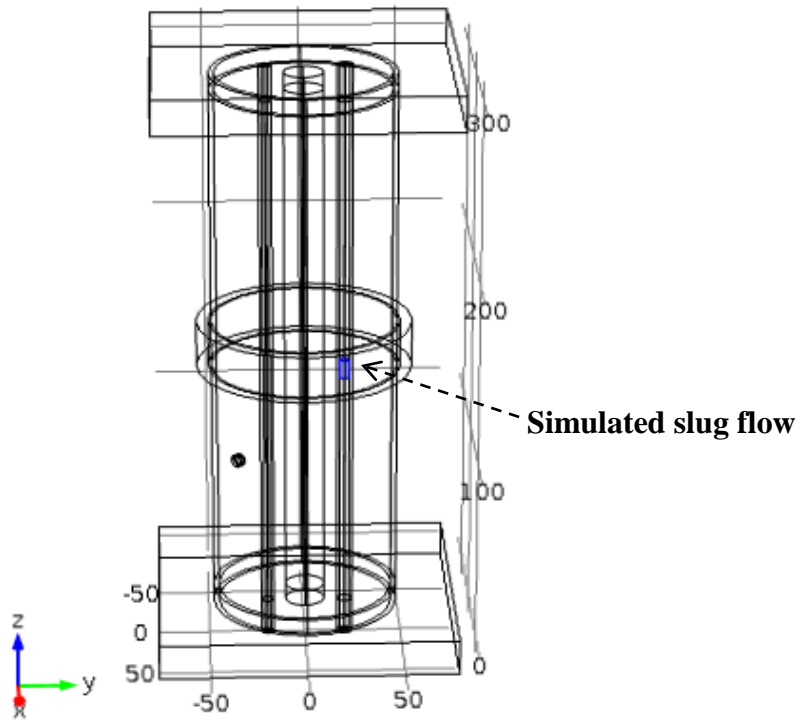


Figure 4-31 Simulated geometry containing a 10 mm air pocket

Figure 4-32 clearly illustrates the effects of adding the air pocket. The acoustic pressure drops as it comes into contact with the air domain which has a much lower density. This area is highlighted in Figure 4-32. As the amount of air in the structure increases, the overall elastic properties of the system change. As a result of the addition of the air column, if viewed as a continuum, the fluid will experience greater volume changes at the same applied pressure. This occurs as a result of a lower Bulk modulus. The Bulk modulus measures the resistance of a substance to uniform compression. The bulk of modulus of air is four orders of magnitude lower than water, consequently if evaluating the same starting volume, a defined amount of air will experience a volume change 10,000 times greater than water at the same applied pressure. Overall, the pressure profile experiences a decrease in pressure amplitude and a shift in the location of the pressure antinodes. Both of these quantities are observed in Figure 4-32.

Due to pressure changes observed in Figure 4-32, new conditions were imposed upon the PZT ring. The PZT will respond with a different admittance value, while still being stimulated at the same frequency. These changes in the elastic properties of the system are discussed in Appendix A.4. Similar changes can be seen in the electrical admittance when plotted as a function of frequency for the cases with and without the air pocket (Figure 4-33). As the volume of the air pocket rises, the amplitude of the impedance decreases. The impedance presents maximum changes in the 14 to 14.5 kHz range. The local impedance maximum was studied for a frequency range varying from 14 kHz to 14.5 kHz. The PZT ring structure presents a resonance frequency in this frequency range (see Figure 4-34).

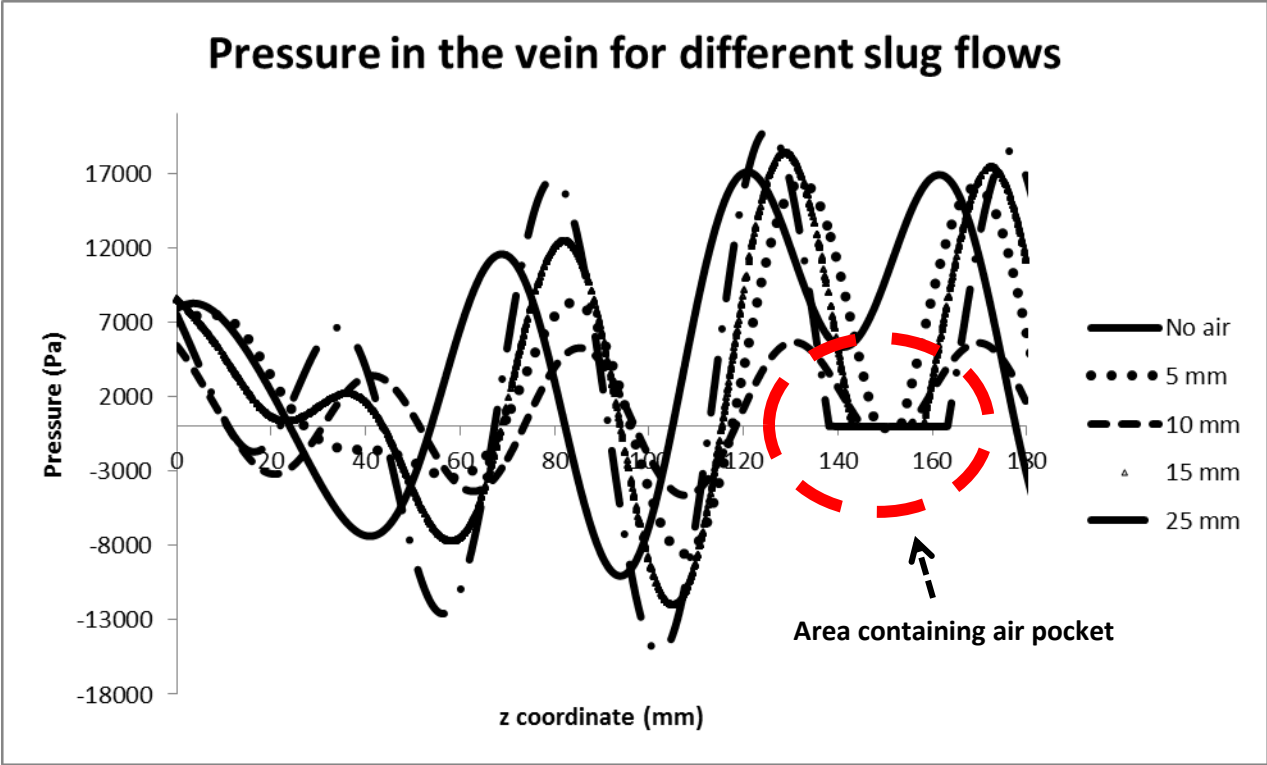


Figure 4-32 Longitudinal pressure profile inside the vein (half arterial change shown, due to symmetry) for different slug flow conditions at 13.01 kHz

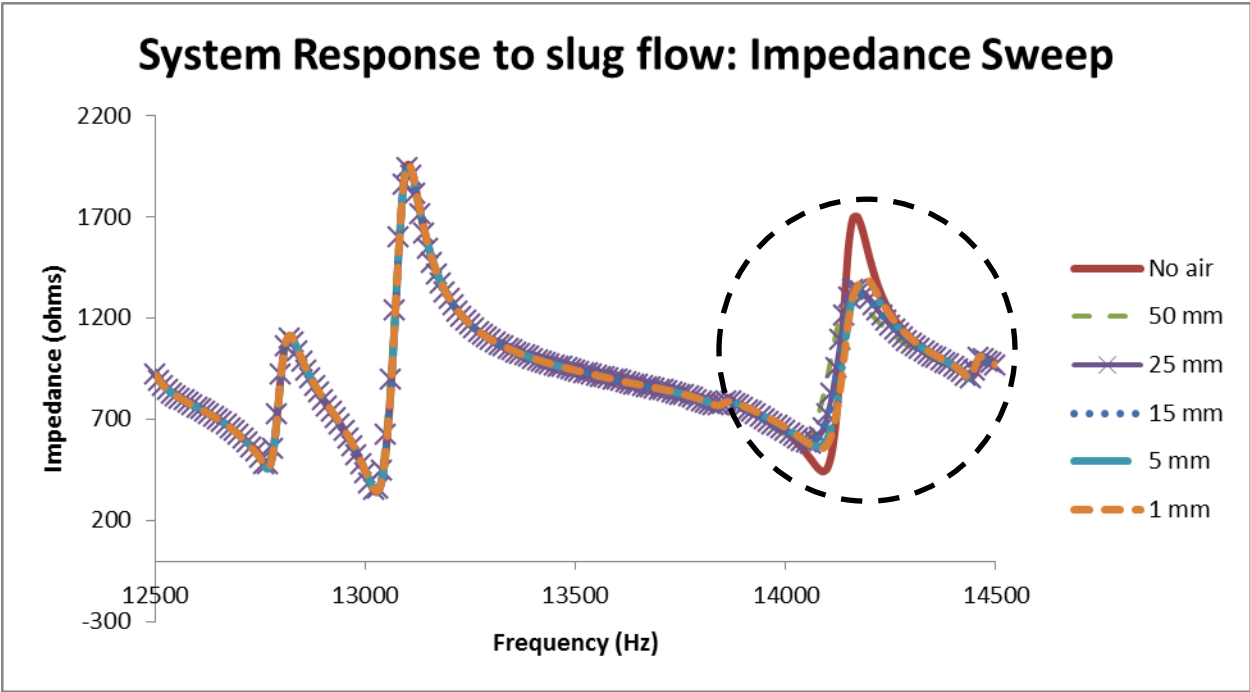
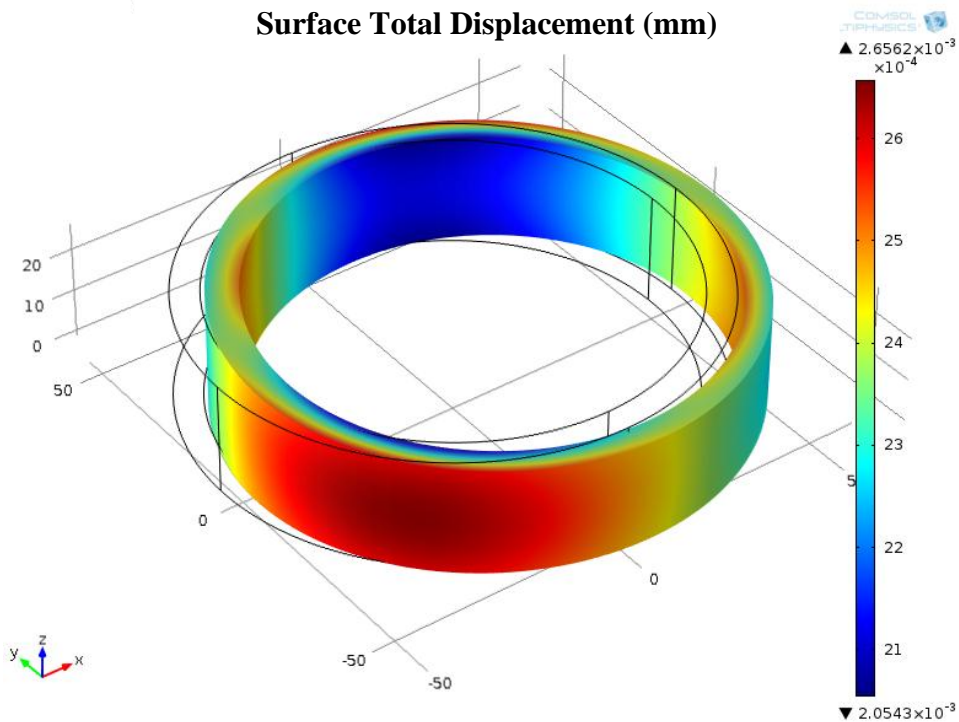


Figure 4-33 Impedance Frequency Sweeps for different slug flows, highlighting the 14 to 14.5 kHz range, where the greatest difference can be observed, corresponding to an eigenfrequency of the PZT ring structure



**Figure 4-34 Surface total displacement at 14.193 kHz obtained from an eigenfrequency analysis**

A decreasing trend in the maximum impedance in the mentioned frequency range is observed. Not only is the impedance magnitude altered, but the frequency presenting the maximum value is also shifted depending on the volume of the air pocket. In this frequency range there is shift in the frequency displaying the maximum impedance value. This is explained by the change in elastic properties caused by the air column; decreasing the Q factor of the artificial thigh as can be observed in the circled frequency range in Figure 4-33. Figure 4-35 presents the PZT ring impedance at 14.17 kHz. This frequency was the frequency which presented the maximum impedance in simulations without air. Thirteen different air volumes were analyzed from 0.5 mm in height to 50 mm in height. The results for the impedance at 14.17 kHz are presented in Figure 4-35.

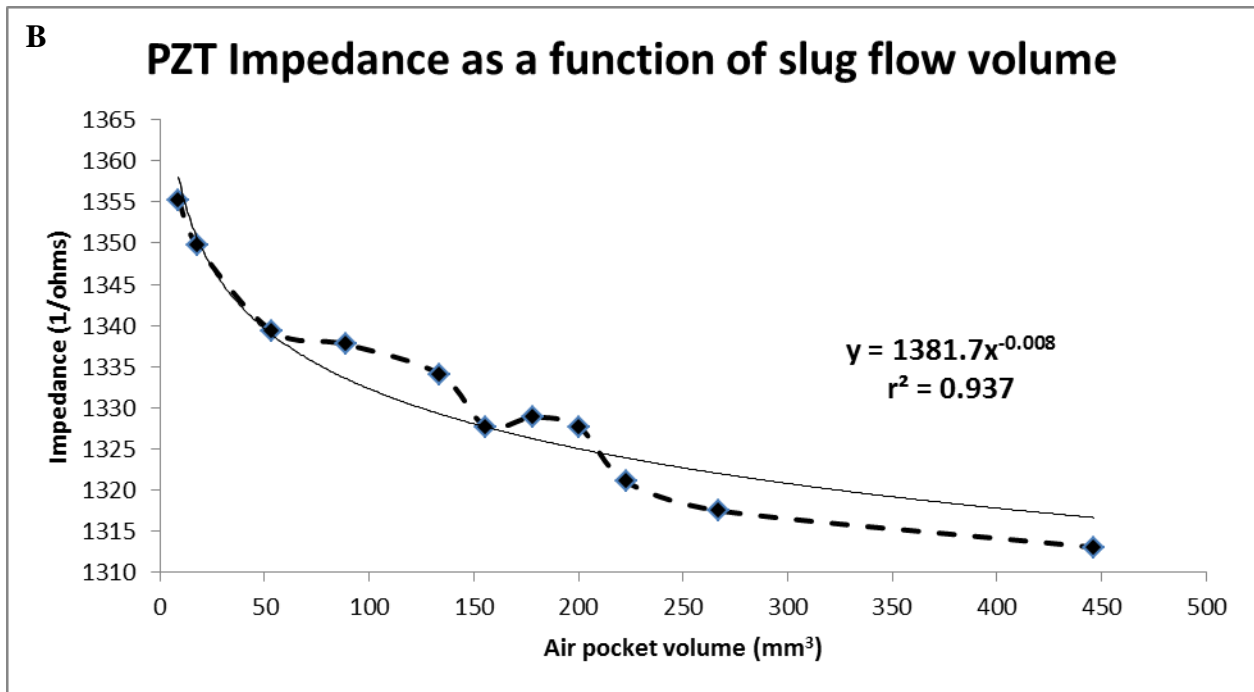
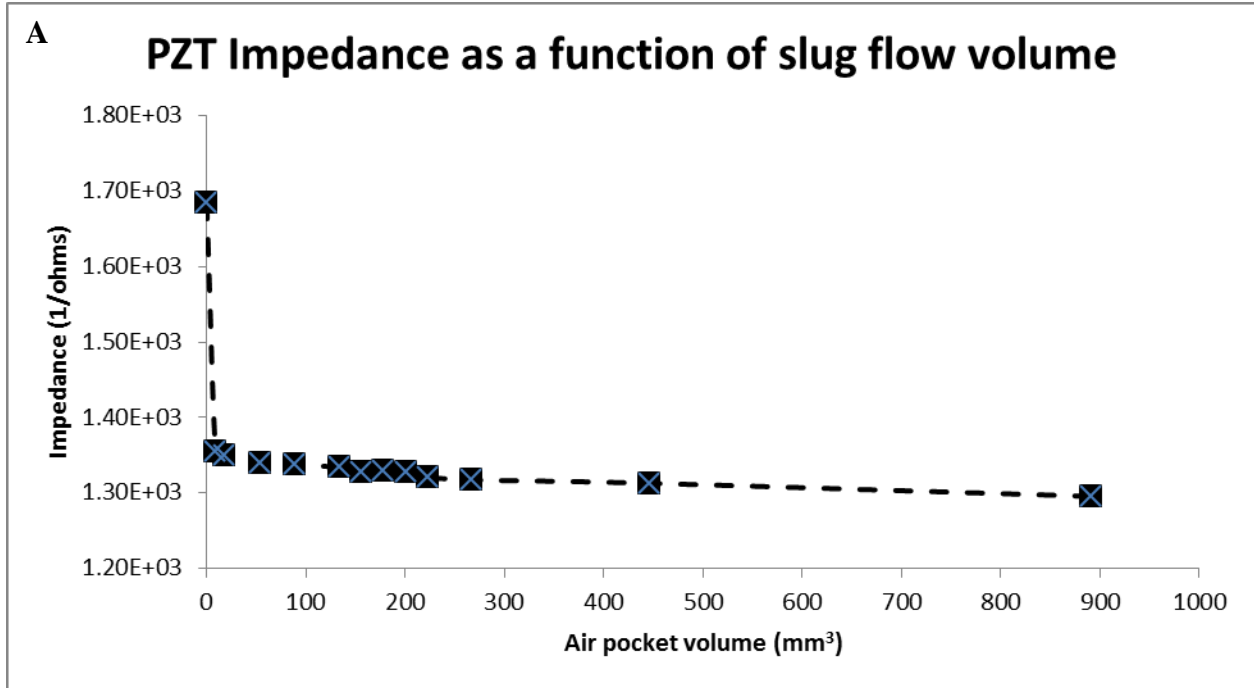


Figure 4-35 A) PZT Ring impedance as a function of slug flow volume B) Selected air pocket volume range corresponding to 0.5 to 25.07 column heights. A power correlation between these two variables is presented.

Figure 4-35 (A) presents the collected impedance values for the different air pocket volumes. An impedance drop is observed as soon as there is an air column within the inner tubes. Figure 4-35 (B) presents a power function correlation for a range of air pocket volumes corresponding to 0.5 to 25.07 column heights. From these results it can be concluded that the range of studied air pocket volumes should be extended, since the results of the simulations support the hypothesis of obtaining an algorithm relating maximum impedance values to the volume of the air pocket.

Furthermore, the response of the pill microphones to the presence of air pockets is presented in Figure 4-36. Unlike impedance measurements, no frequency shift demonstrating the absolute voltage is observed in the pill microphone. The absolute value of voltage in the pill microphone at 12.78 kHz is plotted against the air pocket volume (see Figure 4-37). 12.78 kHz was the frequency displaying the maximum absolute voltage in a 12.5 kHz to 14.5 kHz range. There is a decreasing pill microphone voltage trend as the air volume increases. Nevertheless, further simulations must be performed in order to define a correlation between microphone pill and air volume, since no correlations were obtained from the processed data. The center of the air column agreed with the center of the PZT ring height. However, the center of the air column was located at 53 mm from the center of the pill microphone. Perhaps, in order to establish a voltage to air volume correlation the air column should be located closer to the pill microphone and the analysis of other frequencies such as 14.17 kHz should be performed.

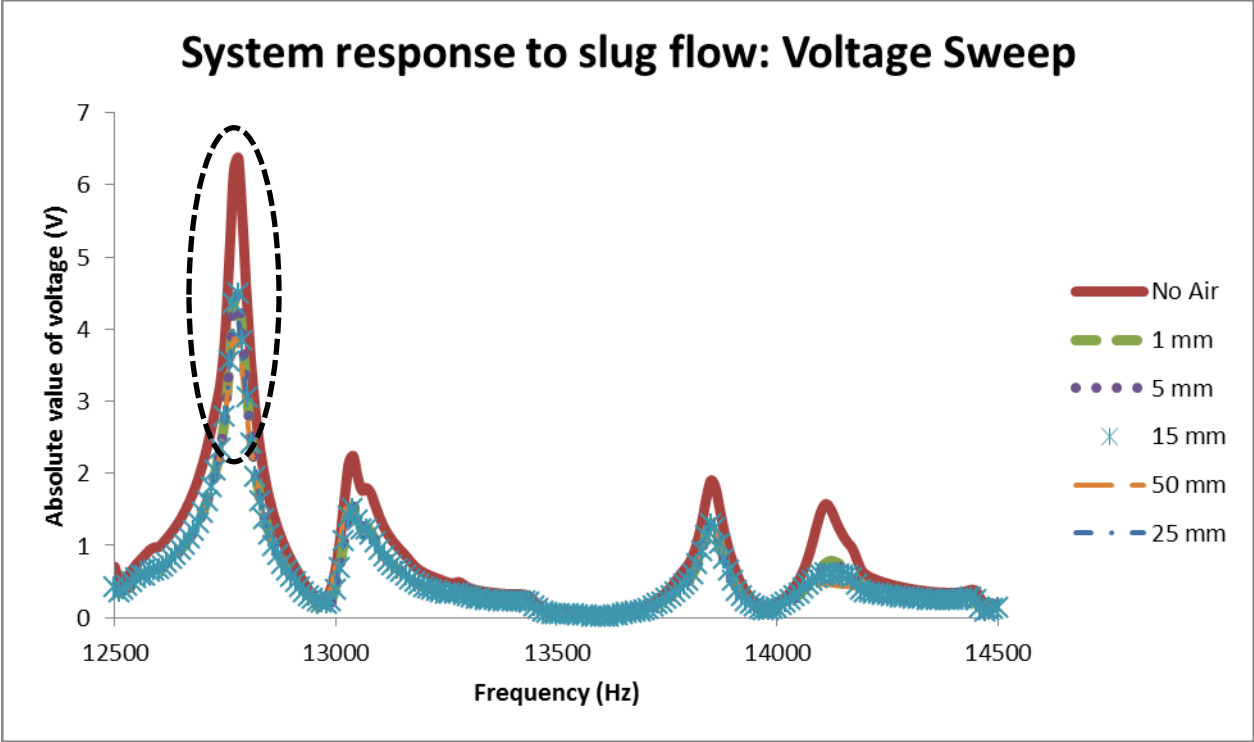


Figure 4-36 Pill microphone voltage frequency Sweeps for different slug flows

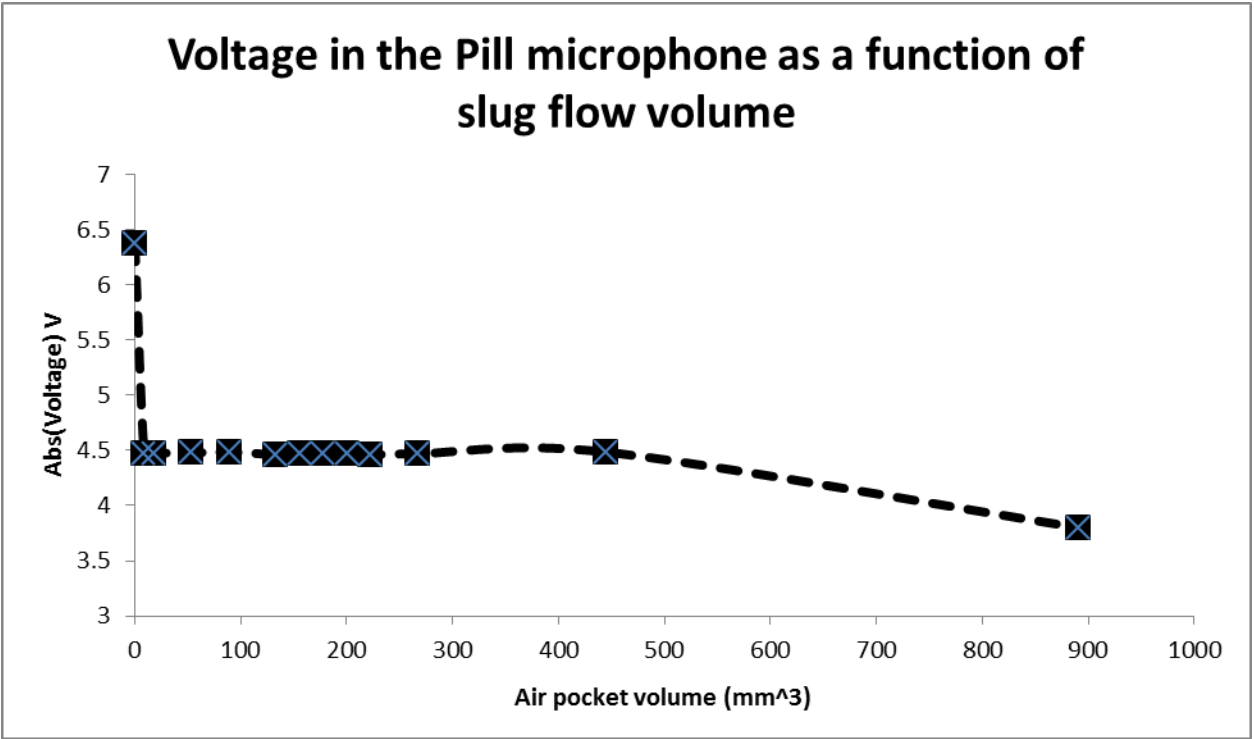


Figure 4-37 Pill microphone voltage as a function of the air pocket volume at 12.78 kHz displaying a general decreasing trend

These results demonstrate the proficiency of the system in responding to changes in the bulk properties of the fluid. Figure 4-35 (B) illustrates a power function regression correlating the PZT ring signal amplitude to bubble volume. Moreover the results presented in Figure 4-32, Figure 4-33, and Figure 4-35 through Figure 4-37 indicate that it is possible to correlate variables: impedance, voltage, and resonance frequency shift to bubble size.

## 5 EXPERIMENTAL RESULTS AND ANALYSIS

### Chapter overview:

In this chapter the experimental results of the experiments described in chapter 3 are presented and discussed. Therefore, references will be frequently made to the details explained in that chapter. Analysis of the results include: the determination of the resonant frequency of the structure (see Figure 3.3), and an analysis and comparison of the proposed bubble detection schemes. Experimental results will also be compared to numerical data in several sections of this chapter.

### 5.1 Artificial Thigh Characterization

#### 5.1.1 Determination of the Resonance Frequency

The resonance frequency of the acoustic chamber was determined for each experiment during the first five minutes of operation. The wave generator was set to produce a sinusoidal wave at specified range of frequencies. The voltage supplied to the PZT ring was set to 40 V. The resonant modes in the artificial thigh were determined through two methods, previously discussed in Chapter 3. The first method consisted on scanning in frequency the electrical admittance ( $|Y| = |I| / |V|$ ) on the piezoelectric material. Figure 5-1 displays admittance as a function of frequency. This curve was obtained by averaging admittance values for eight trials performed on different days. Error bars represent the measured standard deviation of the admittance values measured for each frequency. By extracting the real part of admittance, conductance was obtained as presented in Figure 5-2. Maximum conductance values provide the mechanical resonance frequency of the system (Wilson, 1988).

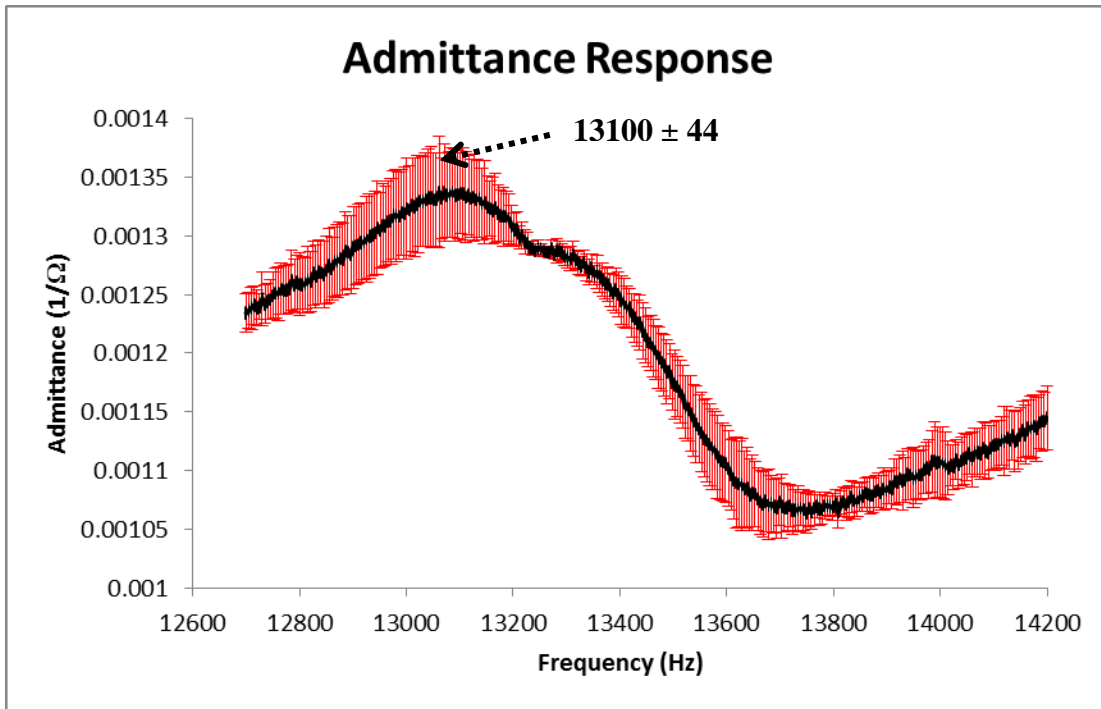


Figure 5-1 Electrical admittance as a function of frequency measured in the PZT Ring; showing average values for eight trials

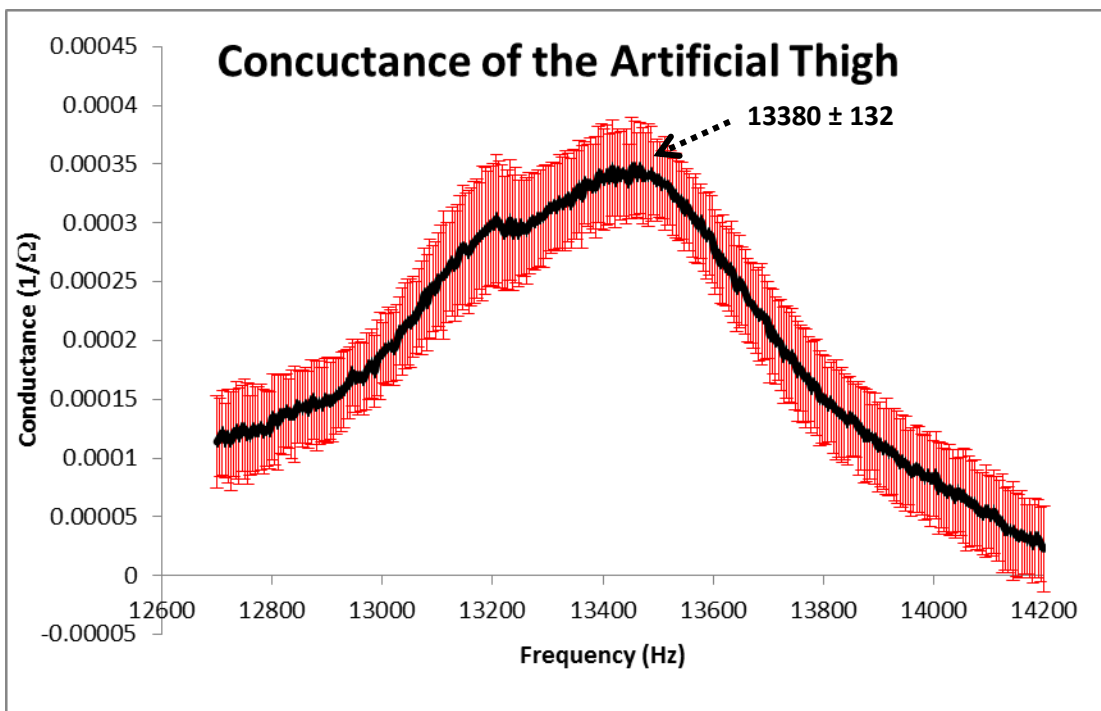
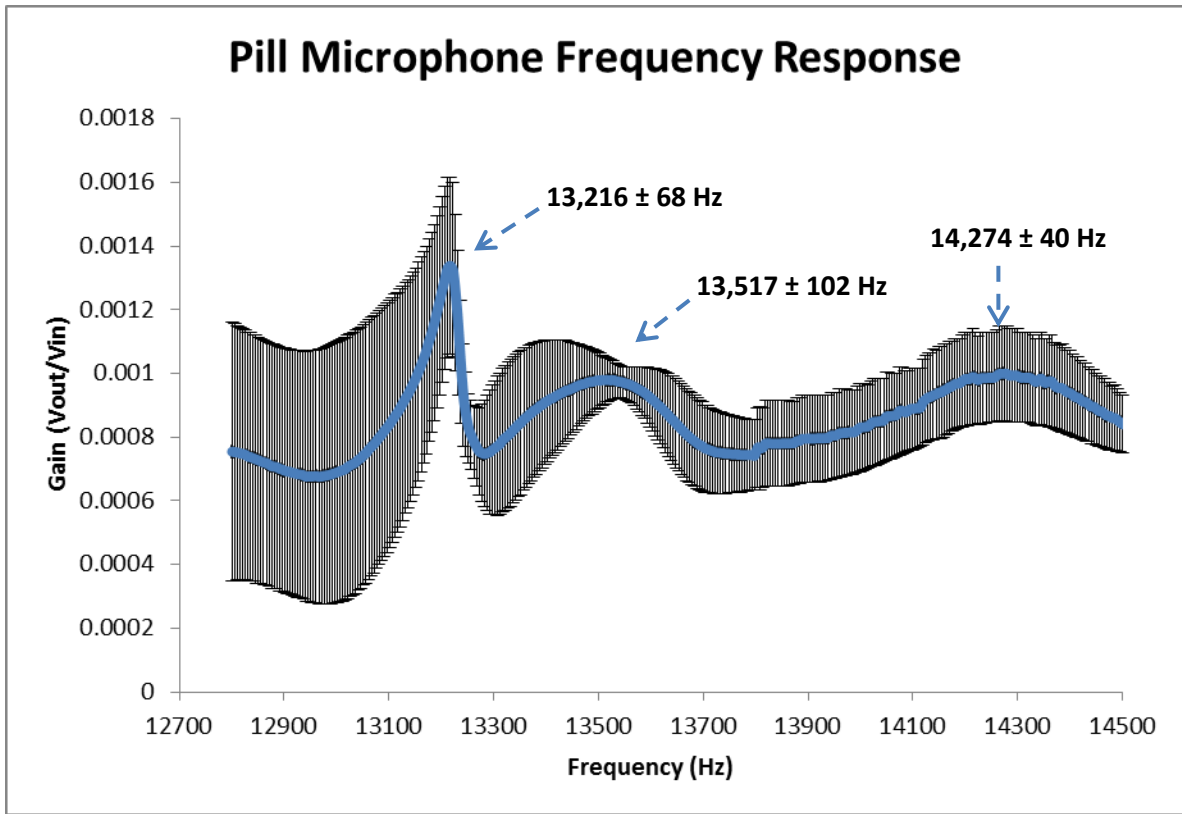


Figure 5-2 Conductance as a function of frequency measured in the PZT Ring; showing average values for eight trials

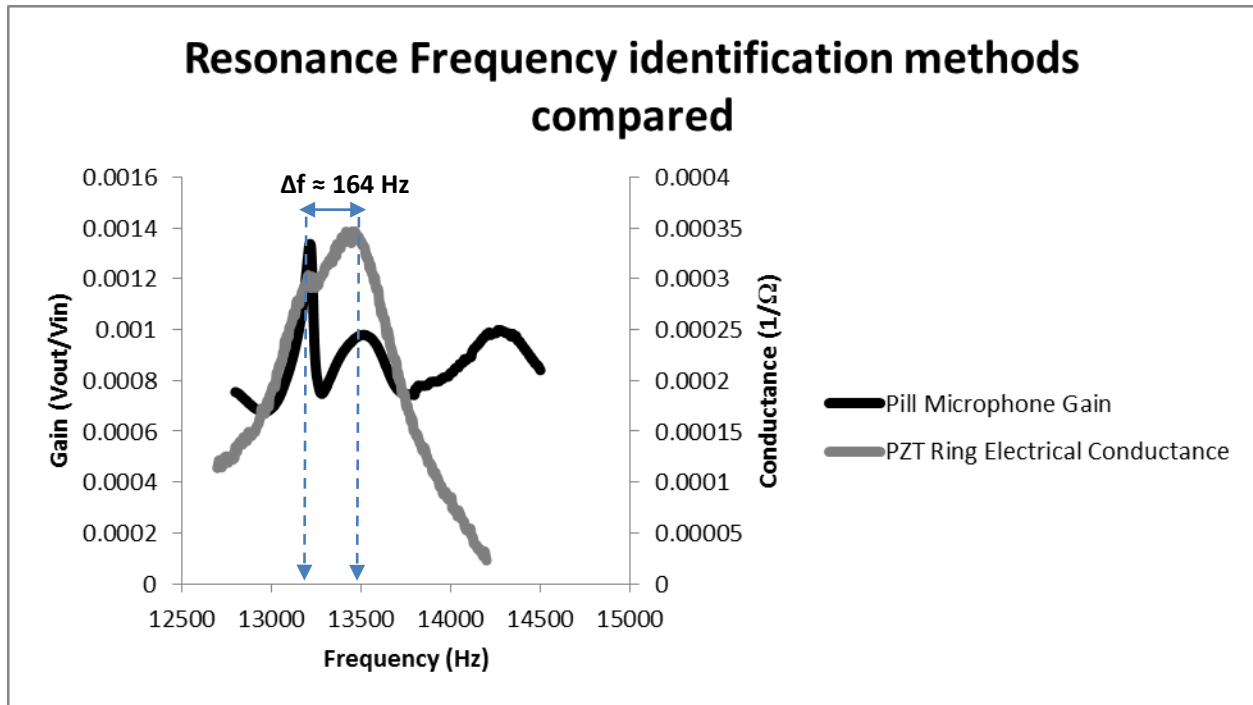
Resonance frequency was also measured using the pill microphones: indirectly confirming frequencies of maximum pressure in the fluid (see Figure 5-3). Numerical simulations show that the pill microphone voltage is proportional to the acoustic pressure inside the acoustic chamber as illustrated in Figure 4-20, where frequencies which generate maximum pressure match those displaying maximum voltage in the pill microphone. Similar procedures utilizing transducers in order to monitor fluid pressure were utilized by Gaitan et al., (1992) in sonoluminescence experiments. In such experiments calibrations were performed relating fluid pressure to microphone voltage. Cancelos et al., (2010) calibrated the pill microphone through the use of a hydrophone which directly measured pressure in the fluid within an acoustic chamber. Due to the design of the artificial thigh which included fittings with smaller openings than the available hydrophones, it was not possible to obtain direct measurements of fluid pressure. Nevertheless exact pressure amplitude values were unnecessary, since only an accurate value of the frequency producing the maximum fluid pressure was of interest. Experiments were carried out at the respective resonant condition.

Figure 5-3 represents the average values of eight measurements taken at different trials. Three different peaks are observed and labeled in this figure. These three peaks represent three possible resonant frequencies of the system which were also observed in numerical simulations (see Figure 4-19).



**Figure 5-3** Frequency response measured with the microphone pill

Figure 5-4 shows the comparison between pill microphone voltage and electrical conductance on the PZT ring where the correspondence of maximum gain and conductance peaks is observed. This implies an agreement between the system mechanical motion, extracted from the electrical admittance value, and fluid behavior within the structure. These values obviously agree in a range at which the maximum values appear. The percentage difference between these values is approximately 1.2%.



**Figure 5-4 Correspondence of frequencies displaying maximum conductance (measured in the piezoelectric ring) and gain (measured in the pill microphone).**

The admittance plots presented in Figure 5-1, obtained by averaging the data acquired in eight experiments, represent the average admittance values for approximately sixty percent of the analyzed experiments. For the other forty percent of the conducted trials the measured admittance was one order of magnitude higher than the average value shown in Figure 5-1. Admittance plots corresponding to these cases are presented in Figure 5-5. An increase in the admittance value corresponds to a tenfold increase in electrical current given that the voltage was kept at a constant value. This type of system response must be further studied in order to explain this behavior. This response could be attributed to the level of air concentration in the water.

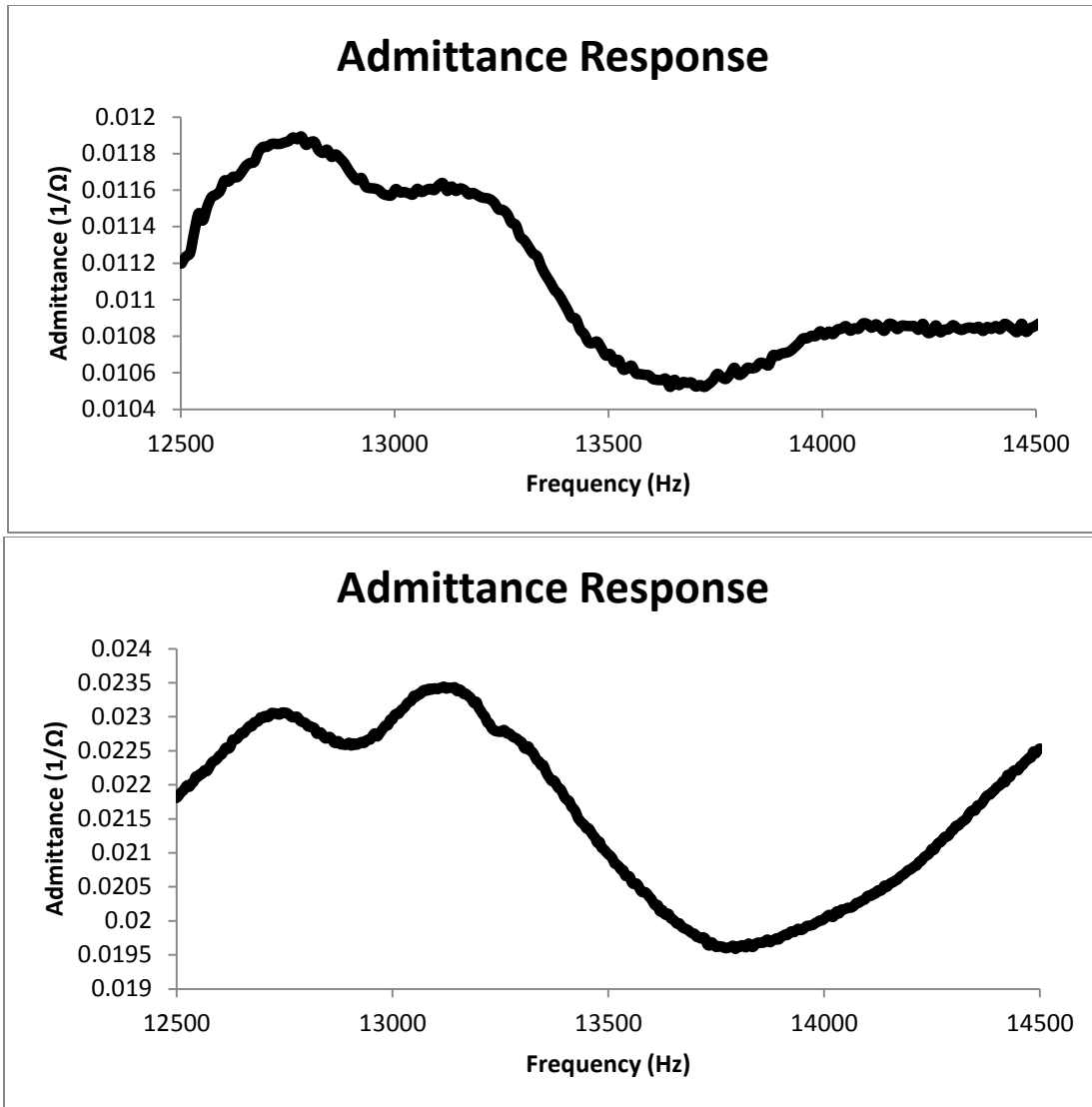


Figure 5-5 Admittance measured in the PZT Ring presenting admittance values higher than average values (each represent an average from three conducted trials)

### 5.1.2 Comparison of Numerical and Experimental Results

Experimental results characterize the artificial thigh as presenting a resonance frequency of  $13.4 \pm 0.1$  kHz based on maximum conductance. Numerical results presented in Chapter 4 (see Figure 4-11) display pressure amplitude peaks at  $13.030 \pm 0.005$  kHz thus confirming an agreement between experimental and numerical values. Figure 5-6 and Figure 5-7 show the comparison between numerical and experimental data. Figure 5-6 displays the electrical

admittance on the PZT ring as a function of frequency and Figure 5-7 shows the corresponding pill microphone readings. A greater level of agreement can be observed in the behavior of the pill microphone than the admittance readings in the PZT Ring.

Concerning Figure 5-6, numerical data displays a greater number of peaks than those observed experimentally; although the percentage difference obtained between peaks corresponding to maximum admittance is below 3.3%. The maximum numerical admittance is twice the maximum experimental value. These differences, as well as the additional peaks observed numerically, are most likely attributed to underdamped structural damping coefficient parameters defined at the PZT Ring and solid domains. In addition, no damping was added to the fluid domain which would also account for additional losses. All in all, it can be observed that the Q factor of the artificial thigh is much lower than the Q factor of the simulated system. This Q factor difference is clearly observed in the peak bandwidth. The Q factor is Also, as described in Chapter 4 the boundary condition defined in the inner PZT boundary consisted of 10 V. This value is constant thus simulating a perfect source. Experimentally, 40 V were supplied to the PZT Ring during these trials. However, COMSOL works in the linear region therefore admittance values should be independent of the applied voltage on the PZT ring. Furthermore, sources of discrepancies could arise in the voltage supplied to the PZT Ring. Experimentally, it is the function of the PZT amplifier to maintain this value; however fluctuations were measured in these values. Although small, the maximum voltage oscillations measured on the PZT represented one percent of the average voltage values. For example if the average voltage value was 0.55 V, a standard deviation corresponding to this voltage would be  $6.7 \times 10^{-3}$  V. These measurements represent average values taken in the PZT Ring through continuous readings taken in the current divider in a time period of approximately ten seconds. Nevertheless, this type of

agreement is characteristic of this type of calculations (Cancelos et al., 2005) and is typically attributed characteristics of the experimental model which were excluded from the simulation. In our experimental model, three tube fittings located at the top and bottom of the test section were not included in the numerical simulations. Consequently, the difference in the location of the pressure antinodes is likely due to the lack of symmetry.

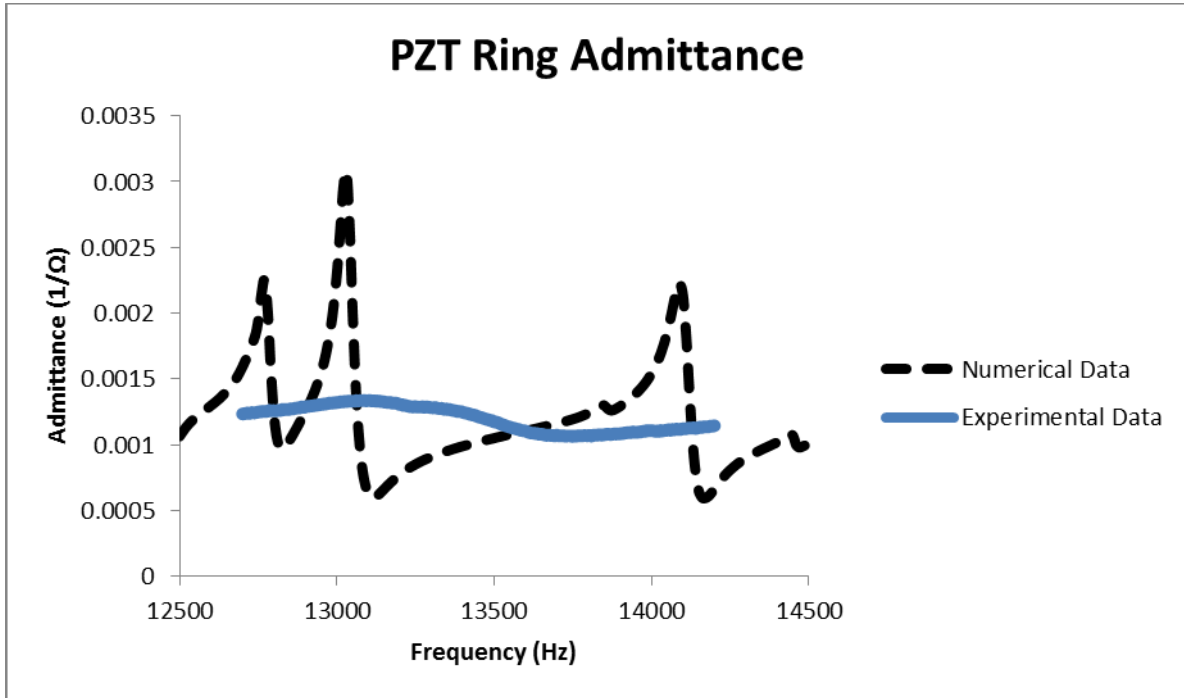


Figure 5-6 Comparisons of numerical and experimental admittance plots

On the other hand Figure 5-7 displays a greater agreement between experimental and numerical data; as observed in the correspondence of pill microphone peaks. The difference in resonance frequency is 3.3 % and reasons for this were addressed in the last paragraph. Numerical results present two peaks near 14 kHz while experimental data only shows one voltage peak in this region. This might be as a result of the closeness of the peaks and the amplitude similarity. This could be explained by the underestimation of losses in the numerical model. As a result the pressure might maintain a similar pressure amplitude in a wider frequency

range than the one obtained from numerical data. In addition there is a difference of two orders of magnitude between the measured voltage amplitude and the one obtained numerically. Since pill microphones act as receptors of harmonic oscillations transferred from the fluid to the wall the dissimilarity in amplitude is believed to be a consequence of using no damping in the fluid region on numerical simulations.

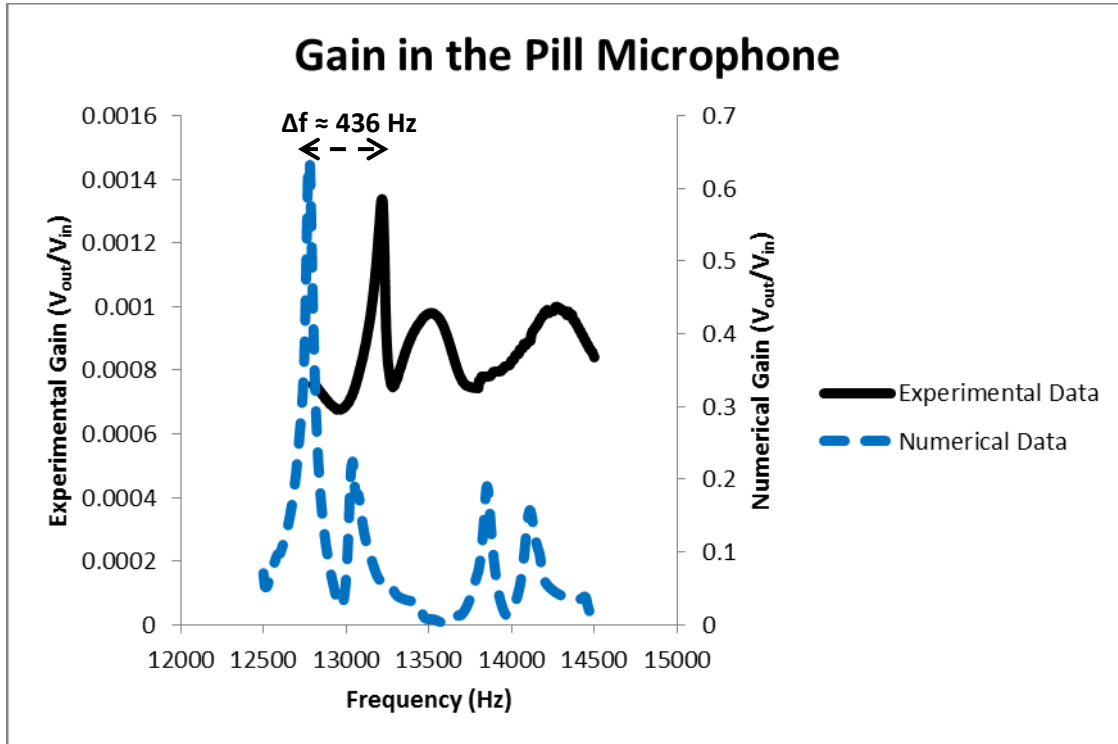


Figure 5-7 Comparisons of numerical and experimental gain plots

### 5.1.3 Pill Microphone Characterization

The pill microphones were key components in the bubble detection device since they would respond to pressure changes in the artificial thigh due to the presence of bubbles as presented in Chapter 3, and predicted by numerical simulations in Chapter 4. Experiments were generally conducted in a two hour time period. Experiments were performed in order to detect voltage fluctuations in the pill microphone as a function of time. The RMS voltage was

measured on the pill microphone at 5 minute intervals for approximately one hour. This was done while supplying 100 volts to the PZT Ring at the calculated resonant frequency of the particular trial as discussed in section 5.1.1. The results of two particular tests are shown in Figure 5-8 (A) and (B).

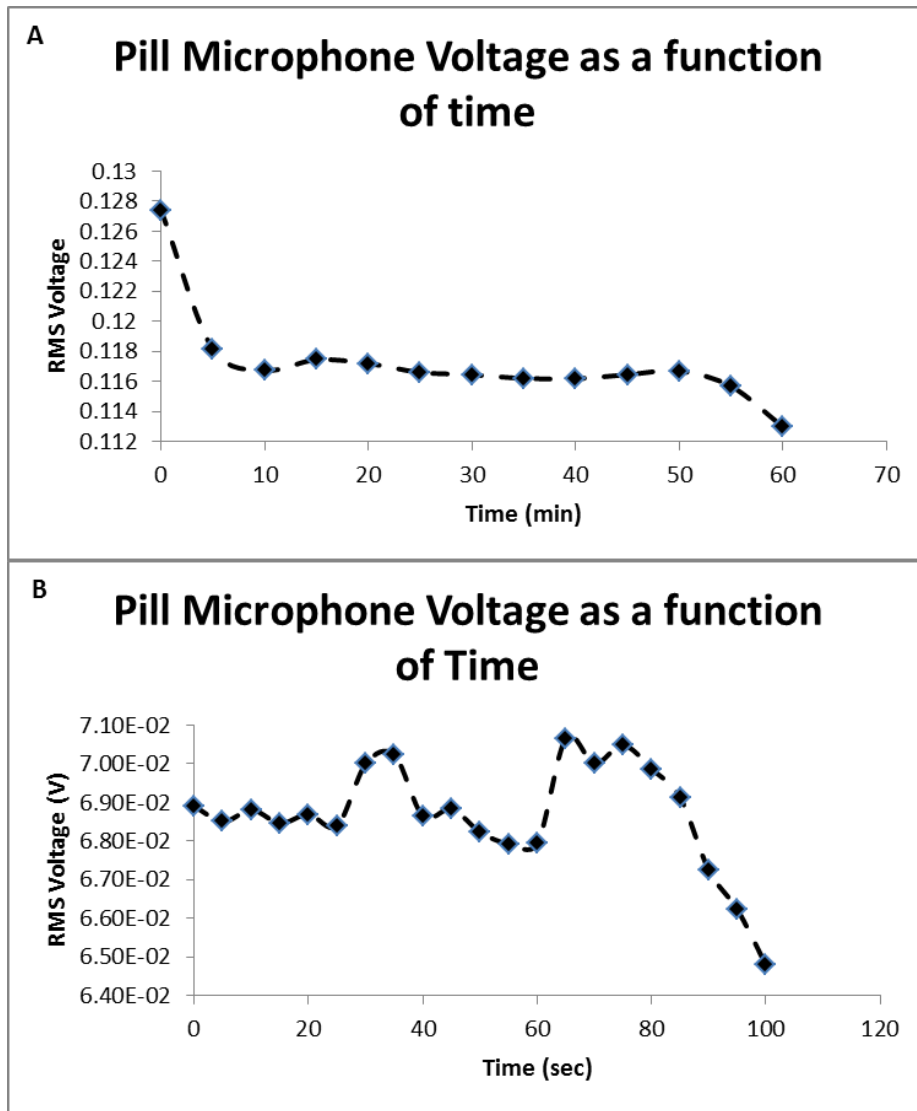


Figure 5-8 Pill microphone RMS voltage as a function of time

The results presented in Figure 5-8 (A) depict a maximum voltage drop of 0.12 V. This represents 11% of the starting voltage. Figure 5-8 (B) presents a 6% drop over one hundred minutes time period while displaying a maximum 3% growth over the initial voltage. These

fluctuations are a result of changes in experimental conditions. They might be due to the overall air leaks discussed in the previous section. A rise in the pill microphone voltage corresponds to an increment in fluid pressure. The increment in fluid pressure is a result of larger wall oscillations caused by increased oscillations in the PZT ring. Since there is a steady voltage supplied to the PZT Ring increased fluid pressure must be a result of an increase in the magnitude of the current passing through the PZT Ring which results from an overall increment in the admittance of the system. This could be a consequence of a temperature change and consequently a resonance frequency change.

Future experiments should include additional studies on pill microphone fluctuations in order to report the effect of bubbles on pill microphone voltages taking into consideration the overall contribution of possible voltage fluctuations under the same experimental conditions. This would lead to an accurate correlation between voltage differences and bubble presence excluding false positives.

## **5.2 Bubble Entrapment**

The forces influencing bubble motion within the artificial thigh were presented in chapter 2. The dominant forces inside the artificial thigh are the Bjerknes forces, which are a result of the generated acoustic field, and buoyancy. It was also stated that a balance of these forces would lead to an entrapped bubble which is necessary in order to carry out voltage readings in the presence of bubbles; otherwise the bubble would be lost by the effect of buoyancy. This last mentioned phenomenon was observed in instances where the Bjerknes force was not strong enough to trap the bubble.

As presented in Figure 4-27 and Figure 4-28, the overall distributions of the Bjerknes force in the radial and longitudinal directions would lead to bubble entrapment. Experiments confirmed

results of numerical simulations. A bubble in free flow was eventually forced towards the walls of the tube (motion dominated by the radial force component) while the longitudinal Bjerknes force determined the entrapped vertical position at particular pressure nodes for the corresponding pressure profile generated by the excitation frequency. This behavior was continuously observed experimentally as bubbles entering the chamber were eventually driven into the tube walls (see Figure 5-9). This behavior has been discussed by several investigators in which bubbles are always driven into rigid boundaries (Leighton T. , 1994).

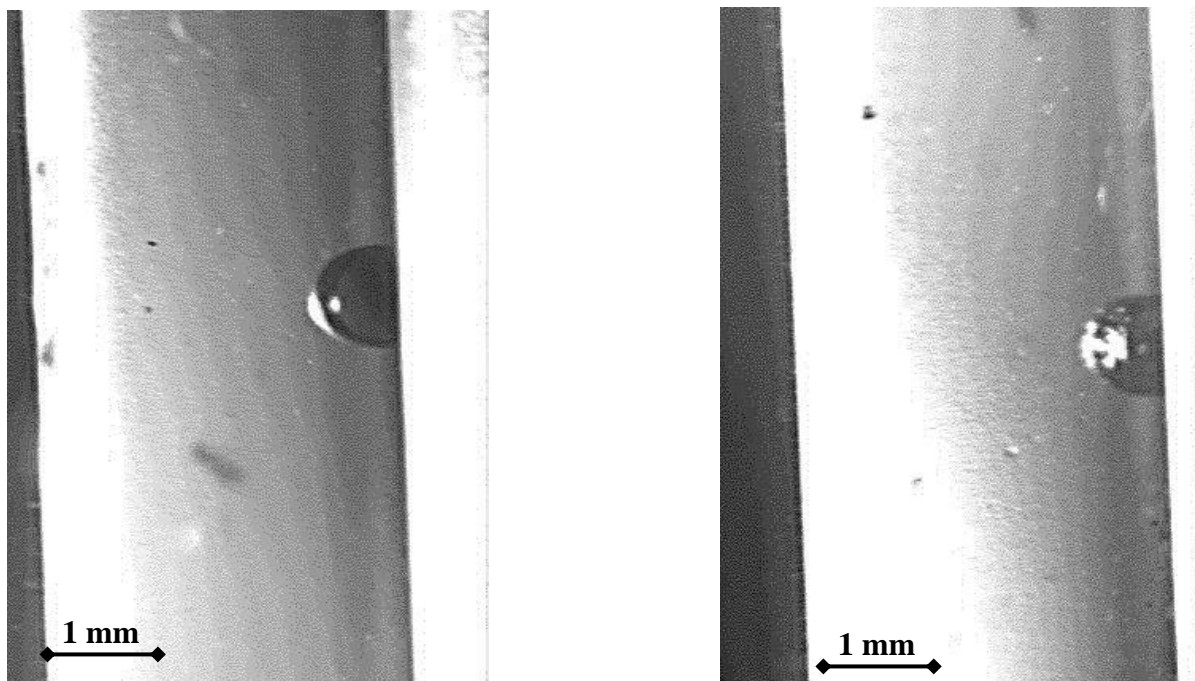


**Figure 5-9 Two images of a bubble entrapment due to the generated Bjerknes force within the artery like tubes, giving the opportunity to carry out measurements**

Experiments confirmed that the actual entrapment location was dominated by the vertical component of the Bjerknes force. Figure 5-10 (A) shows a vertical pressure profile at a defined line inside the acoustic chamber taken 10 mm away from the outside of the wall of the small tube. The pressure distribution obtained within the small tube presented a combination of the overall fluid domain pressure plus additional oscillations caused by the tube deformation.

However, as can be seen from the y-z plane presenting the overall pressure distribution inside the chamber shown in Figure 5-11, the pressure profiles inside and outside the tubes only present a magnitude difference, consequently, the pressure distribution outside the small tube gives a proper representation of the pressure distribution inside it. The overall behavior of the bubble is dominated by fluid pressure gradients as those observed in Figure 5-11 and not by pressure fluctuations induced by structural deformation.

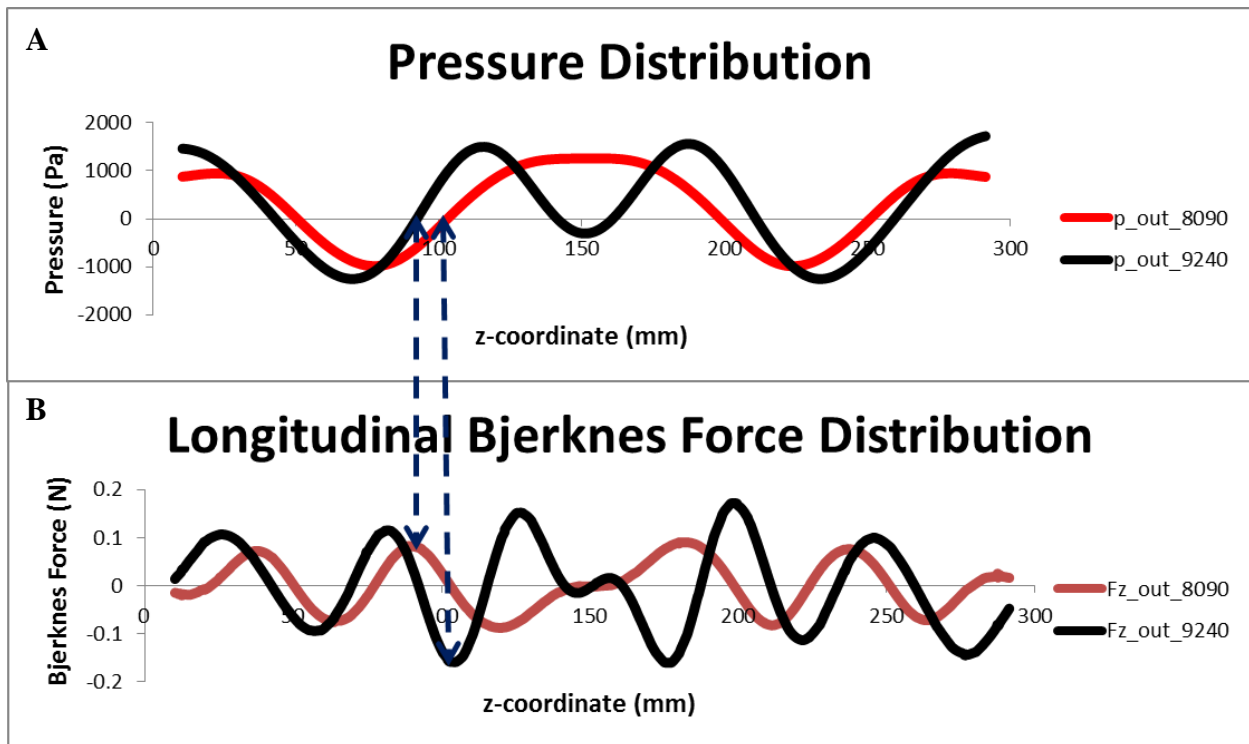


**Figure 5-10** A) Pressure distribution adjacent to the small tube showing particular pressure nodes of these frequencies corresponding to experimentally observed nodes. B) Bjerknes force distribution at the same location as the pressure distribution shown in A) displaying Bjerknes force nodes which correspond to bubble entrapment locations ( $R_0=0.5$  mm).

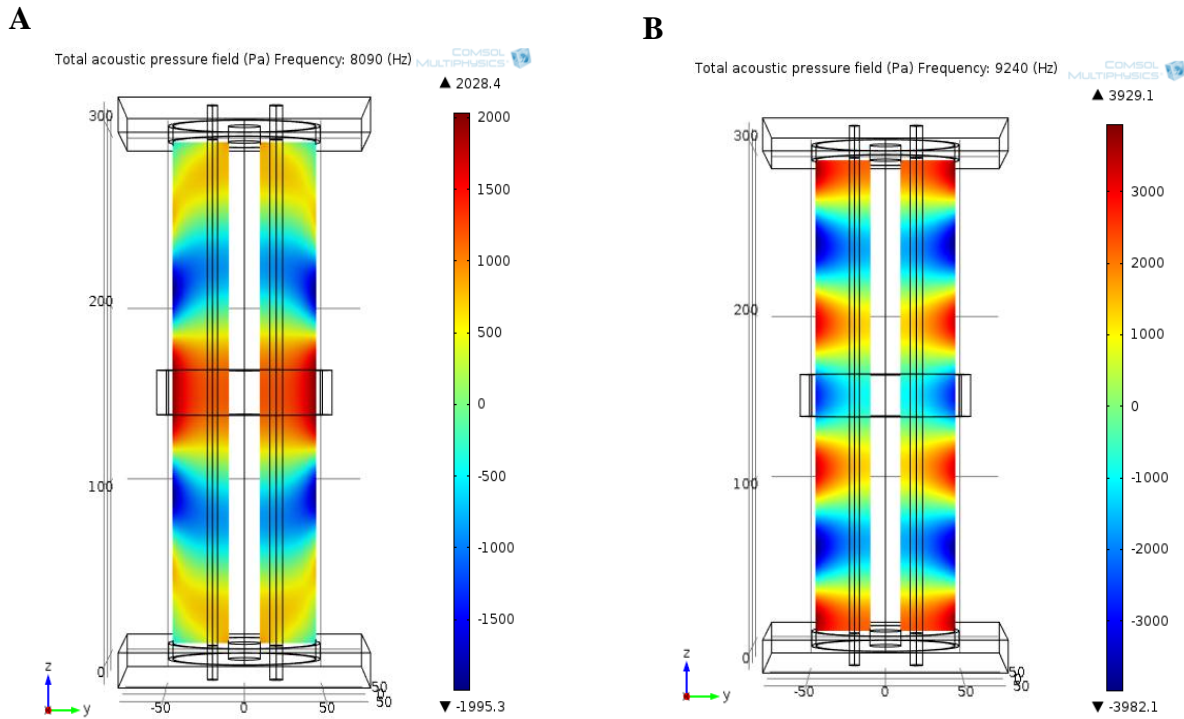


**Figure 5-11 Pressure inside acoustic chamber displaying similar fluid behavior on the outside and inside of the small tubes. A) At 8.09 kHz and B) at 9.24 kHz**

Figure 5-10 (A) shows the acoustic pressure for two different values of excitation frequencies and Figure 5-10 (B) shows the corresponding Bjerknes force on a 1 mm diameter bubble. A 1 mm in diameter bubble has a resonance frequency of 6.4 kHz, which is lower than the excitation frequency being considered in Figure 5-10. Since bubbles with a resonance frequency lower than the excitation frequency will migrate towards pressure nodes, the pressure nodes in Figure 5-10 (A) represent multiple bubble allocation possibilities. For the pressure distribution at 9.24 kHz a pressure node is located at 92mm. Experimentally, at a frequency of 9.2 kHz, the bubble was translated to a position of stable equilibrium at  $z = 111\text{mm}$  (see Figure 5-12 (A)); this will be defined as one of the pressure nodes at this frequency. There was a 6.7% difference between the computed positions of the nodes with respect to those measured experimentally.

At this particular pressure node, the bubble is in a stable equilibrium. From Figure 5-10 (B) it can be observed that this particular position agrees with a Bjerknes force node. Therefore the bubble will be trapped because of a balance of forces in this particular position. When a new driving frequency is provided (8.09 kHz), a new pressure profile will be induced; driving the bubble to a new equilibrium position defined by the closest pressure node at this frequency located at  $z=103\text{mm}$ . Bubble translation at this new frequency is observed in Figure 5-12 (C). In this case, the Bjerknes force (see Figure 5-10 (B)) is positive and will provide the means to move the bubble to this new position. At this second pressure node, at 8.09 kHz, a Bjerknes force node is also observed; thus once again arriving to a position of stable equilibrium as it experiences the downward and upward pull of the Bjerknes force.

If the excitation frequency is changed back to 9.2 kHz, Bjerknes force at this particular position is negative (see Figure 5-10 (B)). Thus, the bubble will be translated in the negative  $z$  direction towards the closest node at this frequency, once again located at 92 mm. Experimental translation at this frequency is displayed from Figure 5-12 (D) to Figure 5-12 (F). When in equilibrium the bubble will remain at this location.

Figure 5-12 shows a series of images selected from a video filming the experimental procedure. Figure 5-12 (A) presents a stationary bubble attached to the smaller of the inner tubes. As the frequency was being changed to 8.6 kHz, oscillations at the bubbles surface were captured, representing a build-up of Bjerknes force necessary prior to bubble translation (Figure 5-12 (B)). As it can be observed the bubble surface exhibits high mode oscillations, corresponding to an excitation frequency higher than the bubble resonance frequency. Figure 5-12 (C) presents the bubble position reached as the Bjerknes force induces bubble translation towards this frequency closest pressure node. This new achieved equilibrium position was

estimated at  $(10.4 \pm 1.05)$  mm from the starting position of vertical displacement. The error corresponds to the maximum measured node position difference between individual trials and the average location of the node. Excellent agreement is found between the distance traveled by the bubble and the numerical distance between adjacent nodes of different frequencies, which has a value of  $10.7 \text{ mm} \pm 0.3 \text{ mm}$ . Figure 5-12 (D) presents the new location of the bubble in response to the new pressure field as the excitation frequency applied on the PZT is changed to a value of approximately 8.6 kHz. This bubble migration pattern was repeated 6 times over a time period of 13 seconds.

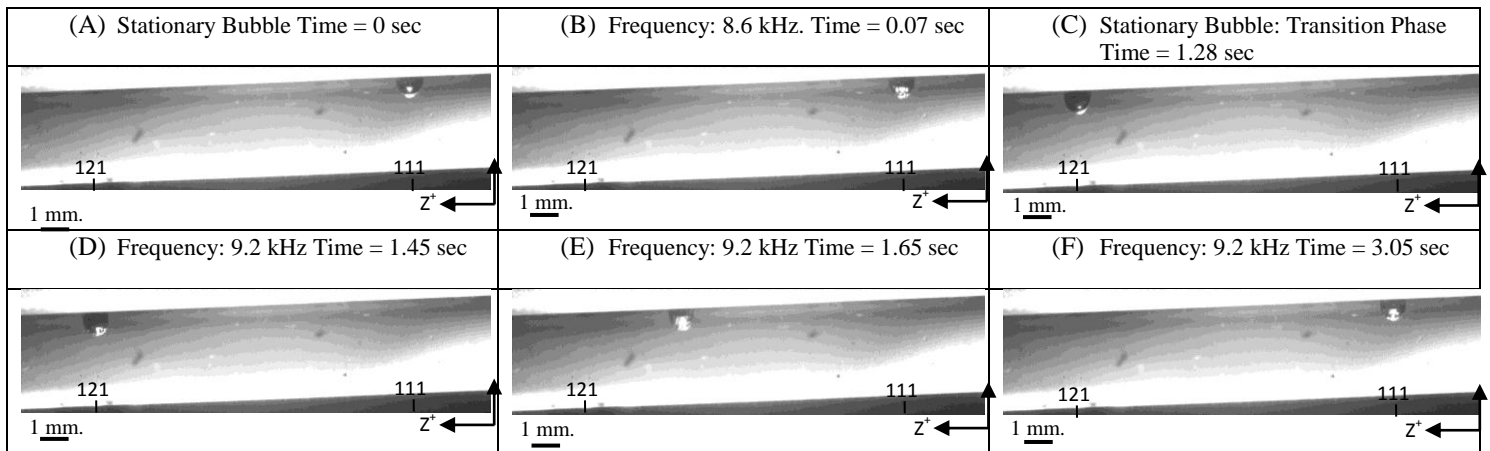


Figure 5-12 Experimental Bubble displacement. Images captured with a resolution of 1200 x 300 pixels and at 600 fps

In these experiments bubble translational patterns observed in bubbles injected into the artery tubes concurred with bubble migration patterns established from numerical pressure data measured outside of the tubes. These results suggest that although the pressure profiles within the tubes present many pressure nodes to which the bubble might be forced to, the overall behavior of the bubble can be predicted based on the overall pressure profile of the fluid. Thus, confirming structural vibrations and the pressure gradients created by these structural vibrations as well, have less influence on overall migration patterns, than those pressure gradients resulting from the overall changes in fluid pressure.

## 5.3 Pill Microphone Response to Presence of Bubbles

### 5.3.1 Effect of multiple bubbles within the vein and artery on the pill microphone signal

Prior to evaluating the effect of a single bubble on the measured sinusoidal signals, multiple bubbles were injected (see Figure 5-13). This was done in an attempt to reveal the overall trends of bubbly flow within the artificial thigh. These experiments would establish an upper limit presenting the utmost difference between signals measured at two instants: moments with bubbles and those without. Logically, the differences observed in the presence of a single bubble should be less than the differences obtained in the case of multiple bubbles. Figure 5-14 presents the results of these tests. The upper figure displays the sinusoidal voltage applied on the PZT ring. Simultaneously, the lower part of Figure 5-14 displays the deformed sinusoidal signal measured in the pill microphone when bubbles are present.

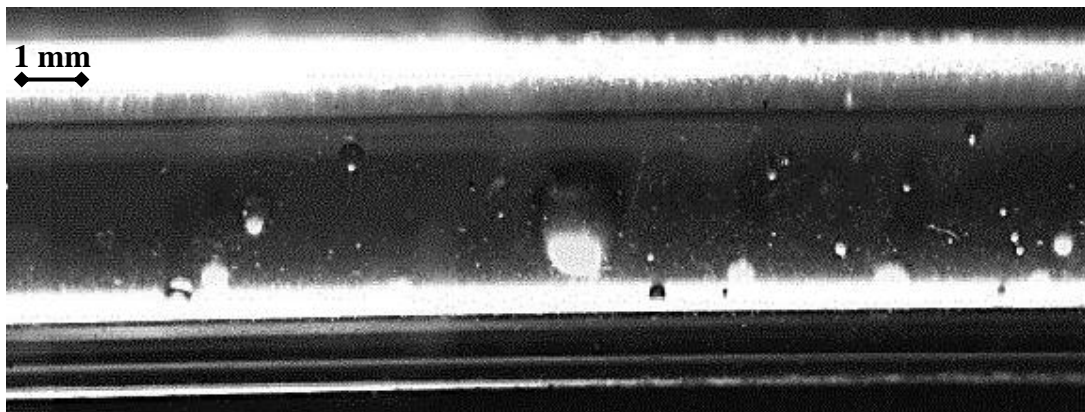


Figure 5-13 Representative image of the amount of bubbles present along the inner tubes during these readings

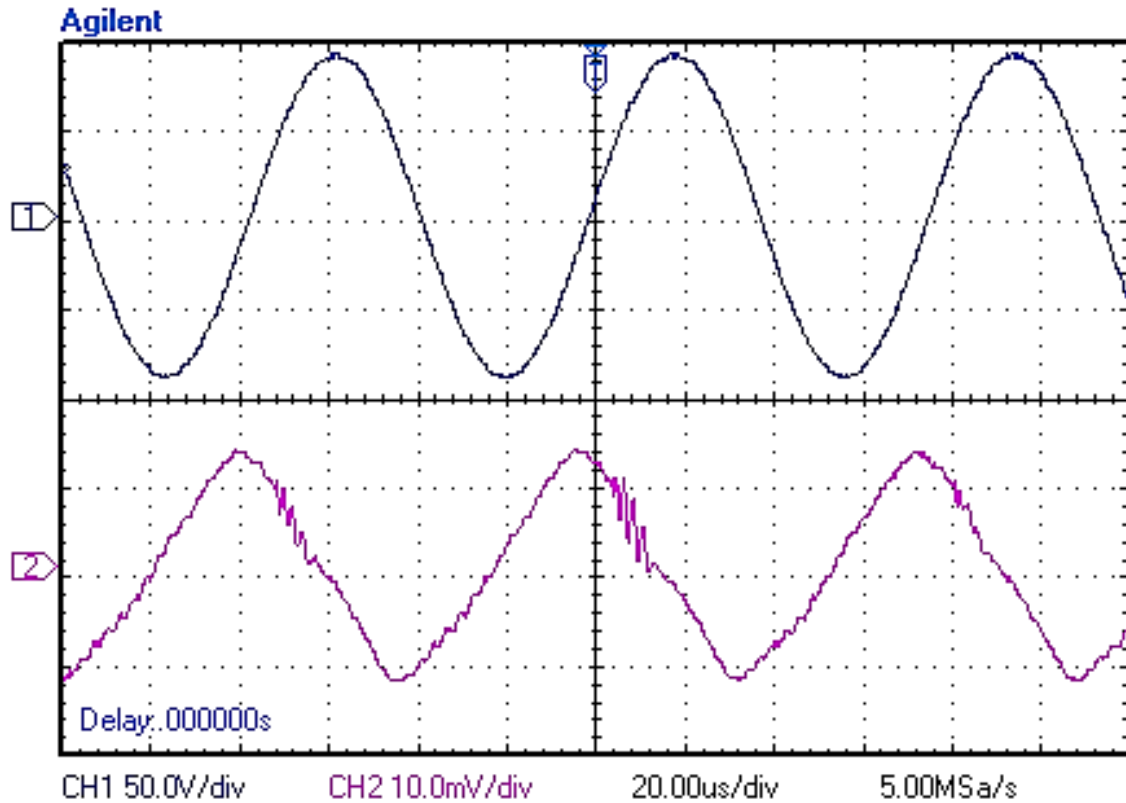


Figure 5-14 Upper: Clean signal driving the PZT. Lower: Perturbed signal due to the presence of multiple bubbles.

These results highlight a positive system response to air bubbles presence. The voltage signal measured on the pill microphone is a function of the displacement of the outer diameter of the glass cylinder which harmonically oscillates at a frequency equal to the excitation frequency applied on the PZT ring. In the absence of bubbles the pill microphone responds with a clean sinusoidal wave signal (with lower amplitude than the one supplied to the PZT ring), and at the same frequency as the excitation frequency (with a phase shift).

As discussed in Chapter 3, in the overview of experiments (see Figure 3-9), a forced solid structure will naturally vibrate in one of its natural resonance frequencies or a combination of these. In the same way, if struck by a pulse, the glass cylinder will break up this pulse into its

many frequency components and will be stimulated only by frequencies corresponding to one of its resonance frequencies; other frequency components will experience destructive interference and as a result these other frequencies will not be propagated. With this discussed physical phenomenon in mind, shock waves are known to emanate from the surface of pulsating bubbles undergoing steady inertial cavitation. These shock waves will travel toward the outer cylinder wall and act very much like the pulse described in the previous paragraph, thus, exciting additional vibrational modes of the cylindrical structure. These, modes will be distinguished as additional harmonic components of the sinusoidal wave. Thus, the measured deformed sinusoidal wave in the presence of bubbles is a combination of the vibration of the cylinder by the PZT excitation, plus additional frequency components as a result of the excitation, product of the shock waves produced by the pulsating bubbles surface.

### **5.3.2 Effect of a Single Bubble on the pill microphone voltage**

Tests were performed to accurately detect differences in pill microphone signals due to the presence of a single bubble injected within the artery like tubes of the artificial thigh. Voltage readings in the pill microphones were taken prior to and following the presence of a single bubble within the vein and artery. These tests were carried out in the artificial thigh for a wide range of bubble sizes (bubble radii ranging from 1.7485 mm to 39.5  $\mu\text{m}$ ). A bubble histogram describing the bubble sizes used for this type of experiments is illustrated in Figure 5-15.

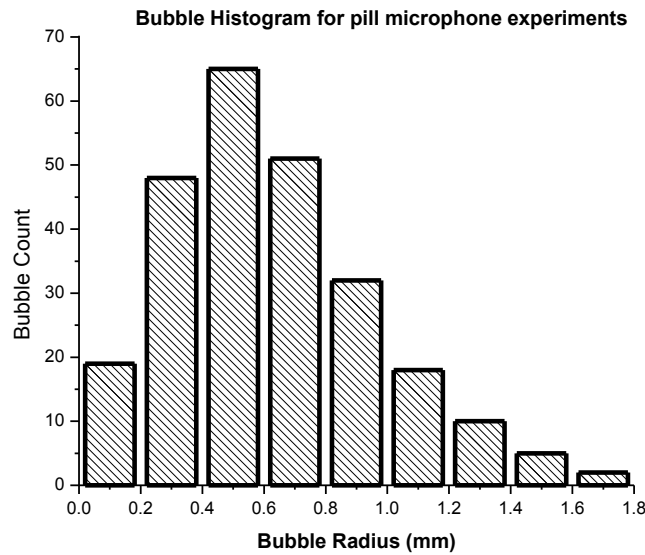


**Figure 5-15 Histogram of bubble sizes for single bubble experiments measuring the effect of single bubbles inside the vein and artery like tubes on the pill microphone voltage for a total of 250 experiments conducted**

Conclusions following the analysis of the pill microphone signals which are beneficial for bubble detection purposes are discussed below.

### ***5.3.2.1 Analyzing differences in pill microphone voltage signal induced by bubble presence***

Voltage signals in the pill microphone in the absence of bubbles were compared for each trial. Figure 5-16 displays two microphone signals taken in the absence of bubbles and their difference. One of the measurements ( $V_i(t)$ ) was captured before injecting the bubble. A bubble was then inserted and after the bubble dissolves, a second measurement ( $V_f(t)$ ) was collected prior to injecting the following bubble. Consequently, measurements  $V_i(t)$  and  $V_f(t)$  taken in the absence of bubbles, were approximately measured 30 to 45 minutes apart. The comparison between  $V_i(t)$  and  $V_f(t)$  was done by subtracting the voltages and inspecting the amplitude of this difference; where this difference is given by:

$$\Delta V = V_f(t) - V_i(t) = (\hat{V}_f - \hat{V}_i)e^{j\omega t} \quad (5.1)$$

The difference ( $\Delta V$ ) could display time to time peaks which were ignored. Only the average amplitude ( $\hat{V}_f - \hat{V}_i$ ) was taken into consideration. From these measurements, pill microphone measurement errors for the specific trials were determined by averaging the amplitude of the difference over the number of periods captured.

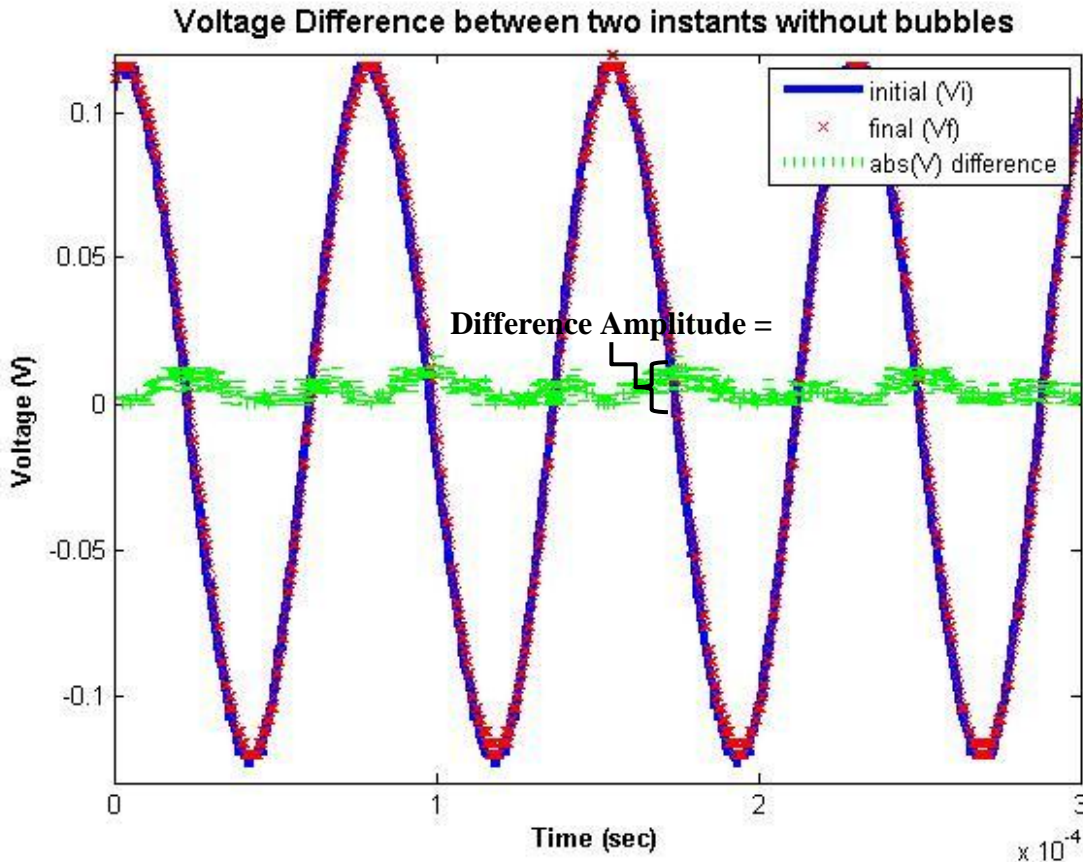


Figure 5-16 Pill microphone voltage signals taken in the absence of bubbles displaying a signal difference amplitude of 0.01 V. Time interval: 45 minutes.

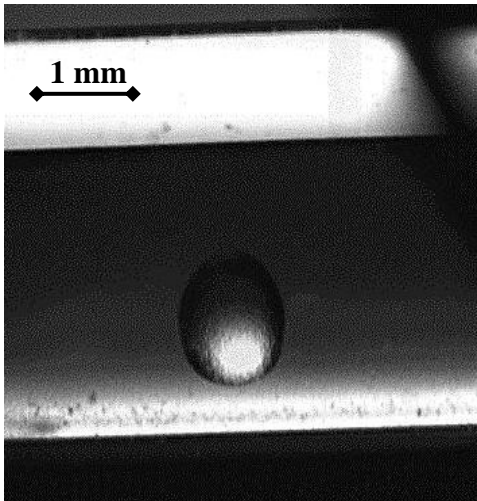
Bubbles were injected following the method described in Chapter 3 section 3.2 and 3.5.2.1. The voltage signal in the presence of a bubble was compared to a signal taken prior to the bubble injection. The amplitude of the difference between these two signals was computed

and compared to the amplitude of the voltage difference corresponding to two measurements taken in the absence of bubbles. If the difference in signals during the presence of a bubble was greater than the difference between measurements without bubbles, the effect of a bubble on the pill microphone signal was confirmed and taken into account. Out of a total of 114 cases 43% were found to display a voltage amplitude difference greater than the difference displayed by two measurements in the absence of bubbles. Out of this 43%, 57% displayed lower amplitude than the signal taken before bubble injection.

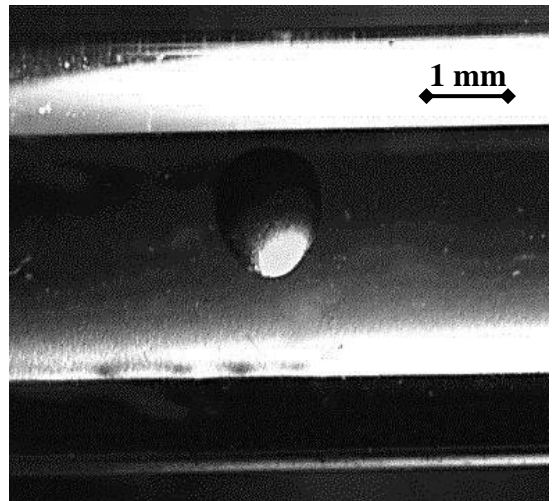
#### 5.3.2.1.1 Signals Displaying lower signal difference amplitude

Figure 5-17(A) and Figure 5-17 (B) present two examples of the response of the pill microphones to a bubble within the chamber. Figure 5-17 (C) and Figure 5-17(D) present sinusoidal signals prior to and after bubble injection. As expected a, decreased signal amplitude is observed (see Figure 5-17(C)). Figure 5-17 illustrates a general trend observed in the majority of trials (57%). This signal presents a 43% decrease in signal amplitude compared to instances without bubbles. The signal in the presence of the bubble shown in Figure 5-17 (D) presents an 11% amplitude decrease. This percentage decrease is among the highest recorded among the cases presenting lower amplitudes than the signal in the presence of bubbles.

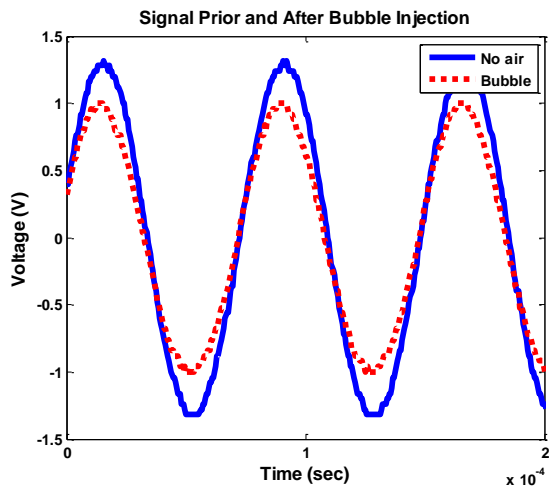
A)



B)



C)



D)

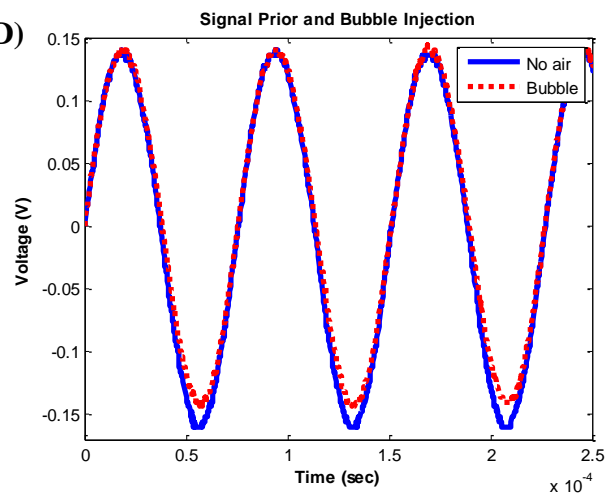


Figure 5-17 Bubble with a 0.66 mm radius within the “artery like” tubes. B) Bubble with a 454  $\mu\text{m}$  diameter. C) Signal Prior and Following Bubble injection from Bubble presented in (A). D) Signal Prior and Following Bubble injection from Bubble presented in (B).

Signal damping is explained by increased dissipation; bubbles will alter the bulk properties of the fluid, attenuating the signal. Attenuation of a propagating wave in a medium in the presence of a bubble can be explained in terms of the bubble extinction cross section discussed in Chapter 2. In addition, bubbles introduce signal scattering, which converts a coherent signal into an incoherent one. This incoherent signal will disperse in the fluid, thus decreasing the amount of signal amplitude captured by the pill microphone transducers. In addition to this, the attenuation of acoustic waves in air is much higher than the attenuation in water. These two phenomena add up to the decrease of the acoustic signals captured by the pill microphones expressed as a decrease in voltage amplitude.

The previously reported results pertain to measurements in which the amplitude of the signal captured in the presence of bubble decreased in comparison to a signal taken in the absence of the bubble. However it was concluded that the pill microphone signal in the absence of bubbles could experience a maximum 11% decrease in the RMS voltage in a one hour period (see Figure 5-8 (A)). This suggests that additional trials must be performed in order to correctly exclude false positives. A statistical analysis must be performed comparing instant to instant values in order to accurately determine the instruments precision under the influence of the same variables. Later, the influence of bubble presence on measurements can be determined significant based on their comparison to these obtained values. Although this procedure was attempted, measurements in the absence of bubbles were taken on time periods too far away (30 to 45 minutes depending on the bubble life) and as a result of the changing voltage values described in time (section 5.1.3) the error was too big therefore most values fell within the

calculated pill microphone error, therefore most measurements fell within values that the instrument could measure for two instances without bubbles.

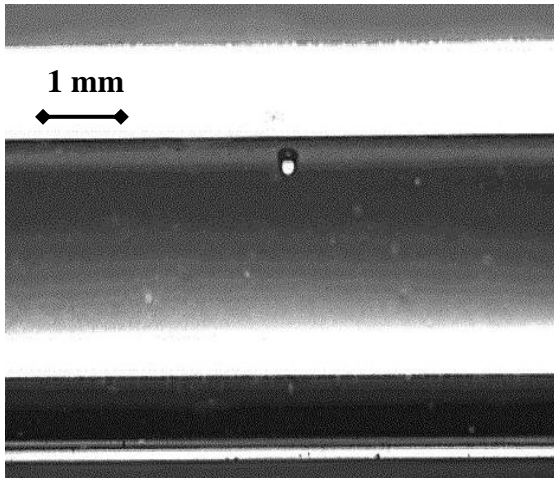
Further studies must be carried out to differentiate when these readings could be attributed to the pill microphone response to bubble violent oscillations or to changes in pill microphone voltages due to changes in the amount of current in the PZT ring as a result of admittance changes in the system.

#### 5.3.2.1.2 Signals Displaying higher signal difference amplitude

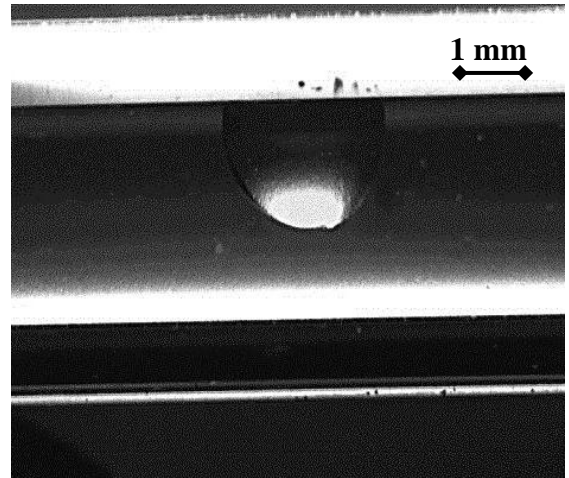
As described in section 5.3.2.1, 43% of studied cases presented higher signal difference amplitudes. The physical phenomenon dominating these observations is still under study. Increased pill microphone voltages could be a result of random increases in pill microphone voltage due to changes in the system admittance as discussed in section 5.1.3 and illustrated in Figure 5-8 (B). It was also found that 76% of the cases presenting an augmentation of the signal amplitude correspond to radii lower or equal to 0.65 mm. Bubbles of these radii would be characterized with resonance frequencies  $\geq 5$  kHz. The other 24% was measured for bubbles larger than this size.

Figure 5-18 (A) displays an example of a relatively small bubble whose oscillations caused the amplified signal (in red) when compared to signals taken prior to bubble injection (blue). The signal difference (between red and blue) is greater than the measured difference error for those trials, which highlights a positive system response to small bubbles; exploiting bubble resonant qualities. The signal experienced a 20% increase in relation to the signal captured before its injection. Figure 5-18 (B) illustrates a relatively large bubble whose amplitude demonstrated a 15 % increment.

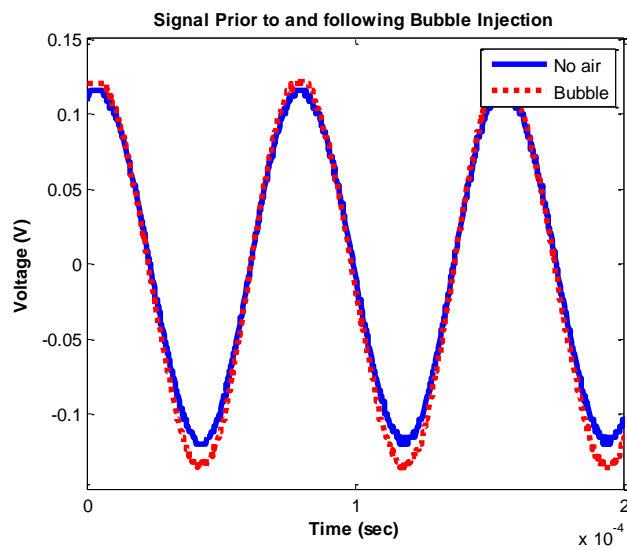
A)



B)



C)



D)

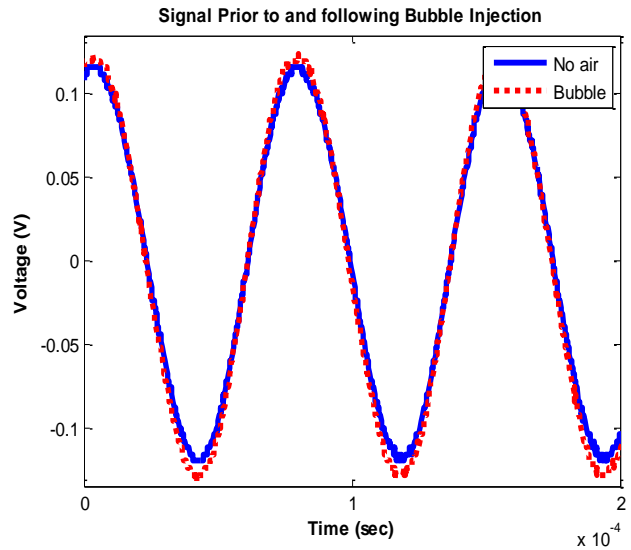


**Figure 5-18 A) Bubble with a 150  $\mu\text{m}$  radius within the “artery like” tubes. B) Bubble with a 558  $\mu\text{m}$  radius with resonant frequencies: 21,292 Hz and 5,740 Hz respectively. C) Signal Prior and Following Bubble injection from Bubble presented in (A). D) Signal Prior and following bubble injection presented in (B).**

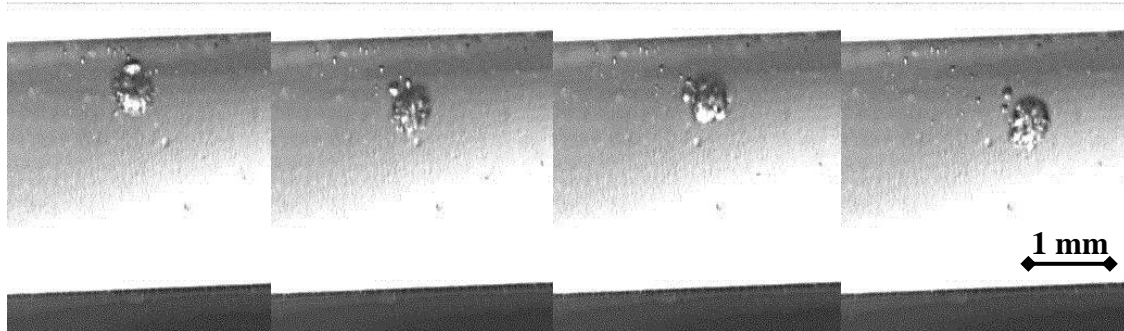


Figure 5-19 Successive images of a violent oscillating bubble. Average radius:  $264\ \mu\text{m}$ ,  $\omega_0 \approx 12.2\ \text{kHz}$

Violent bubble oscillation was captured in many instances within the artificial thigh. This type of oscillation was observed for small bubble sizes. From Eq. (2.26) it was concluded that the resonant bubble size (diameter) corresponding to an excitation frequency of  $13.2\ \text{kHz}$  was  $485\ \mu\text{m}$ . Experimentally, it was observed that as bubbles approached or surpassed this minimum diameter, drastic oscillation occurred (see Figure 5-19).

As mentioned in the beginning of this section additional studies must be carried out, to attribute voltage increments in the pill microphone signal (in relation to the signal measured before injecting the bubble) to the oscillating bubble. However, it is possible that this effect is related with the violent bubble oscillations. It is known that the bubble absorption coefficient becomes dominant for bubbles close to resonant or smaller. In these regions, thermal and viscous effects become significant; where for bigger bubbles, their contribution to the overall extinction coefficient could be ignored (Eller, 1970). In addition this increase in the pill microphone voltage might be also related to the oscillation phase change experienced by a bubble near resonance. A bubble insonated by a pressure field at a frequency higher than its resonance frequency will oscillate in phase with the acoustic fields; whereas at frequencies higher than bubble resonance the bubble oscillates  $\pi$  out of phase with the excitation pressure

field. In summary, the effect of bubble oscillations on fluid pressure and the capabilities of the pill microphone to accurately respond to bubble oscillations are still under study.

### ***5.3.2.2 Analyzing voltage signal ratios***

The previous analysis involved differences in the amplitude of the voltage difference from signals taken with and without bubbles. A second method to analyze the signal was performed, and it was found more effective than analyzing the amplitude of voltage differences, because it took into consideration the voltage at each time step; not only signal amplitudes.

It was observed that the overall measured voltage amplitudes values could differ by as much as ten times from day to day trials, depending on a variety of experimental factors, particularly the amount of air dissolved in water. Because of this, voltage normalization was performed on the voltage signals pertaining to each particular trial. The normalization of voltage parameters was obtained by taking the sum of the squares of the voltage values in the presence of the bubble and dividing it by the squared of the voltage sum taken prior to bubble injection and is shown below with  $N$  being the total number of data samples, equal to four thousand:

$$\sum_{i=1}^{i=N} V_{i \text{ Bubble}}^2 / \sum_{i=1}^{i=N} V_{i \text{ without}}^2 \quad (5.2)$$

The error range for the particular trial was found by applying the same formula between measurements performed in the absence of bubbles. In order for the measurement in the presence of bubbles to be taken into account the ratio had to be over the upper and lower limit defined by the ratio of measurements taken without bubbles:

$$\sum_{i=1}^{i=N} V_{i \text{ without } 1}^2 / \sum_{i=1}^{i=N} V_{i \text{ without } 2}^2 \quad (5.3)$$

The applied formula resembles the RMS calculation for values containing discrete data; were RMS for  $x$  variable is defined as:

$$X_{RMS} = \sqrt{\frac{1}{N} (\sum_{i=1}^{i=N} X_i^2)} \quad (5.4)$$

Similar methods were utilized by Ozeri et al. (2006), where bubbles passed through a tube surrounded by two piezoelectric transducers. One of these transducers acted as the transmitter, the other as the receiver. The calculation of energy of the received signal was based on:

$$E = \sum_{n=0}^{n=N-1} y^2[n], \quad (5.5)$$

and was later followed by an energy normalization normalized:

$E_n = E/E_{max}$ , where  $E_{max}$  corresponds to the energy measured in the absence of bubbles. These ratios were later correlated to bubble volume.

By studying this method and comparing the ratio obtained in the presence of bubbles 87% of the studied bubbles out of 105 cases presented values smaller or larger than the ratio measured between two instants containing no bubbles. 57% of trials report ratios smaller than the lower limit established by the predetermined ratio without bubbles. This percentage is the same as when studying amplitude differences since it was the case that a lower voltage summation in the presence of a bubble also corresponded to lower voltage amplitude.

In Figure 5-20 and Figure 5-27 through Figure 5-29 the legend provided displays: Bubble A, Bubble B, Bubble C, ect. These figures display results performed on a single bubble. A large bubble was initially trapped inside the tubes (radius ranging from 1 to 1.6 mm) with its diameter changing over time. Due to a low concentration of air in water, the bubble would start dissolving and its size decreases in time. Consequently, multiple measurements were performed. This analysis follows from the bubble breakage method described in section 3.4.3. This was done in an attempt to investigate patterns in electrical measurements due to the presence of the bubble and additionally, correlate this signal changes to a decreasing bubble size.

Figure 5-20 presents data collected for three particular trials. The normalized voltage is expected to be less than unity due to the signal scattering and energy absorption qualities of bubbles which have been discussed. As can be observed, there are measurements exceeding this value. Some of these fall within the calculated instrumentation area zone; however cases in which this ratio is greater than unity are still under study and up to date are attributed to admittance changes in the system.

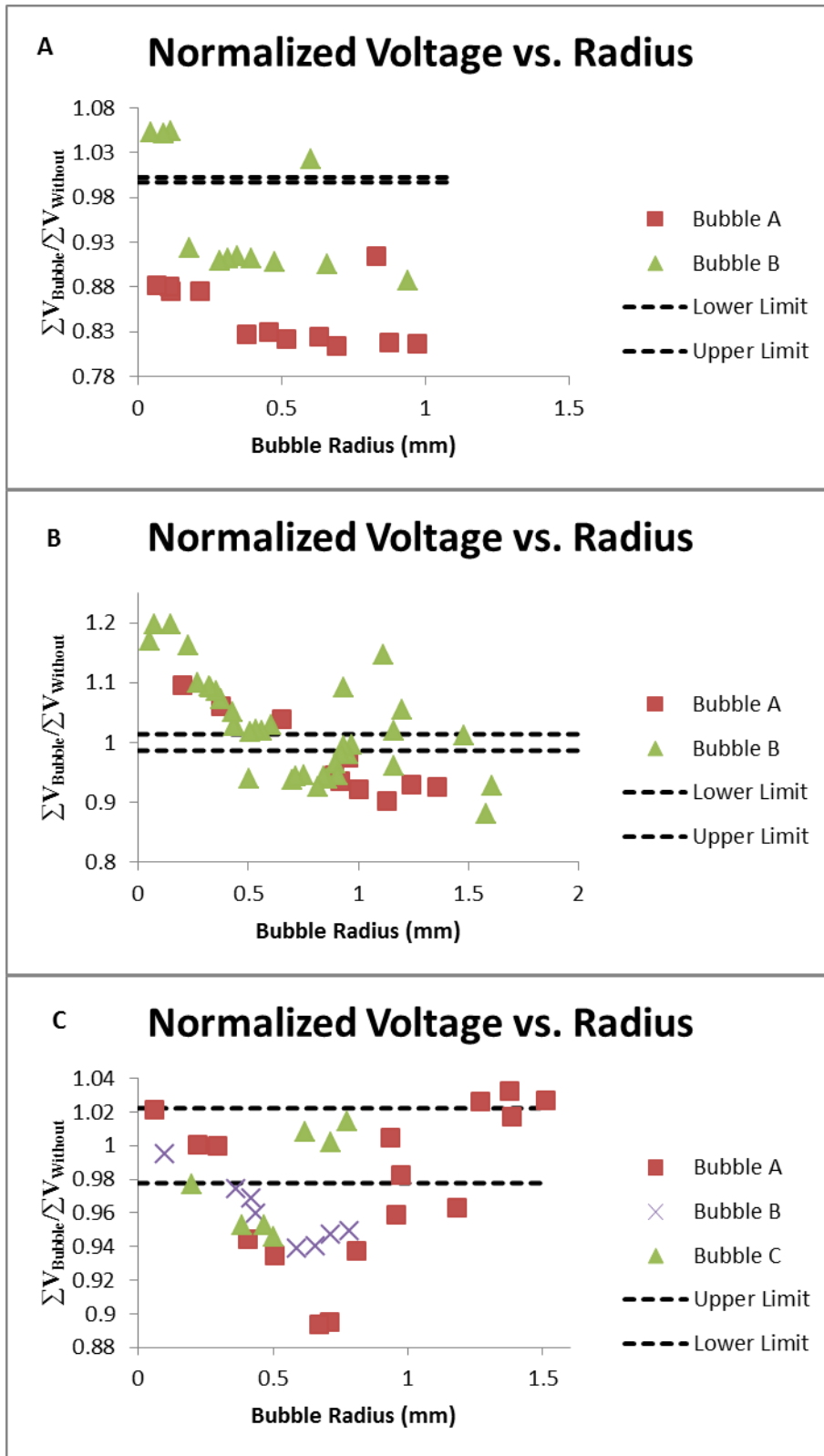


Figure 5-20 Three trials presenting the normalized voltage as a function of bubble radius. Patterns were observed which could lead to bubble size to voltage signal correlation.

A decreasing pattern was expected; since larger bubbles are expected to scatter a greater amount of energy due to a larger cross section. This was the general trend, as presented in Figure 5-20 (A) and Figure 5-20 (B). It can be observed, that there are certain bubble radii (see Figure 5-20 (C)), for which the signal voltage is much less than unity. It is prudent to say that at these specific trials, the bubble extinction coefficient was maximized; thus scattering and absorbing more energy from the acoustic field. This kind of observed ‘V’ shape trend could also be attributed to the change in bubble phase oscillation as it undergoes resonance. These cases must be carefully studied and a greater amount of trials must be carried out, since this could lead to identify a specific bubble size as could also be done if a linearly decreasing trend was obtained.

These results expose the capabilities of the pill microphone to accurately detect bubble presence based on voltage summations at the resonance frequency of the artificial thigh. The dotted black lines in Figure 5-20 represents the upper and lower bounds of ratios comparing measurements made in the absence of bubbles. This indicates that the majority of the voltage readings (87%) fall outside of the “instrumentation error”; range of measurements captured in the absence of bubbles.

Further experimentation should be carried out in order to accurately determine this error zone in order to exclude false positives. Further experimentation should also take into account changes in the pill microphone voltage as a result of overall changes in the admittance of the system which will cause unwanted fluctuation in the PZT current, and to establish the degree in which these factors affect pill microphone sensibility to bubble presence as has been previously discussed.

### 5.3.2.3 Fast Fourier Detection Analysis

Signal processing techniques such as, Fourier transforms, were useful in the analysis of the measured electric signals. Fourier transforms denote the decomposition of a signal into its sinusoidal components. It transforms data from a time domain into a frequency domain (Proakis & Manolakis, 1998). For instance, a sinusoidal voltage signal was used to excite the PZT device through the inverse piezoelectric effect as previously described. A Fourier Transform of this signal results in a multiple of a Dirac's delta, whose frequency corresponds to the frequency supplied by the wave generation device. A sinusoidal signal of this type will contain only one single frequency component. If a sinusoidal signal of the form  $Asin(Bt + \phi)$  is analyzed, the observed Fourier Transform will be a single component of magnitude  $\infty$  and frequency  $2\pi/B$ .

Figure 5-21 presents data from a sinusoidal signal that was gathered from a wave generator at 1 V (amplified 5x) and 10 kHz. The plot on the right displays a Fast Fourier Transform of this signal. In this case, a peak is observed at 10 kHz with expected amplitude of 5 and not a delta, as previously described. This occurs because the FFT is obtained from discrete data points and not from a continuous sinusoidal signal. The peak bandwidth is related to the time interval between the points in the sinusoidal discrete signal.

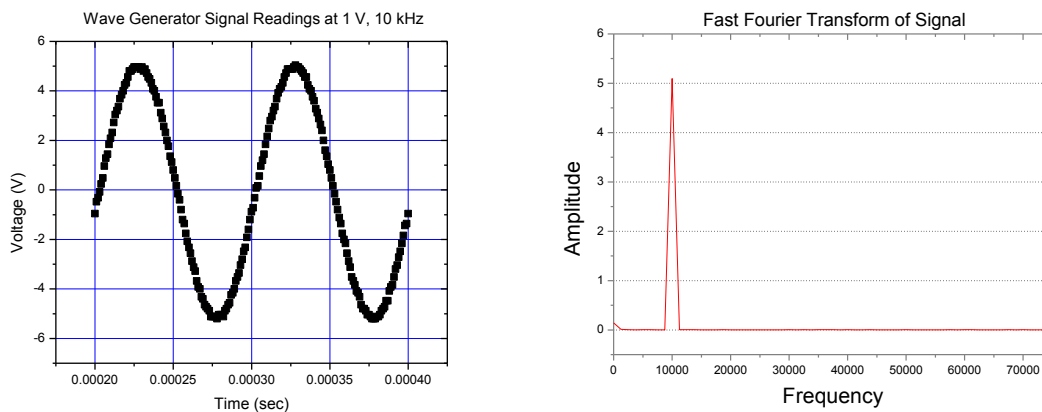


Figure 5-21 Readings obtained from wave generator at 5 V, 10 kHz (left) Fast Fourier Transform (Right)

The use of Fourier Transforms allows for a detailed study of the emitted and received signals. Obtaining a detailed analysis of the components adding up to the measured signals and their magnitudes will allow for a complete comparison between instants affected by bubble presence. As demonstrated in section 5.3.1, the presence of air alters the measured pill microphones transducer signal. Similarly, a noticeable response was observed in the frequency spectrum of the signal. The signal was no longer characterized by a single frequency component, which was induced by the wave generator, but it was characterized by additional frequency components which arise from bubble excitation and harmonics. As will be discussed in successive sections, the appearance of these frequency components was correlated to the presence bubbles. A correlation was attempted between FFT component magnitudes and bubble size.

In the absence of a bubble, the pill microphone signal presents a clean sinusoidal shape. Instabilities in the signal were observed at the onset of bubble presence. The signal in the presence of bubbles is distorted by one of two cases:

- 1) The presence of bubbles results in an overall change of the bulk properties of the fluid media; presence of the two phase flow induces changes in the structure resonance conditions which are sensitive to minor elastic changes within the structure such as those offered by bubbles. In these cases amplitude differences in the FFT components are observed.
- 2) FFT spectrum is disrupted by higher harmonics as a result of non-linear oscillations at the bubble's wall such as those observed in Figure 3-8 presenting examples of these non-linear wall oscillations obtained within the artificial thigh.

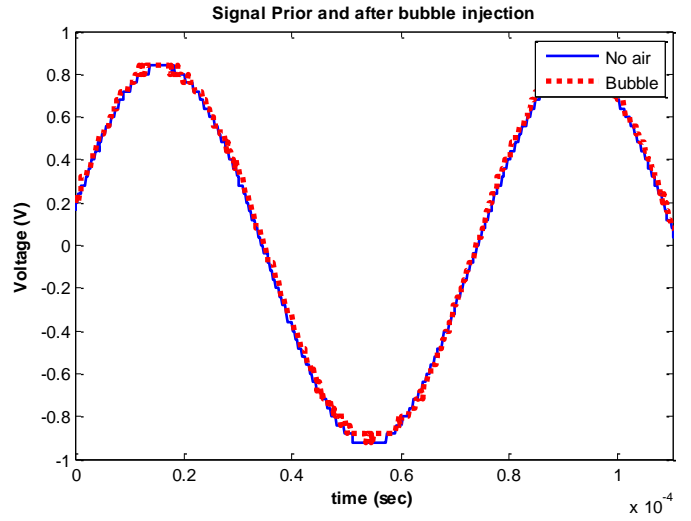
### 5.3.2.3.1 Preliminary Results

Fast Fourier Transforms were performed on sinusoidal signals. Figure 5-22 B presents two signals; one taken before the injection of a bubble (continuous line) and the other one taken in the presence of a 3.2 mm bubble (dashed line). Initial inspection of both signals presents no clear distinction between them. Figure 5-22 C presents a comparison between the Fast Fourier transform of the signal taken in the absence of bubbles with the one taken in the presence of bubbles. As expected in the absence of a bubble, a peak is obtained whose frequency corresponds to the working frequency. However an FFT of the signal in the presence of bubble shows additional frequency components, specifically a composition of the driving frequency and high order harmonics. The difference of both FFTs is presented in Figure 5-22 D and it shows that the additional peaks clearly observed in Figure 5-22 D are multiples of the excitation frequency ( $\approx 13,300$  Hz).

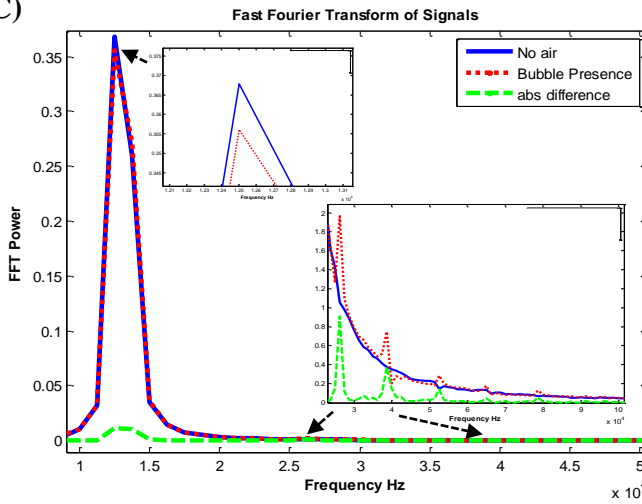
A)



B)



C)



D)

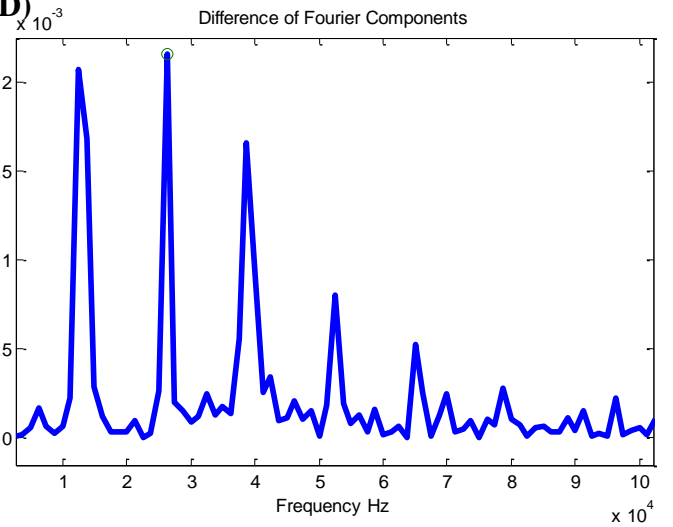
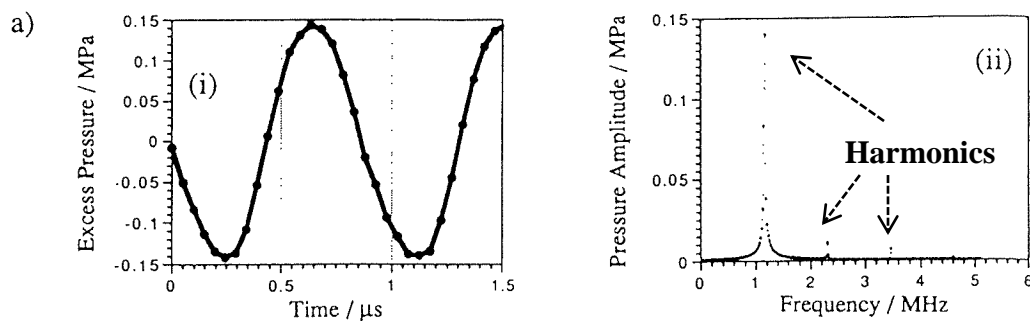


Figure 5-22 A) 3.2 mm diameter bubble near PZT ring B) Measured signal prior and after bubble presence C) Fast Fourier Transform of signals presented in (B) D) Difference between signals in (C) corresponding additional frequency components

### 5.3.2.3.2 Harmonic analysis through the use of Fast Fourier Transforms

It was concluded that signals measured through the pill microphone presented harmonics in the absence of bubbles. This is so because the propagated signal, generated by the mechanical source (the PZT transducer) and propagating through the medium is not a perfect sinusoid. Nevertheless, harmonics differed from the fundamental frequency by two to three orders of magnitude. Similar results have been obtained by Leighton and Hardwick who performed pressure measurements through the use of a positively polarized hydrophone on a continuous-wave field generated by an ultrasound transducer at 1 MHz (see Figure 5-23). The continuous wave was produced by oscillations of a transducer upon a faceplate. They obtained harmonic patterns, multiples of the fundamental frequency. This occurs since the signal is not necessarily a pure sine wave.



**Figure 5-23 Data for the (i) waveform and (ii) the corresponding spectra recorded at 1.0m from an ultrasound transducer faceplate operating in water at 1 MHz with a hydrophone (Leighton, 1994)**

Due to the appearance of harmonics in the voltage signals captured in the absence of bubbles the analysis of voltage signals was a challenging process. After closely analyzing 114 cases of signals containing bubbles, the effects induced by the presence of a bubble and its oscillation after being insonated by the acoustic pressure field inside the artificial thigh over signal harmonics are still unclear. A bubble radius threshold was expected to exist; where this threshold would be a function of the bubble resonance frequency. Above this threshold bubble

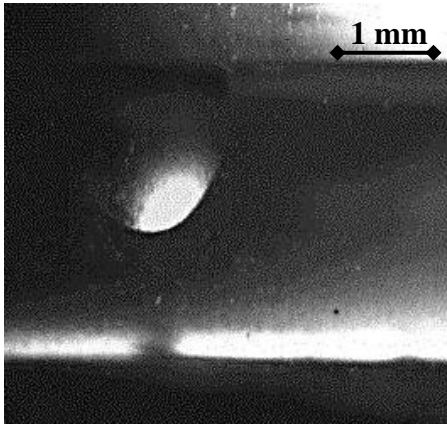
oscillations would be small (due to a larger inertia) and signal attenuation induced by bubble damping would dominate, as a greater amount of energy was subtracted from the incident acoustic pressure field due to a larger bubble volume. Above this threshold harmonics were expected to decrease. Below this threshold bubble wall oscillations would increase. Additional oscillations were expected to cause fluid perturbations, which could be seen as an additional pressure source within the structure. The oscillating bubble would cause additional pressure waves which would affect the wall oscillation and would have an effect on the harmonics of the system. In this area, harmonics above the first harmonic were expected to increase. Although both effects were observed (the attenuation and the increment of harmonics), the threshold defining both behaviors could not be established. Further trials should search for the existence of this threshold, which could aid in identifying specific bubble sizes.

Figures obtained for Fourier analysis present the relation between “FFT Power” and frequency. The Fast Fourier transform data was obtained through the use of a Matlab defined function “FFT”. This function calculates the discrete Fourier transform (DFT) of a vector. FFTs return a complex modulus. “FFT Power” was defined as the square of the magnitude of the complex number multiplied by the Nyquist frequency:

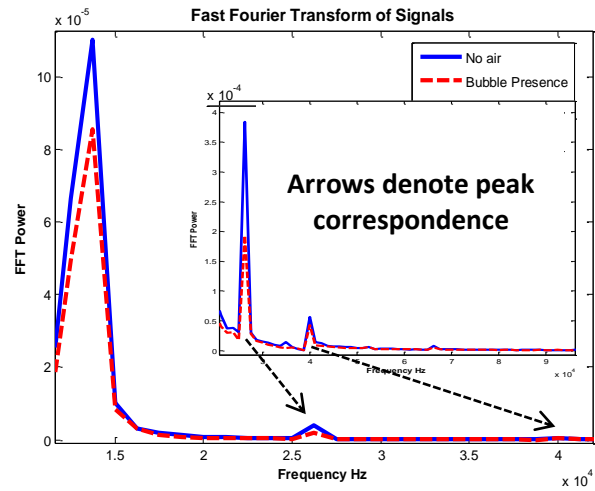
$$Power = abs(FFT(voltage))^2 \times \left(\frac{N}{2}\right) \quad (5.6)$$

where the Nyquist frequency is defined as half the sampling frequency ( $N$ ) of a discrete signal. Figure 5-24 through Figure 5-26 display representative examples of the types of harmonics that were obtained as a result of bubble presence.

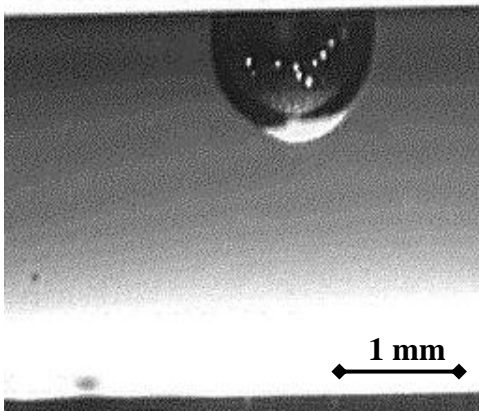
A)



B)



C)



D)

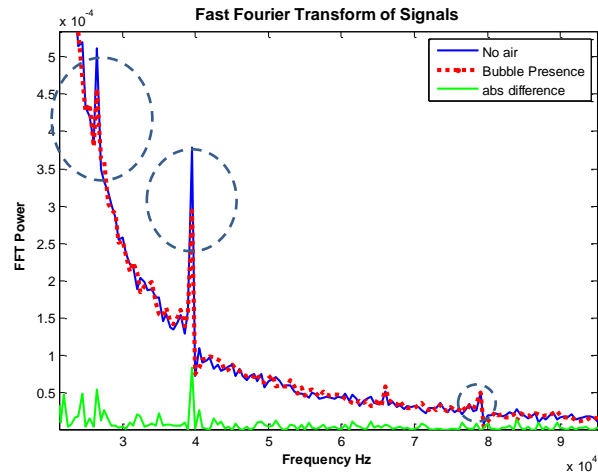
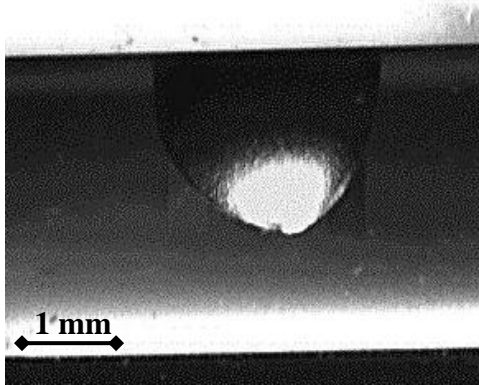


Figure 5-24 A) Bubble radius: 0.890 mm B) FFT of the signal before and after injection of bubble in (A) C) Bubble radius: 0.630 mm D) FFT of the signal before and after injection of bubble in (C). Fourier components experiencing decreased amplitude in relation to the signal obtained before bubble injection

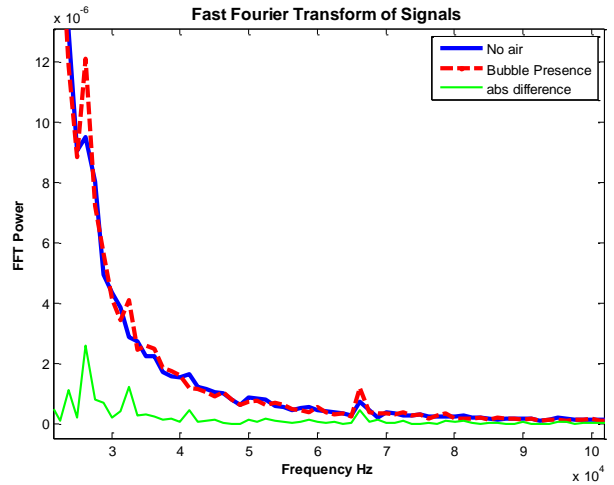
Figure 5-24 shows the effect of the bubble over the amplitude of the Fourier components of the voltage signals as a result of the signal attenuation introduced by the presence of a bubble. This effect was more drastic in a second pill microphone transducer located farther away from the bubble; therefore this transducer would be less affected by overall bubble oscillations, but still experience a reduction in signal amplitude due to signal attenuation. As observed in Figure

5-24 (B) and Figure 5-24 (D), Fourier components corresponding to multiples of the fundamental frequency experience a decrease in amplitude ( $\approx 13, 26, 39, 52, 65$  and  $78$  kHz.).

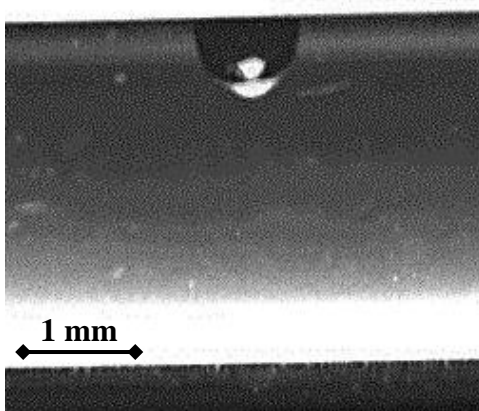
A)



B)



C)



D)

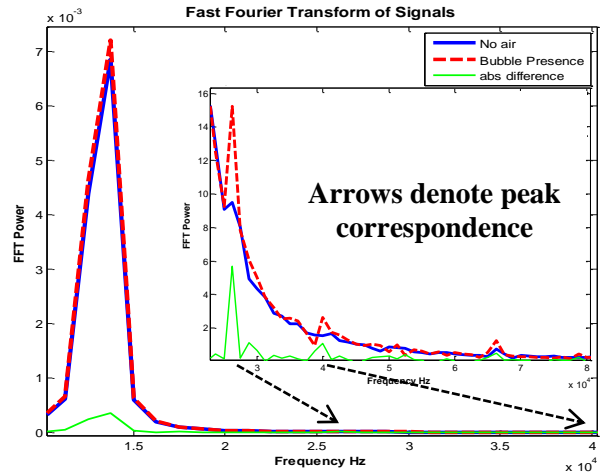


Figure 5-25 A) Bubble of 1.16 mm radius B) FFT Transforms of signal before and after injecting bubble in (A). C) Bubble radius: 0.431 mm D) FFT Transform of signal before and after injecting bubble in (C). Fourier components exhibit increased amplitude in relation to signals before bubble injection

Bubbles presented in Figure 5-25 present the opposite effect to those exemplified by Figure 5-24. These effects were observed as a magnitude increase in Fourier components. Figure 5-25 illustrates that all Fourier components are dominated by the signal in the presence of bubbles. As can be observed, higher differences are observed in all excitation frequency multiples. These

results were thought to be a result of small bubbles reacting violently to the excitation frequency as discussed in section 5.3.2.2. However, the increase in the amplitude of harmonic components was also observed in bubbles larger than resonance as shown in Figure 5-25 (A) and Figure 5-25 (B).

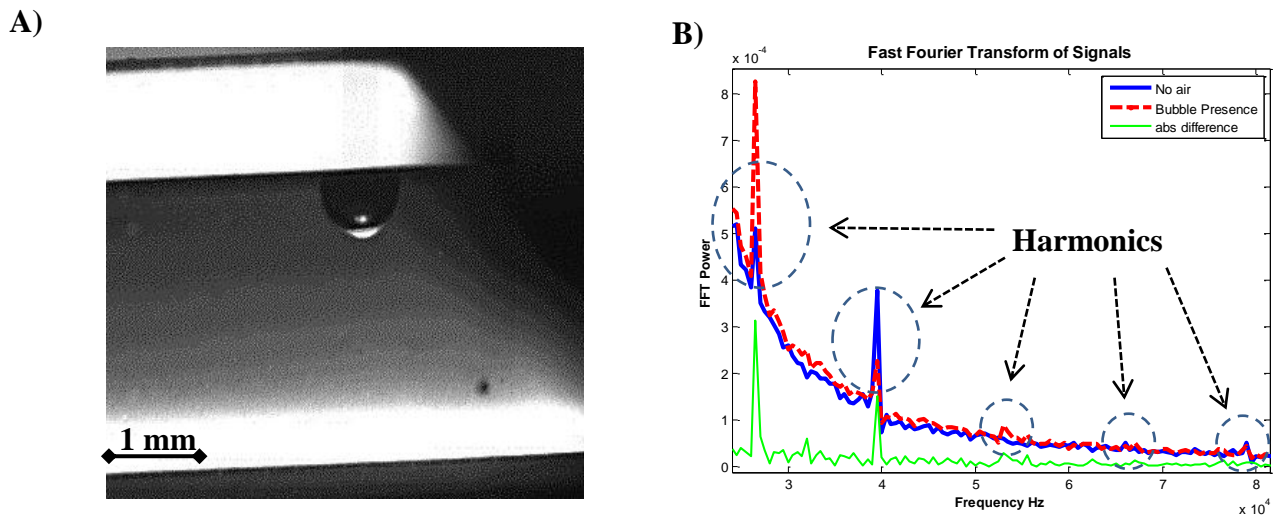


Figure 5-26 A) Bubble radius: 0.303 mm B) FFT of the signal corresponding to bubble in (A)

Results presented in Figure 5-26 further extended the number of different results which could be obtained. As shown in Figure 5-26 there is a magnitude increase in certain harmonics and a decrease in others. This complicated the analysis since not all harmonic components decreased nor increased in the presence of a bubble but could experience a combination of these. This made it difficult to actually attribute a specific higher frequency component to the presence of bubbles or its oscillation. Alternate methods were developed in order to analyze data obtained from Fourier transforms. Three main techniques were used and will be discussed below.

### 5.3.2.3.2.1 Analyzing Fourier Component summations

The correlation between sums of Fourier components and bubble diameters was attempted taking into consideration a range of bubble diameters (50  $\mu$  - 3mm). This type of analysis was defined by:

$$\text{Difference of FFT} = \sum_{i=1}^{i=N} (\text{FFT Component}(i)_{Bubble}^2 - \text{FFT Component}(i)_{No Bubble}^2) \quad (5.7)$$

In this type of analysis the amplitude difference is expected to increase as the bubble size increases and approach zero as bubble size decreases. This is expected since the extinction cross section of bubbles is maximal at resonance. Therefore resonant bubbles will scatter more energy than none resonant ones. Nevertheless, a particular bubble radius with resonant frequency  $\omega_0$  is expected to respond with high bubble oscillation which might induce greater amplitude in the sinusoidal wave (at the moment  $\omega_0 = \omega$ ). As bubble size approaches zero, it is expected that this difference approaches zero as well. Results of two distinct trials presenting this kind of described behavior are presented in Figure 5-27 and Figure 5-28.

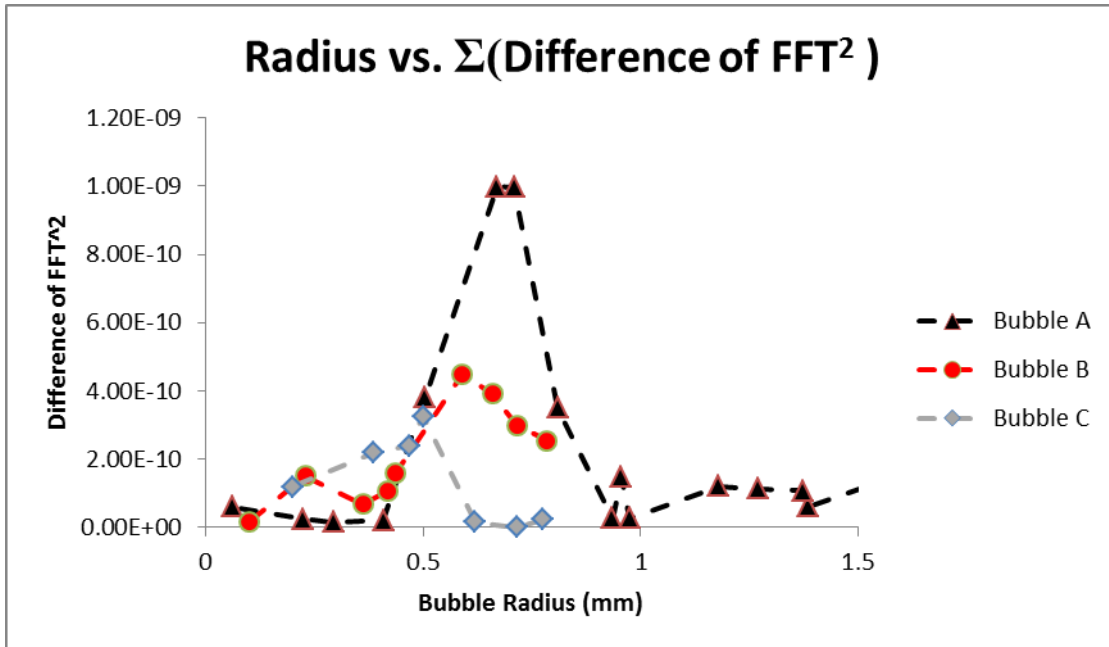


Figure 5-27 Sum of FFT Differences against bubble radius at transducer 1 located closest to the injected bubble

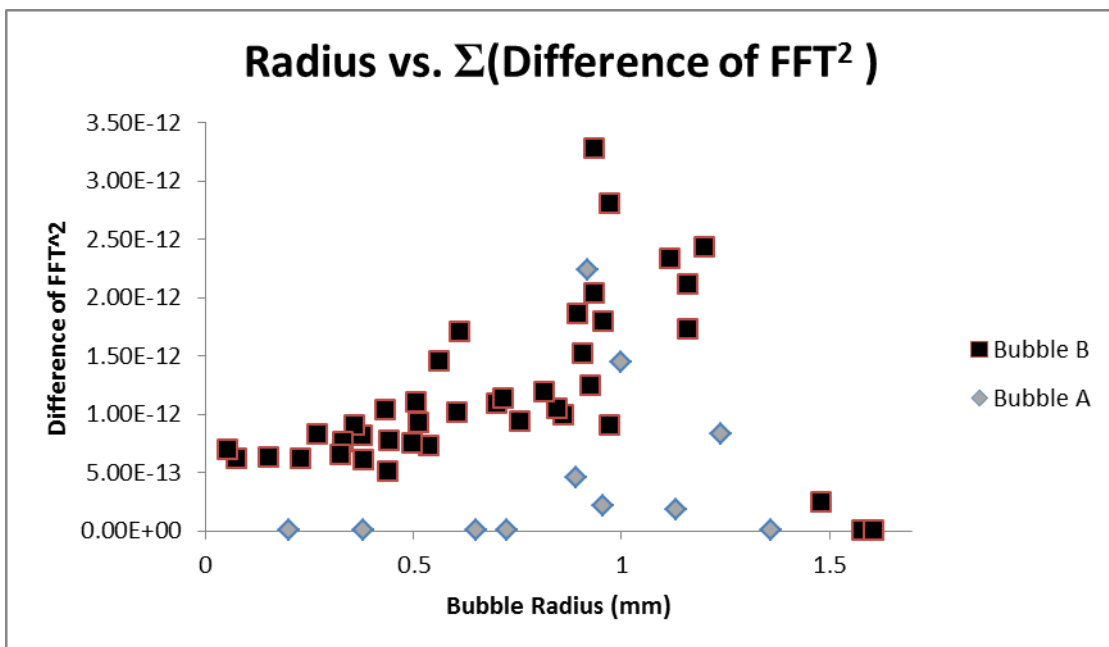


Figure 5-28 Sum of FFT Differences against bubble radius at transducer 2 located farther away from the injected bubble

The results obtained through this method take into account point to point differences of the FFT components. Later, the summation of this difference is plotted against the specific bubble radius. FFT data was also analyzed according to:

$$\text{Normalized sum of FFT} = \frac{\sum_{i=1}^{i=N} \text{FFT Component}(i)_{\text{Bubble}}}{\sum_{i=1}^{i=N} \text{FFT Component}(i)_{\text{Without}}} \quad (5.8)$$

The data displayed in Figure 5-29, was obtained by plotting the ratio obtained from Eq. (5.8) to the specific bubble size.

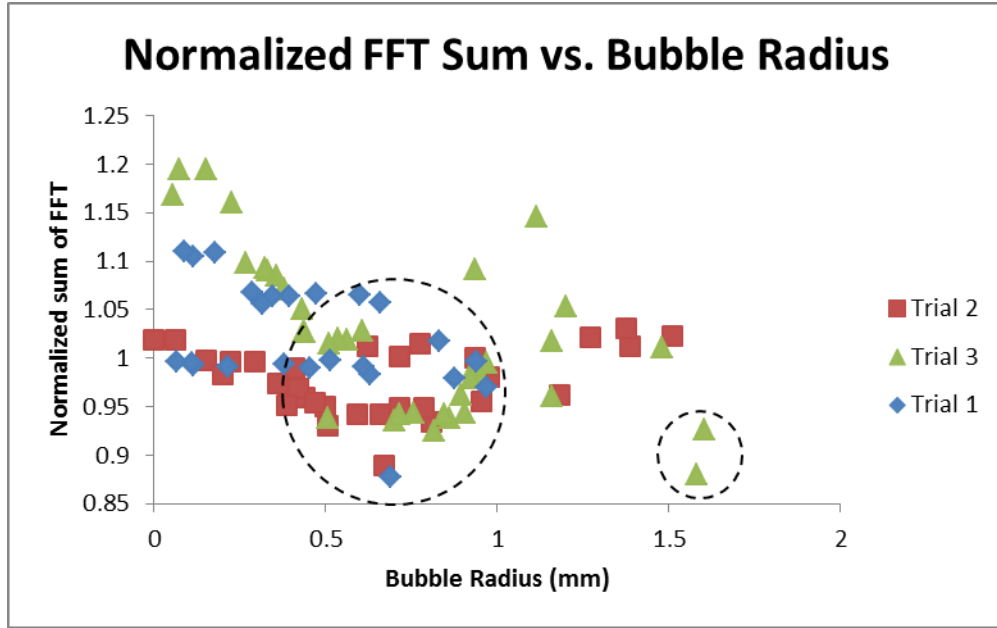


Figure 5-29 Normalized sum of FFT (Eq. (5.8)) components as a function of bubble radius for three different trials totaling 93 measured bubbles

Areas presenting minimum ratios are marked. These bubble radii could be a result of greater signal attenuation and scattering, minimizing the signal captured by the pill microphones. 94% of the data (104 bubbles) analyzed in this form (Eq. (5.8)) present differences greater than the ratio calculated for measurements taken in the absence of bubbles. These results, which are a consequence of analyzing the frequency spectrum of the signal, have proven so far to be the most reliable based on differences among measurements.

Figure 5-27 through Figure 5-29 support the theory that a bubble threshold must exist for which the difference between the signal captured in the presence of a bubble and the signal taken prior to bubble injection displays a mayor difference. However as can be observed in these

figures, there is a range of bubble radii which display the maximum difference; it is not a defined peak as it would have been desired. The radius displaying maximum difference in the components is believed to vary according to the specific response of the artificial thigh and to admittance curves for the specific trial. The bubble radius displaying the maximum difference does not correspond to a resonant bubble, whose resonant frequency corresponds to the excitation frequency; therefore additional variables should be influencing the response of the system.

Nevertheless these results demonstrate, that a threshold must exist for which signal differences are augmented. If this threshold is defined through further trials, the possibility to separate a bubble population above or below some specific radius size is tangible.

#### *5.3.2.3.2 Analyzing the Ratio of the Fourier Component of the Fundamental Frequency*

Although the results discussed in section 5.3.2.3.2.1 show great promise, in order to further understand the relevance of these results and what factors induced by the bubble behavior actually affect pill microphone signals and should be taken into account for further studies, a new analysis aimed to separate the Fourier components into its fundamental frequency and higher order harmonics. The second proposed method took into account the ratio of the FFT power of the FFT component at the frequency which corresponded to the excitation frequency. This ratio can be described as:

$$\text{Ratio at peak} = \text{FFT power}_{\text{Bubble}} / \text{FFT power}_{\text{no bubble}} \text{ at } \omega = \omega_{\text{excitation}} \quad (5.9)$$

When this ratio is plotted against bubble radius, results are similar to the patterns observed in Figure 5-20. This was expected since the fundamental frequency was orders of magnitude higher and would dominate any expression which took into account all frequency components.

Results taking into consideration the ratio of FFT power at the fundamental frequency demonstrated differences from measurements in the absence of bubbles in 85.6% of times.

As was mentioned when discussing Figure 5-20, these are all trends subject to further investigation. Experimentation should continue since they could reveal specific patterns leading to a bubble size detection algorithm.

### 5.3.2.3.2.3 *Analyzing the Ratio of higher order harmonics*

A third study was carried out which took into consideration FFT components of the signal excluding the excitation frequency. The first harmonic was orders of magnitude higher than higher order harmonics which would lead any analysis which took into consideration the first harmonic to be dominated by this term. In addition the acoustic field generated by PZT transducer would generate acoustic pressure orders of magnitude higher than the acoustic pressure generated by an oscillating bubble. Because of this, it was believed that a study of higher order harmonics would lead to detecting bubble presence within the artificial thigh. This analysis was carried out by performing a summation on the FFT power pertaining to frequencies 20 kHz and higher:

$$\text{Normalized sum of higher harmonics} = \frac{\sum_{f=20 \text{ kHz}}^{f=2.5 \text{ MHz}} \text{FFT Component}(i)_{\text{Bubble}}}{\sum_{f=20 \text{ kHz}}^{f=2.5 \text{ MHz}} \text{FFT Component}(i)_{\text{Without}}} \quad (5.10)$$

This analysis was carried out for a total of 101 bubbles for which 75% of the cases demonstrated a normalized sum of higher harmonics, higher or lower than the values corresponding to measurements taken in the absence of bubbles. Of this 75%, 55% demonstrated a ratio higher than the one obtained without bubbles. It is believed that when the bubble presence attenuates the signal, lower amplitude is obtained in the harmonics. On the other hand, oscillating bubbles

would result in increased amplitude of harmonics. This is a correspondence which has still not been confirmed.

## **5.4 Piezoelectric Ring Response to Bubble Presence**

A second approach for bubble detection was based on the use of the electrical measurements taken on the PZT ring using the electrical set up shown in Figure 3.9 B. The experimental procedure is described in Chapter 3.5.3. The detector was the PZT ring. For these experiments the PZT ring continued being the excitation source (through the inverse piezoelectric effect) but in addition also functioned as transducer (through the direct PZT effect).

Initially, voltage and current measurements were taken on the PZT ring. However, the PZT amplifier functions by maintaining a constant voltage on the PZT, therefore overall changes were observed in the PZT ring by analyzing current values. While the pill microphone was sensible to bubble harmonic oscillations it was expected that the PZT ring would be mostly affected by changes in bulk properties of the medium due to the presence of bubbles.

Experiments performed using the PZT as bubble detector consisted as explained in Chapter 3 on two basic types of tests. “Variable sample size” transient experiments were carried out by capturing voltage, current and phase angle readings from the moment the bubble entered the acoustic chamber until the bubble left the chamber, due to a constant fluid flow provided by the peristaltic pump. “Fixed sample size” transient experiments were performed by having bubbles captured in the chamber through the use of the acoustic force. Once successful bubble entrapment was accomplished, readings were captured. “Fixed sample size” time analysis captured the readings shown in one oscilloscope frame, which consisted of 4000 data points captured at 50  $\mu$ s intervals.

### 5.4.1 Transient Effect of Large bubbles: Slug flow

The passage of a large bubble within the vein and artery was recreated by injecting controlled amounts of air into a water environment until an air pocket within the system was attained. As the air pocket (also known as slug flow) moved in and out of the artificial thigh, voltage, current, and phase angle measurements were taken on the PZT ring as a function of time. These bubbles ranged from 0.25cm to 2cm in height and from 0.3175cm to 0.47625cm in diameter (depending on whether they traveled through the vein or the artery). Examples of this flow type are presented in Figure 5-30.

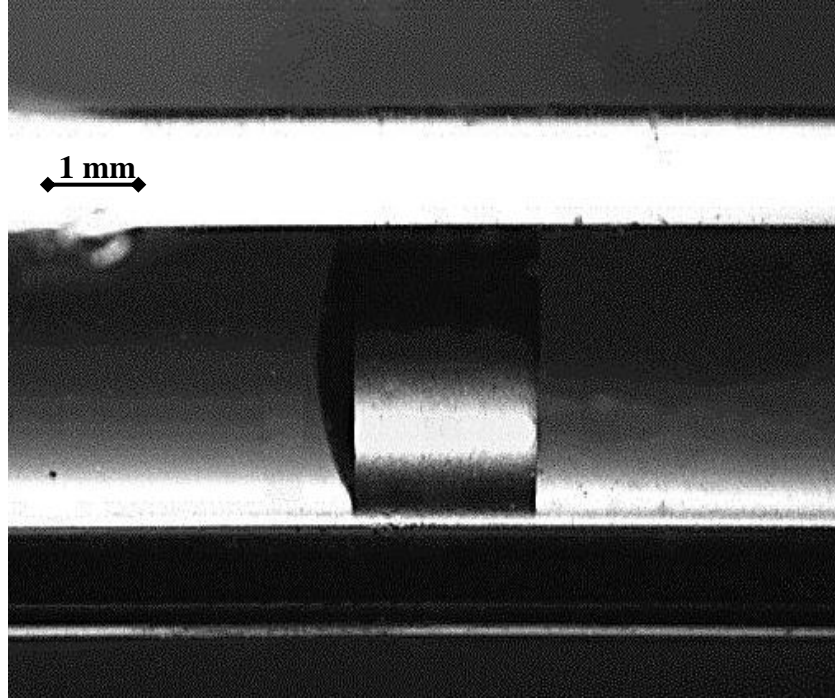
Voltage readings constant as expected, since the PZT amplifier is designed to keep voltage constant. However, as an air column approached the PZT ring vicinity, a drop on the current value was observed (see Figure 5-31 (A)), which also matched a peak appearing in the phase readings as shown in Figure 5-31 (B). Electrical measurements shown in Figure 5-31 were obtained while a bubble was pushed through the “vein” tube. Consistent results enable bubble detection possibilities by monitoring the electric signals on the PZT. A single peak in the current and phase angle values were correlated to the response obtained by the presence of a single bubble. Twelve trials were performed injecting this type of flow. All trials demonstrated a marked current drop. Phase angles peaks occurred in 80% of trials.

The electrical admittance of the artificial thigh changes due to the presence of air within the inner tubes. Since voltage is maintained constant by the PZT amplifier, changes in electrical admittance are observed as changes in PZT current. The increase in phase angle is explained by the change on the elastic properties of the media induced by the presence of the air column which changes the electrical admittance. As observed in Figure 5-32, two different phase angle values are obtained at the same excitation frequency due to changes in capacitance values of the

simulated piezoelectric materials. The capacitance corresponding to conditions 2, was 40% higher than the capacitance for conditions 1. Recall, as illustrated in Appendix A.4 the conditions being referred to, are values of: resistance, capacitance and inductance of a simplified equivalent circuit for a piezoelectric material. Similarly, the presence of slug flow within the system provides higher elastic properties which influence the response of the PZT ring.

Resonance conditions are extremely sensitive to minor changes in the elastic properties of the medium. The presence of a bubble within the cylinder induced pressure variations, departing from normal conditions. Bubbles caused significant changes in the elastic properties of the medium since they are compressible and greatly affected by frequency fluctuations and acoustic fields due to pressure oscillations.

A)



B)

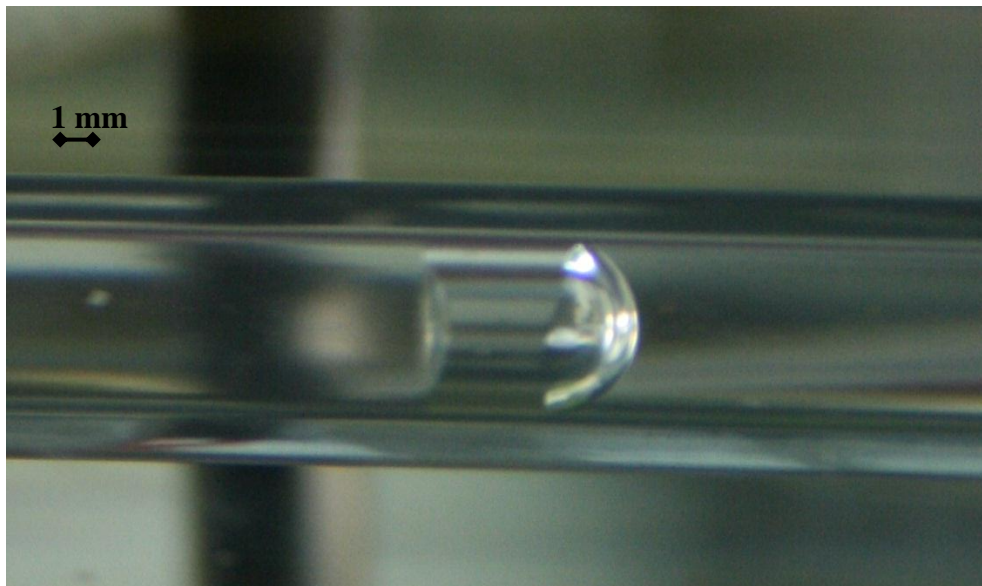


Figure 5-30 Slug Flow present within the artery-like tube (A), vein-like tube (B)

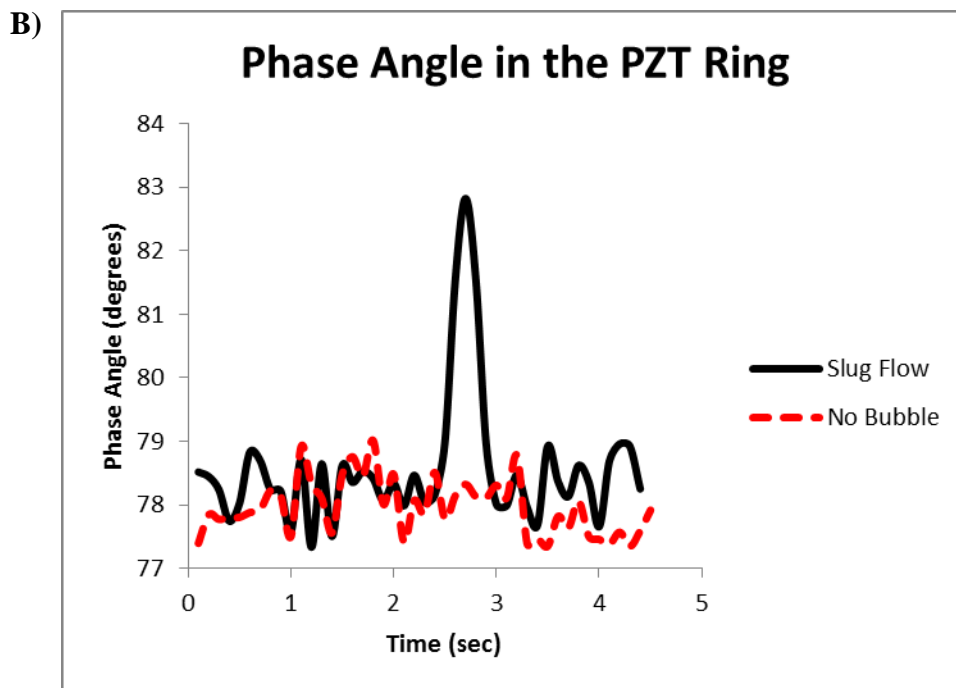
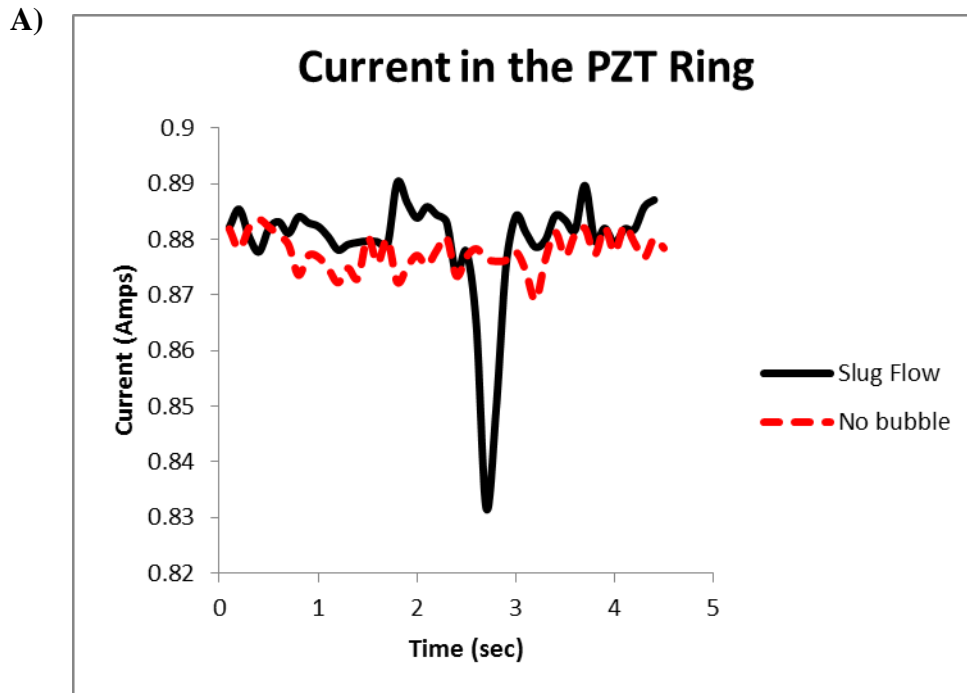


Figure 5-31 Electric measurements on the PZT. Column of air injected in the “vein”. (A) Corresponds to current and (B) to the phase angle between the current and voltage in the PZT.

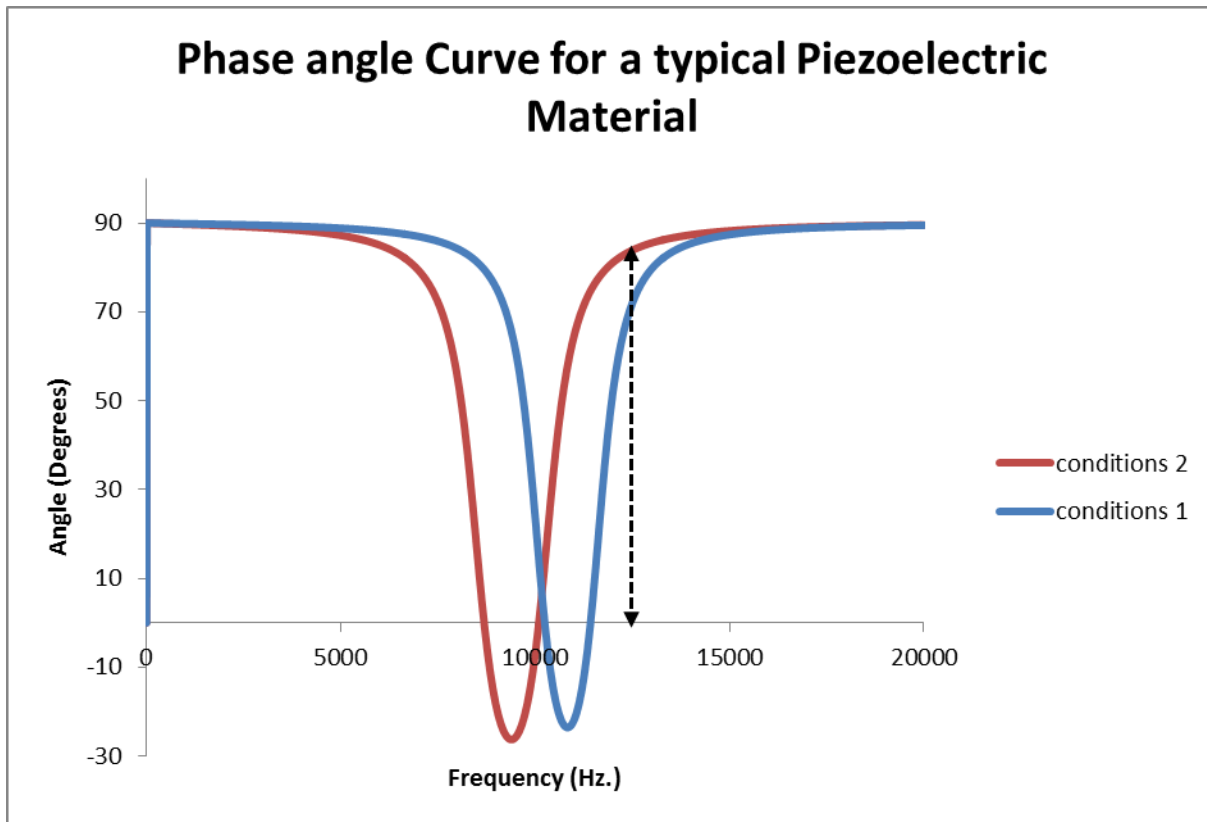


Figure 5-32 Two typical phase angle curves showing differences in resonance conditions due to changes in material properties

This type of analysis was continued through the injection of single bubbles instead of air pockets into the artery and vein like tubes. In this case, observed peaks were not as marked not as consistent as those obtained for the slug flow. Thirty trials were performed. The correspondence between current and phase angle peaks and the quantity of bubbles was accurate in approximately 50 percent of trials. Reasons for this lack of consistency in detecting bubbles as opposed to slug flow will be discussed in the next section.

Figure 5-33 illustrates an example of this type of experiments. In this case three bubbles were injected into the artery. Measurements were carried out from while the bubble entered and left the artery. As presented in Figure 5-34 (A) there are marked current peaks, which are attributed to the passage of the three bubbles. Peaks illustrated in Figure 5-34 (B) correspond to phase angle peaks. However in Figure 5-34 (B) there are two additional peaks. It is believed

that these peaks correspond to fluctuations in the PZT voltage which are presented in Figure 5-34 (C).

Additional studies should develop signal analysis tools which automatically monitor fluctuations in current values and attribute changes to the passage of a bubble. Later this information can be confirmed through phase angle changes taking into consideration voltage fluctuations.

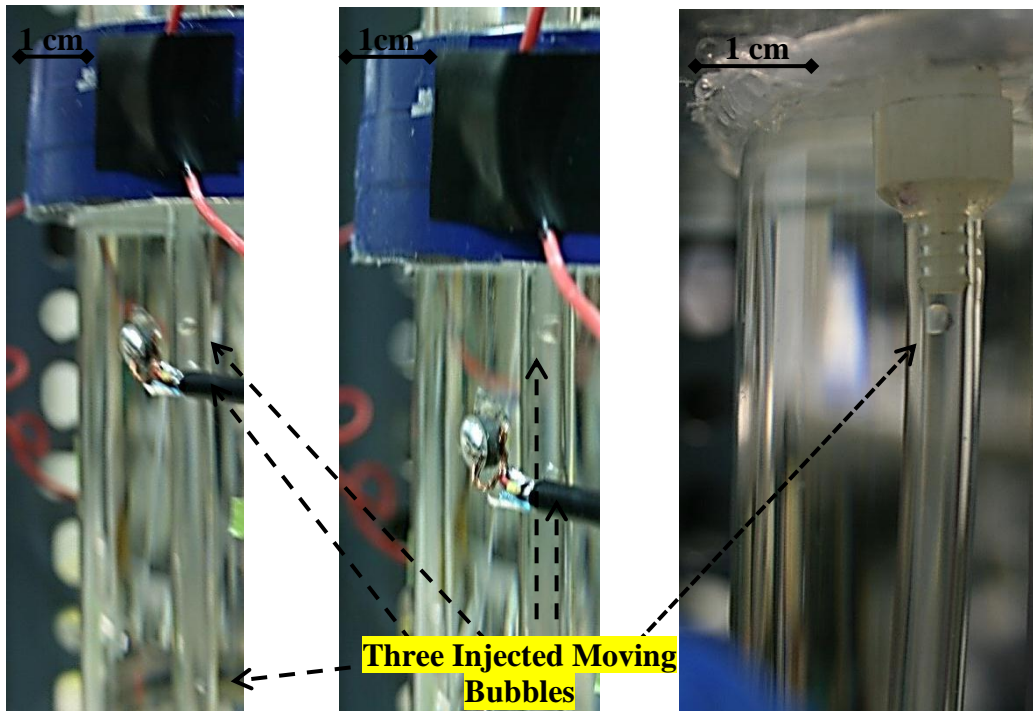


Figure 5-33 Three injected bubbles moving through the artery-like tubes.

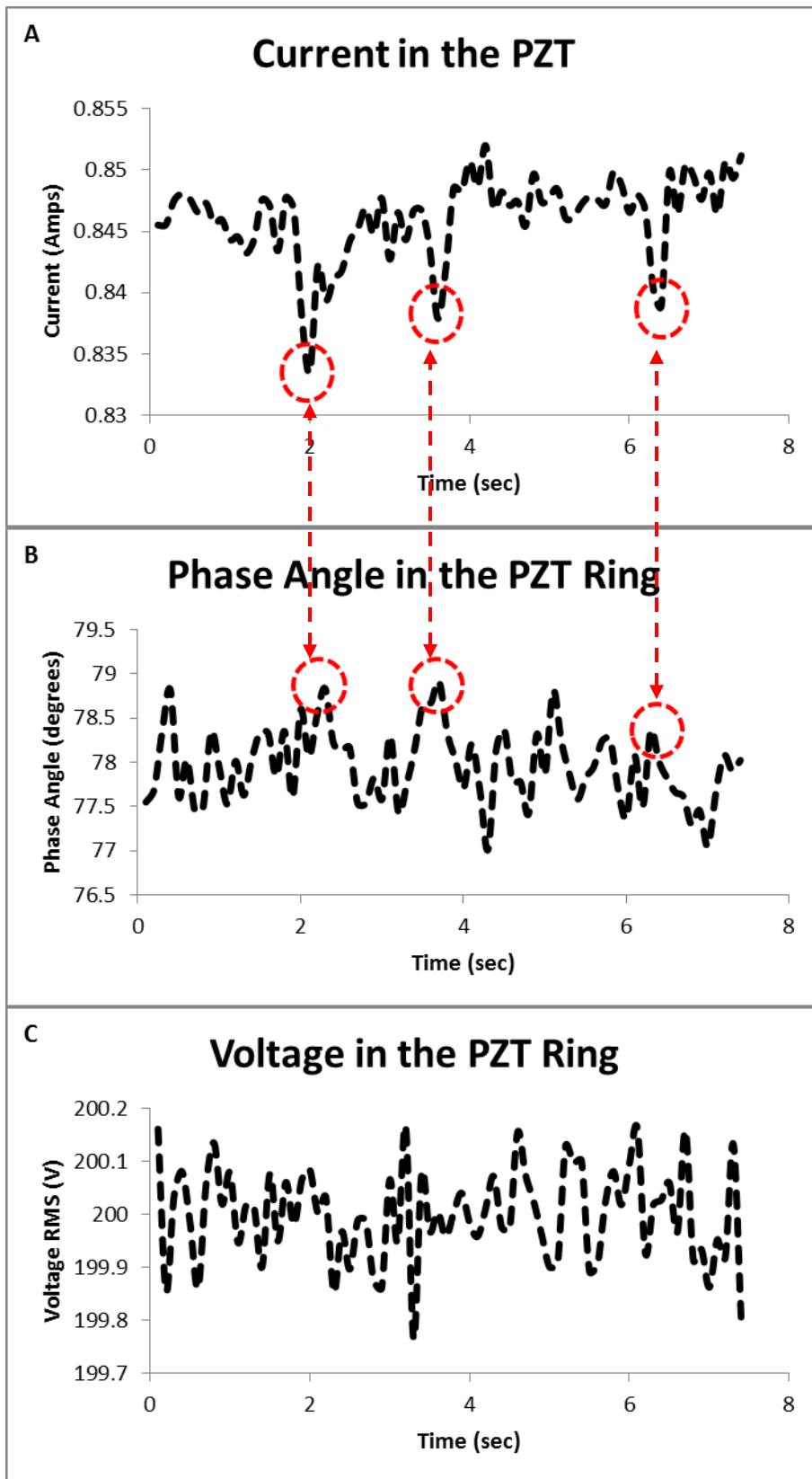


Figure 5-34 Current (A) and Phase angle (B) and Voltage (C) in the PZT ring as three bubbles move through the artery

## 5.4.2 Continuous bubble injection outside tubes

Having observed the significant trend discussed in the last section, a similar procedure was attempted through the continuous injection of bubbles directly into the fluid outside of the veins which would constitute the soft body tissue, shown in Figure 5-35 while exciting the PZT ring at the chamber resonance frequency ( $\approx 13.3$  kHz). Data was acquired through the use of the GPIB card interface, while using the LabVIEW code described in Chapter 3, section 3.4.3. It was observed that the motion of big bubbles (with  $R_0$  larger than 0.5 mm) was dominated by buoyancy forces. Thus upon injection they would rise to the top of the artificial thigh. However smaller bubbles ( $R_0 \leq 0.5$  mm) like the one presented in Figure 5-35, behaved according to predicted by Bjerknes forces; translating toward the pressure antinode of the fluid domain located near the center of the structure close to the PZT excitation source.

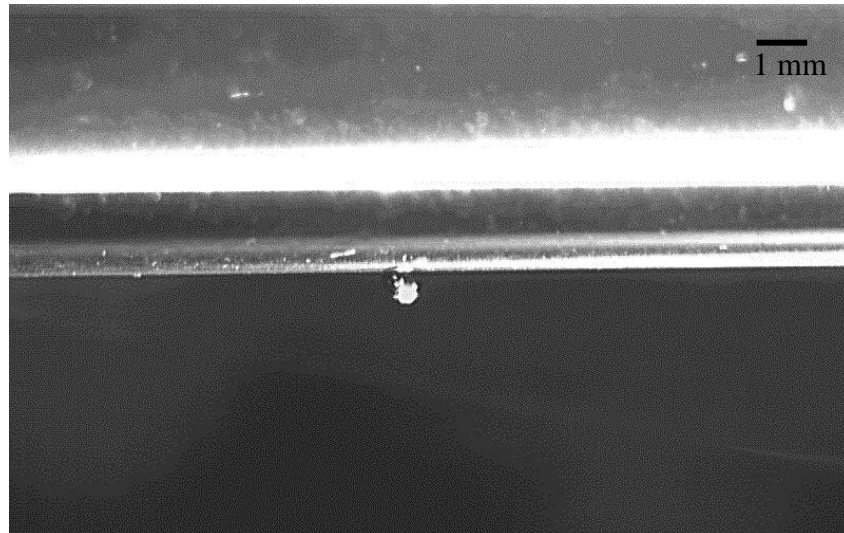


Figure 5-35 Bubble injected outside the inner tubes forced towards the middle of the chamber ( $R_0 = 418 \mu\text{m}$ ).

Experiments performed injecting bubbles outside the tubes were carried out by performing some changes to the experimental setup. As described in Section 3.5.4, the tubes leaving the bubble generation system which would usually enter through the artery like tube,

would be connected to a third fitting used for filling and draining purposes (see Figure 3-2). This would lead bubbles directly outside the inner tubes towards the water in the rest of the cylinder.

Sixty trials were carried out. During these trials measurements were captured while injecting one and up to thirty bubbles. These bubbles were released at an approximate rate of one bubble every second. Acquiring images with the high speed camera of the continuous passage of bubbles resulted challenging due to the presence of the bone and inner tubes in the inspection area. Electric measurements describing the continuous entrance of bubbles into the artificial thigh present the pattern shown in Figure 5-36. This figure shows that monitoring the electric signals on the PZT also enables bubble detection possibilities. Every spike in the current and phase angle values was correlated to the passage of a single bubble near the center of the artificial thigh; where the PZT ring was located and measurements were being captured. The increase in the phase angle is explained by the change on the elastic properties of the media induced by the continuous presence of bubbles that changes the electrical admittance.

It must be stated that the capture of a bubble passage interpreted as a peak in Figure 5-36 is a probabilistic event, where the electrical reading must be measured in accordance to the movement of the bubble through the PZT line of action; where the line of action was defined as the projected area of the PZT ring which is 25.07 mm in height. In the 60 trials carried, it was estimated that 50 % of the bubbles being injected would be “sensed” by the PZT Ring and could be interpreted as current and phase peaks in their respective plots. Similar results were obtained for bubbles injected within the inner tubes. The measurements presented in Figure 5-36 were carried out after injecting a total of 17 bubbles. Figure 5-36 (A) displays a total of seventeen circles, demarking current peaks. Further experimentation must be carried out in order to confirm the correspondence of these peaks to a bubble passage. This is because even though the

passage of a bubble might not present itself as a global peak, it might correspond to a bubble if analyzed as a local minimum.

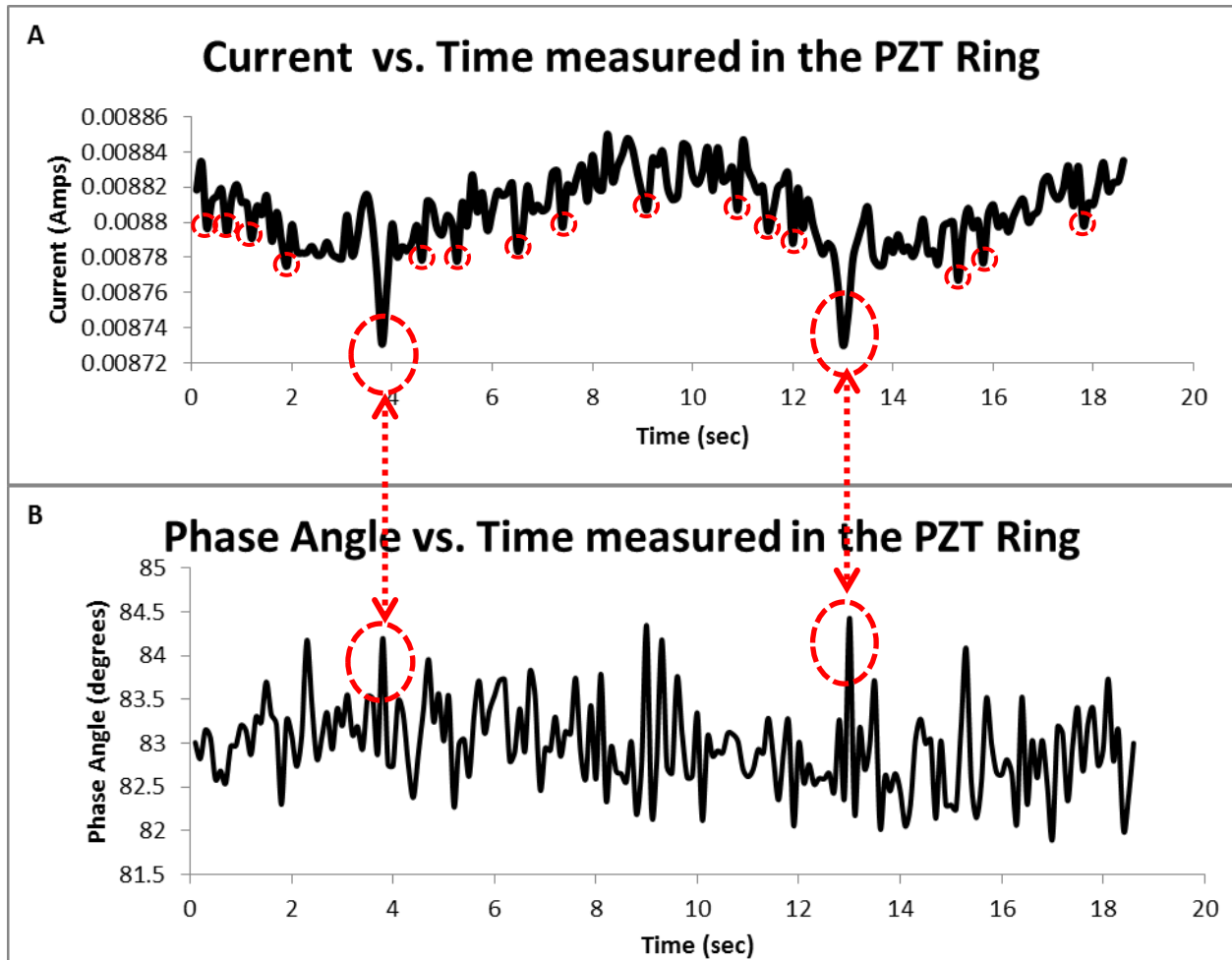


Figure 5-36 (A)Current and (B) Phase Readings, describing the continuous injection of bubbles into the artificial thigh. Seventeen bubbles were injected one at a time. A peak correspondence is highlighted.

Phase angle and current peaks did not always concur. In general it can be concluded that current measurements are more accurate than phase angle measurements. This is because phase angle calculations are also a function of voltage values while current values are independent measurements. Phase angle measurements might be influenced by voltage fluctuations which

were also measured. These could produce a phase shift between the current peak and the phase angle peak.

Based on these results it can be concluded that carrying current and phase angle readings in the PZT ring provides an effective and accurate counter of individual bubbles. Additional variables must be subject to further studying; these include: the definite PZT line of action, defining the accurate area providing accurate bubble detection. Also, the bubble size range which can be detected by the PZT ring. In addition to this, the magnitude of the peaks presented in the current and phase angles must still be subject of further study. Current and phase angle readings also present peaks when measured in the absence of bubbles. These measurements performed in the absence of bubble should be taken into consideration since these might define the chamber while working under normal conditions. Measurements taken in the presence of bubbles could then be compared to this readings. Peaks observed in the presence of bubbles should exceed these previous established limits.

It was stated that capturing the passage of a bubble, and thus producing a current or phase angle peak was a probabilistic event. In the experiments performed with bubbles being injected into the inner tubes or outside of this, accurate bubble detection was produced in 50% of the cases. The bubble identification was performed by visually inspecting the current and phase angle plots and identifying sudden fluctuations which could be related to the passage of a bubble. Future experimentation should target automatic methods to quantify these fluctuations. For the experiments described in this section as well as those discussed in section 5.4.1 while injecting single bubbles the sampling rate was set at 0.1 sec while using the GPIB interphase and the LabVIEW code described in section 3.4.3. If injected bubbles are assumed to rise due to buoyancy, they will rise at speeds determined by the terminal velocity of the bubble. For

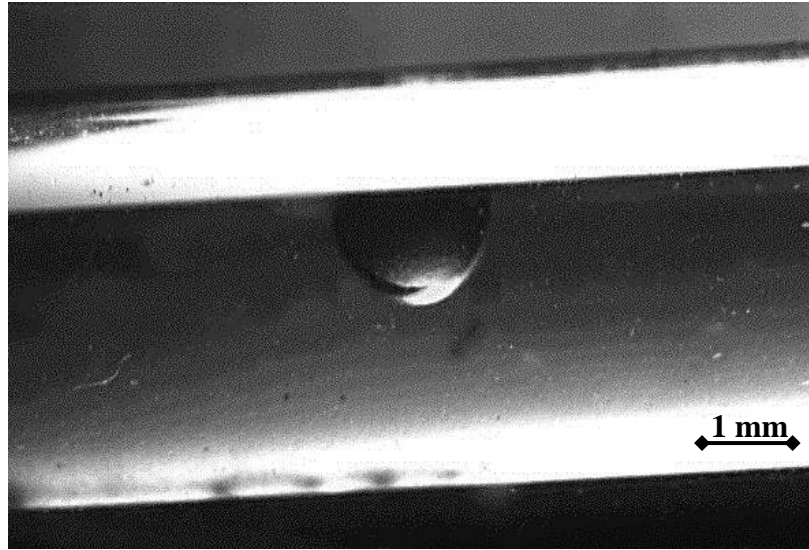
bubbles of approximately 1.6 mm in diameter, bubbles terminal velocity was measured as 26 cm/s in deionized water (Tsao and Koch, 1997). Therefore as a bubble passes through the artificial thigh, approximately 11 measurements would be carried out. This will correspond to approximately 1 measurement in the 25 mm of the PZT ring. This explains why many bubbles were not captured by measurements in the PZT ring. In order for the PZT to accurately detect the passage of a bubble a sampling rate several times smaller than the bubble terminal velocity (at least 5) is suggested. For this to occur, a faster acquisition card than the one available at the time is needed.

Nevertheless this bubble detection scheme offers the advantage that measurements in the absence of bubbles are not necessary. Since a bubble will be detected in accordance to fluctuation in the current measurements as the bubble enters the detection area of the PZT ring.

### **5.4.3 Current Analysis**

“Automated” current measurements in the PZT ring were taken with bubbles injected inside the artery-like tubes. As for the results discussed in section 5.3, bubbles were captured using acoustic force. Results presented compare readings taken in the absence of bubbles to those taken after the bubble was captured. Changes from normal conditions were observed, such as those shown in Figure 5-37.

A)



B)

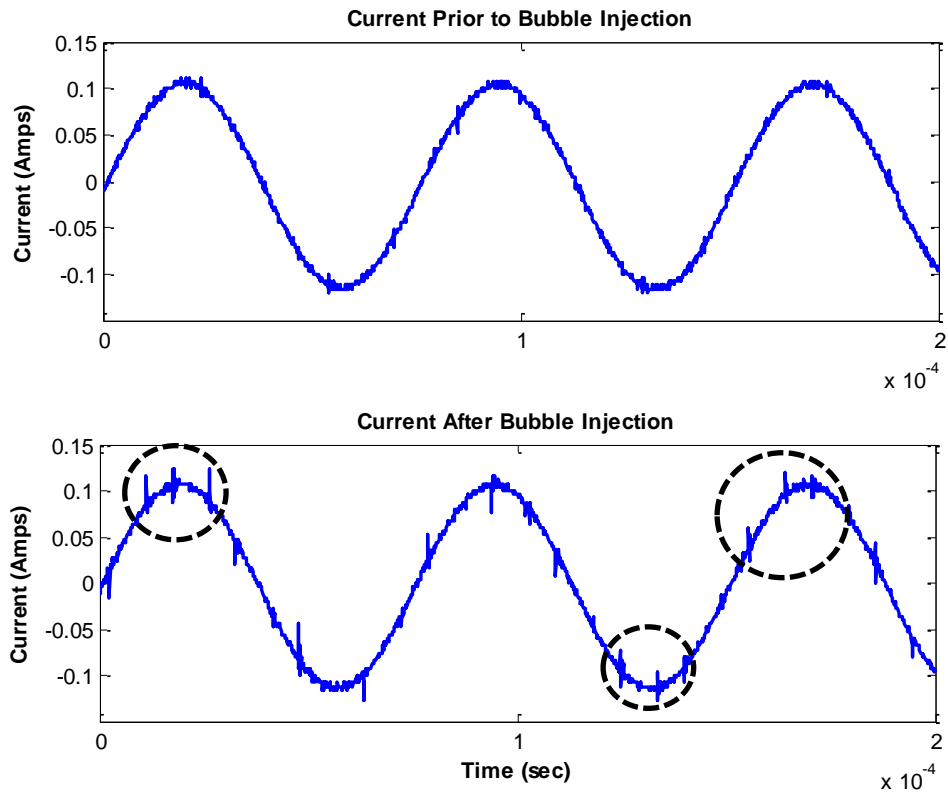


Figure 5-37 A) Bubble radius: 0.8855 mm for which current measurements were taken. B) Measurements comparing current values before and after bubble injection taken in the PZT ring highlighting high frequency components.

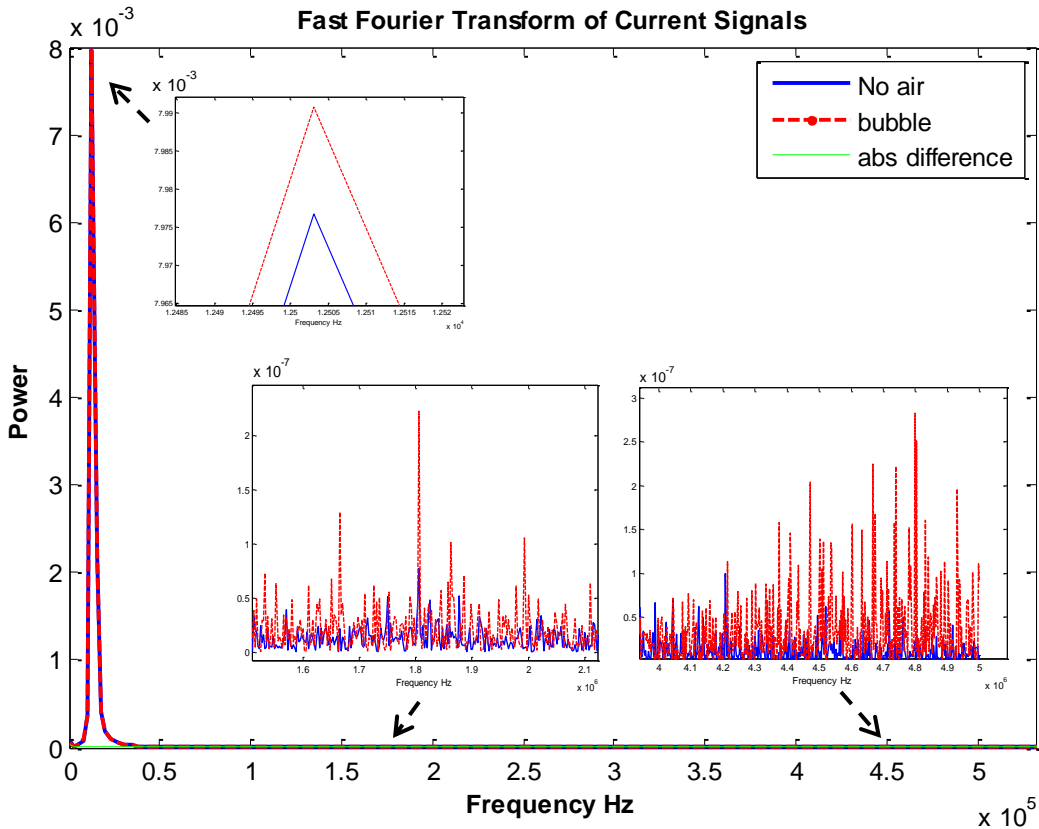


Figure 5-38 Fast Fourier Transform of signals in Figure 0 37 displaying differences in Fourier components

Changes in the PZT current in the presence of a bubble are clearly observed. The high frequency components observed in Figure 5-37 are illustrated in Figure 5-38. Additional frequencies began appearing at 100 kHz. Figure 5-38 illustrates two ranges, displaying maximum frequency differences for this trial; around 1.8 and 4.5 MHz. High frequency components observed in these figures are characteristic of measurements taken in acoustic chambers as a result of bubbles or non-degassed water (Cancelos et al., 2010).

Higher harmonics were studied applying Eq. (5.10). After analyzing the injection of 60 bubbles, 73% of these demonstrated ratios higher or lower than the ratio calculated without bubbles. In general (approximately 70% of the studied cases), the harmonics ratios were greater than one. Future studies should correlate the magnitude of higher harmonic components to the

magnitude of the first harmonic. Therefore, obtaining a ratio higher than one, can be solely attributed to the presence of a bubble and not to fluctuations in the PZT current. Measurements uncertainties are mostly introduced by changes that might occur in the PZT as a result of changes in working conditions. Readings in the PZT involving measurements taken for example, 2 hours after continuous excitation, differ by a 5%.

Analyses were also performed on the obtained data applying Eq.(5.2) and Eq.(5.8). Whereas when utilizing higher order harmonics sums (Eq. 5.10), when applying Eq.(5.8) only 42% of trials (91 trials) presented total harmonic differences greater than the ratio calculated in the absence of bubbles. When analyzing sums of all harmonic components, the first harmonic is around 3 orders of magnitude greater than other components therefore these supports the analysis of higher order harmonics in future bubble identification methods. The use of Eq. (5.2) which would take into consideration individual contributions of current values, demonstrated ratios which a higher difference than those obtained in the absence of bubbles in 71% of trials. Figure 5-39 illustrates a summary of results obtained in this manner. An overall increasing trend is observed for bubbles greater than 0.87mm. After this value, a decreasing trend is obtained. This effect could lead to bubble sizing detection algorithms. Additional tests must be carried out in order to present accurate conclusions relating bubble size. The observed trend should be object of further study. These current fluctuations should be differentiated form current fluctuations in the PZT ring in order to associate this trend with bubble size alone and not to variations in the artificial thigh admittance.

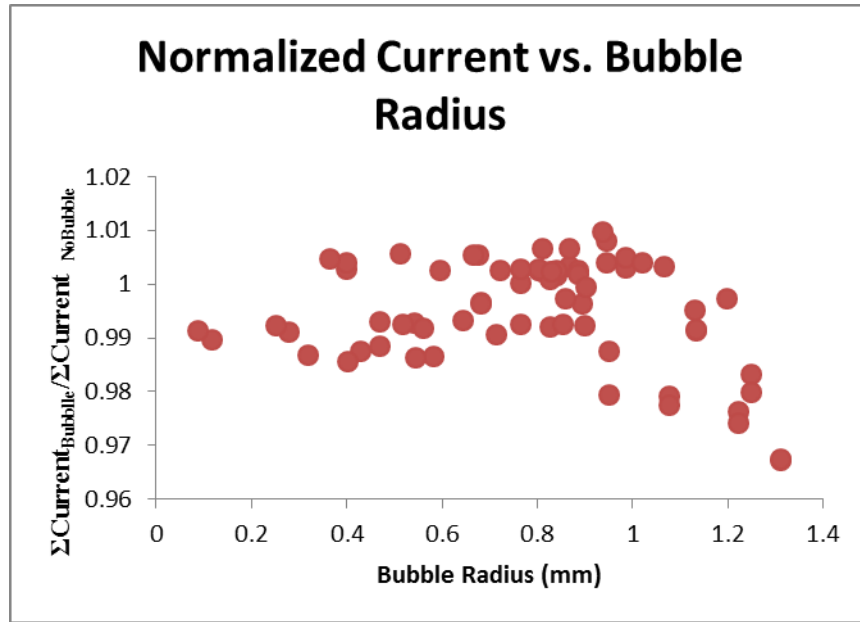


Figure 5-39 Normalized current trend, including the analysis of 61 bubbles

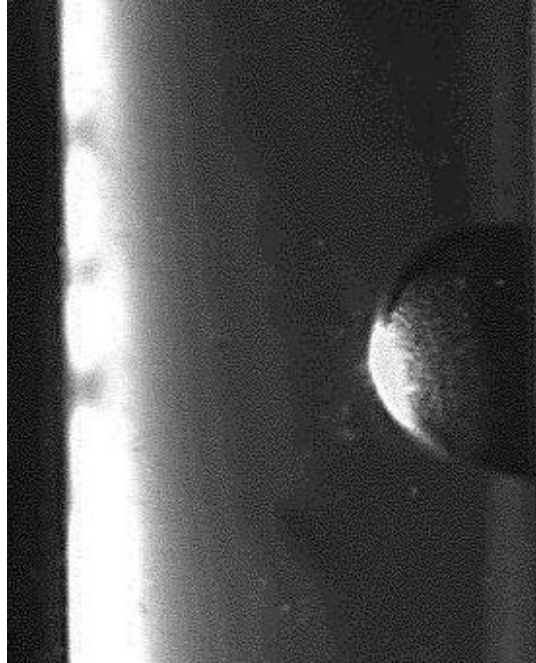
## 5.5 System response around bubble resonant frequency

Bubble oscillation is maximal near the resonance frequency of a bubble. At this frequency the bubble extinction cross section is also maximum. As discussed in Chapter 2, two bubble cross sections make up the bubble extinction cross section: the scattering cross section and the absorption cross section. At low excitation frequencies ( $\omega_{excitation} < \omega_0$ ) the bubble scattering cross section dominates over the absorption cross section. However, at higher frequencies ( $\omega_{excitation} > \omega_0$ ), thermal and viscous effects dominate the bubble behavior and the absorption cross section dominates the overall extinction coefficient. The bubble detection scheme presented in this section exploits these properties by precisely exciting the system at frequencies which coincide with the calculated resonance frequency of the injected bubble. Variations in measurement before and after the resonance threshold were expected as the change in the dominance of the scattering cross section to the absorption cross section occurred.

The same frequency response procedure described in section 3.4.1, for identifying the resonance frequency of the artificial thigh was performed with readings being taken in both the PZT ring and the pill microphone. The range of working frequencies was chosen around this determined value. As discussed in Chapter 2 and Chapter 3, bubble oscillation will experience a translational phase change when crossing the resonance frequency threshold. Thus it was expected that beside the bubble scattering properties being maximized at resonance, this change in the oscillation phase angle oscillation would also produce some measureable effect, captured by the transducers during this analysis. According to the results obtained and discussed so far, it was expected that signal scattering would be maximized in the presence of the bubble; this would lead to measuring a reduction in gain. In addition, phase angles are expected to increase in comparison to frequency responses measured in the absence of bubbles. Similar methods were studied by Phelps and Leighton (1996), although they insonated bubbles near their resonance frequency, this method was used to study bubble harmonics as a bubble identification method.

### **5.5.1 Piezoelectric Ring Response**

Figure 5-40 shows a bubble of 1 mm average radius. Radius measurements were taken vertically and horizontally. According to the Minnaert equation the resonance frequency of this bubble is approximately 5.5 kHz. Figure 5-41 and Figure 5-42 show an example of consistent results obtained with this method. As described in section 3.5.5 after injecting and trapping the bubble in the inner tubes, the bubble was sized with the high speeds cameras. Following this measurement, a frequency response analysis was carried out around the determined bubble resonance frequency.



**1 mm**

**Figure 5-40 Bubble around which frequency response analysis was carried out**

As observed in Figure 5-41 there is an admittance decrease in the presence of the bubble. This decrease was observed in a total of 31 trials carried out. A decrease in admittance identifies a change in the properties of the system in the presence of bubbles, which results as an increase in the electrical resistance resulting in a lower current measured in the PZT ring. Other consistent results can be seen in the instability of the phase angles values in the presence of bubbles.

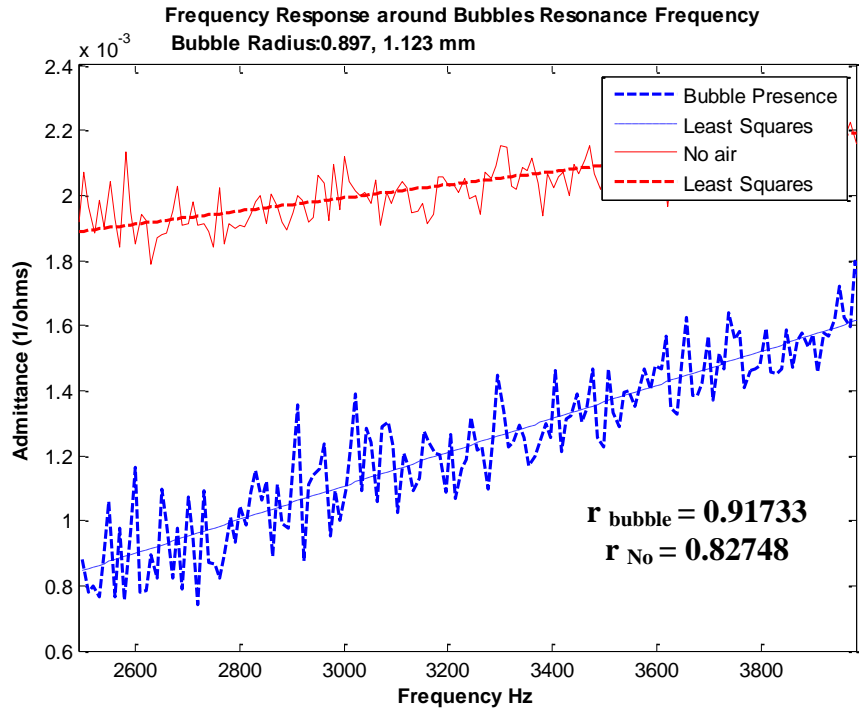


Figure 5-41 Admittance in the PZT decreases upon sensing a bubble due to signal attenuation which intensifies damping. A higher correlation coefficient is also measured. ( $r_{\text{bubble}} > r_{\text{No}}$ )

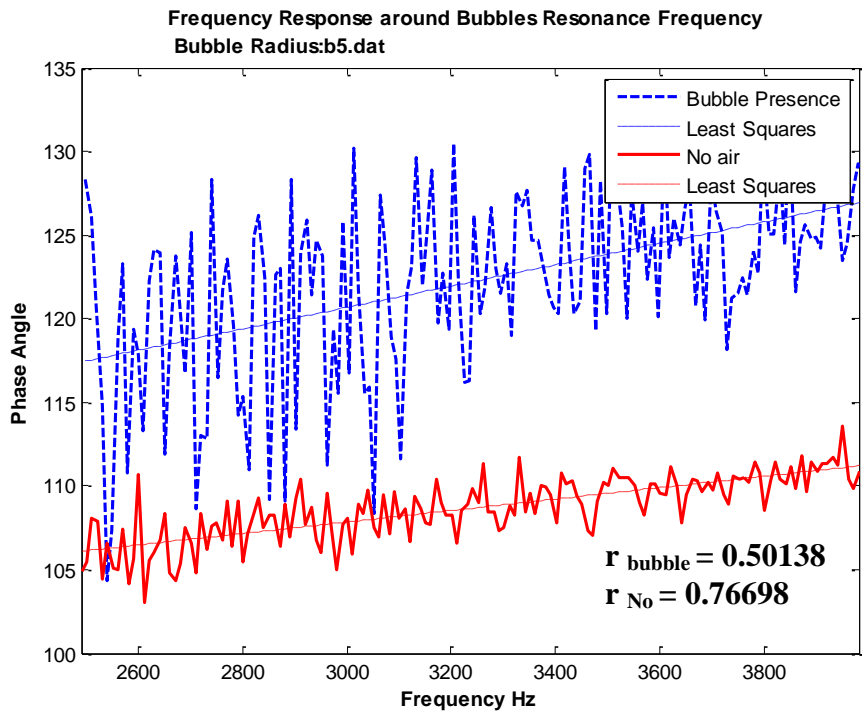
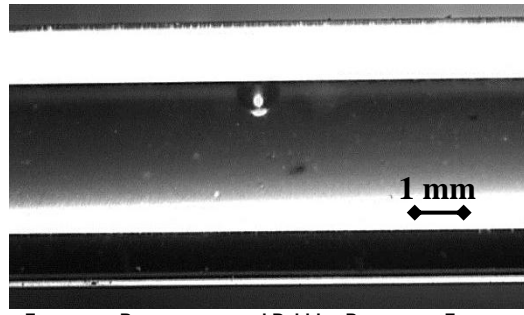


Figure 5-42 Phase angle variations due to changes in electrical inductance in the properties of the media due to the presence of a bubble. Higher correlation coefficient is calculated without bubbles. ( $r_{\text{No}} > r_{\text{bubble}}$ )

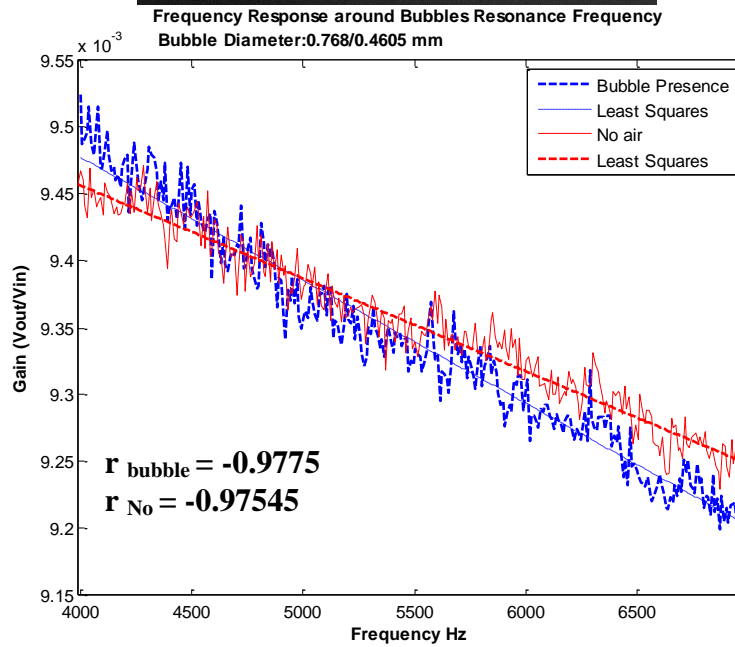
After observing a linear trend in admittance as a function of frequency for 1 to 10 kHz, a linear regression was carried out using the least squares method in order to compare measurements carried in the presence of bubbles with the response obtained in their absence. After performing the linear regression, the Pearson product-moment correlation coefficient (typically denoted by  $r$ ) was inspected in order to confirm the effect of the bubble on the linear dependence between the variables: admittance, phase angle and frequency. 80 % out of the 46 trials reveal when inspecting admittance trends, Pearson's  $r$  is closer to a value of one in the presence of bubbles. On the other hand 83% of trials display a Pearson's  $r$  closer to one in the absence of bubbles when measuring phase angle trends. These results indicate that admittance values are less dispersed in the presence of bubbles. This is due to the signal damping induced by the bubble. This bubble damping effect is likewise reflected in the increased dispersion observed in phase angles.

This type of analysis was carried out with signals measured by in the pill microphone transducers as well. Up to date inconclusive results have been obtained. Approximately 50% of thirty trials display similar trends corresponding to correlation coefficient. Additional trials must be carried out to confirm this behavior. Figure 5-43 (A) shows an example of one of the bubbles around which a frequency response analysis was carried out. Figure 5-43 (B) and Figure 5-43 (C) show the pill microphone response in the presence of the described bubble. Comparison of both signals displays similar trends to those observed when this kind of analysis was carried out with readings in the PZT ring. The adverse trend concerning correlation coefficients is illustrated in Figure 5-44. Further trials must be performed to confirm the behavior dominating pill microphone readings in this type of analysis.

A)



B)



C)

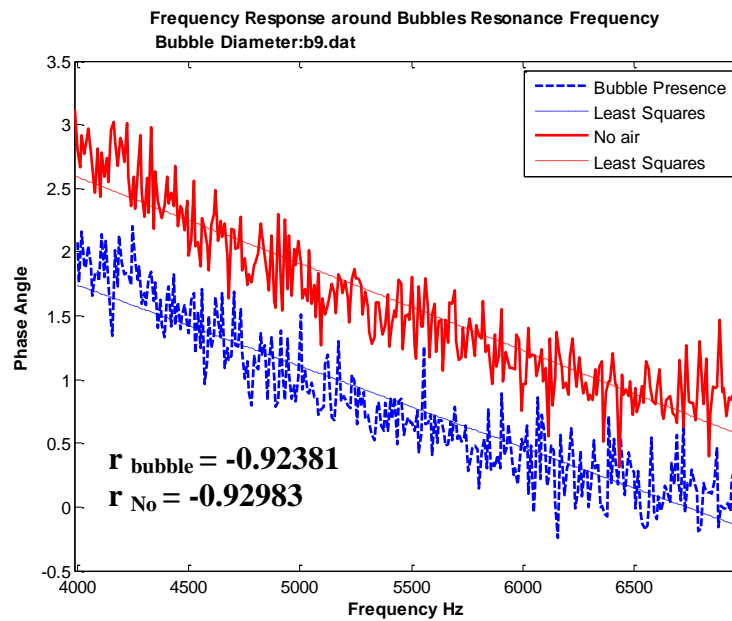
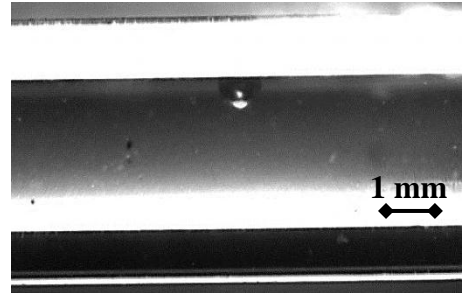
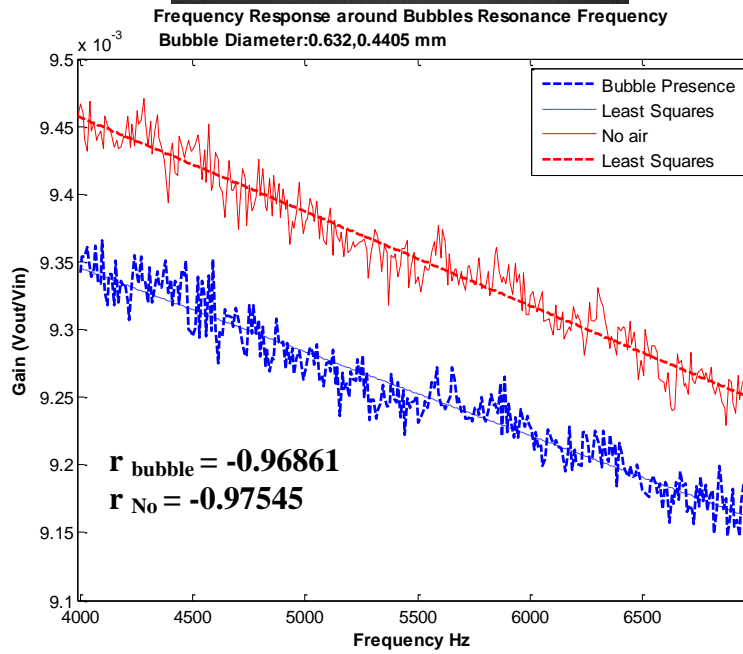


Figure 5-43 A) Bubble object of analysis, radius: 0.6 mm Gain (B) and phase angle (C) in the pill microphone displaying similar correlation coefficients to the PZT ring analysis

A)



B)



C)

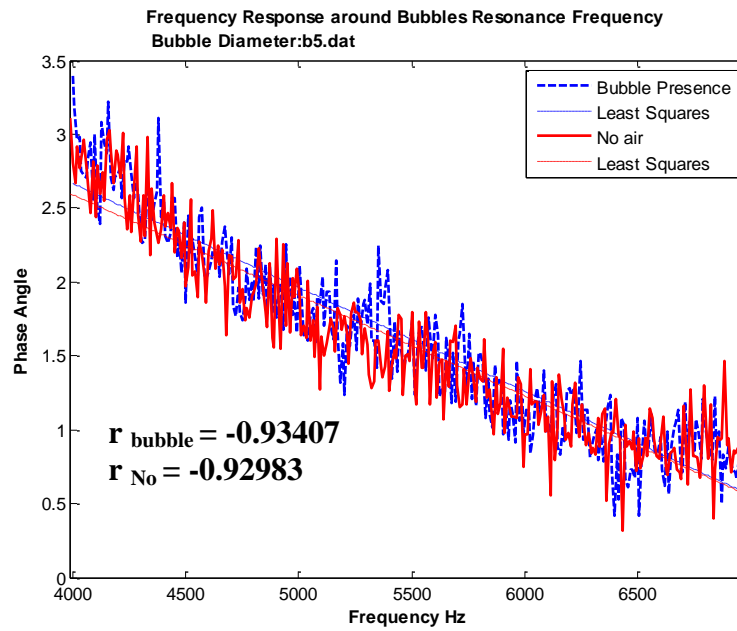


Figure 5-44 A) Bubble object of analysis, radius: 0.6 mm Gain (B) and phase angle (C) in the pill microphone displaying adverse trend in correlation coefficients in comparison to the PZT ring analysis

The standard deviations of gain and phase angle measurements were also calculated. Gain and phase angle measurement experienced a decrease in 90% and 71% of the cases respectively.

## **5.6 Closing Remarks**

This chapter has extensively discussed the response of the artificial thigh to the presence of bubbles. Detailed analyses of the capabilities of the proposed bubble detection method have been examined. The potential of the individual components: the pill microphones and the PZT ring, to respond to changes in the system corresponding to the presence of bubbles within the artificial thigh structure have been studied.

The proposed system based on the knowledge of acoustic chambers proved to be effective in the entrapment of bubbles. Bubble entrapment was necessary in order to carry out readings in the presence of bubbles. The pill microphone responded to the presence of multiple simultaneous bubbles within the inner tubes; similar results have been obtained by other researchers, however these results marked the viability of the proposed method. Concerning the detection of a single bubble within the artificial thigh, analyzing the contribution of individual voltage values in comparison to the signal obtained in the absence of bubbles (Eq. 5.1), proved to be the most effective method. This occurs because the bubble will not have an effect on the fundamental frequency interpreted by the transducer; the transducer will rather respond to higher frequency components which are included in this summation. 87% of the analyzed results demonstrated ratios higher than the limits established by measurements taken in the absence of bubbles. In relation to the pill microphone transducer, when used as an effective bubble detection method, the most reliable results were obtained when analyzing total summations of

the Fourier components (section 5.3.2.3.2.1). This method, distinguished 94% of the cases with bubbles.

Pill microphone bubble detection capabilities reflect the necessity of accurate readings in the absence of bubbles. These readings would define the boundaries of readings that can be obtained in the absence of bubbles; later to be compared to the readings obtained with bubbles. These boundaries might need to be constantly updated in order to adapt to changes in the artificial thigh structure which might occur as a result of changes in working conditions. Pill microphone readings were carried out in a time range of one micro second approximately. This time range should be expanded in order to capture transient effects in the artificial thigh as a result of bubble oscillation. In addition pill microphone response in relation to bubble size is still an object of further studies.

Measuring current values in the PZT ring proved to be 100% effective in slug flow detection. Measuring current and phase angle fluctuation in the PZT ring has been observed to have accurate bubble detector capabilities if the capture of readings is correctly timed with the passage of a bubble. This method could result in an effective bubble counter. The PZT ring also proved to be 80% effective when responding to individual bubbles who are insonated in a frequency close to their respective resonance frequencies.

## 6 CONCLUSIONS AND FUTURE WORK

### 6.1 Conclusions

The present study has shown the feasibility of adapting the acoustic chamber concept and implementing it as a bubble detecting device. For the purpose of this study, a PZT ring was fed a continuous sinusoidal signal. The potential of the individual components: the pill microphones and the PZT ring, to respond to changes in the system corresponding to the presence of bubbles within the artificial thigh structure have been experimentally and numerically studied.

Measuring current values in the PZT ring proved to be 100% effective in slug flow detection. Measuring current and phase angle fluctuations in the PZT ring has been observed to have accurate bubble detecting capabilities if the captured readings are correctly timed with the passage of a bubble. The only drawback in this technique is that current and phase angle peaks were attributed to the passage of a bubble near the actuation area of the PZT ring; thus requiring a moving bubble. This method could result in an effective bubble counter. Numerical simulations substantiate the possibility of obtaining an algorithm relating air pocket volume to the electrical impedance in the PZT ring. In addition, the PZT ring also proved to be 80% effective when responding to individual, non-moving bubbles insonated at a frequency close to their respective resonance frequencies.

Concerning the second component of the proposed acoustic method, the pill microphone clearly responded to the presence of multiple simultaneous bubbles within the inner tubes. Concerning the detection of a single bubble within the artificial thigh, the most reliable results were obtained when analyzing total summations of the Fourier components. These method, distinguished 94% of the cases with bubbles. A drawback of this technique is that pill microphone bubble detection capabilities reflect the necessity of accurate readings in the absence

of bubbles. These readings would define the boundaries of readings that can be obtained in the absence of bubbles; later to be compared to the readings obtained with bubbles. These boundaries might need to be constantly updated in order to adapt to changes in the artificial thigh structure which might occur as a result of changes in working conditions.

Furthermore, the proposed system proved to be effective in the entrapment of bubbles. Bubble entrapment was necessary in order to carry out readings in the presence of bubbles. The potential of the Bjerknes force as a bubble driver was studied numerically implementing a linearized form of the Bjerknes force and Raleigh-Plesset equation in a complicated geometry. The experimental measurements confirm that our numerical model can be used to predict bubble translation at specific frequencies. Bubble entrapment through the use of sonic waves was accomplished in an experimental model for bubble dynamics research. The radial Bjerknes force pushed the bubble towards the tube walls while the longitudinal Bjerknes force determined the entrapped vertical position at particular pressure nodes.

As demonstrated by Bjerknes, bubbles subjected to an acoustic field are expected to travel either up or down the pressure gradients towards the nodes or antinodes of pressure depending on their radius and the frequency at which the system is being driven. Therefore, knowing the pressure profile at specific frequencies it is possible to identify locations at which the bubble would most likely translate to. Experimentally it was observed that the bubble position within the test section was altered by the driving frequency. Therefore, frequencies were obtained which drove the bubble in the positive and negative  $z$  direction. By carefully selecting the frequencies it was possible to manipulate the bubble towards selected positions. The behavior of the bubble was numerically explained and agreed with Bjerkness known theory of bubble dynamics. From these experiments it can also be concluded that the overall behavior of

the bubble is dominated by fluid pressure gradients and not by pressure fluctuations induced by structural deformation.

## **6.2 Future Work**

In this work, a device has been proposed that could function as an air bubble detector in the blood vessels of human explorers. If the device is to have this anticipated use, a more complicated structure that simulates the human thigh should be constructed. The new design should take into consideration the use of materials that possess mechanical properties that are closer to those of real life models. All components should be scaled. The use of a gel outside the inner tubes instead of water could be used as artificial soft tissue. In addition, a material simulating a skin layer between the PZT ring, the pill microphone and the artificial thigh, should be identified.

Concerning bubble generation, greater control over the size and amount of bubbles should be pursued. The use of automated systems, such as automated syringe pumps would be useful to achieve this control. Procedures for bubble sizing should also be improved. The use of two high speed cameras should be considered, to effectively carry out bubble sizing.

Additional studies should be performed on the pill microphone fluctuations in order to report the effect of bubbles on pill microphone voltages taking into consideration the overall contribution of possible voltage fluctuations under the same experimental conditions. This would lead to an improved correlation between pill microphone voltage and bubble presence, reducing false positives. The time range of the pill microphone readings should be expanded in order to capture transient effects in the artificial thigh that result from bubble oscillation. In addition, pill microphone response in relation to bubble size should continue to be an object of further studies. The possibility that bubble presence can be performed by placing multiple pill

microphones around the structure and correlating their response to bubble presence and size could be investigated.

In experiments with current and phase angle measurements in the PZT ring, future experimentation should target automatic methods that quantify peaks in current and phase and that associate these peaks with the passage of a bubble. Future studies should also correlate the magnitude of higher harmonic components with the magnitude of the first harmonic. If a correlation is shown to exist, this would imply that the increase in harmonics is due to the presence of a bubble, and not to fluctuations in the PZT current.

## 7 REFERENCES

- (1907). *Admiralty Report: Deep Water Diving*. London: His Majesty's Stationary Office.
- Akhatov, I., Mettin, R., Ohl, C., Parlitz, U., & Lauterborn, W. (1997). Bjerknes force threshold for stable single bubble sonoluminescence. *Phys. Rev. E*, 3747-3750.
- Apfel, R. (1984). Acoustic cavitation inception. *Ultrasonics*, 25-28.
- Auld, B. (1990). *Acoustic Fields and Waves in Solids, Vols. I and II, 2nd ed.* Malabar, FL: Krieger Pub Co.
- Axisa, F., & Antunes, J. (2007). *Modelling of Mechanical Systems Fluid-Structure Interaction*. Great Britain: Elsevier Ltd.
- Badash. (2008, July 1). *Third Age Articles*. Retrieved May 25, 2009, from <http://www.thirdage.com/health-wellness/decompression-sickness-caisson-disease-altitude-sickness-dysbarism-the-bends-dcs>
- Balldin, U., Pilmanis, A., & Webb, J. (2002). Pulmonary decompression sickness at altitude: early symptoms and circulating gas emboli. *Aviat Space Environ Med*, 996-9.
- Bollinger, B., Wilbur, J., Donoghue, T., Knaus, S., Magari, P., Alvarenga, D., et al. (2009). Dual-frequency ultrasound detection of stationary microbubbles in tissue. *Undersea Hyperb Med*, 127-136.
- Bove, A. (1997). *Bove and Davis' Diving Medicine*. Philadelphia: Saunders.
- Boycott, A., Damant, C., & Haldane, J. (1908). The Prevention of Compressed Air Illness. *Journal of Hygiene*, 342-443.
- Brennen, C. (1995). *Cavitation and Bubble Dynamics*. New York: Oxford University.
- Broome, J., Dick, E., & Dutka, A. (1994). Multifocal CNS hemorrhage as a cause of recompression treatment failure in a pig model of neurological decompression illness (DCI). *Undersea Hyperb Med*, 69.
- Brown, J., & Antuñano, M. J. (2010). *Federal Aviation Administration*. Retrieved June 27, 2010, from <http://www.faa.gov/pilots/safety/pilotsafetybrochures/media/dcs.pdf>
- Bruneasu, M. (2006). *Funamentals of Acoustics*. London: ISTE Ltd.
- Buckey, J., Knaus, D., Alvarenga, D., Kenton, K., & Magan, P. (2005). Dual-frequency ultrasound for detecting and sizing bubbles. *Acta Astronaut*, 1041-1047.

- Cancelos, S., Moraga, F., Lahey, R., & Bouchilloux, P. (2005). The design of acoustic chambers for bubble dynamics research. *Multiphas Sci Tech*, 257-291.
- Cancelos, S., Moraga, F., Lahey, R., Shain, W., & Parsons, R. (2010). The effect of acoustically-induced cavitation on the permeance of a bullfrog urinary bladder. *J Acoust Soc Am*, 2726-38.
- Chapel, M. (2006). Modelling and Measurement of Bubbles in Decompression Sickness. *PHD*. St. Hugh's and Linacre Colleges, University of Oxford.
- Command, U. N. (2006). *US Navy Diving Manual, 6th revision*. United States.
- Comsol, M. (2011). *Acoustic Module User's Guide*. Massachusetts.
- Daniels, S. (1984). Ultrasonic monitoring of decompression procedures. *Philos Trans R Soc Lond B Bio Sci*, 153-75.
- Daniels, S., Davies, J., Paton, W., & Smith, E. (London). The Detection of Gas Bubbles in guinea-Pigs after Decompression from air Saturation Dives Using Ultrasonic Imaging. *Journal of Physiology*, 369-383.
- Dick, A., & Massey, E. (1985). Neurologic presentation of decompression sickness and air embolisms in sport divers. *Neurology*, 667-71.
- Eller, A. (1970). Damping constants of pulsating bubbles . *J Acoust Soc Am*, 1469-1470.
- Ellis, K. (2000). Human Body Composition: In Vivo Methods. *Physiol Rev*, 649-680.
- Enflo, B., & Hedberg, C. (2004). *Theory of Nonlinear Acoustics in Fluids*. New York: Kluwer Academic Publishers.
- Flam, E., Berry, S., Coyle, A., Dardik, H., & Raab, L. (1996). Blood-Flow Augmentation of Intermittent Peumatic Compression Systems Used for the Prevention of Deep Vein Thrombosis Prior to Surgery. *The American Journal of Surgery* , 312-315.
- Fowler, B., Ackles, K., & Porlier, G. (1985). Effects of inert gas narcosis on behavior-a critical review. *Undersea Biomed. Res.*, 369-402.
- Francis, T., & Gorman, D. (1993). Pathogenesis of decompression disorders. In P. Bennett, & D. Elliott, *The Physiology and Medicine of Diving, 4th* (pp. 454-480). London: WB Saunders.
- Francis, T., & Mitchell, S. (2003). Manifestations of decompression disorders. In A. Brubakk, & T. Neuman, *Bennett and Elliott's Physiology and Medicine of Diving 5th edition* (pp. 578-99). London: Saunders.

- Francis, T., Griffin, J., Homer, L., Pezeshkpour, G., Dutka, A., & Flynn, E. (1990). Bubble-induced dysfunction in acute spinal cord decompression sickness. *J Appl Physiol*, 1368-75.
- Francis, T., Pearson, R., Robertson, A., Hodgson, M., Dutka, A., & Flynn, E. (1988). Central nervous system decompression sickness: latency of 1070 human cases. *Undersea Biomed Res*, 403-17.
- Fromy, B., Legrand, M., Abraham, P., Ileftheriotis, G., Cales, P., & Saumet, J. (1997). Effects of positive pressure on both femoral venous and arterial blood velocities and the cutaneous microcirculation of the forefoot. *CardioVascular Research*, 372-376.
- Fujishima, S. (2000). The history of ceramic filters. *IEEE transactions on ultrasonics, ferroelectrics and frequency control*, 1-7.
- Gaitan, D., Crum, L., Church, C., & Roy, R. (1992). Sonoluminescence and bubble dynamics for a single, stable, cavitation bubble. *J. Acoust. Soc. Am*, 3166-3183.
- Gibby, G. (1993). Real-time automated computerized detection of venous air emboli in dogs. *J Clin Monit*, 354-63.
- Gray, T. (2009). *The Elements: A Visual Exploration of Every Known Atom in the Universe*. New York: Black Dog & Leventhal Publishers.
- guide, S. o. (n.d.). *Diseases, Bubble Related*. Retrieved Jan 16, 2012, from Brooksidepress.org: <http://www.brooksidepress.org/Products/OperationalMedicine/DATA/operationalmed/Manuals/SeaBee/Fieldcombatopssection/BubbleRelatedDiseases.pdf>
- Haberman, R. (2003). *Applied Partial Differential Equations 4th ed*. Prentice Hall.
- Holzfluss, J., Ruggeberg, M., & Mettin, R. (1998). Boosting Sonoluminescence. *Phys. Rev. Lett*, 1961-1964.
- Jallul, S., Osman, A., & El-Masry, W. (2006). Cerebro-spinal decompression sickness: report of two cases. *Spinal Cord*45, 116-120.
- Jenderka, K., & al, e. (2002). Detection and Sizing of Micro Bubbles in Streaming Fluids with Ultrasound. *Proc. IEEE Sensors*, 528-531.
- Joiner, J. (2009). *NOAA Diving Manual, 4th Edition*. Arizona: Best Publishing Pages.
- Jordan, R., & Ounaies, Z. (2001). *Piezoelectric ceramics characterization*. Hampton, Virginia: ICASE, NASA Langley Research Center.
- Kao, J., Wang, J., Xu, J., & Attinger, D. (2007). A bubble-powered micro-rotor: conception, manufacturing, assembly and characterization. *J Micromech. Microeng.*, 2454-2460.

- Lam, K., Drake, J., & Cobbold, R. (1999). Non-invasive cerebrospinal fluid shunt flow measurement by Doppler Ultrasound using ultrasonically excited bubbles: A feasibility study. *Ultrasound Med. Biol.*, 371-389.
- Lee, K., Lee, J., Won, J., Rhee, K., & Chung, S. (2011). Micromanipulation using cavitation microstreaming generated by acoustically oscillating twin bubbles. *Sens. Actuators A: Phys*, doi:1.1016/j.sna.2011.11.037.
- Leighton, T. (1994). *The Acoustic Bubble*. San Diego: Academic Press.
- Leighton, t., Ramble, D., & Phelps, A. (1995). Comparison of the abilities of multiple acoustic techniques for bubble detection. *Proc. of the Inst. of Acoust.*, 149-160.
- Leighton, T., Waltont, A., & Pickworth, M. (1990). Primary Bjerknes Forces. *European journal of Physics*, 47-50.
- Liu, R., Yang, J., Pindera, M., Athavale, M., & Grodzinski, P. (2002). Bubble-induced acoustic micromixing. *Lab. Chip* 2, 151-157.
- Machay, R., & Rubisson, J. (1978). Decompression studies using ultrasonic imaging of bubbles. *Trans Biomed Eng*, 537-544.
- Mathieu, D. (2006). *Handbook on Hyperbaric Medicine*. Netherlands: Springer.
- Mettin, R., Akhatov, I., Parlitz, U., Ohl, C., & Lauterborn, W. (1997). Bjerknes forces between small cavitation bubbles in a strong acoustic field. *Phys. Rev. E*, 2924-2931.
- Miller, D. (1984). Gas body activation. *Ultrasonics*, 261-269.
- Miller, D., Williams, A., & Gross, D. (1984). Characterization of cavitation in a flow-through exposure chamber by means of a resonant bubble detector. *Ultrasonics*, 224-230.
- Minnaert, M. (1933). On musical air-bubbles and sounds of running water. *Philos. Mag.* , 235-248.
- Nishi, R. (1993). Doppler and ultrasonic bubble detection. In P. Bennett, & E. D, *The Physiology and Medicine of Diving, 4th* (pp. 433-453). London: Saunders.
- Nishi, R., Brubakk, A., & Eftedal, O. (2003). Bubble Detection. In A. Brubakk, & T. Neuman, *Bennett and Elliott's Physiology and Medicine of Diving, 5th edition* (pp. 501-529). London: Saunders.
- Orfanidis, S. (2008). *Electromagnetic Waves and Antennas*. NJ: Piscataway.
- Ozeri, S., Shmilovitz, D., & Fainguelernt, J. (2006). Ultrasonic Air Bubble Detection Employing Signal Processing Techniques. *ISIE*, 2840-2845.

- Phelps, A., & Leighton, T. (1996). High-resolution bubble sizing through the detection of the subharmonic response with a two-frequency excitation technique. *J. Acoust. Soc. Am*, 1985-1992.
- Pollock, N., Natoli, M., Gerth, W., Thalman, E., & Vann, R. (2003). Risk of decompression sickness during exposure to high cabin altitude after diving. *Aviat Space Environ Med*, 1163-8.
- Proakis, J., & Manolakis, D. (1998). *Tratamiento Digital de Señales: Principios, Algoritmos y Aplicaciones*. Madrid: Prentice Hall.
- Reuter, M., tetzlaff, K., Hutzelmann, A., Fritsch, G., Steffens, J., & Bettinghausen, E. (1997). MR imaging of the central nervous system in diving-related decompression illness. *Acta Radiol*, 940-4.
- Rubissow, G., & mackay, R. (1971). Ultrasonic imaging of in vivo bubbles in decompression sickness. *Ultrasonics*, 225-34.
- Shaikh, N., & Ummunisa, F. (2009). Acute management of vascular air embolism. *J Emerg Trauma Shock*, 180-5.
- Sharifian, H., & Gharekhanloo, F. (2003). Evaluation of Average Diameter of lower extremity veins in acute and chronic Thrombosis and comparison with normal persons by doppler sonography. *Medica Iranica Acta*, 180-182.
- Spencer, M., & Johanson, D. (1974). Investigation of New Principles for Human Decompression Schedules Using the Doppler Ultrasonic Blood Bubble Detector. *Institute for Environmental Medicine and Physiology*.
- Steele, G., & Bramblett, C. (1988). *The Anatomy and Biology of the Human Skeleton*. TX: Texas A&M University Press.
- Towne, D. (1967). *Wave Phenomena*. New York: Dover Publications.
- Treiber, F., Papavassiliou, D., Gutin, B., Malpass, D., Wang, Y., Islam, S., et al. (1997). Determinants of Endothelium-dependent femoral artery vasodilation in Youth. *Psychosomatic Medicine*, 376-381.
- Tsao, H.-K., & Koch, D. (1997). Observations of high Reynolds number bubbles interacting with a rigid wall. *Physics of Fluids*, 44-56.
- Vann, R., Grimstad, J., & Nielsen, C. (1980). Evidence for Gas Nuclei in Decompressed Rats. *Undersea Biomedical Research*, 107-112.
- Vaughan, P., & Leeman, S. (1989). Acoustic cavitation revisited. *Acustica*, 109-119.

- Warren, L., Djang, W., Moon, R., Camporesi, E., Salle, D., & Anthony, D. (1988). Neuroimaging of scuba diving injuries to the CNS. *AJR Am J Roentgenol*, 1003-8.
- Wilson, O. (1988). *Introduction to Theory and Design of Sonar Transducers*. California: Peninsula .
- Yamakoshi, Y., & Koganezawa, M. (2005). Bubble manipulation by self-organization of bubbles inside ultrasonic wave. *Jpn J Appl Phys*, 4583-4587.

## Appendix A

### A.1 Linearized Wave Equation Derivation

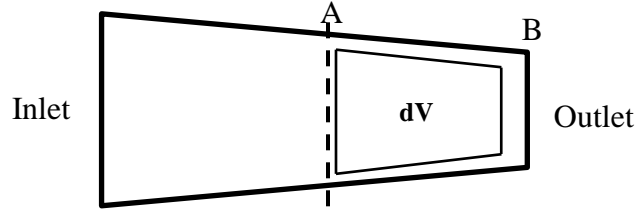


Figure A-1 Flow of water through nozzle; fluid velocity varies with location and with time.

In order to derive a linearized expression for the wave equation, we must begin by deriving the known Euler's Equation. Consider Figure A-1 with only one inlet and outlet as specified. We will consider a fluid element with volume  $dV$  moving between points A and B. Newton's second Law will be applied considering negligible viscous and thermal effects becoming:

$$\left(\rho \vec{g} - \vec{\nabla} P(\vec{r}, t)\right) \cdot dV = \rho dV \cdot \vec{a} \quad (\text{A.1.1})$$

In Eq. (A.1.1)  $\vec{a}$  represents the analyzed acceleration of the element and  $\vec{g}$  is the acceleration of gravity acting downward. Equation (A.1.1) can be generalized to include any particular body force. Also, considering that at any defined location, the fluid velocity  $\vec{v}$ , is expected to vary both as function of time and space, the particle velocity can be written in terms of two partial differentials:

$$\Delta \vec{v} = \Delta \vec{v}_r + \Delta \vec{v}_t = \left. \frac{\partial \vec{v}}{\partial \vec{r}} \right|_t d\vec{r} + \left. \frac{\partial \vec{v}}{\partial t} \right|_{\vec{r}} dt \quad (\text{A.1.2})$$

Furthermore, taking the time derivative of Eq. (A.1.2) and introducing the so called "material derivative" in order to more conveniently express the fluid particle acceleration:

$\vec{a} = \dot{\vec{v}} + (\vec{v} \cdot \vec{\nabla})\vec{v}$ . The pressure in the fluid under inviscid conditions can then be expressed in terms of the flow and taking into account the addition of body forces ( $\phi_B$ ), we arrive at the well-known Euler's equation:

$$-\vec{\nabla}P(\vec{r}, t) = \rho(\dot{\vec{v}} + (\vec{v} \cdot \vec{\nabla})\vec{v} + \vec{\nabla}\phi_B) \quad (\text{A.1.3}).$$

Incompressible flow assumptions and negligible body forces will lead to a linear form of Euler's equation:

$$\vec{\nabla}p(\vec{r}, t) = -\rho_0\dot{\vec{v}} \quad (\text{A.1.4}).$$

These assumptions are valid, if the only component of the liquid pressure with a finite spatial variation is the acoustic component. This would suggest that particle velocity perturbations are small, therefore:  $|(\vec{v} \cdot \vec{\nabla})\vec{v}| \ll |\dot{\vec{v}}|$ . Also, since the flow is assumed incompressible, spatial density variations are deemed negligible suggesting a constant density value:  $\rho_0$ . Finally, all these assumptions, including the negligible effects of body forces, leads to consider  $\vec{\nabla}P$  equaled to  $\vec{\nabla}p$ ;  $p$  being the acoustic pressure.

Moving on, providing terms relating spatial density variations are negligible the equation of continuity states:

$$\frac{\dot{\rho}}{\rho} + \vec{\nabla} \cdot \vec{v} = 0 \quad (\text{A.1.5})$$

Taking the derivative of Eq. (A.1.5) with respect to time, eliminating second order terms, taking the divergence of Eq. (A.1.4) and combining, we obtain an expression relating the change in pressure to a density value which fluctuates in time:

$$\frac{\dot{p}}{\rho} - \frac{\nabla^2 p}{\rho_0} = 0 \quad (\text{A.1.6})$$

By introducing the definition of adiabatic bulk modulus it is possible to transform this expression into an equation relating only spatial and time varying pressure fluctuations. The adiabatic bulk

modulus, describes the change in pressure experienced by the fluid in response to a change in volume; for a fixed fluid mass, it can be defined in terms of density as:  $B = \rho \frac{\partial p}{\partial \rho}$ . The bulk modulus expression can be derived with respect to time. Under the assumption that  $(\rho/\rho_0) \ll 1$  and introducing the speed of sound as  $c$ , the linearized wave equation in pressure is obtained:

$$\nabla^2 p = \frac{1}{c^2} \ddot{p} \quad (\text{A.1.7})$$

## A.2 Wave Equation generalization for any material described by a bulk modulus

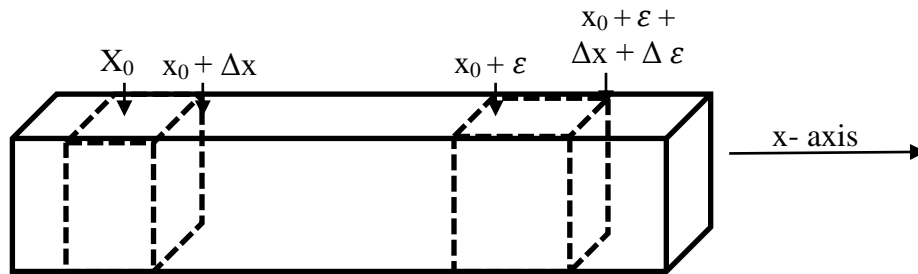


Figure A-2 Bulk Material

The wave equation will be deduced pertaining to the case of longitudinal waves in a continuum. This equation describes any material behaving as a compressible continuum and characterized by bulk modulus  $B$  where the material Bulk modulus is defined as:

$$B = -V \frac{dp}{dV} \quad (\text{A.2.1})$$

where  $V$  is the element volume and  $dp$  is the change in pressure from an equilibrium value in response to a change in volume  $dV$ .

Consider a sound wave travelling through a material. Due to the passage of a sound wave, particles located at equilibrium positions  $x=x_0$  and  $x=x_0 + \Delta x$  will be displaced to final positions  $x=x_0 + \epsilon$  and  $x=x_0 + \epsilon + \Delta x + \Delta \epsilon$ . For a constant cross sectional area  $A$ , the induced

volume change of  $\Delta V = A\Delta\varepsilon$ . Replacing these values into the material bulk modulus definition; Eq. (A.2.1) becomes:

$$B = -A\Delta x \frac{\Delta p}{A\Delta\varepsilon} \quad (\text{A.2.2})$$

Performing a similar force analysis on the element in Figure A-19 the material force will be opposite to the particle displacement and the net force experienced by the element between positions  $x=x_0$  and  $x=x_0 + \Delta x$  due to the passage of the wave would be:

$$F(x_0) - F(x_0 + \Delta x) = -\Delta x \frac{\partial F}{\partial x} \quad (\text{A.2.3})$$

evaluated at  $x=x_0$ . If we combine Eq. (A.2.3) with Newton's Second Law of motion, the right side of Eq. (A.2.3) could also be expressed in terms of displacement as  $\rho A\Delta x\ddot{\varepsilon}$ . Recalling absolute pressure is defined as force per unit area and the change in acoustic pressure expressed as  $dp$ , force at location  $x=x_0$  could be expressed as:  $F(x_0) = Adp$ . Combining this expression with Eq. (A.2.2) and Eq. (A.2.3) we obtain an expression describing the propagation of a longitudinal bulk wave:

$$\ddot{\varepsilon} = \frac{B}{\rho} \frac{\partial^2 \varepsilon}{\partial x^2} \quad (\text{A.2.4}).$$

Mathematically the type of behavior defined by Eq. (A.2.4) represents any function  $\varepsilon$  which propagates as a wave like function. Therefore this can be extended to any material which behaves as a compressible medium with a given bulk modulus.

### A.3 Bjerknes Force Derivation

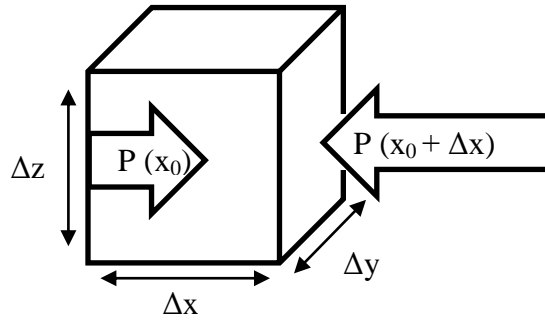


Figure A-3 stationary volume element in the fluid

Referring to Figure A-3, the pressure acting over the face located at  $x=x_0$  is  $p(x_0)$  and the pressure acting over the face located at  $x=x_0 + \Delta x$  is  $p(x_0) + (\delta p/\delta x)\Delta x$ . The  $x$  component of the force will be defined by the difference in pressure, multiplied by the cross sectional area of the face perpendicular to the  $x$  direction. Therefore the  $x$  component of the radiation force will be:

$$F_x = -\left.\frac{\partial p}{\partial x}\right|_{x_0} \Delta x \Delta y \Delta z \quad (\text{A.3.1})$$

The same analysis can be carried out for the other two axes. If pressure values vary sinusoidally in time, the net force on the body corresponds to the time average of the total force. Thus we obtain the known expression for the Bjerknes force:

$$\langle \vec{F} \rangle = -\langle V \vec{\nabla} P \rangle \quad (\text{A.3.2})$$

## A.4 Piezoelectric Material Supplementary Information

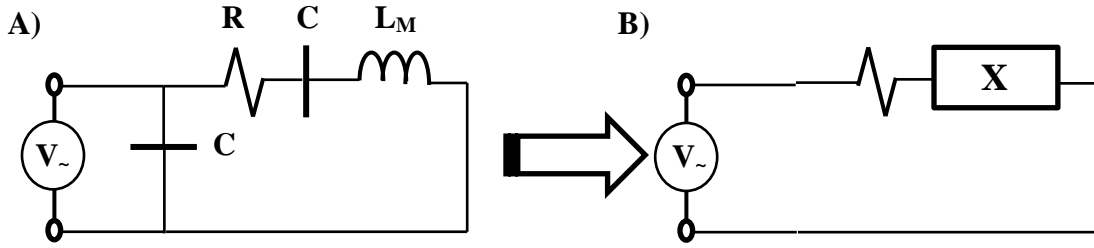


Figure A-4 A) Simplified equivalent R-L-C circuit describing motional impedance B) Form of equivalent circuit separating elements with real and imaginary components

A very simple equivalent electrical circuit for a piezoelectric-type transducer is shown in Figure A-4. This model is only valid in the neighborhood of the mechanical resonance. This type of R-L-C circuit in parallel with another capacitance is often used to simulate the motional impedance of this type of materials. By simple inspection the admittance of the circuit presented in Figure A-4 is:

$$Y_{eq} = j\omega c_0 + \frac{1}{R_M + j\left(\omega L_M - \frac{1}{\omega C_M}\right)} \quad (\text{A.4.1})$$

In Eq. (A.4.1) the usual convention applied to electrical circuits is used, where  $Y_{eq}$  denotes the equivalent admittance,  $c_0$  refers to the blocked capacitance,  $R_M$ ,  $L_M$ ,  $C_M$  denote material resistance, inductance and capacitance, and  $\omega$  denotes the angular frequency equal to  $2\pi f$ .

In order to separate into imaginary and real parts, some algebra is needed.

Expanding the bottom part of Eq. (A.4.1):

$$Y_{eq} = j\omega c_0 + \frac{1}{R_M + j\left(\frac{\omega^2 L_M C_M - 1}{\omega C_M}\right)} \quad (\text{A.4.2})$$

By multiplying the right side of Eq. (A.4.2) by its conjugate:

$$Y_{eq} = j\omega c_0 + \frac{R_M - j\left(\frac{\omega^2 L_M C_M - 1}{\omega C_M}\right)}{R_M^2 + \left(\frac{\omega^2 L_M C_M - 1}{\omega C_M}\right)^2} \quad (\text{A.4.3})$$

By separating the right hand fraction of Eq. (A.4.3), the material admittance can be separated into real and imaginary parts:

$$\underbrace{\frac{R_M}{R_M^2 + \left(\frac{\omega^2 L_M C_M^{-1}}{\omega C_M}\right)^2}}_{\text{Real Part}} + j\omega C_0 - \underbrace{\frac{j\left(\frac{\omega^2 L_M C_M^{-1}}{\omega C_M}\right)}{R_M^2 + \left(\frac{\omega^2 L_M C_M^{-1}}{\omega C_M}\right)^2}}_{\text{Imaginary Part}} \quad (\text{A.4.4})$$

The real part of Eq. (A.4.4) is known as the conductance of the material, while the imaginary part is the susceptance. The angle between the imaginary and real components is known as the phase angle. All these quantities are functions of the excitation angular frequency  $\omega$ . Conductance, susceptance, admittance and phase angle are shown in Figure A-5 through Figure A-8 as functions of frequency for a piezoelectric material having a characteristic mechanical resonance:

$$f = \frac{\omega}{2\pi} = \frac{1}{\sqrt{LC}} = 10 \text{ kHz}, \text{ obtained from the following properties:}$$

$$\begin{aligned} C_0 &= 1.5 \text{ nF} \\ R_M &= 3.2 \text{ kohms} \\ C_M &= 0.5 \text{ nF} \\ L_M &= 0.5 \text{ H} \end{aligned}$$

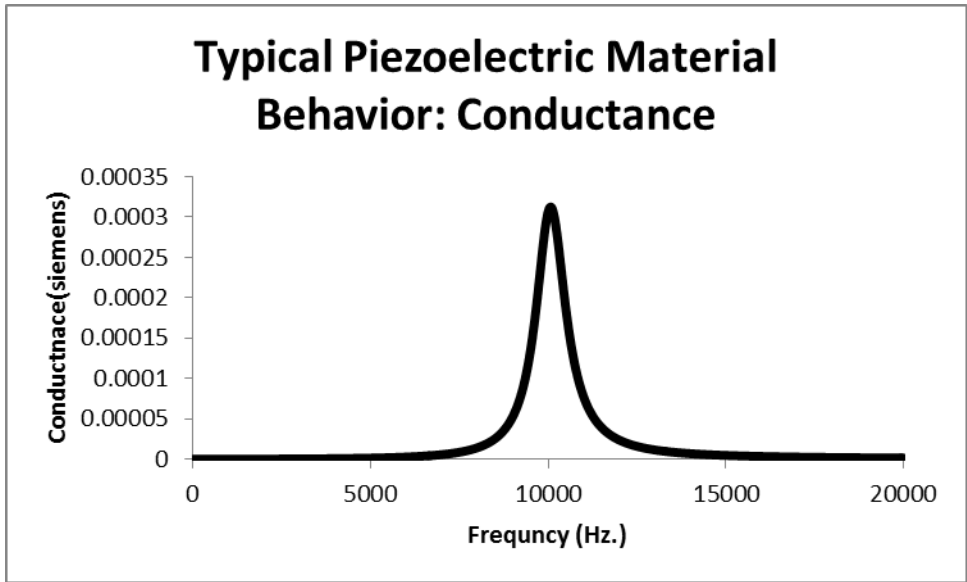


Figure A-5 Piezoelectric material conductance

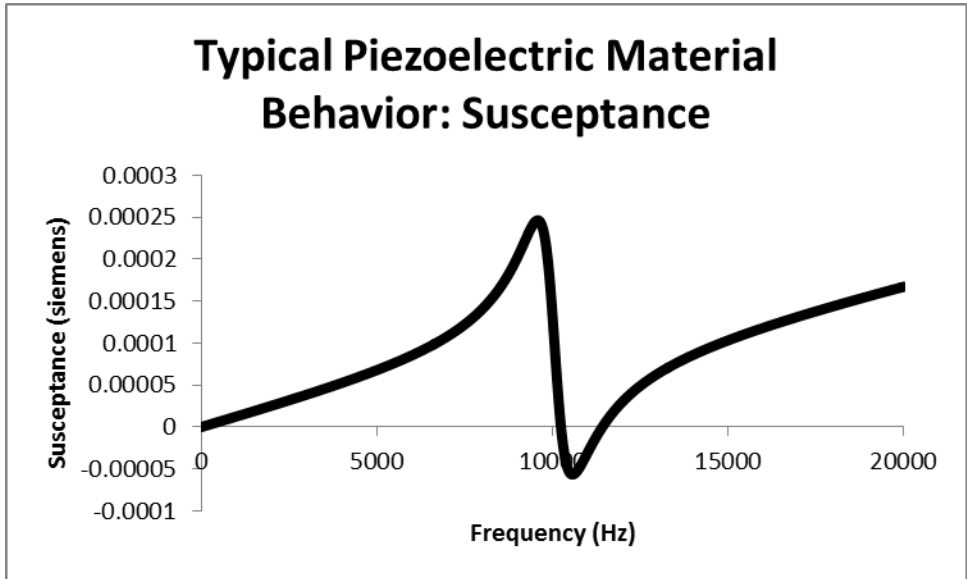


Figure A-6 Piezoelectric material susceptance

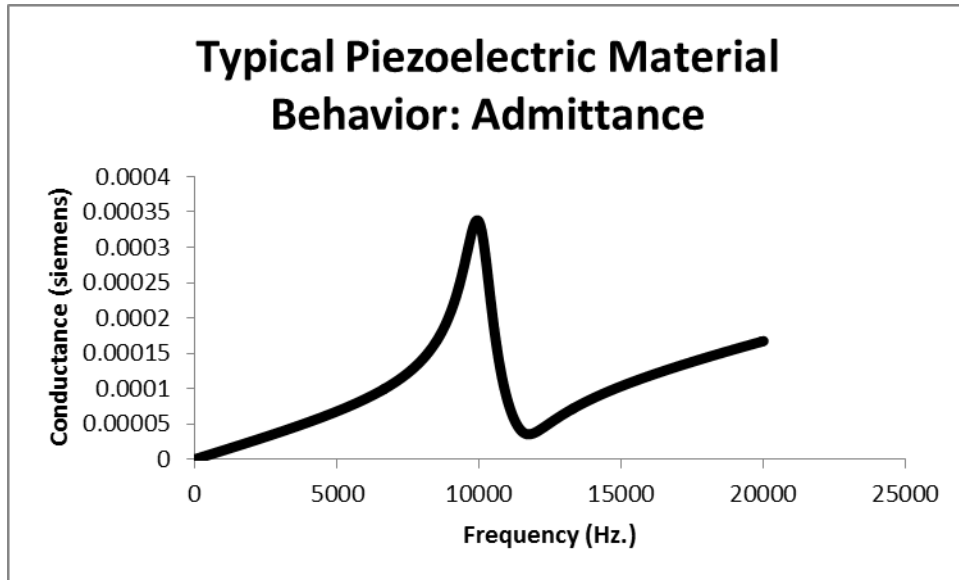


Figure A-7 Piezoelectric material admittance

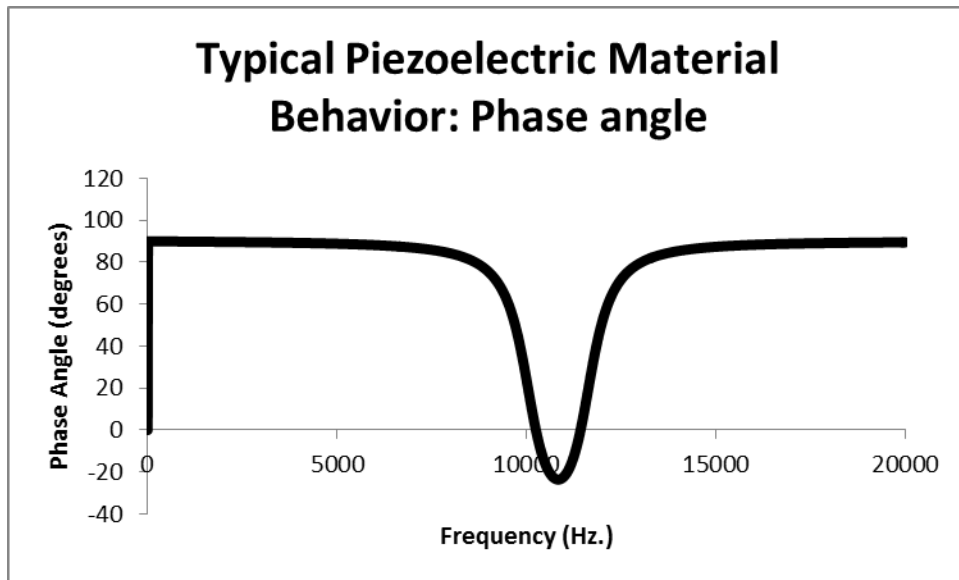


Figure A-8 Piezoelectric material phase angle

Note the behavior of each variable near the material resonance frequency. In addition to this, if the resistance is set to zero, all material behavior would then be a result of the imaginary components. These are shown in Figure A-9 through Figure A-11. As can be observed when the material resistance is zero, susceptance and admittance values are only defined at resonance and are equal. Also, the phase angle is either ninety or minus ninety degrees.

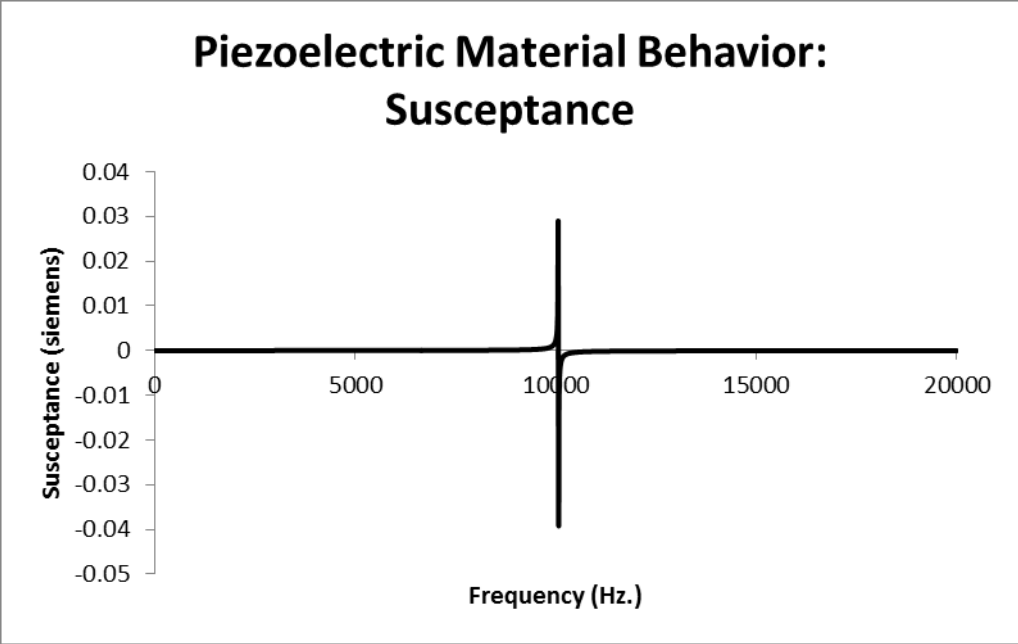


Figure A-9 Piezoelectric material susceptance,  $R_M=0$

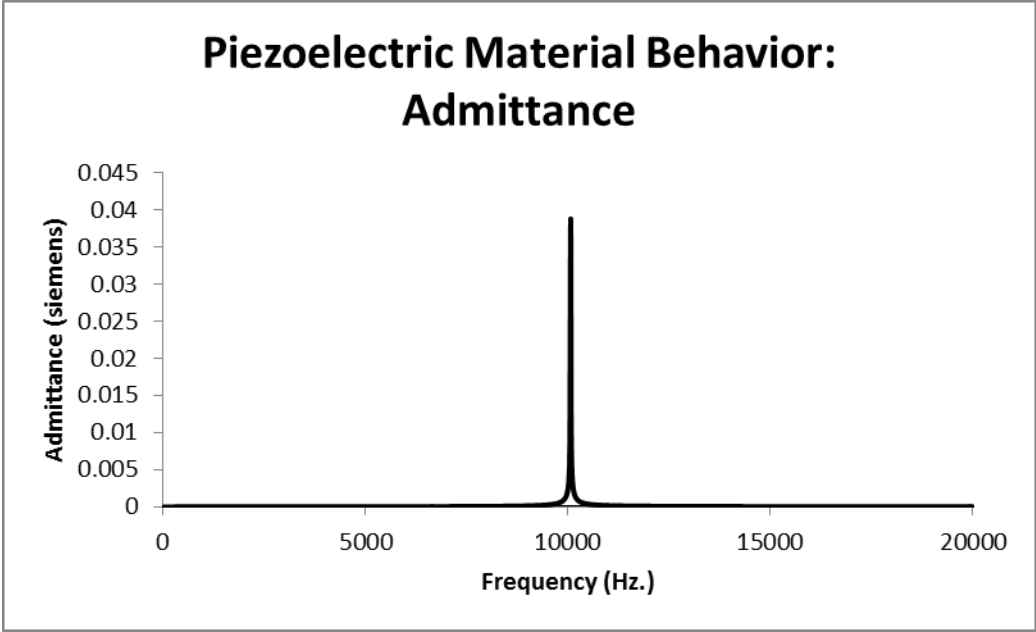


Figure A-10 Piezoelectric material admittance,  $R_M=0$

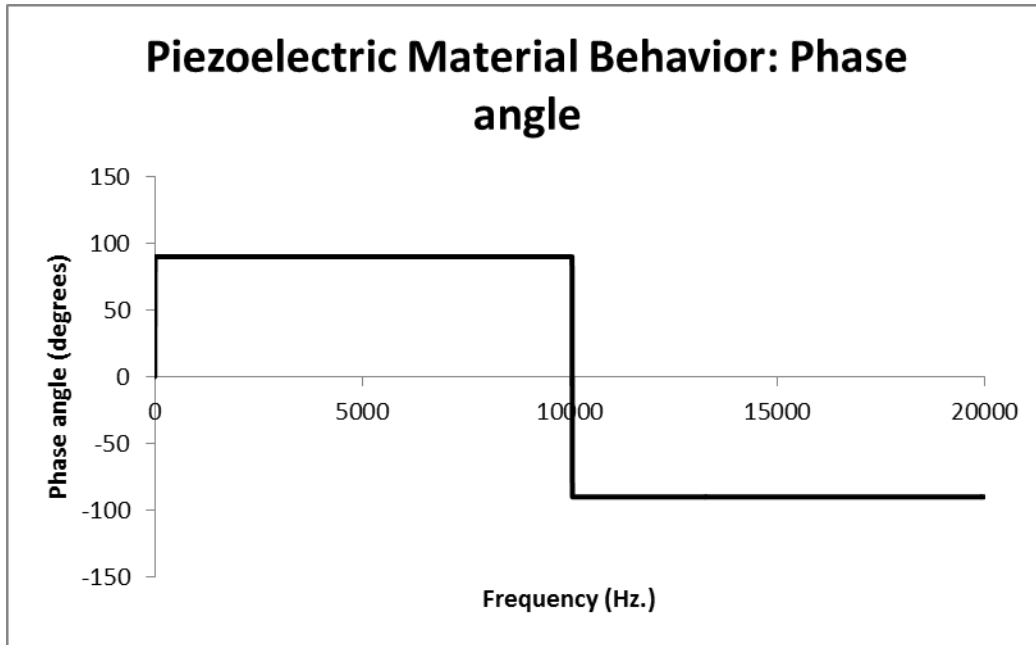


Figure A-11 Piezoelectric material phase angle,  $R_M=0$

As can be expected, changing any of these material properties shown in of the electrical components shown in Figure A-4 will have an effect on the amplitude of the value, the resonance frequency or even both. Chapter 5 presents figures displaying these resonance frequency shift and amplitude changes as a result of material property changes. The analysis presented involving the description presented for the circuit in Figure A-4 can be extended in order to describe any system in terms of these electrical properties. Like changes in the property of an electrical component provide overall changes in these electrical readings, similarly changes in the properties of the domain of the system will results in overall changes in measurements involved in these electrical measurements.

## A.5 Understanding the forced lightly damped oscillator through an electrical circuit comparison

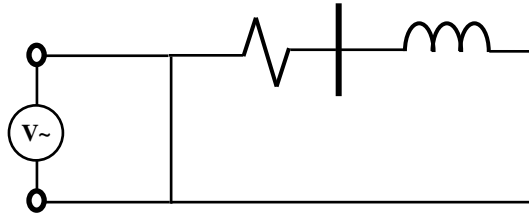


Figure A-12 Electrical circuit containing a resistor, a capacitor and an inductor in parallel; resembling a lightly damped oscillator system.

The dynamic of bubble behavior, in simple terms, can be described as the behavior of a slightly damped linear oscillator. In this section this behavior will be discussed in electrical terms through the circuit presented in Figure A-12.

The voltage in the electrical components: resistor, capacitor, and inductor can be described according to:

$$V_R = iR = \dot{Q}R \quad (\text{A.5.1})$$

$$V_C = \frac{Q}{C} \quad (\text{A.5.2})$$

$$V_L = L \frac{di}{dt} = L\ddot{Q} \quad (\text{A.5.3})$$

where  $Q$  is the charge ( $\pm$ ).

Therefore the total node to node voltage is:

$$V_T = V_R + V_C + V_L \quad (\text{A.5.4})$$

Replacing Eq. (A.5.1) through Eq. (A.5.3) into Eq. (A.5.4):

$$V_T = \dot{Q}R + \frac{Q}{C} + L\ddot{Q} \quad (\text{A.5.5})$$

Comparing Eq. (A.5.5) to the equation obtained from a bob-spring system Eq. (A.5.6) it is possible to relate mechanical and electrical elements:

$$F(t) = m\ddot{x} + c\dot{x} + kx \quad (\text{A.5.6})$$

where  $c$  is the viscous damping coefficient,  $k$  is the spring stiffness and  $F(t)$  is an applied external force. The  $1/C$  term resembles the material stiffness  $k$ , therefore is a function of the young modulus. The electrical inductance corresponds to the system mass inertia and it relates to  $R$  in Eq. (A.5.5).

If a harmonic solution is assumed where:  $V_T = V_0 e^{j\omega t}$  and  $i = i_0 e^{j\omega t}$  and replacing in Eq.(A.5.5):

$$V_0 = i_0 \left( R + j\omega L - \frac{j}{\omega C} \right) \quad (\text{A.5.7})$$

Finally, as a result of the assumed solution:

$$V_T = \left( i_0 \left( R + j\omega L - \frac{j}{\omega C} \right) \right) e^{j\omega t} \quad (\text{A.5.8})$$

## A.6 Analytical solution for the wave equation in a hollow water cylinder surrounded by air

In order to validate numerical results obtained with Comsol Multiphysics regarding the normal modes of oscillation of our test section, we obtained an analytical solution for a simplify geometry.

Consider,

$$P = p_0 + p \quad (\text{A.6.1})$$

where  $p_0$  represents the equilibrium pressure in the absence of acoustic perturbations and  $p$  is the acoustic pressure. In order to obtain a solution for the acoustic pressure, the wave equation (Eq. (A.6.2)) is solved in the fluid domain presented in Figure A-13. This geometry portrays a hollow water cylinder

$$\nabla^2 p = \frac{1}{c^2} \frac{\partial^2 p}{\partial t^2} \quad (\text{A.6.2})$$

Boundary conditions:

$$\left. \begin{aligned} p(r_1, z, t) &= 0 \\ p(r_2, z, t) &= 0 \\ p(r, 0, t) &= 0 \\ p(r, L, t) &= 0 \end{aligned} \right\} \quad (\text{A.6.3})$$

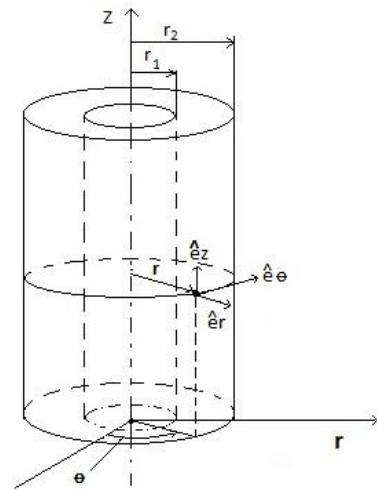


Figure A-13 Geometry of the problem

where  $c$  is the speed of sound,  $t$  is refers to time,  $r_1$ ,  $r_2$ , and  $L$  are the inner and outer radius and the length of the cylinder respectively. Water is contained between the radii  $r_1$  and  $r_2$  of the

hollow cylinder (refer to Figure A-13). In cylindrical coordinates equation (A.6.2) can be written as

$$\frac{1}{r} \frac{\partial}{\partial r} \left( r \frac{\partial p}{\partial r} \right) + \frac{\partial^2 p}{\partial z^2} + \frac{1}{r^2} \frac{\partial^2 p}{\partial \theta^2} = \frac{1}{c^2} \frac{\partial^2 p}{\partial t^2} \quad (\text{A.6.4})$$

where by symmetry condition:  $\frac{\partial p}{\partial \theta} = 0$

Since the partial differential equation and the boundary conditions are linear and homogeneous, we can apply the separation variables method (Haberman 2003). Then, we define

$$P(r, z, t) = R(r)Z(z)T(t) \quad (\text{A.6.5})$$

Replacing Eq. (A.6.5) in Eq. (A.6.3) and Eq. (A.6.4), we obtain,

$$\frac{1}{R} \frac{d^2 R}{dr^2} + \frac{1}{Rr} \frac{dR}{dr} + \frac{1}{Z} \frac{d^2 Z}{dz^2} = \frac{1}{c^2 T} \frac{d^2 T}{dt^2} \quad (\text{A.6.6})$$

$$\left. \begin{array}{l} Z(0) = 0 \quad , \quad R(r_1) = 0 \\ Z(L) = 0 \quad , \quad R(r_2) = 0 \end{array} \right\} \quad (\text{A.6.7})$$

The left side of equation (Eq. (A.6.6)) is a function of  $r$  and  $z$  and the right side is a function of  $t$ .

Therefore, the only possibility is that both sides are equal constants.

Then, using constants  $\alpha$ ,  $\beta$ , and  $\lambda$ , in Eq. (A.6.6) the problem is converted into three sub-problems,

$$\underbrace{\frac{1}{R} \frac{d^2 R}{dr^2} + \frac{1}{Rr} \frac{dR}{dr}}_{-\lambda} + \frac{1}{Z} \frac{d^2 Z}{dz^2} = \underbrace{\frac{1}{c^2 T} \frac{d^2 T}{dt^2}}_{-\lambda}$$

$$\left. \begin{aligned} \frac{1}{R} \frac{d^2 R}{dr^2} + \frac{1}{Rr} \frac{dR}{dr} &= -\alpha \\ R(r_1) = 0, \quad R(r_2) &= 0 \end{aligned} \right\} \quad (\text{A})$$

$$\left. \begin{aligned} \frac{1}{Z} \frac{d^2 Z}{dz^2} &= \alpha - \lambda = -\beta \\ Z(0) = 0, \quad Z(L) &= 0 \end{aligned} \right\} \quad (\text{B})$$

$$\left. \begin{aligned} \frac{1}{c^2 T} \frac{d^2 T}{dt^2} &= -\lambda \\ p(r, z, 0) = f_0(r, z), \quad \frac{\partial p}{\partial t}(r, z, 0) &= g_0(r, z) \end{aligned} \right\} \quad (\text{C})$$

### Solving the sub problem A

From (A) we obtain,

$$\left. \begin{aligned} r \frac{d^2 R}{dr^2} + \frac{dR}{dr} + r\alpha R &= 0 \\ R(r_1) = 0, \quad R(r_2) &= 0 \end{aligned} \right\} \quad (\text{A.6.8})$$

The equation (A.6.8) represents a regular Sturm-Liouville eigenvalue problem(S-L) (Haberman 2003). Where the form of S-L is,

$$\frac{d}{dx} \left( P(x) \frac{d\phi}{dx} \right) + Q(x)\phi + \zeta\sigma(x) = 0$$

The boundary conditions must be linear and homogeneous. From eq. (A.6.8) we obtain,

$$r \left( r \frac{d^2 R}{dr^2} + \frac{dR}{dr} + \alpha r R \right) = 0$$

Where,

$$\varphi(x) = R(r) \quad P(x) = P(r) = r \quad Q(x) = Q(r) = \alpha r \quad \sigma(x) = \sigma(r) = 0$$

$r > 0$  Physical parameter

The Rayleigh quotient from S-L show that for problem (A) the eigenvalues  $\alpha$  are real and greater than or equal to zero (Haberman 2003).

Indeed, the Rayleigh quotient yields,

$$\alpha = \frac{-P(r)R \frac{dR}{dr} \Big|_{r_1}^{r_2} + \int_{r_1}^{r_2} \left( P(r) \left( \frac{dR}{dr} \right)^2 - Q(r)R^2 \right) dr}{\int_{r_1}^{r_2} R^2 \sigma(r) dr}$$

Simplifying, gives

$$\alpha = \frac{\int_{r_1}^{r_2} r \left( \frac{dR}{dr} \right)^2 dr}{\int_{r_1}^{r_2} r R^2 dr}, \quad \text{where } \left( \frac{dR}{dr} \right)^2 \geq 0, \quad r > 0, \quad R^2 > 0$$

Therefore,  $\alpha \geq 0$ , and  $\alpha < 0$  is not eigenvalue.

**Analyzing for  $\alpha = 0$**

Substituting  $\alpha = 0$  in equation (A.6.8) we obtain,

$$\frac{d}{dr} \left( r \frac{dR}{dr} \right) = 0, \quad \text{where the general solution is: } R(r) = C_1 \ln(r) + C_2.$$

Applying the boundary conditions from equation (A.6.8),

$$C_1 \ln(r_1) + C_2 = 0$$

$$C_1 \ln(r_2) + C_2 = 0$$

$$C_1 = 0 \text{ and } C_2 = 0$$

Therefore,  $\alpha = 0$  is a *trivial solution*.

**Analyzing for  $\alpha > 0$**

From (A.6.8), applying a change in variables:  $r' = r\sqrt{\alpha}$  we obtain the known Bessel differential equation,

$$r'^2 \frac{d^2 R}{dr'^2} + r' \frac{dR}{dr'} + r'^2 R = 0 \quad (\text{A.6.9})$$

The general solution of Eq. (A.6.9) is a combination of Bessel function of first and second kind of orders zero (Morse & Feshbach 1953).

$$R(r) = C_3 J_0(\sqrt{\alpha} r) + C_4 Y_0(\sqrt{\alpha} r) \quad (\text{A.6.10})$$

Applying the boundary conditions from Eq. (A.6.8)

$$R(r_1) = 0 \quad , \quad R(r_2) = 0$$

and using the following properties,

$$\frac{d}{dx}(J_0(cx)) = -cJ_1(cx) \quad \text{and} \quad \frac{d}{dx}(Y_0(cx)) = -cY_1(cx)$$

using the boundary condition  $R(r_1) = 0$  Eq. (A.6.10) can be written as:

$$C_3 J_0(\sqrt{\alpha} r_1) + C_4 Y_0(\sqrt{\alpha} r_1) = 0$$

$$C_3 = -C_4 \frac{Y_0(\sqrt{\alpha} r_1)}{J_0(\sqrt{\alpha} r_1)}$$

Using the second boundary condition  $R(r_2) = 0$  and substituting for  $C_3$

$$R(r_2) = C_4 \left[ \frac{-Y_0(\sqrt{\alpha} r_1)}{J_0(\sqrt{\alpha} r_1)} J_0(\sqrt{\alpha} r_2) + Y_0(\sqrt{\alpha} r_2) \right] = 0$$

$$C_4 \neq 0 \quad (\text{If } C_4 = 0, R(r) = 0 \rightarrow p(r, z, t) = 0 \text{ is trivial solution})$$

Then,

$$-Y_0(\sqrt{\alpha} r_1) J_0(\sqrt{\alpha} r_2) + Y_0(\sqrt{\alpha} r_2) J_0(\sqrt{\alpha} r_1) = 0$$

$$\text{We define, } F(\sqrt{\alpha}) = -Y_0(\sqrt{\alpha} r_2) J_0(\sqrt{\alpha} r_1) + Y_0(\sqrt{\alpha} r_1) J_0(\sqrt{\alpha} r_2)$$

The zeros of  $F$  are the  $\alpha_n$ , where  $\alpha_n$  is called  $n$ -th eigenvalue, and  $n=1,2,3,\dots$

Finally the solution for sub problem (A) is.

$$R(r) = C_{4n} \left[ \frac{-Y_0(\sqrt{\alpha_n} r_1)}{J_0(\sqrt{\alpha_n} r_1)} J_0(\sqrt{\alpha_n} r) + Y_0(\sqrt{\alpha_n} r) \right]$$

Where,

$\alpha_n$  is the zero of  $F(\alpha) = -Y_0(\sqrt{\alpha} r_2) J_0(\sqrt{\alpha} r_1) + Y_0(\sqrt{\alpha} r_1) J_0(\sqrt{\alpha} r_2)$  ,  $n = 1, 2, 3, \dots$

(A.6.11)

### ***Solving the sub problem (B)***

From (B)

$$\frac{d^2 Z}{dz^2} + \beta Z = 0 \quad , \quad \text{with} \quad Z(0) = 0 \quad , \quad Z(L) = 0$$

This problem is a S-L (Haberman 2003) which shows that the eigenvalue  $\beta$  is greater than or equal to zero.

Hence, using the characteristic polynomial method and simple integration we obtain the following general solutions for the sub problem (B).

$$\text{For } \beta = 0, \quad Z(z) = C_5 z + C_6 \quad (A.6.12)$$

$$\text{For } \beta > 0, \quad Z(z) = C_7 \cos(\sqrt{\beta} z) + C_8 \sin(\sqrt{\beta} z) \quad (A.6.13)$$

Applying the boundary conditions to equation (A.6.12), we can easily see that  $\beta = 0$  is a *trivial solution*.

Using the boundary conditions in equation (A.6.13),

$$Z(0) = C_7 \cos(\sqrt{\beta} 0) + C_8 \sin(\sqrt{\beta} 0) = 0 \quad \rightarrow \quad C_7 = 0$$

$$\text{Hence, } Z(z) = C_8 \sin(\sqrt{\beta} z)$$

$$Z(L) = C_8 \sin(\sqrt{\beta} L) = 0 \quad \rightarrow \quad C_8 \neq 0 \quad (\text{If } C_8 = 0, Z(z) = 0 \rightarrow p(r, z, t) = 0 \text{ is trivial solution})$$

Therefore,

$$\sin(\sqrt{\beta} L) = 0 \quad \rightarrow \quad \sqrt{\beta} L = m\pi \quad \text{since } \beta > 0, \quad m = 1, 2, 3, \dots$$

Finally the solution for sub problem (B) is.

$$Z(z) = C_{8m} \sin(\sqrt{\beta_m} z) \quad , \quad \text{Where} \quad \beta_m = \left(\frac{m\pi}{L}\right)^2 \quad , \quad m = 1, 2, 3, \dots$$

(A.6.14)

**Solving the sub problem (C)**

From (B) we have that  $\lambda = \beta + \alpha$  and because  $\alpha$  and  $\beta$  are real and greater than zero, this implies that  $\lambda > 0$ .

If, from (C) we define  $\omega^2 = \lambda c^2$  hence,

$$\omega = c\sqrt{\lambda} = c\sqrt{\beta + \alpha} \quad (A.6.15)$$

Replacing eq. (A.6.15) in eq. (B), gives

$$\frac{d^2 T}{dt^2} + \omega^2 T = 0$$

Using the characteristic polynomial method, we determinate the general solution as,

$$T(t) = C_{9m,n} \cos(\omega_{m,n} t) + C_{10m,n} \sin(\omega_{m,n} t) \quad , \quad \text{where} \quad \omega_{m,n} = c\sqrt{\beta_m + \alpha_n}$$

(A.6.16)

Finally replacing equations (A.6.11), (A.6.14), and (A.6.16) in (A.6.5), and considering all the non-trivial solutions, we obtain:

$$p(r, z, t) = \sum_{m=1}^{\infty} \sum_{n=1}^{\infty} \left\{ \left( \frac{-Y_0(\sqrt{\alpha_n} r_1)}{J_0(\sqrt{\alpha_n} r_1)} J_0(\sqrt{\alpha_n} r) + Y_0(\sqrt{\alpha_n} r) \right) \sin\left(\frac{m\pi}{L} z\right) [A \cos(\omega_{m,n} t) + B \sin(\omega_{m,n} t)] \right\}$$

$$\text{Where,} \quad \omega_{m,n} = c\sqrt{\left(\frac{m\pi}{L}\right)^2 + \alpha_n} \quad m, n = 1, 2, 3, \dots$$

$$\alpha_n \text{ is the zero of } F(\alpha) = -Y_0(\sqrt{\alpha} r_2) J_0(\sqrt{\alpha} r_1) + Y_0(\sqrt{\alpha} r_1) J_0(\sqrt{\alpha} r_2)$$

(A.6.17)

Specifying the two necessary initial conditions for the problem and applying the orthogonality method, we can determinate the constants  $A$  and  $B$  in equation (A.6.17).

$$\text{With } \psi_{m,n}(r, z) = \left( \frac{-Y_0(\sqrt{\alpha_n} r_1)}{J_0(\sqrt{\alpha_n} r_1)} J_0(\sqrt{\alpha_n} r) + Y_0(\sqrt{\alpha_n} r) \right) \sin\left(\frac{m\pi}{L} z\right)$$

$$p(r, z, 0) = \sum_{m=1}^{\infty} \sum_{n=1}^{\infty} \left\{ \psi_{m,n}(r, z) [A \cos(\omega_{mn} 0) + B \sin(\omega_{mn} 0)] \right\} = f_0(r, z)$$

$$\frac{\partial p}{\partial t}(r, z, 0) = \sum_{m=1}^{\infty} \sum_{n=1}^{\infty} \left\{ \psi_{m,n}(r, z) [-A \omega_{mn} \sin(\omega_{mn} 0) + B \omega_{mn} \cos(\omega_{mn} 0)] \right\} = g_0(r, z)$$

Applying orthogonality method we obtain,

$$A = \frac{\int_0^L \int_{r_1}^{r_2} f_0(r, z) \psi_{m,n}(r, z) dr dz}{\int_0^L \int_{r_1}^{r_2} \left\{ \psi_{m,n}(r, z) \right\}^2 dr dz} \quad B = \frac{1}{\omega_{m,n}} \frac{\int_0^L \int_{r_1}^{r_2} g_0(r, z) \psi_{m,n}(r, z) dr dz}{\int_0^L \int_{r_1}^{r_2} \left\{ \psi_{m,n}(r, z) \right\}^2 dr dz} \quad (\text{A.6.18})$$

In wave theory infinite  $\omega_{m,n}$  values exist, and are referred to as normal modes of oscillation or resonance modes. A specific case when  $m=1$  and  $n=1$  ( $\omega_{1,1}$ ) exists and is known as the *fundamental frequency*. Using the property of wave reflection (due to the pressure boundaries in our problem) and the interference phenomenon a standing pressure wave is obtained in the fluid produced by a permanent external excitation of frequency  $\omega_{m,n}$ . Therefore, from Eq. (A.6.17) and by taking  $A = 1$ , the general form of a standing pressure wave can be written as,

$$\boxed{p(r, z, t) = \left( \frac{-Y_0(\sqrt{\alpha_n} r_1)}{J_0(\sqrt{\alpha_n} r_1)} J_0(\sqrt{\alpha_n} r) + Y_0(\sqrt{\alpha_n} r) \right) \sin\left(\frac{m\pi}{L} z\right) \cos(\omega_{m,n} t)} \quad (\text{A.6.19})$$

The first zeros of the function  $F(\alpha)$  were obtained for values of  $r_1 = 0.02\text{m}$  and  $r_2 = 0.065\text{m}$  .

For  $L = 0.3\text{m}$  and  $c = 1490.56 \text{ m/s}$ , the first 4 resonance frequencies are shown in

Table A-1.

**Table A-1** Frequencies obtained analytically for the first 4 resonance modes in Hz.

$A$	$m$	$f$
$\alpha_1=4717.258$	1	16481.80
$\alpha_1=4717.258$	2	17034.22
$\alpha_2=19316.552$	1	33064.63
$\alpha_2=19316.552$	2	33343.43

Where,  $f = \frac{\omega_{m,n}}{2\pi} = \frac{c}{2\pi} \sqrt{\left(\frac{m\pi}{L}\right)^2 + \alpha_n}$  (A.6.20)

Figures A-14 to Figure A-17 present the acoustic pressure fields for the first 4 resonance modes.

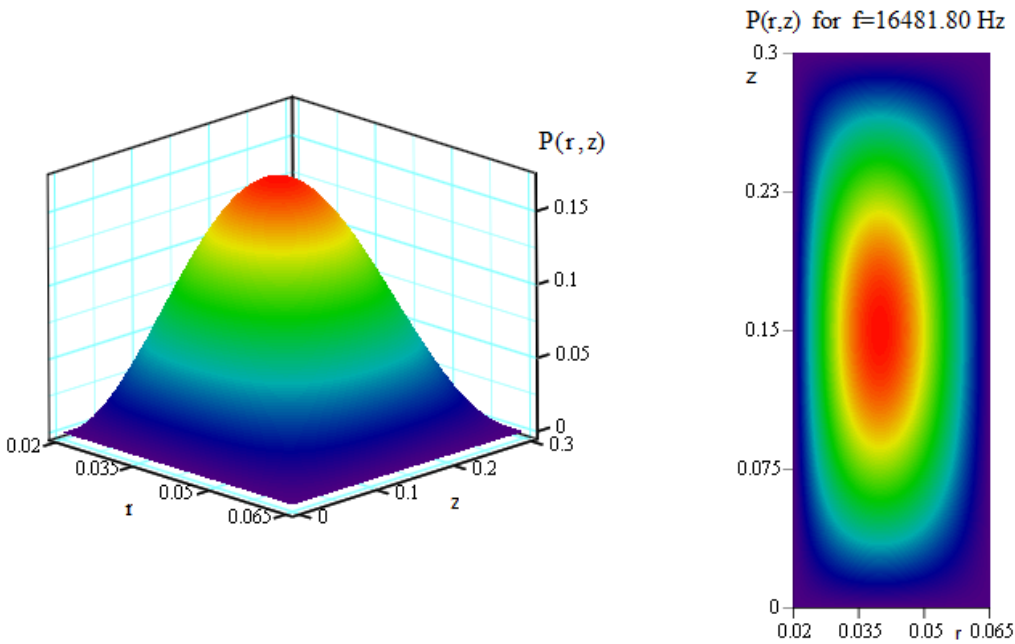


**Figure A-14** Analytical acoustic pressure field for  $m=1$ ,  $n=1$ ,  $c=1490.56\text{m/s}$  and  $f=16481.80\text{ Hz}$

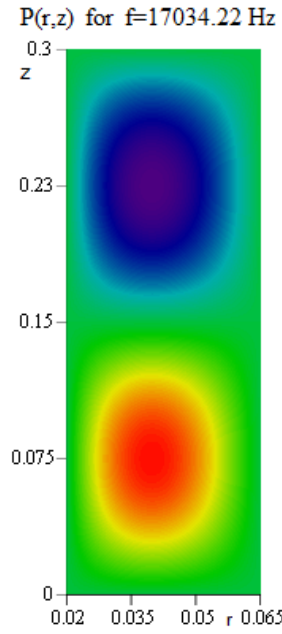
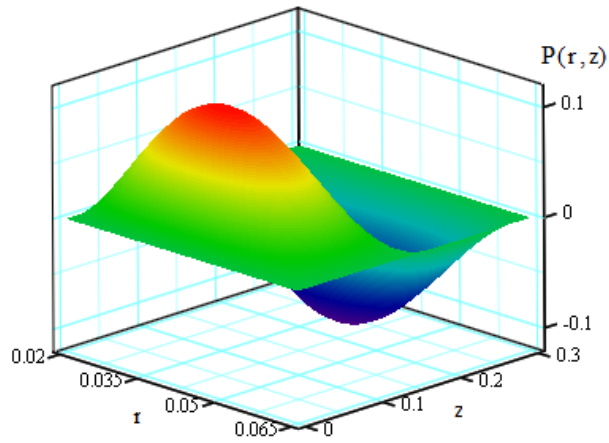


Figure A-15 Analytical acoustic pressure field for  $m=2$ ,  $n=1$ ,  $c=1490.56$  m/s and  $f=17034.22$  Hz

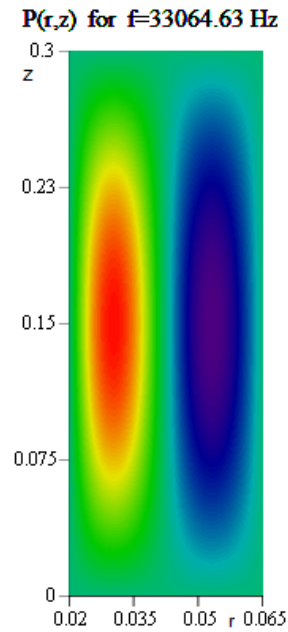
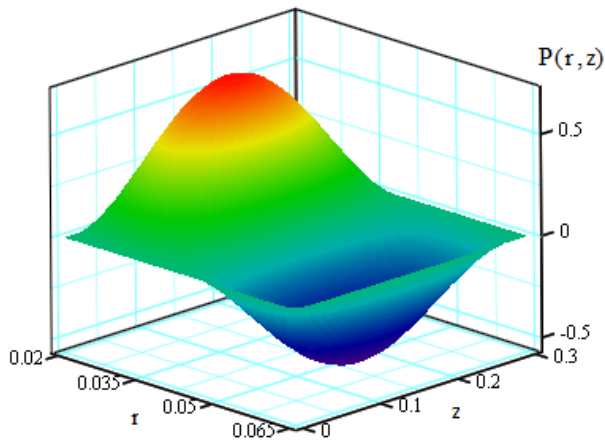


Figure A-16 Analytical acoustic pressure field for  $m=1$ ,  $n=2$ ,  $c=1490.56$  m/s and  $f=33064.63$  Hz

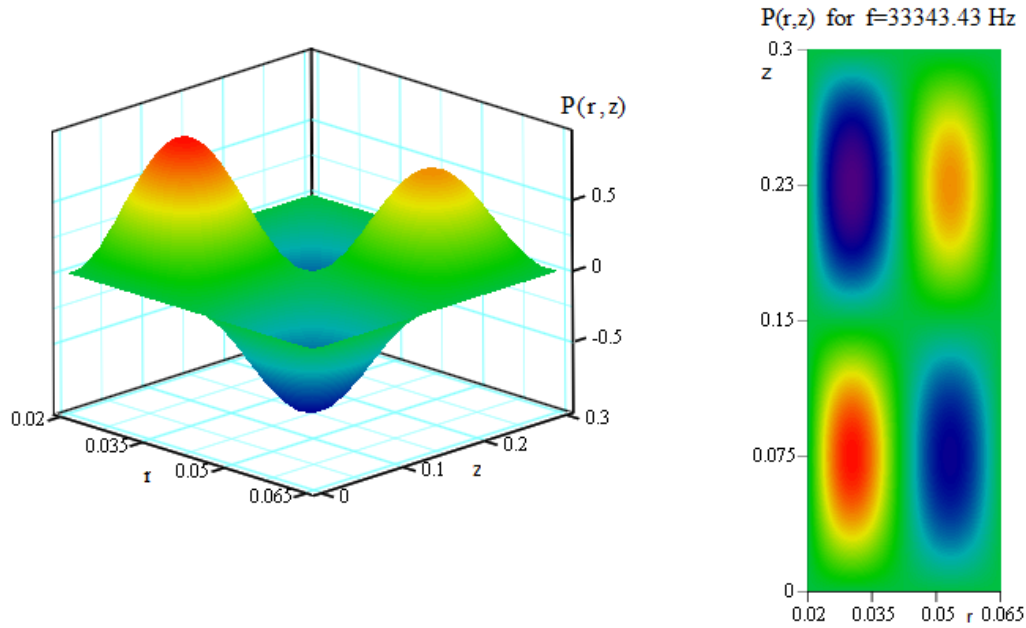


Figure A-17 Analytical acoustic pressure field for  $m=2$ ,  $n=2$ ,  $c=1490.56$  m/s and  $f=33343.43$  Hz

The geometry shown in Figure A-13 was solved using Comsol Multiphysics applying the same boundary conditions (Eq. (A.6.3)). Analytical results and numerical results show excellent agreement.

Table A-2 Numerical resonance modes for the analytically solved problem

$A$	$m$	$F$
$\alpha_1=4717.258$	1	16481.81
$\alpha_1=4717.258$	2	17034.23
$\alpha_2=19316.552$	1	33064.85
$\alpha_2=19316.552$	2	33343.66

These values differ from the analytical results in a maximum 0.0006 %. The numerical error in the determination of the resonance modes are results of the mesh size definition. Numerical pressure distribution profiles agree with the analytical solution as well.

Continuing this analysis, Sub-problem (A) is solved for new boundary conditions. The new boundary conditions applied to Eq. (A.6.10) are:

$$\frac{dR(r_1)}{dr} = 0, R(r_2) = 0.$$

These boundary conditions represent a hard wall boundary condition placed upon the inner cylinder. Results involving this analysis are discussed below. Results display a fluid fundamental frequency of 10.5 kHz. These analytical results represent the behavior of the fluid domain and identify the fundamental mode of the fluid under the two applied boundary conditions. Thus, this analysis gave an initial educated guess on the range of working frequencies (between 16.4 kHz and 10.5 kHz). The numerical and experimental model approached the behavior of the hard wall ( $\nabla p = 0$ ) boundary condition at the inner cylinder due to the bone material properties. Nevertheless, these results provided upper and lower limits of working frequencies.

Consider the following partial differential equation:

$$\nabla^2 p = \frac{1}{c^2} \frac{\partial^2 p}{\partial t^2} \quad (\text{A.6.21})$$

Boundary conditions:

$$\left. \begin{aligned} p(r, 0, t) &= 0 \\ p(r, L, t) &= 0 \\ \frac{\partial p(r_1, z, t)}{\partial r} &= 0 \\ p(r_2, z, t) &= 0 \end{aligned} \right\} \quad (\text{A.6.22})$$

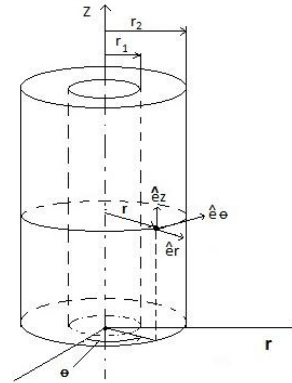


Figure A-18 Geometry of the problem

where  $p$  is the acoustically induced pressure,  $c$  is the speed of sound and  $t$  is the time;  $r_1$ ,  $r_2$ , and  $L$  are the inner radius, outer radius and length of the cylinder respectively.

In cylindrical coordinates Eq. (A.6.21) can be written as:

$$\frac{1}{r} \frac{\partial}{\partial r} \left( r \frac{\partial p}{\partial r} \right) + \frac{\partial^2 p}{\partial z^2} + \frac{1}{r^2} \frac{\partial^2 p}{\partial \theta^2} = \frac{1}{c^2} \frac{\partial^2 p}{\partial t^2} \quad (\text{A.6.23})$$

By symmetry condition:  $\frac{\partial p}{\partial \theta} = 0$

Since the partial differential equation and the boundary conditions are linear and homogeneous, we can apply the separation variables method (Haberman 2003).

Then, we define

$$P(r, z, t) = R(r)Z(z)T(t) \quad (\text{A.6.24})$$

Replacing Eq. (A.6.24) in Eq. (A.6.22) and (A.6.23), we obtain,

$$\frac{1}{R} \frac{d^2 R}{dr^2} + \frac{1}{Rr} \frac{dR}{dr} + \frac{1}{Z} \frac{d^2 Z}{dz^2} = \frac{1}{c^2 T} \frac{d^2 T}{dt^2} \quad (\text{A.6.25})$$

$$\left. \begin{array}{l} Z(0) = 0 \quad , \quad \frac{dR(r_1)}{dr} = 0 \\ Z(L) = 0 \quad , \quad R(r_2) = 0 \end{array} \right\} \quad (\text{A.6.26})$$

The left hand in Eq. (A.6.25) is a function of  $r$  and  $z$  only and the right hand is a function of  $t$  only. Therefore the only possibility is that both sides are equal constants.

Then, using constants  $\alpha$ ,  $\beta$ , and  $\lambda$ , in Eq. (A.6.25) we convert the problem in three sub-problems,

$$\underbrace{\frac{1}{R} \frac{d^2 R}{dr^2} + \frac{1}{Rr} \frac{dR}{dr} + \frac{1}{Z} \frac{d^2 Z}{dz^2}}_{-\lambda} = \underbrace{\frac{1}{c^2 T} \frac{d^2 T}{dt^2}}_{-\lambda}$$

$$\left. \begin{aligned} \frac{1}{R} \frac{d^2 R}{dr^2} + \frac{1}{Rr} \frac{dR}{dr} &= -\alpha \\ \frac{dR(r_1)}{dr} &= 0, \quad R(r_2) = 0 \end{aligned} \right\} \quad (A)$$

$$\left. \begin{aligned} \frac{1}{Z} \frac{d^2 Z}{dz^2} &= \alpha - \lambda = -\beta \\ Z(0) &= 0, \quad Z(L) = 0 \end{aligned} \right\} \quad (B)$$

$$\left. \frac{1}{c^2 T} \frac{d^2 T}{dt^2} = -\lambda \right\} \quad (C)$$

**Solving the sub problem A**

From (A) we obtain,

$$\left. \begin{aligned} r^2 \frac{d^2 R}{dr^2} + r \frac{dR}{dr} + r^2 \alpha^2 R &= 0 \\ \frac{dR(r_1)}{dr} &= 0, \quad R(r_2) = 0 \end{aligned} \right\} \quad (A.6.27)$$

The Eq. (A.6.27) represents a regular Sturm-Liouville eigenvalue problem(S-L) (Haberman 2003).

Where the form of S-L is,

$$\frac{d}{dx} \left( P(x) \frac{d\phi}{dx} \right) + Q(x)\phi + \zeta\sigma(x) = 0$$

The boundary conditions must be linear and homogeneous.

From Eq. (A.6.27) we obtain,

$$\frac{d}{dr} \left( r \frac{dR}{dr} \right) + \alpha r R = 0$$

Where,

$$\varphi(x) = R(r) \quad P(x) = P(r) = r \quad Q(x) = Q(r) = 0 \quad \sigma(x) = \sigma(r) = r \quad \zeta = \alpha$$

$r > 0$  Physical parameter

The Rayleigh quotient from S-L show that for problem (A) the eigenvalues  $\alpha$  are real and greater than or equal to zero (Haberman 2003).

Indeed, the Rayleigh quotient yields,

$$\alpha = \frac{-P(r)R \frac{dR}{dr} \Big|_{r_1}^{r_2} + \int_{r_1}^{r_2} \left( P(r) \left( \frac{dR}{dr} \right)^2 - Q(r)R^2 \right) dr}{\int_{r_1}^{r_2} R^2 \sigma(r) dr}$$

Simplifying, gives

$$\alpha = \frac{\int_{r_1}^{r_2} r \left( \frac{dR}{dr} \right)^2 dr}{\int_{r_1}^{r_2} r R^2 dr}, \quad \text{where } \left( \frac{dR}{dr} \right)^2 \geq 0, \quad r > 0, \quad R^2 > 0$$

Therefore,  $\alpha \geq 0$  and  $\alpha < 0$  is not eigenvalue.

**Analyzing for  $\alpha = 0$**

From (A.6.27) we obtain,

$$\frac{d}{dr} \left( r \frac{dR}{dr} \right) = 0, \quad \text{where the general solution is } R(r) = C_1 \ln(r) + C_2$$

Applying the boundary conditions from equation (A.6.27), we determine that  $\alpha = 0$  is a *trivial solution*.

**Analyzing for  $\alpha > 0$**

From (A.6.27), changing variables:  $r' = r\sqrt{\alpha}$  we obtain the known Bessel differential equation,

$$r'^2 \frac{d^2 R}{dr} + r' \frac{dR}{dr'} + r'^2 R = 0 \quad (\text{A.6.28})$$

The general solution of equation (A.6.28) is a combination of Bessel function of first and second kind of orders zero (Morse & Feshbach 1953).

$$R(r) = C_3 J_0(\sqrt{\alpha} r) + C_4 Y_0(\sqrt{\alpha} r) \quad (\text{A.6.29})$$

Applying the boundary conditions from equation (A.6.27)

$$\frac{dR(r_1)}{dr} = 0$$

Using the following properties,

$$\frac{d}{dx} (J_0(cx)) = -cJ_1(cx) \quad \text{and} \quad \frac{d}{dx} (Y_0(cx)) = -cY_1(cx)$$

Eq. (A.6.29) yields,

$$R(r) = C_4 \left[ \frac{-Y_1(\sqrt{\alpha} r_1)}{J_1(\sqrt{\alpha} r_1)} J_0(\sqrt{\alpha} r) + Y_0(\sqrt{\alpha} r) \right]$$

Using the second boundary condition

$$R(r_2) = C_4 \left[ \frac{-Y_1(\sqrt{\alpha} r_1)}{J_1(\sqrt{\alpha} r_1)} J_0(\sqrt{\alpha} r_2) + Y_0(\sqrt{\alpha} r_2) \right] = 0$$

$C_4 \neq 0$  (If  $C_4 = 0$ ,  $R(r) = 0 \rightarrow p(r, z, t) = 0$  is trivial solution)

Then,

$$-Y_1(\sqrt{\alpha} r_1) J_0(\sqrt{\alpha} r_2) + Y_0(\sqrt{\alpha} r_2) J_1(\sqrt{\alpha} r_1) = 0$$

We define,  $F(\sqrt{\alpha}) = -Y_1(\sqrt{\alpha} r_1) J_0(\sqrt{\alpha} r_2) + Y_0(\sqrt{\alpha} r_2) J_1(\sqrt{\alpha} r_1)$

The zeros of  $F$  are the  $\sqrt{\alpha_n}$ , where  $\alpha_n$  is called  $n$ -th eigenvalue, and  $n=1, 2, 3, \dots$

Finally the solution for sub problem (A) is.

$$R(r) = C_{4n} \left[ \frac{-Y_1(\sqrt{\alpha_n} r_1)}{J_1(\sqrt{\alpha_n} r_1)} J_0(\sqrt{\alpha_n} r) + Y_0(\sqrt{\alpha_n} r) \right]$$

Where,

$\sqrt{\alpha_n}$  are the zeros of  $F(\sqrt{\alpha_n}) = -Y_1(\sqrt{\alpha_n} r_1)J_0(\sqrt{\alpha_n} r_2) + Y_0(\sqrt{\alpha_n} r_2)J_1(\sqrt{\alpha_n} r_1)$  ,  $n = 1,2,3...$

(A.6.30)

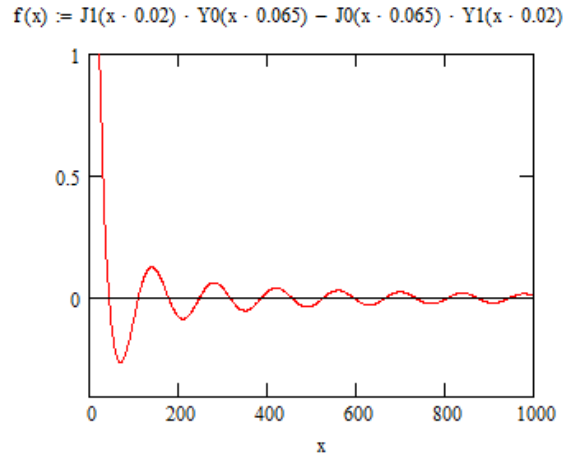


Figure A-19 Zeros of  $f(x)$ , where  $x = \sqrt{\alpha_n}$

### Solving the sub problem (B)

From (B)

$$\frac{d^2 Z}{dz^2} + \beta Z = 0 \quad , \quad \text{with} \quad Z(0) = 0 \quad , \quad Z(L) = 0$$

This problem is a S-L (Haberman 2003) which shows that the eigenvalue  $\beta$  is greater than or equal to zero.

Hence, using the characteristic polynomial method and simple integration we obtain the following general solutions for the sub problem (B).

$$\text{For } \beta = 0, \quad Z(z) = C_5 z + C_6 \tag{B.1.11}$$

$$\text{For } \beta > 0, \quad Z(z) = C_7 \cos(\sqrt{\beta} z) + C_8 \sin(\sqrt{\beta} z) \tag{B.1.12}$$

Applying the boundary conditions to Eq. (A.6.31), we can easily see that  $\beta = 0$  is a trivial solution.

Using the boundary conditions in equation (A.6.32),

$$Z(0) = C_7 \cos(\sqrt{\beta}0) + C_8 \sin(\sqrt{\beta}0) = 0 \rightarrow C_7 = 0$$

$$\text{Then, } Z(z) = C_8 \sin(\sqrt{\beta}z)$$

$$Z(L) = C_8 \sin(\sqrt{\beta}L) = 0 \rightarrow C_8 \neq 0 \text{ (If } C_8 = 0, Z(z) = 0 \rightarrow p(r, z, t) = 0 \text{ is trivial solution)}$$

Therefore,

$$\sin(\sqrt{\beta}L) = 0 \rightarrow \sqrt{\beta}L = m\pi \text{ due to } \beta > 0, \quad m = 1, 2, 3, \dots$$

Finally the solution for sub problem (B) is.

$Z(z) = C_{8m} \sin(\sqrt{\beta_m}z) \quad , \quad \text{Where } \beta_m = \left(\frac{m\pi}{L}\right)^2 \quad , \quad m = 1, 2, 3, \dots$
--

(A.6.33)

***Solving the sub problem (C)***

From (B) we have that  $\lambda = \beta + \alpha$  , and due to  $\alpha$  and  $\beta$  are real and greater than zero; this implies that  $\lambda > 0$  .

If, from (C) we define  $\omega^2 = \lambda c^2$  hence,

$$\omega = c\sqrt{\lambda} = c\sqrt{\beta + \alpha} \tag{A.6.34}$$

Replacing Eq. (A.6.34) in eq. (B), gives

$$\frac{d^2T}{dt^2} + \omega^2 T = 0$$

Using the characteristic polynomial method, we determinate the general solution as,

$T(t) = C_{9m} \cos(\omega_m t) + C_{10} \sin(\omega_m t) \quad \text{where, } \omega_m = c\sqrt{\beta_m + \alpha_n}$
---

(A.6.35)

Finally replacing the equations (A.6.30), (A.6.33), and (A.6.35) in (A.6.34), and considering all

the no trivial solutions, we obtain:

$$p(r, z, t) = \sum_{m=1}^{\infty} \sum_{n=1}^{\infty} \left\{ \frac{-Y_1(\sqrt{\alpha_n} r_1)}{J_1(\sqrt{\alpha_n} r_1)} J_0(\sqrt{\alpha_n} r) + Y_0(\sqrt{\alpha_n} r) \right\} \sin\left(\frac{m\pi}{L} z\right) [A \cos(\omega_{mn} t) + B \sin(\omega_{mn} t)]$$

Where,  $\omega_{mn} = c \sqrt{\left(\frac{m\pi}{L}\right)^2 + \alpha_n}$   $m, n = 1, 2, 3, \dots$

$\sqrt{\alpha_n}$  are the zeros of  $F(\sqrt{\alpha_n}) = -Y_1(\sqrt{\alpha_n} r_1) J_0(\sqrt{\alpha_n} r_2) + Y_0(\sqrt{\alpha_n} r_2) J_1(\sqrt{\alpha_n} r_1)$

(A.6.36)

Specifying the two necessary initial conditions for the problem and applying the orthogonality method, we can determinate the constants A and B in equation (A.6.36).

### ***Stationary acoustic pressure field***

When one particular frequency:  $\omega_{mn}$ , is excited by the presence of an external force oscillating at  $\omega_{mn}$  a standing wave is formed. Table A-3 presents a summary of analytical and numerical results obtained by carrying out numerical simulations following the geometry shown in Figure A-18 and the boundary condition defined by Eq. (A.6.22). Figure A-20 through Figure A-23, presents the analytical results of four eigenfrequencies:  $\omega_{1,1}$ ,  $\omega_{2,1}$ ,  $\omega_{1,2}$ ,  $\omega_{2,2}$ . These pressure profiles support previous arguments, in which it was discussed that a zero pressure gradient boundary condition on the inner radius of the water cylinder in Figure A-18 would resemble the pressure distribution obtained in the artificial thigh; as can be seen in the pressure profile agreement between these four figures and Figure 4.14 and Figure 4.19 through Figure 4.21. These results show a maximum error of 0.04% between analytical and numerical computed values.

$$p(r, z, t) = \left( \frac{-Y_1(\sqrt{\alpha_n} r_1)}{J_1(\sqrt{\alpha_n} r_1)} J_0(\sqrt{\alpha_n} r) + Y_0(\sqrt{\alpha_n} r) \right) \sin\left(\frac{m\pi}{L} z\right) \cos(\omega_{mn} t)$$

(A.6.37)

**Table A-3** Frequencies obtained analytically for the first 4 resonance modes in Hz.

$\alpha$	$m$	$f_{analytical}$	$f_{numerical}$	% error
$\alpha_1=1865.268$	1	10542.55	10537.96	0.04
$\alpha_1=1865.268$	2	11386.83	11382.6	0.037
$\alpha_2=11806.496$	1	25896.30	25902.32	0.02
$\alpha_2=11806.496$	2	26251.35	26257.37	0.02

where,  $f = \frac{\omega_{m,n}}{2\pi} = \frac{c}{2\pi} \sqrt{\left(\frac{m\pi}{L}\right)^2 + \alpha_n}$  (A.6.38)

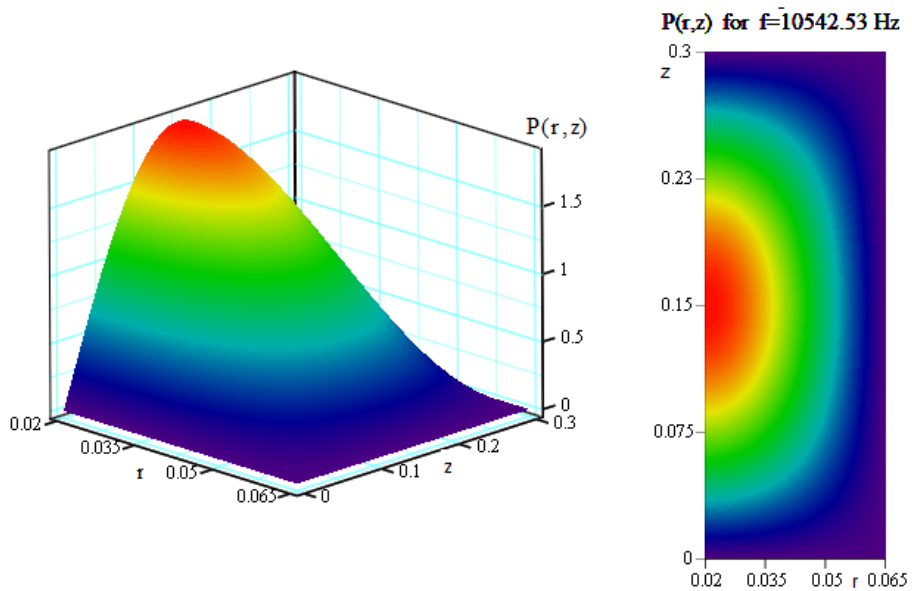


**Figure A-20** Analytical acoustic pressure field for  $m=1, n=1, c=1490.56\text{m/s}$  and  $f=10542.53$  Hz

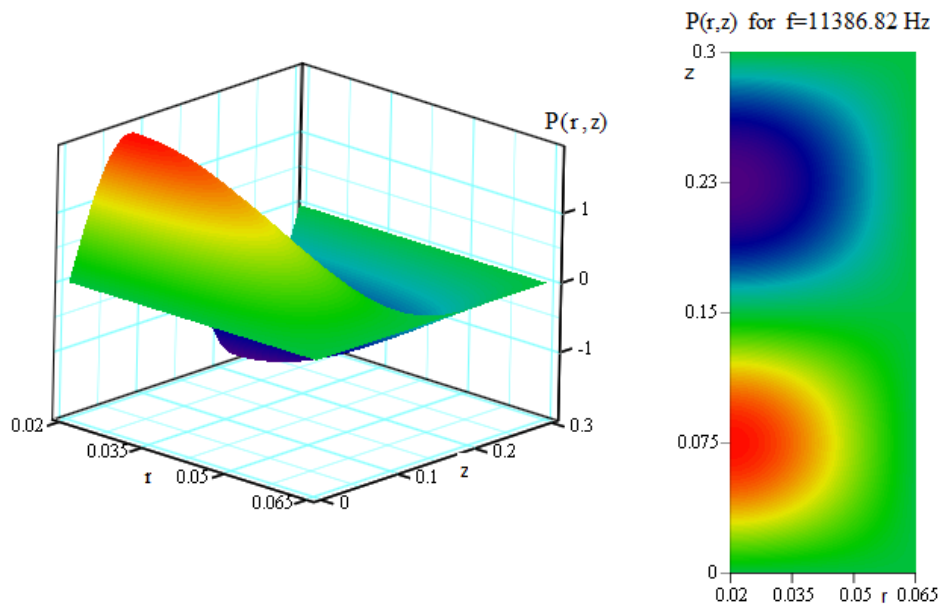


Figure A-21 Analytical acoustic pressure field for  $m=2$ ,  $n=1$ ,  $c=1490.56\text{m/s}$  and  $f=11386.82\text{ Hz}$

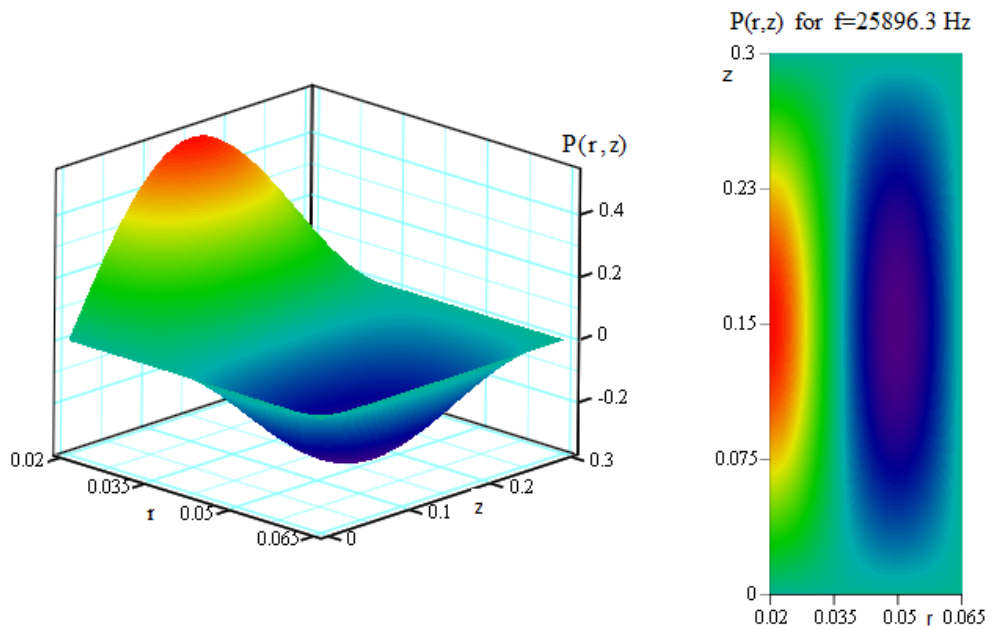
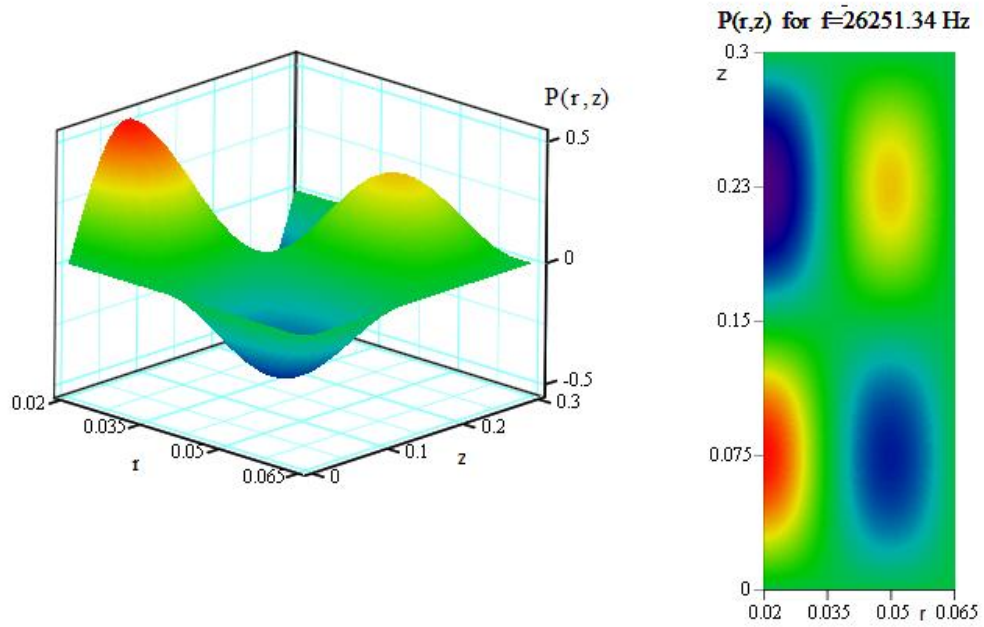


Figure A-22 Analytical acoustic pressure field for  $m=1$ ,  $n=2$ ,  $c=1490.56\text{m/s}$  and  $f=25896.3\text{ Hz}$



**Figure A-23 Analytical acoustic pressure field for  $m=2$ ,  $n=2$ ,  $c=1490.56\text{m/s}$  and  $f=26251.34\text{ Hz}$**

## Appendix B

### B.1 Changes induced by the addition of acrylic flanges

As concluded from numerical simulations using COMSOL Multiphysics v4.2, simulations performed with the acrylic flanges display similar pressure profile as those obtained in simulations performed replacing the acrylic structure with a soft wall boundary condition (pressure = 0; see Figure B-1). Moreover, changes in resonance frequency present only a 1 % difference.

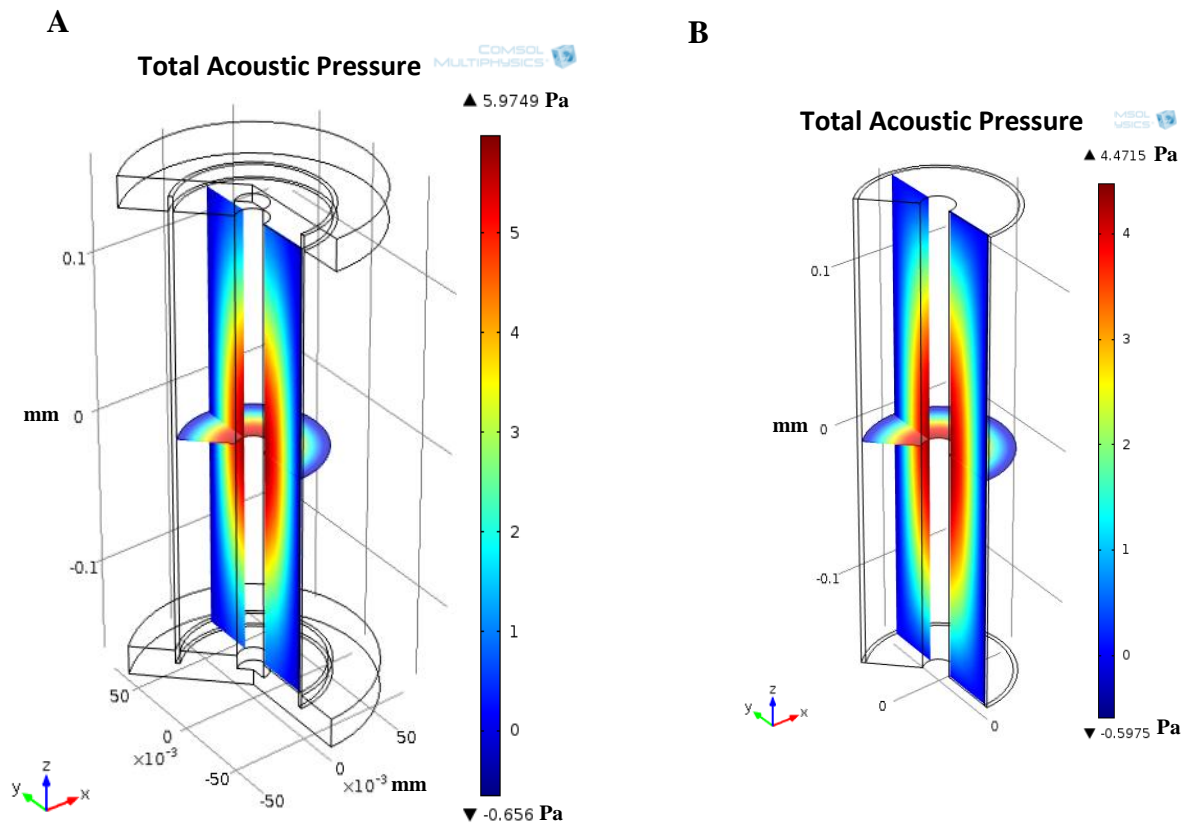


Figure B-1 A) Structure with flanges, resonance frequency: 15,302 Hz B) No flanges, resonance frequency: 15, 452 Hz. Simulations product of 2D axisymmetric eigenfrequency analysis.

## **B.2 Different material properties at outer cylinder**

In this section the effects of different materials composing the outer cylinder are presented. This was done in order to justify the selection of glass. As can be observed in Figure B-2 (A), Figure B-2 (C), and Figure B-2 (D), glass and acrylic materials result in pressure profiles within the liquid resembling a soft wall boundary condition ( $P=0$ ) at the outer wall. However if a different material with much higher density and young modulus is used, in this case steel, acoustic differences will result in a pressure profile displaying various multiple changes in the concavity of the pressure field, as can be observed in Figure B-2 (D).

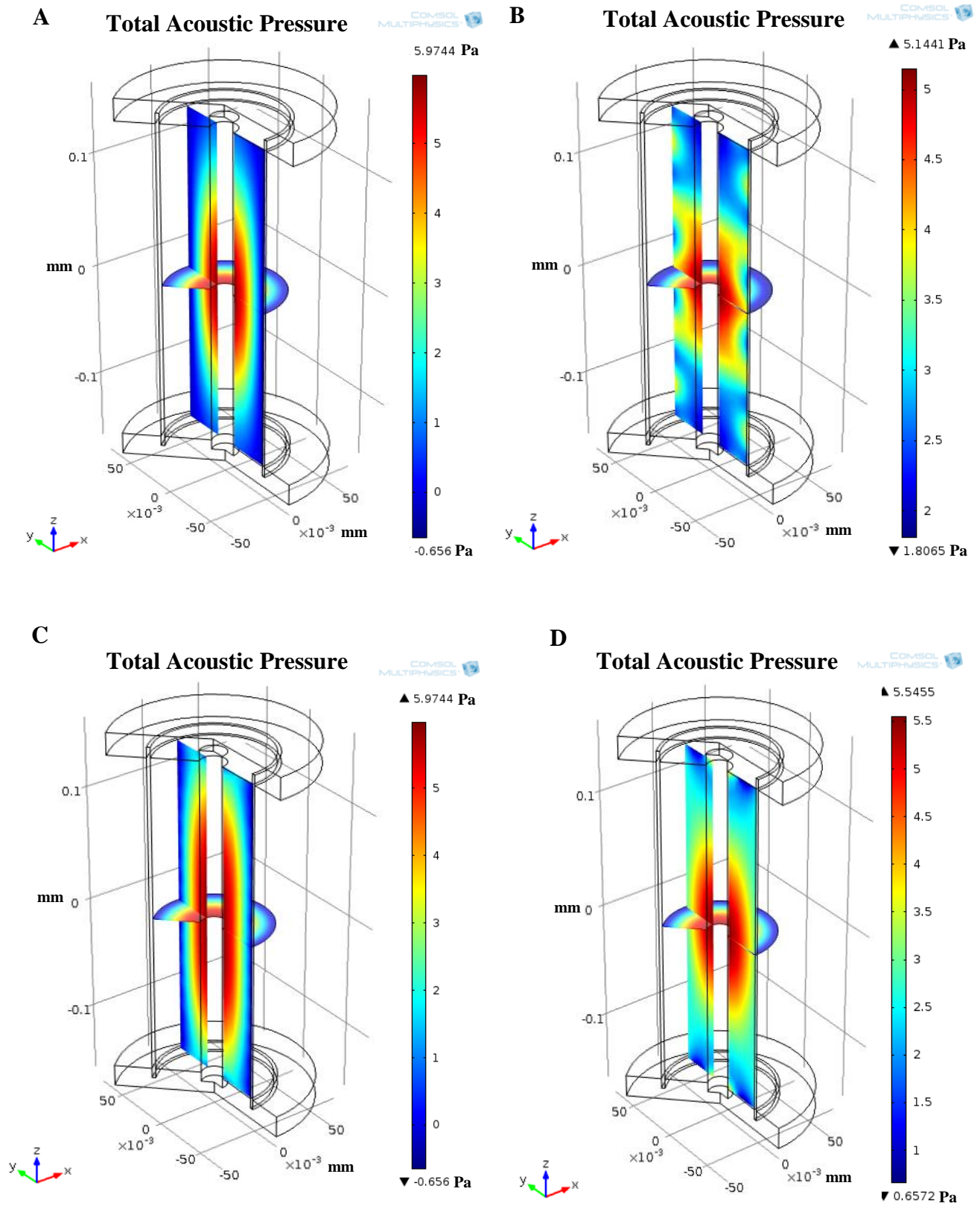


Figure B-2 A) Glass outer cylinder, Frequency: 15,302 Hz B) Steel outer cylinder, Frequency: 15,318 Hz C) Acrylic outer cylinder, Frequency: 13,145 Hz D) Acrylic outer cylinder, Frequency: 13,518 Hz

As can be observed from Figure B-2 although similar pressure profiles are obtained between acrylic and glass, the use acrylic with a lower density introduces a shift of  $\approx 2$  kHz. Differences among these pressure profiles as a result of changes in material properties can be explained due to variations in the transmission and reflection coefficients between the wall, flanges and the fluid. Reflection and transmission coefficients can be defined for a plane acoustic wave in terms of the incident and reflected energy. This definition discussed in Chapter 2 section 2.3.1.1 in terms of characteristic impedances ( $Z$ ) is defined as follows:

$$T_{ac} = \frac{2Z_2}{Z_1 + Z_2} \quad (\text{B.2.1})$$

and

$$R_{ac} = \frac{Z_2 - Z_1}{Z_1 + Z_2} \quad (\text{B.2.2})$$

where  $Z_2$  and  $Z_1$  are the characteristic impedances of: the medium where the acoustic wave is being transmitted to and the medium, source of the acoustic wave respectively (Orfanidis, 2008).

If the flanges are assumed as the recipient of the acoustic wave and the outer cylinder the source of the acoustic vibrations, Table B-1 presents the transmission and reflection acoustic coefficients as the outer cylinder material is changed:

**Table B-1 Transmission and reflection coefficients between outer cylinder and flanges for different outer cylinder materials**

	Acrylic	Glass (Pyrex)	Steel
<b>T<sub>ac</sub></b>	1	0.39	0.129
<b>R<sub>ac</sub></b>	0	0.61	0.87

As can be seen from Table B-1 steel presents lower transmission coefficients and higher reflection coefficients, as a result of a different density.

Similarly reflection and transmission coefficients can be calculated, describing the interaction between the fluid within the acoustic chamber (source) and the flanges (recipients). These results are presented in Table B-2.

**Table B-2 Transmission and reflection coefficients between the fluid and flanges for different flange materials**

	Acrylic	Glass (Pyrex)	Steel
Tac	1.36	1.8	1.94
Rac	0.363	0.797	0.937

### **B.3 Simulations performed with two piezoelectric rings**

Simulations were performed with two piezoelectric rings.

Figure B-3 illustrates the response of the artificial thigh at several frequencies of interest. Figure B-3 (A) displays a similar pressure profile to the fundamental mode of the fluid obtained with one PZT ring. However, as expected, resonant modes of higher order can be excited at lower frequencies than while using only one PZT ring. As illustrated in Figure B-3 (B), resonant modes of the fluid can be stimulated that were not possible to obtain with one PZT ring located at the center of the structure. Figure B-3 (B) displays a pressure node at the center of the center and two pressure nodes coincide with the location of the PZT ring. Experimentally it would be difficult to obtain this type of pressure profile with the PZT located at the middle since a pressure node would have to be obtained in a location of maximum displacement.

Two PZT devices brings about the opportunity to investigate additional fluid resonance modes which will bring about additional bubble entrapment opportunities. Observe the pressure profile shown in Figure B-3 (C). This pressure profile will give the opportunity to trap small bubbles (resonance frequency larger than excitation frequency) at the pressure antinodes, and big bubbles (resonance frequency smaller than excitation frequency) at the pressure nodes. In order to experimentally observe additional kinds of pressure profiles other than the first mode, or symmetric distributions, it might be necessary to utilize more than one PZT ring.

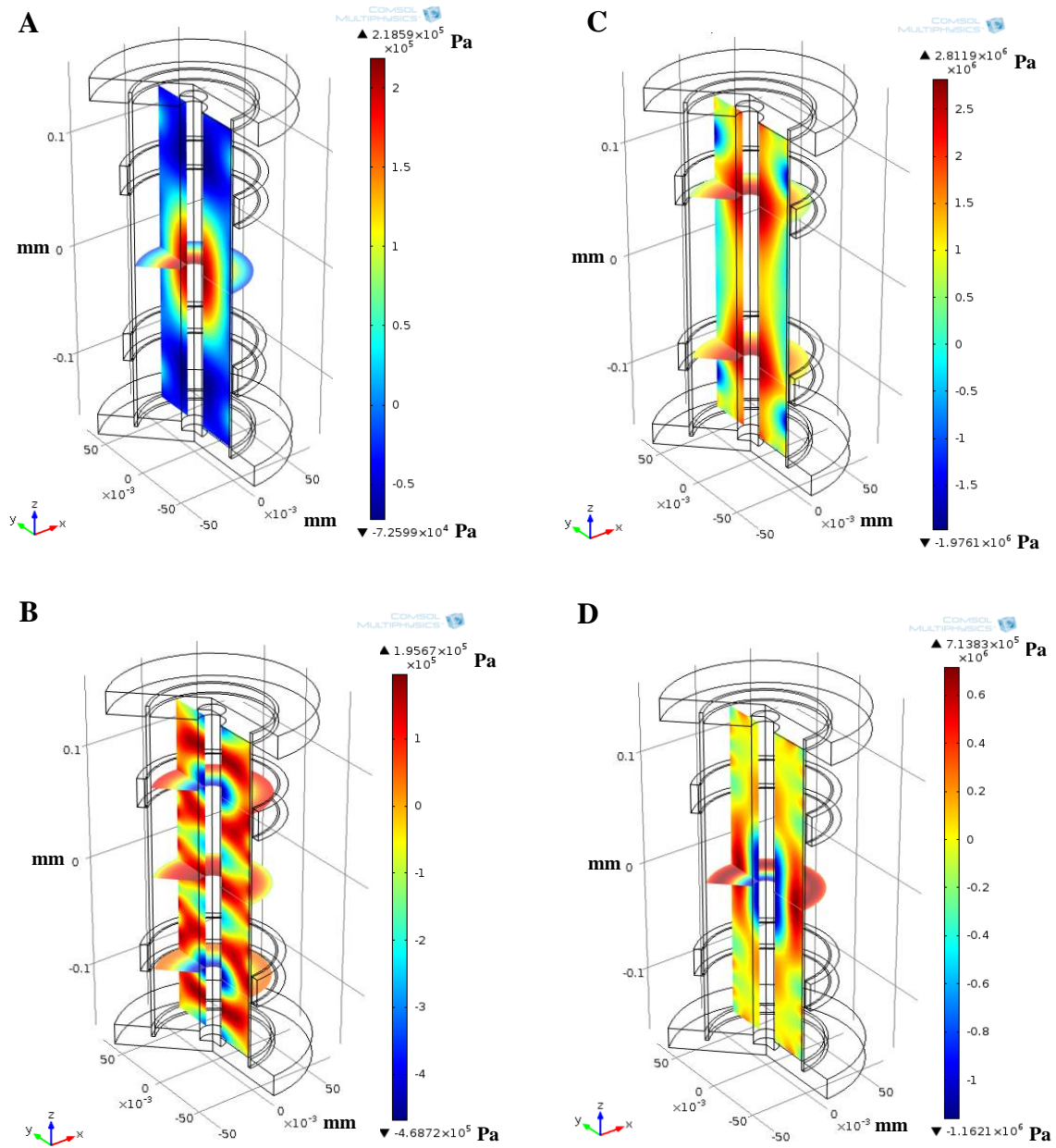
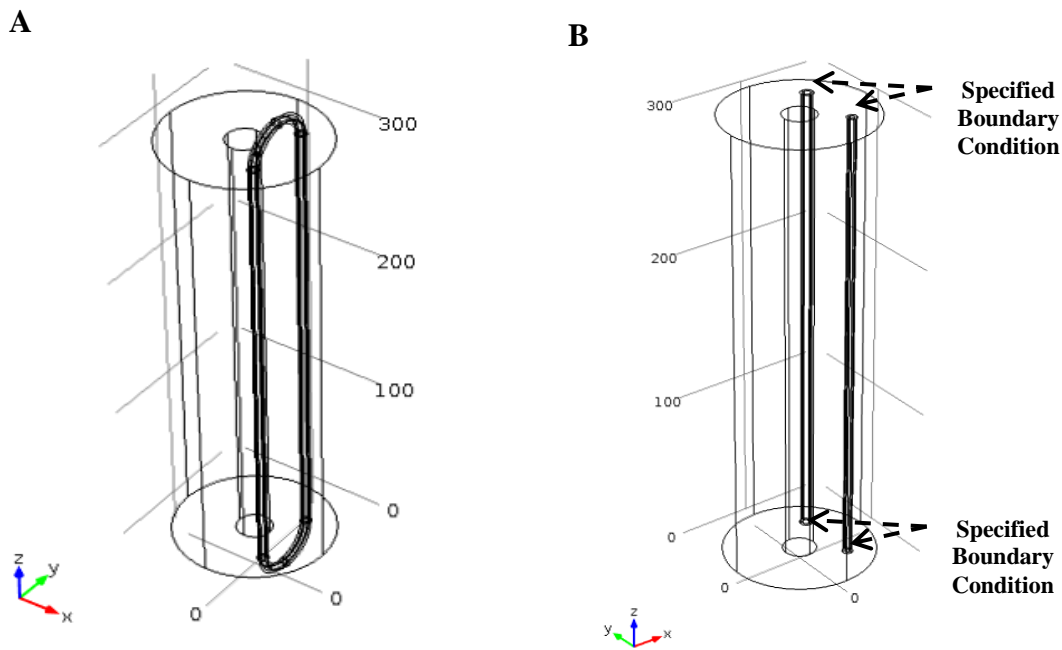


Figure B-3 Acoustic chamber with two piezoelectric rings. A) Frequency: 15,850 Hz. B) Frequency: 14,260 Hz. C) Frequency: 29,310 Hz. D) Frequency: 30,610 Hz.

## B.4 Acoustic impedance boundary condition justification

The simulations discussed in Chapter 4, presented an acoustic impedance boundary condition imposed upon the ends of the inner tubes, on the fluid domain. This type of boundary condition presents a matching impedance condition on either side of the boundary. This

boundary condition represents an extension of the fluid domain. Simulations were carried out in a hollow water cylinder. This cylinder contained two inner vinyl tubes. The tubes were extended and connected to each other on the outside as is the case of the artificial thigh constructed for experimental trials (see Figure B-4 (A)). The results obtained from this simulation were compared to simulations carried out without the outer tubes. Two different boundary conditions were placed at the ends of the inner tubes in the geometry shown in Figure B-4 (B) (i) Acoustic impedance equal to  $\rho_0 c_0 = 1.49 \times 10^6$  (water acoustic impedance) and (ii)  $P = 0$ .



**Figure B-4** A) Geometry with the addition of the outer tubes B) Geometry whose outer boundary was defined by boundary conditions defined in (i) water acoustic impedance and (ii)  $P=0$ .

The fundamental mode of the fluid was analyzed through an Eigen frequency analysis. At this frequency the pressure profile inside the tubes was analyzed. Figure B-5(A) shows the pressure profile within one of the inner tubes, solving the geometry shown in Figure B-4 (A). Figure B-5 (B) shows the pressure profile for zero pressure boundaries in Figure B-4 (B) and Figure B-5 (C) illustrates the pressure profile within the inner tube applying an acoustic

boundary condition at the boundaries described in Figure B-4 (B). Similar pressure distributions can be observed in Figure B-5 (A) and Figure B-5 (C); and dissimilarities between Figure B-5 (A) and Figure B-5 (B). From these results we can conclude that the boundary condition of matching acoustic impedances is more appropriate. Although these simulations were carried out for a much simpler geometry, similar results were expected in a more complicated geometry, and in order to reduce computational time and obtain a more refined mesh in areas of interest the outer tubes were replaced with the acoustic impedance boundary condition.

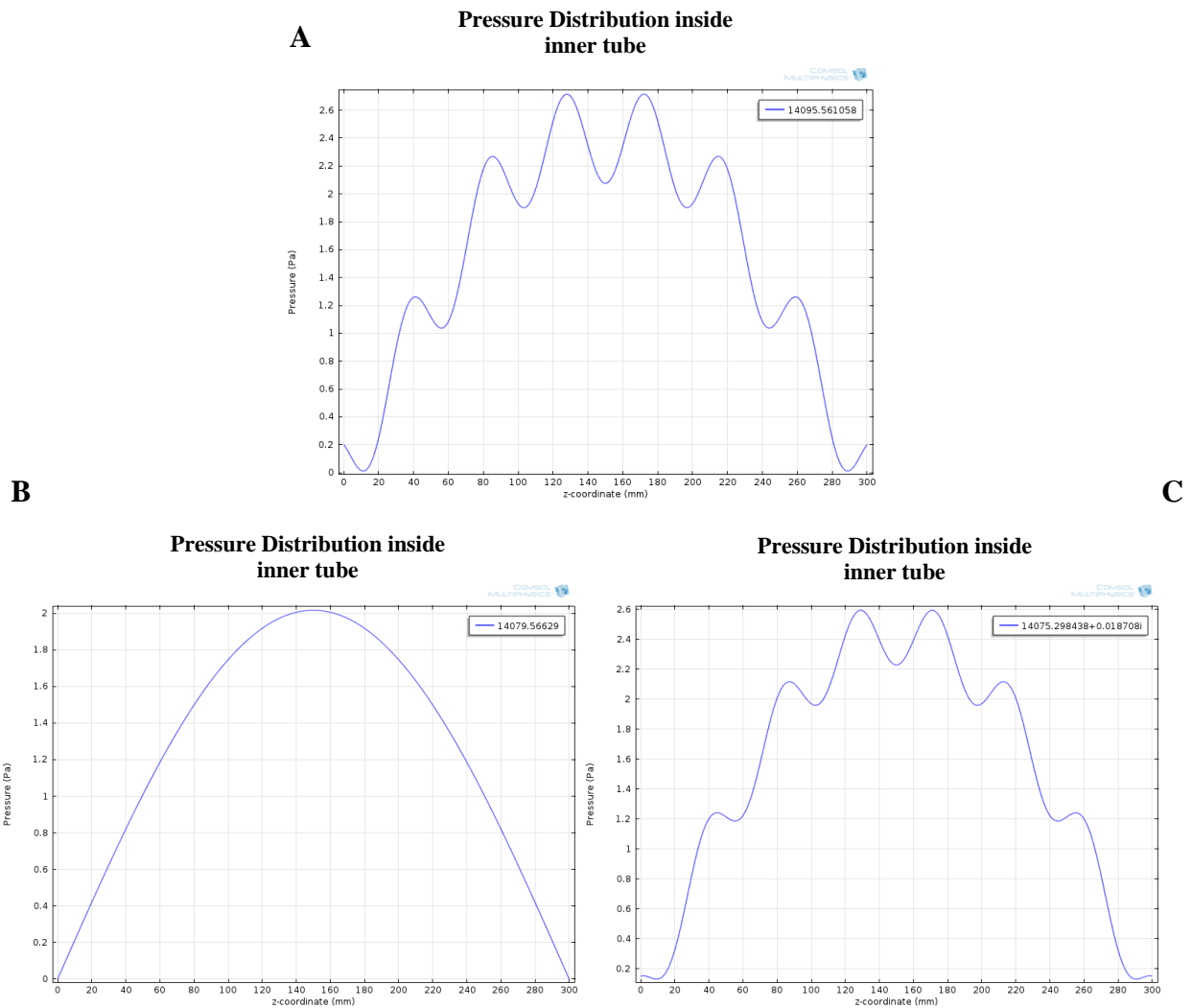


**Figure B-5 Pressure Profile inside the inner tubes; A) Addition of outer tubes (geometry shown in**

## B.5 Inner tube displacement

The pressure distribution obtained inside the tubes was studied in order to better understand oscillations in pressure profiles obtained in numerical simulations inside the inner tubes. Part of this analysis was presented in Chapter 4, in which the Fourier components of profiles obtained on the outside and on the inside of these tubes were compared. In this analysis additional high frequency components could be observed as a result of the solid-structure interaction. In this section we extend the analysis of Chapter 4 by presenting an analysis of tube deformation.

Tube deformation at 14.07 kHz inside the artificial thigh is presented in Figure B-6. The total displacement in the artery (left smaller tube) is illustrated in Figure B-7. Figure B-8 illustrates the Fourier components of the profile presented in Figure B-7. As seen, two frequencies dominate tube displacement,  $k = 10$  and  $k = 120$ , which correspond to the excitation frequency ( $k = 10$ ) and a product of a solid-structure interaction.

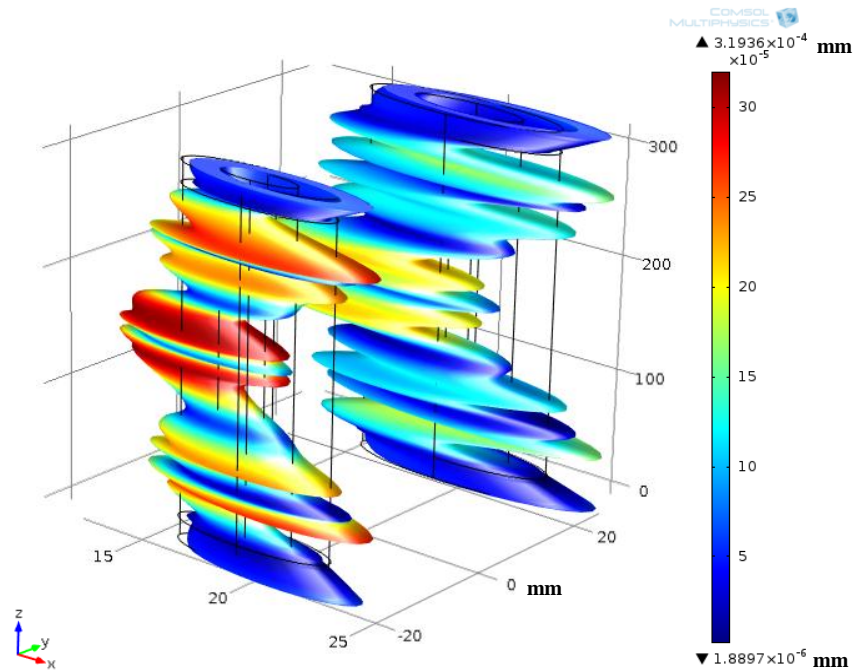


Figure B-6 Inner tube deformation inside the artificial thigh at 14.07 kHz

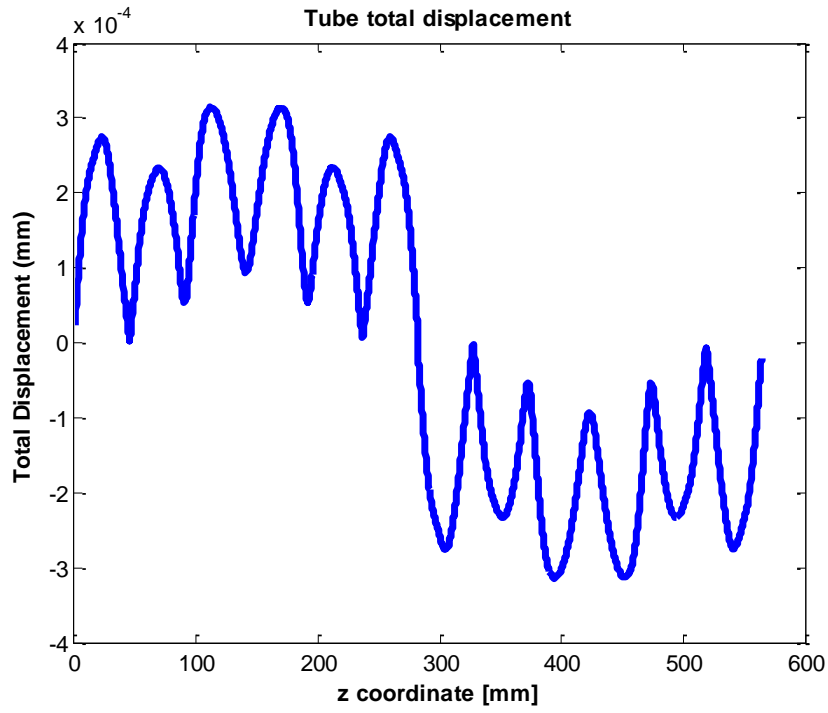


Figure B-7 Total artery displacement at 14.07 kHz

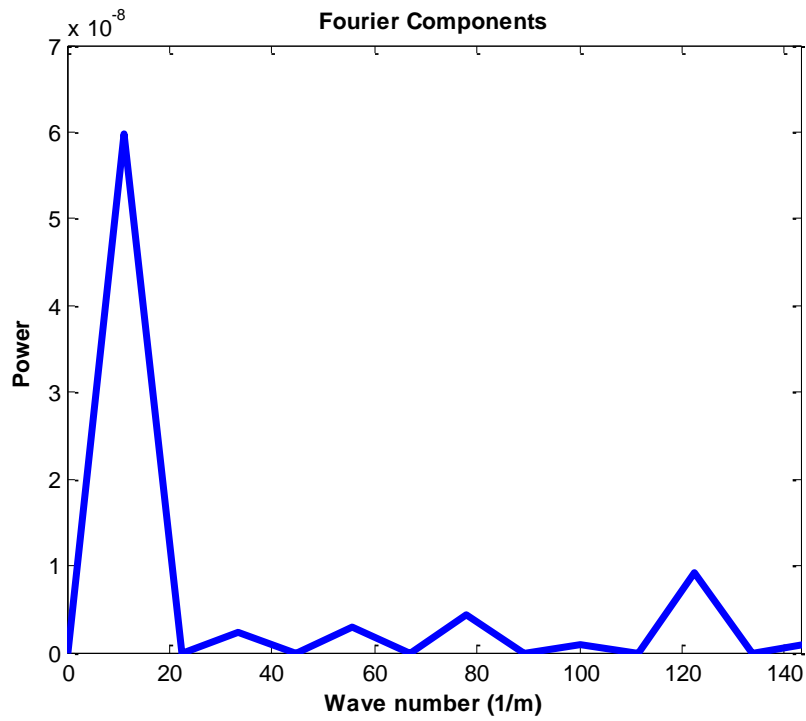
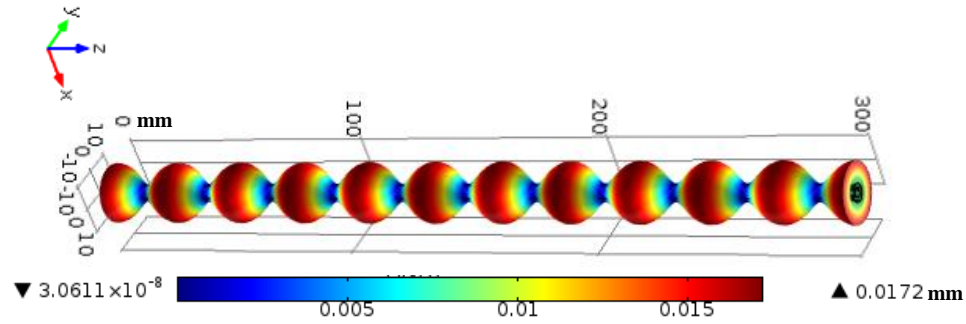


Figure B-8 Fourier components of total displacement signal

Tube vibrations will in turn affect fluid pressure, as observed in the pressure profiles obtained within the inner tubes. This is better understood by studying the eigenfrequencies of the tube structure independently.

Figure B-9 displays the mode shape of the artery at one of its eigenfrequencies found close to the studied frequencies of 14 kHz. Figure B-10 illustrates both, tube total displacement and the Fourier components of this signal.



**Figure B-9 Artery deformation shown as surface displacement (mm), Eigen frequency: 14.29 kHz**

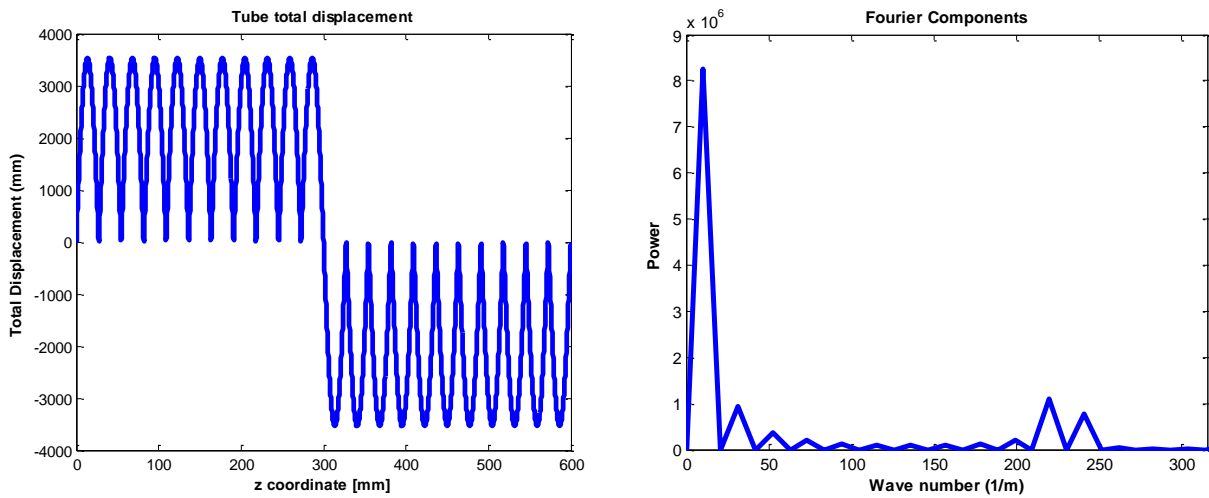


**Figure B-10 A) Tube total displacement and B) Fourier Transform of signal shown in (A)**

An eigenfrequency study was carried out in a geometry including the artery tube and the fluid within it. The results show the same behavior as the ones presented in this section, with only a magnitude change.

## B.6 Mesh Refinement Analysis

The mesh used for the numerical simulations presented in Chapter 4, were the results of a mesh refinement analysis. This analysis took into consideration the minimum recommended mesh resolution when solving acoustic propagation problems and the amount of computational power required. The analysis was performed by using an automatic option provided by COMSOL Multiphysics which executes local mesh refinements according to a specified error norm, resolving those areas where the error is large thus improving accuracy and adapting the mesh to the physical behavior of the problem. The artificial thigh geometry was solved by implementing 3 mesh refinements beginning with a “coarser” mesh parameter defined throughout the structure.

The following parameters define a “coarser” mesh as provided by COMSOL Multiphysics:

**Table B-3 "Coarser" mesh parameters as defined by COMSOL Multiphysics**

<b>Maximum element size</b>	<b>11.2 mm</b>
<b>Minimum element size</b>	0.48 mm
<b>Maximum element growth rate</b>	1.35
<b>Resolution of curvature</b>	0.3
<b>Resolution of narrow regions</b>	0.85

Figure B-11 illustrates the mesh solved under “coarser” parameters. These mesh consisted of 16,247 tetrahedral and triangular elements. After 3 successive refinements the final mesh is shown in Figure B-12. The final problem contained 4.39 million degrees of freedom. It

was observed that the number of degrees of freedom and consequently the number of elements per refinement increases by a factor of approximately four.

The mesh was not further refined because of limitations with the available computer power. In order to produce a fourth refinement approximately 270 Gigabytes of RAM memory would be required and 192 GB were available. Nevertheless, the solved meshes were more than acceptable, based on the number of elements per wavelength as described in Chapter 4. The percentage differences in resonance frequency per refinement are presented in Table B-4.

**Table B-4 Estimated Resonance Frequency Percentage Difference per Refinement**

<b>Mesh Refinement</b>	<b>% difference</b>
<b>1</b>	2.81
<b>2</b>	0.57
<b>3</b>	0.34

The difference between the automatic obtained mesh and the user defined mesh is of 28,795 elements. Therefore the automatic mesh is 2% denser than the user defined mesh. The reason for not using this mesh lies in the mesh definition obtained within the inner tubes of the artificial thigh. This difference is illustrated in Figure B-13 and Figure B-15. As can be seen Figure B-13 does not present round tubes, thus the mesh density defined in this areas was higher than for the rest of the structure; thus giving a finer mesh in the area of interest since the inner tubes was the domain were bubbles would be moving through for most of the experiments as discussed in Chapter 5.

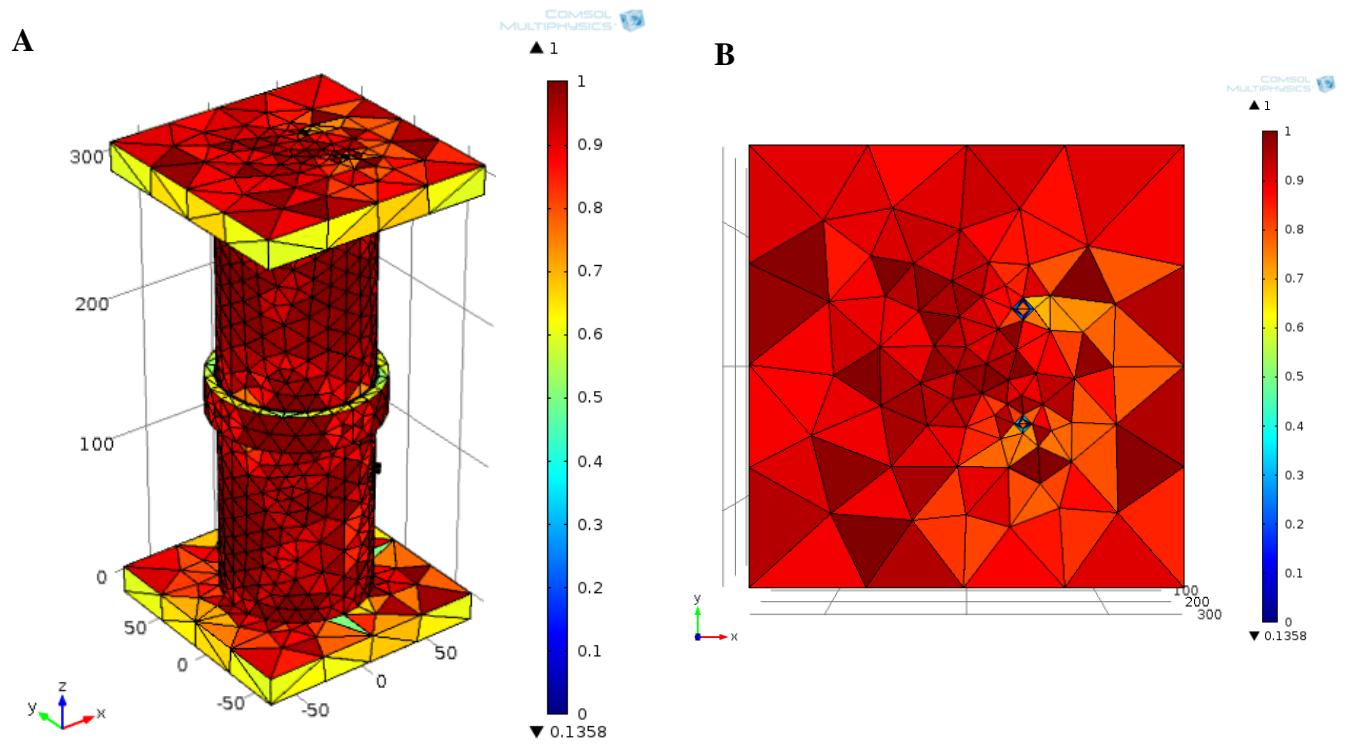


Figure B-11 "Coarser" mesh. Starting mesh of mesh refinement analysis A) Isometric view B) Top view

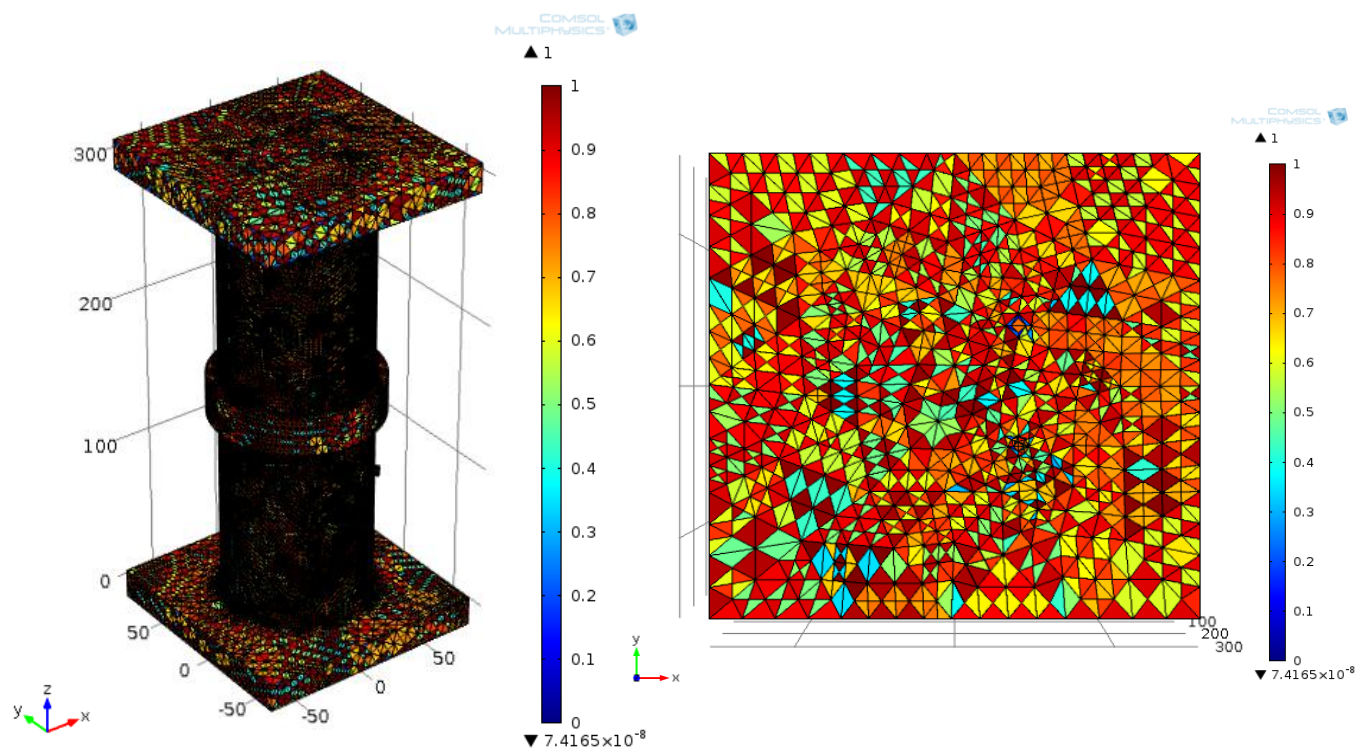


Figure B-12 Mesh after 3 mesh refinements. Number of elements: 1,214,717

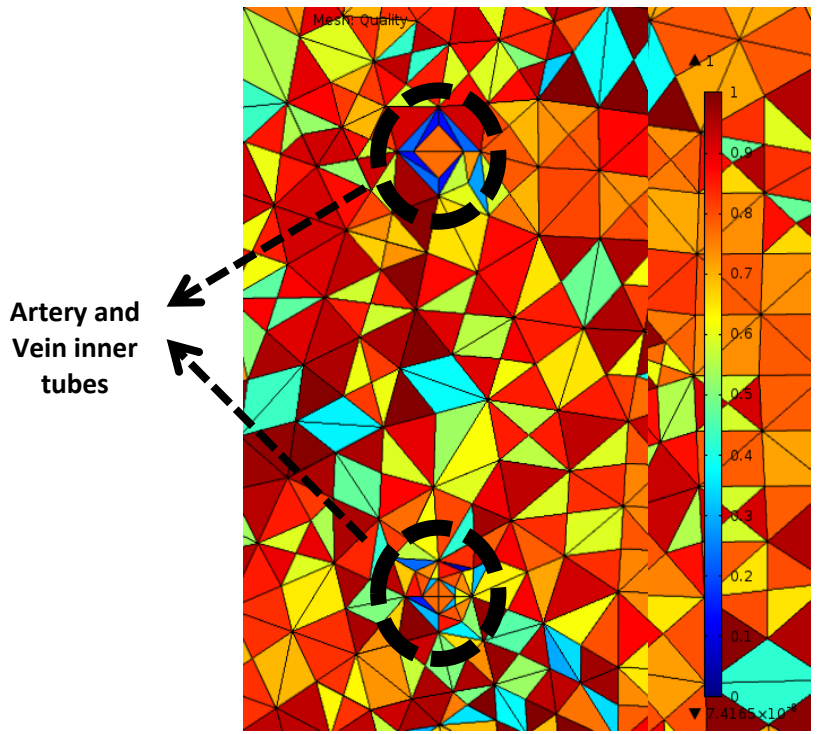


Figure B-13 Zoom in of inner tubes area in the automatic refined mesh

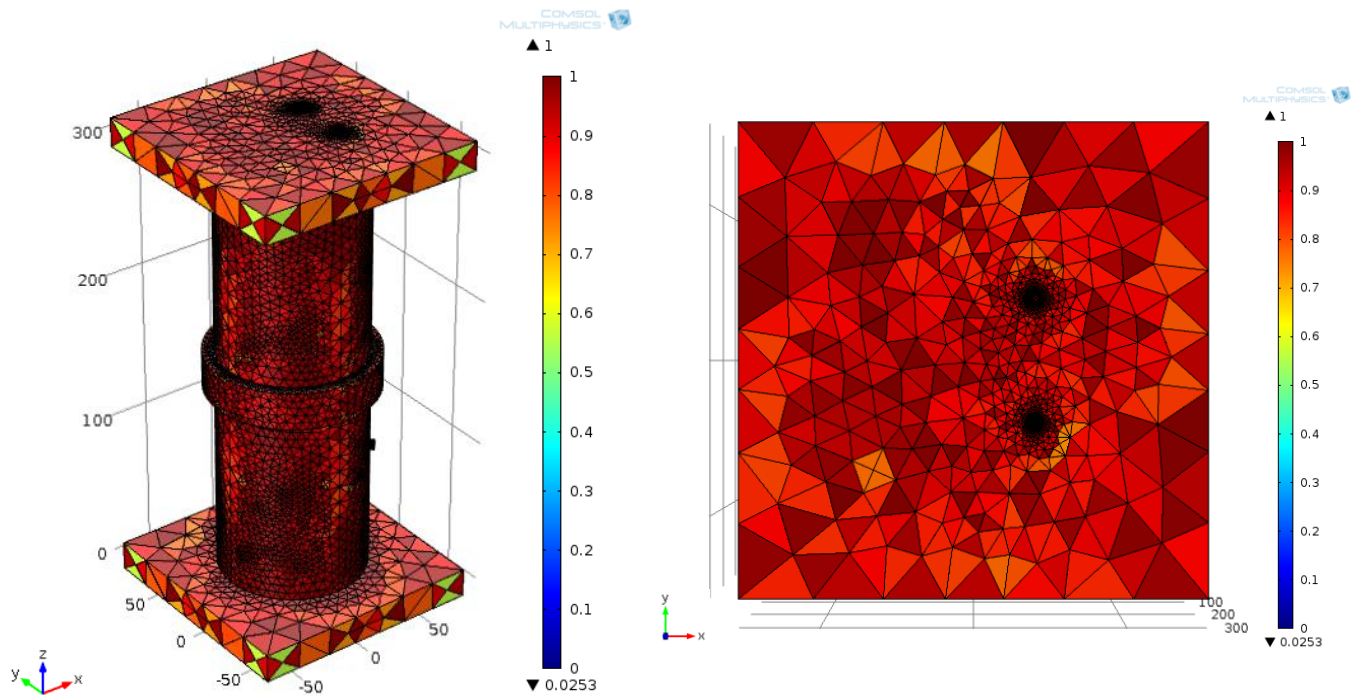


Figure B-14 User defined mesh consisting of three different meshing parameters throughout the structure. Total number of elements: 1,185,922

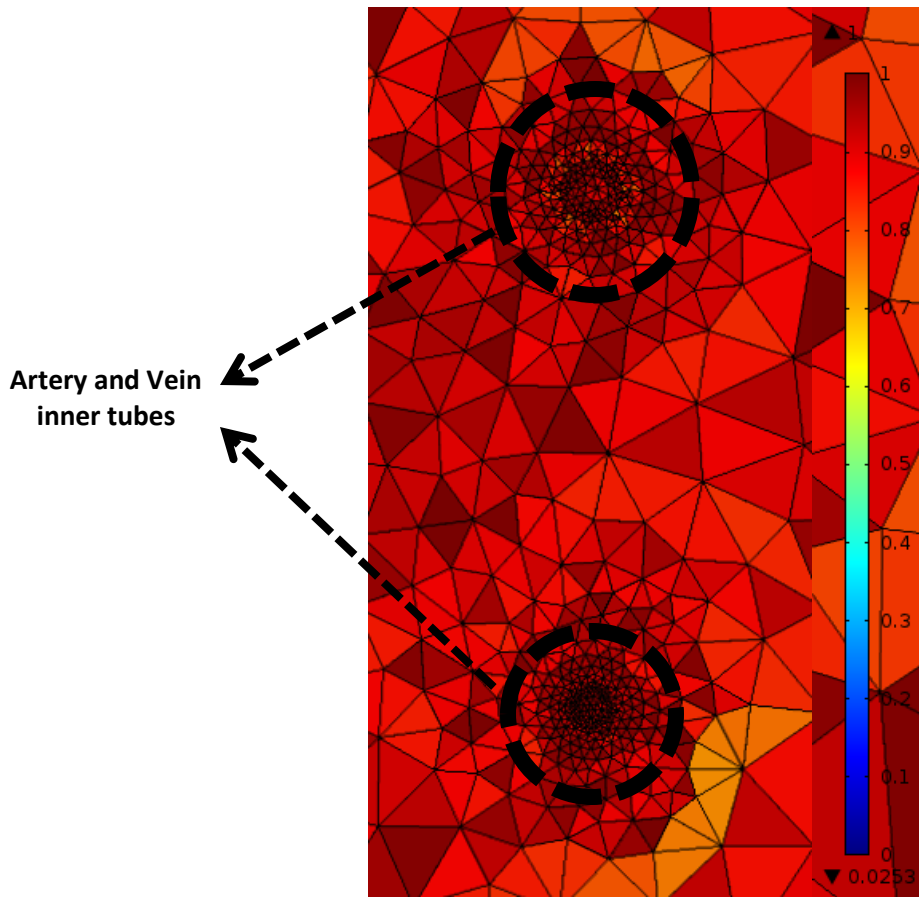


Figure B-15 Zoom in of inner tubes in the user defined mesh.

## B.7 Three dimensional analysis justification

Several details in the geometry required numerical simulations to be solved in a three dimensional environment. A symmetric structure could have been solved in a two dimensional axisymmetric environment and thus provide less computational power and decrease solution convergence times. Figure B-16 illustrates the pill microphone structure. The pill microphone was necessary in order to compare numerical and experimental values. Figure B-17 illustrates the two inner tubes, resembling the vein and artery in the artificial thigh environment. These two structures augmented the level of non-symmetry in the total structure. The addition of the inner tubes contributed to changes in the pressure profiles. Pressure profiles were symmetric in the absence of tubes. The effects of these components which create a non-symmetric structure can

be observed in Figure B-18. Also observe the shift in resonance frequency. These effects were more intensified at certain frequencies.

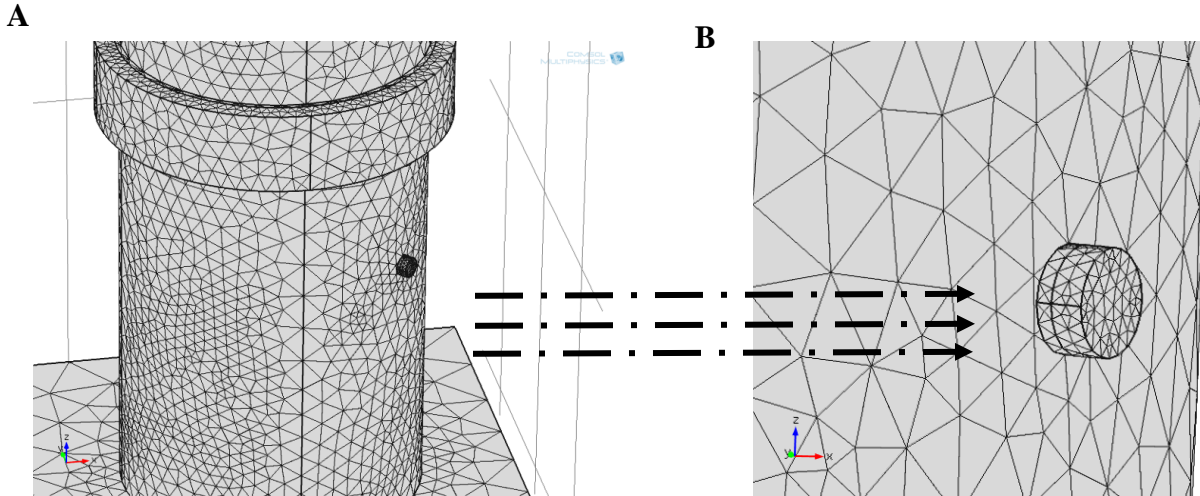


Figure B-16 Pill microphone structure and mesh

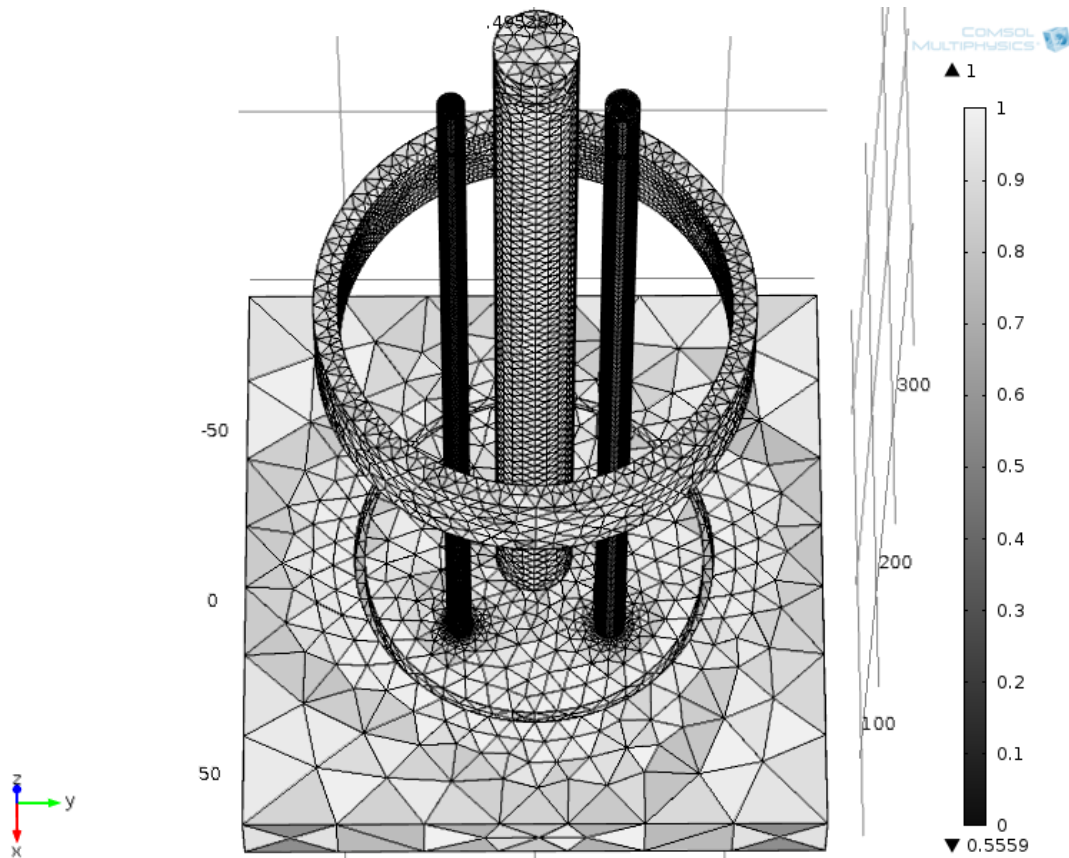
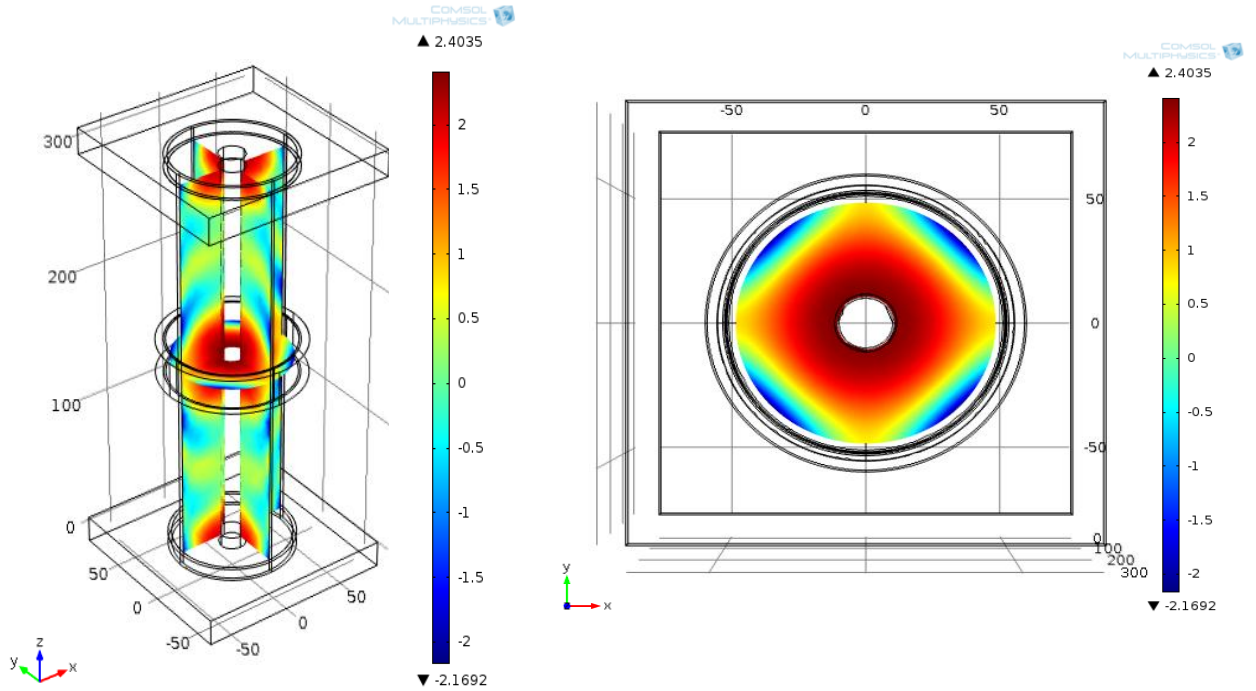


Figure B-17 Inner tubes structure and mesh

A)



B)

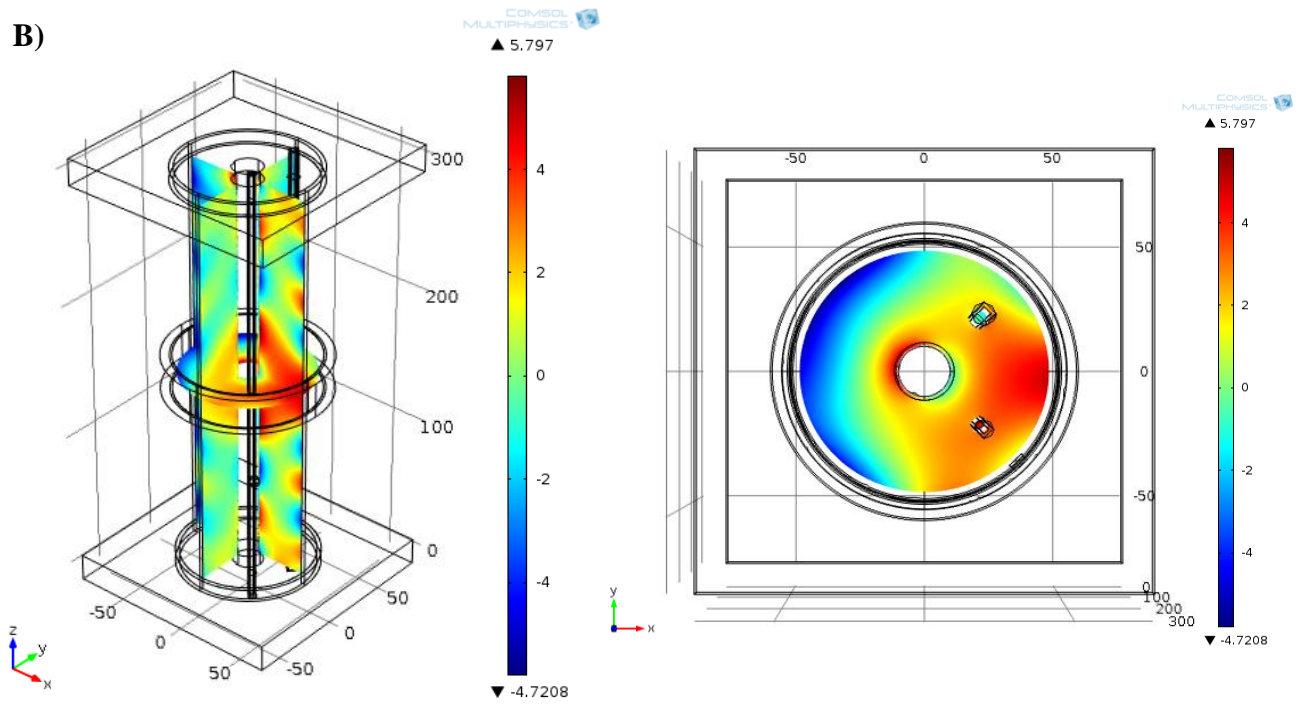


Figure B-18 Pressure profiles comparing symmetric (A) and non-symmetric (B) structures. Frequencies: 12,708 Hz and 12,694 Hz respectively